Gesellschaft für Mikro- und Nanoelektronik

The Society for Micro- and Nanoelectronics

Annual Report

2004

Vienna, November 2005

Gesellschaft für Mikro- und Nanoelektronik

The Society for Micro- and Nanoelectronics

Annual Report

2004

Society for Micro- and Nanoelectronics
c/o Vienna University of Technology
Institute of Industrial Electronics and Material Science
Gusshausstrasse 27-29/366, A-1040 Vienna, Austria

Vienna, November 2005

Editor: Karl Riedling

Layout: Claudia Benedela
Karl Riedling

ISBN: 3-901578-14-5

c/o Technische Universität Wien
Institut für Industrielle Elektronik und Materialwissenschaften
Gusshausstraße 27-29/366, A-1040 Wien

The Society for Micro- and Nanoelectronics (GMe — Gesellschaft für Mikro- und Nanoelektronik)

E. Gornik, K. Riedling

Gesellschaft für Mikro- und Nanoelektronik,
c/o Institut für Sensor- und Aktuatorsysteme,
TU Wien
Gußhausstraße 27 – 29, A-1040 Wien

Goals of the Society for Micro- and Nanoelectronics

The Society for Micro- and Nanoelectronics (GMe) has been founded in 1985 as "*Society for Microelectronics - Gesellschaft für Mikroelektronik*" with the aim to "*support microelectronics technology and its applications*" in Austria. With the shift of the focus in research from micro to nano technologies the goals of the GMe changed accordingly. Therefore, the GMe has changed its name into "*Society for Micro- and Nanoelectronics — Gesellschaft für Mikro- und Nanoelektronik*" in 2003.

The GMe defines its tasks as follows:

- Support of university-based "high-tech" research in the areas of micro- and nanoelectronics, semiconductor technology, sensors, and opto-electronics;
- Operation of research facilities;
- Support and consulting for industry, in particular, for small and medium enterprises, within the area of micro- and nanoelectronics.

The central task of the GMe is to provide an internationally competitive *infra-structure* in the area of micro- and nanoelectronics technology. The GMe allocates funds to maintain research projects in the fields of semiconductor technology, sensors, opto-electronics, and ASIC design. Thus the infra-structure support generates a base for research projects that are funded by other funding agencies.

Activities of the Society

Due to funding constraints, the present focal point activity of the GMe is the operation of university-based laboratories for microelectronics technology, where its main task is the operation of the cleanroom laboratories in Vienna and Linz. The GMe has coordinated the construction of the Center for Micro- and Nanostructures (ZMNS — *Zentrum für Mikro- und Nanostrukturen*; previously, MISZ — *Mikrostrukturzentrum*) in Vienna; the funds were supplied by the Austrian Federal Ministry of Science and Research. The GMe now finances a significant part of the operation costs for the cleanroom laboratories in Vienna and Linz.

Microelectronics Technology — Cleanroom Vienna

The following university institutes receive support within this focal point activity:

- TU Wien:
  - Institut für Festkörperelektronik
  - Institut für Sensor- und Aktuatorsysteme

Microelectronics Technology — Cleanroom Linz

The following university institutes receive support within this focal point activity:

- Johannes Kepler Universität Linz:
  - Institut für Halbleiter- und Festkörperphysik

Other Activities of the Society

In 2004, the GMe prepared its biennial seminar, the "*GMe Forum*", which meanwhile has taken place at the Vienna University of Technology on March 17 and 18, 2005. The intention of the "*GMe Forum*" is to present application-oriented results of international industrial and academic research and to indicate trends for future applications of research results. The "GMe Forum 2005" focused on the latest technologies and approaches such as carbon nanotubes, spintronics, or bioelectronics. Eight distinguished speakers from research and industry in Europe and the USA gave plenary lectures. In five invited oral and 29 poster presentations, members of the university institutes that receive support from the GMe presented their results, which would have been impossible to achieve without the contributions of the GMe to the laboratory infrastructure.

The program of the "GMe Forum 2005" was as follows:

Thursday, March 17, 2005

10:00 – 10:30 Welcome, Coffee

Opening:

10:30 – 11:00 E. GORNIK (President of the GMe)

P. SKALICKY (President of the Vienna University of Technology)

Nanoelectromechanical Systems:

11:00 – 11.45 R. BLICK: *From Classical Mechanics to Quantum-Electro-Mechanics*

11:45 – 12:30 Ch. HIEROLD: *From MEMS to NEMS*

12:30 – 14:00 Lunch Break

Micromachining with Femtolasers:

14:00 – 14:45 A. ISEMANN: *Micromachining with Femtolasers*

Bioelectronics:

14:45 – 15:30 H.U. DODT: *Bioelectronics and Bioimaging - New Approaches for the Investigation of Brain Microcircuits*

15:30 – 16:00 Coffee Break

Spintronics:

16:00 – 16:45 L. ALFF: *Spintronics: A New Spin for the World of Electronics*

Carbon Nanotubes:

16:45 – 17:30 W. HÖNLEIN: *Carbon Nanotubes – A Successor to Silicon Technology?*

17:30 – 17:45 Break

Evening Session:

17:45 – 18:00 E. GORNIK: *Presentation of the Activities of the GMe*

18:00 – 19:00 Panel Discussion: "*Who supports technology in Austria?*"

Friday, March 18, 2005

Technology:

09:00 – 09:45 R. MINIXHOFER: *Semiconductor Process Simulation*

09:45 – 10:30 H. OKORN-SCHMIDT: *Using Extreme Sono-Effects to Improve on the Selectivity of Particle Removal to Microelectronic Structure Damage below 65 nm*

10:30 – 11:00 A. LUGSTEIN: *Focused Ion Beam Technology*

11:00 – 11:30 Coffee Break

Quantum Devices:

11:30 – 12:00 T. MÜLLER: *Carrier Dynamics at Quantum Dots*

Opto-Electronics:

12:00 – 12:30 K. HINGERL**:** *Photonic Crystals: Optical materials for the 21st century*

12:30 – 13:00 G. SPRINGHOLZ**:** *Lead-Salt Lasers*

Sensors:

13:00 – 13:30 D. ROCHA: *Sensor Interface Electronics*

Poster Exhibition:

13:30 Snacks and Poster Exhibition

One of the declared tasks of the GMe is to provide information on current Austrian academic activities in the field of microelectronics to industry, in particular to Austrian small- and medium enterprises (SMEs). To enhance the distribution of the results of the research work done with GMe support, the GMe has put the contents of its annual reports — 1995 through 2004 — and the proceedings of the latest seminars organized by the GMe on its Web server. This server provides a variety of search facilities into the reports, thus acting as a Microelectronics Knowledge Base. The GMe Web server is available under the address:

http://gme.tuwien.ac.at/

The Annual Report for 2004 of the Society for Micro- and Nanoelectronics

The GMe is currently supporting the microelectronics technology activities of the cleanroom laboratories in Vienna and Linz. All projects described in this report were carried out in the cleanrooms in Vienna and Linz, respectively. They are *not* specific projects of the GMe but were funded by a variety of other sources. They all have in common that they use the infra-structure provided by the GMe. It would therefore not have been possible to carry out these projects without the support by the GMe.

Contents

Microelectronics Technology — Cleanroom Vienna

Cleanroom Vienna

G. Strasser

Center for Micro- and Nanostructures
of the Vienna University of Technology,
Floragasse 7, A-1040 Vienna, Austria

In this annual report a summary of the main activities in the ZMNS TU Wien (*Zentrum für Mikro- und Nanostrukturen der Technischen Universität Wien*) during the year 2004 will be given. Within this report we describe projects making intensive use of the cleanroom and the available technologies within. This includes state of the art growth of III-V nanostructures and silicon processing, structuring techniques utilizing standard contact lithography, the production of patterned masks, ion milling as well as dry etching and plasma enhanced chemical vapor deposition, electron beam writing, focused ion beam etching and depositing, and various metallization techniques. A major part of the mission of the ZMNS is the development and production of microelectronic, optoelectronic, and nanoelectronic prototype devices. A list of the people involved in the cleanroom activities is added. The list of scientific publications published last year is a direct measure of the activities within the ZMNS cleanroom.

Introduction

An overview of the main research efforts with a high need of technological input is presented within this scientific report. This summary includes the majority of experimental projects of the solid state electronics institute (*Festkörperelektronik TU Wien*) during the last twelve months. All the projects described below like transport studies in low dimensional semiconductor nanostructures, scanning probe spectroscopy, realization of new and improved optoelectronic devices, quantum cascade lasers, THz sources, and the characterization of microelectronic devices take full advantage of the technologies installed in the cleanroom of the ZMNS (*Reinraum des Zentrums für Mikro-und Nanostrukturen der TU Wien*). A detailed up-to-date list of the existing cleanroom equipment including benchmark data are given on the actual webpage of the cleanroom (http://zmns.tuwien.ac.at/).

To structure the yearly increasing number of various activities within the cleanroom of the ZMNS, six research areas are introduced, namely:

- Optoelectronics & THz technology
- Quantum Dots
- Transport in III-V Semiconductors
- Silicon Device Testing
- Focused Ion Beam Developments
- Novel Characterization Techniques and Devices

To satisfy this variety of topics and demonstrate e.g. optoelectronic devices as well as basic research and the development of new tools for semiconductor industries, different technologies have to be kept at state of the art performance.

This includes growth of semiconductor nanostructures (molecular beam epitaxy), as well as a complete process line including structure definition (lithography), structure transfer (reactive ion etching, focused ion beam etching, ion milling, wet chemical etch-

ing techniques) and coating with metals and/or dielectrics (plasma-enhanced chemical vapor deposition, sputtering, electron gun evaporation, focused ion beam deposition). Surface morphology as well as local carrier concentrations probing is done with a conventional Atomic Force Microscope (AFM) in combination with a Scanning Capacitance Microscopy (SCM) extension.

All the equipment necessary for the above mentioned technologies needs the cleanroom environment (cooling, filtered air, constant temperature and humidity, high quality water, different inert gases) as well as periodic maintenance of the equipment and the cleanroom itself, e.g. pumping systems (rotary pumps, turbo pumps), exhaust filtering, liquid nitrogen, and cleaning and repair. Testing of the cleanroom quality and adjustment (laminar airflow, filters, cooling, humidity, and temperature) is done periodically.

For a more general overview the listed projects and the attached publication list may give more insides on the broad range of activities in our facility.

Research Activities

Optoelectronics and THz technology

G. FASCHING *et al.* (TU Vienna): "*Terahertz Quantum Cascade Lasers Operating in Magnetic Fields*"

M. AUSTERER *et al.* (TU Vienna): "*Surface-Emitting Single-Mode Quantum Cascade Lasers*"

Quantum Dots

W. BREZNA *et al.* (TU Vienna): "*Quantitative Scanning Capacitance Spectroscopy on GaAs and InAs Quantum Dots*"

G. FASCHING *et al.* (TU Vienna): "*Photocurrent Spectroscopy of Single InAs/GaAs Quantum Dots*"

T. MÜLLER *et al.*: "*Carrier Dynamics in Quantum Dots*"

F.F. SCHREY *et al.* (TU Vienna): "*Ultrafast Intersublevel Spectroscopy of a Single Quantum Dot*"

Transport in III-V Semiconductors

D. RAKOCZY *et al*. (TU Vienna): "*Cross Sectional Ballistic Electron Emission Microscopy for Schottky Barrier Height Profiling on Heterostructures*"

Silicon Device Testing

V. DUBEC *et al*. (TU Vienna): "*Thermal Imaging at Multiple Time Instants for Study of Self-Heating and ESD Phenomena*"

J. KUZMÍK *et al*. (TU Vienna): "*Degradation Mechanisms in AlGaN/GaN HEMTs under Electrostatic Discharge*"

Focused Ion Beam Developments

M. FISCHER *et al*. (TU Vienna): "*Direct-Write Deposition Utilizing a Focused Electron Beam*"

A. LUGSTEIN *et al*. (TU Vienna): "*A New Approach for the Formation of Size and Site Controlled Metallic Nano Dots Seeded by Focused Ion Beams*"

Novel Characterization Techniques and Devices

S. GOLKA et al. (TU Vienna): "*Inductively Coupled Plasma Reactive Ion Etching of GaN*"

Project Information

Project Manager

Associate Prof. Dr. G. Strasser

Institute of Solid State Electronics,
Floragasse 7, A-1040 Vienna

Project Group

Last Name	First Name	Status	Remarks
Andrews	A. Maxwell	postdoc	
Auer	Erwin	dissertation	
Austerer	Maximilian	dissertation	
Bae	Kim Heung	dissertation	
Bertagnolli	Emmerich	o. prof.	
Blaho	Matej	dissertation	
Bychikhin	Sergey	postdoc	
Brezna	Wolfgang	dissertation	
Coquelin	Michael	dissertation	
Dalibor	Kovac	dissertation	
Darmo	juraj	postdoc	
Dominizi	Karl	student	
Dubec	Viktor	dissertant	
Dzigal	Elvira	technician	
Fasching	Gernot	dissertation	
Fischer	Markus	dissertation	
Golka	Sebastian	dissertation	
Gornik	Erich	o. prof.	
Gottsbachner	Josef	student	
Gruber	Karl	student	
Hagl	Peter	student	
Harasek	Stefan	dissertation	
Hobler	Gerhard	ao. prof.	
Kast	Michael	dissertation	
Kröll	Josef	student	
Kröll	Peter	technician	
Kuzmik	Ian	postdoc	
Langfischer	Helmut	dissertation	
Lugstein	Alois	univ. ass.	

Last Name	First Name	Status	Remarks
Müller	Thomas	dissertation	
Otto	Gustav	dissertation	
Pacher	Christoph	dissertation	
Pogany	Dionyz	ao. prof.	
Prinzinger	Johannes	technician	
Pflügl	Christian	dissertation	
Rakoczy	Doris	dissertation	
Riegler	Erich	technician	
Roch	Tomas	postdoc	
Schartner	Stefan	student	
Schinnerl	Markus	technician	
Schenold	Helmut	technician	
Schramböck	Matthias	dissertation	
Schrenk	Werner	cleanroom director	
Schrey	Frederik	dissertation	
Schwaha	Philipp	student	
Smoliner	Jürgen	ao. prof.	
Steinesberger	Gernot	dissertant	
Strasser	Gottfried	ao. prof.	
Tamosiunas	Vincas	postdoc	
Unterrainer	Karl	prof.	
Wanzenböck	Heinz	univ. ass.	
Zahel	Thomas	student	
Zobl	Reinhard	postdoc	

Books and Contributions to Books

1. S Anders, G. Strasser, E. Gornik:
   "*Long wavelength laser diodes*";
   in: "Handbook of Laser Technology and Applications", IoP Publishing, Bristol. UK, 2004, S. 271 - 286.

Publications in Reviewed Journals

2. S. Anders, W. Schrenk, T. Roch, C. Pflügl, G. Strasser:
   "*Tuning quantum-cascade lasers by postgrowtz rapid thermal processing*";
   Applied Physics Letters, **84** (2004), 2; S. 164 - 166.
3. S. Anders, V. Tamosiunas, W. Schrenk, G. Strasser:
   "*Optical modes in mesoscopic quantum cascade ring lasers*";
   Physical Review B, **69** (2004), S. 0733091 - 0733093.
4. Y. Baryshnikov, P. Heider, W. Parz, V. Zharnitsky:
   "*Whispering Gallery Modes Inside Aymmetric Resonant Cavities*";
   Physical Review Letters, **93** (2004), 13; S. 1339021 - 1339024.

5. B. Basnar, H. Hirner, E. Gornik, G. Strasser:
"*Fast characterisation of InAs quantum dot structures using AFM*";
Journal of Crystal Growth, **264** (2004), S. 26 - 30.

6. B. Basnar, A. Lugstein, E. Bertagnolli, E. Gornik:
"*Spectroscopic ellipsometry study of focused ion beam induced GaAs surface modification*";
Thin Solid Films, **1** (2004), S. 540 - 544.

7. M. Blaho, L. Zullino, H. Wolf, R. Stella, A. Andreini, H. Gieser, D. Pogany, E. Gornik:
"*Internal Behavior of BCD ESD Protection Devices Under TLP and Very-Fast TLP Stress*";
IEEE Transactions on Device and Materials Reliability, **4** (2004), 3; S. 535 - 541.

8. S. Bychikhin, V. Dubec, D. Pogany, E. Gornik, M. Graf, V. Dudek, W. Soppa:
"*Transient interferometric mapping of smart power SOI ESD protection devices under TLP and vf-TLP stress*";
Microelectronics Reliability, **44** (2004), S. 1687 - 1692.

9. J. Darmo, T. Müller, W. Parz, J. Kröll, G. Strasser, K. Unterrainer:
"*Few-cycle terahertz generation and spectroscopy of nanostruture*";
Philosophical Transactions of the Royal Society of London A, **362** (2004), S. 251 - 262.

10. J. Darmo, V. Tamosiunas, G. Fasching, J. Kröll, K. Unterrainer, M. Beck, M. Giovannini, J. Faist, C. Kremser, P. Debbage:
"*Imaging with a Terahertz quantum cascade laser*";
Optics Express, **12** (2004), 9; S. 1879 - 1884.

11. M. Denison, M. Blaho, P. Rodin, V. Dubec, D. Pogany, D Silber, E. Gornik, M. Stecher:
"*Moving Current Filaments in Integrated DMOS Transistors Under Short-Duration Current Stress*";
IEEE Transactions on Electron Devices, **51** (2004), 10; S. 1695 - 1703.

12. V. Dubec, S. Bychikhin, M. Blaho, M. Heer, D. Pogany, M. Denison, N. Jensen, M. Stecher, G. Groos, E. Gornik:
"*Multiple-time-instant 2D thermal mapping during a single ESD event*";
Microelectronics Reliability, **44** (2004), S. 1793 - 1798.

13. M. Eckhardt, A. Schwanhäußer, L. Robledo, S. Malzer, G. Döhler, M. Betz, S. Trumm, A. Leitenstorfer, T. Müller, K. Unterrainer:
"*Exotic transport regime in GaAs: absence of intervalley scattering leading to quasi-ballistic, real-space THz oscillations*";
Semiconductor Science and Technology, **19** (2004), S. 195 - 198.

14. P. Green, L.R. Wilson, E.A. Zibik, D.G. Revin, J.W. Cockburn, C. Pflügl, W. Schrenk, G. Strasser, A.B. Krysa, J.S. Roberts, C.M. Tey, A.G. Cullis:
"*High-performance distributed feedback quantum cascade lasers grown by metalorganic vapor phase epitaxy*";
Applied Physics Letters, **83** (2004), 23; S. 5529 - 5531.

15. R. Heer, J. Smoliner, J. Bornemeier, H. Brückl:
"*Ballistic electron emission microscopy on spin valve structures*";
Applied Physics Letters, **85** (2004), 19; S. 4388 - 4390.

16. C. Kranz, A. Kueng, A. Lugstein, E. Bertagnolli, B. Mizaikoff:
"Mapping of enzyme activity by detection of enzymatic products during AFM imaging with integrated SECM-AFM probes";
Ultramicroscopy, **100** (2004), S. 127 - 134.

17. J. Kröll, J. Darmo, K. Unterrainer:
"*High-performance terahertz electro-optic detector*";
Electronics Letters, **40** (2004), 12; S. 763 - 764.

18. J. Kuzmik, G. Konstantinidis, S. Harasek, S. Hascik, E. Bertagnolli, A. Georgakilas, D. Pogany:
"*ZrO2/(Al)GaN metal-oxide-semiconductor structures: characterization and application*";
Semiconductor Science and Technology, **19** (2004), S. 1364 - 1368.

19. J. Kuzmik, D. Pogany, E. Gornik, P. Javorka, P. Kordos:
"*Electrical overstress in AlGaN/GaN HEMTs: study of degradation processes*";
Solid-State Electronics, **48** (2004), S. 271 - 276.

20. A. Lugstein, B. Basnar, E. Bertagnolli:
"*Metallic nano dots realized by a subtractive self organization process*";
Superlattices and Microstructures, **36** (2004), S. 107 - 111.

21. A. Lugstein, B. Basnar, E. Bertagnolli:
"*Size and site controlled Ga nano dots on GaAs seeded by focused ion beams*";
Virtual Journal of Nanoscale Science & Technology, **9** (2004), 16.

22. A. Lugstein, B. Basnar, E. Bertagnolli:
"*Size and site controlled Ga nanodots on GaAs seeded by focused ion beams*";
Journal of Vacuum Science and Technology, **22** (2004), S. 888 - 892.

23. A. Lugstein, B. Basnar, E. Bertagnolli:
"Study of the chemical and morphological evolution of the GaAs surface after high fluence focused ion beam exposure";
Nuclear Instruments & Methods B, **217** (2004), S. 402 - 408.

24. A. Lugstein, M. Weil, B. Basnar, C. Tomastik, E. Bertagnolli:
"*A novel fabrication technique for crystallite growth on a (100) InAs surface utilizing focused ion beams*";
Nuclear Instruments & Methods B, **222** (2004), S. 91 - 95.

25. T. Müller, W. Parz, F. Schrey, G. Strasser, K. Unterrainer:
"*Intraband relaxation of photoexcited electrons in GaAs/AlGaAs quantum wells and InAs/GaAs self-assembled quantum dots*";
Semiconductor Science and Technology, **19** (2004), S. 287 - 289.

26. T. Müller, W. Parz, G. Strasser, K. Unterrainer:
"Influence of carrier-carrier interaction on time-dependent intersubband absorption in a semiconductor quantum well";
Physical Review B, **70** (2004), S. 155324-1 - 155324-5.

27. T. Müller, W. Parz, G. Strasser, K. Unterrainer:
"*Pulse-induced quantum interference of intersubband transitions in coupled quantum wells*";
Applied Physics Letters, **84** (2004), 1; S. 64 - 66.

28. C. Pacher, E. Gornik:
"Tunning of transmission function and tunneling time in finite periodic potentials";
Physica E, **21** (2004), S. 783 - 786.

29. C. Pacher, M. Kast, T. Roch, G. Strasser, E. Gornik:
"*Hot electron spectroscopy of the GaAs/AlAs/GaAs band structure*";
Semiconductor Science and Technology, **19** (2004), S. 102 - 103.

30. C. Pflügl, M. Austerer, W. Schrenk, S. Golka, G. Strasser:
"*Surface emitting quantum cascade lasers*";
Opto-Electronics Review (invited), **12** (2004), 4; S. 361 - 363.

31. C. Pflügl, W. Schrenk, S. Anders, G. Strasser:
"*Spectral dynamics of distributed feedback quantum cascade lasers*";
Semiconductor, Science and Technology, **19** (2004), S. 336 - 338.

32. D. Rakoczy, G. Strasser, C. Pacher, J. Smoliner:
"*Ballistic electron microscopy on doped AlAs barriers in the regime of the Mott transition*";
Semiconductor Science and Technology, **19** (2004), S. 8 - 10.

33. F. Rizzi, G. Scamarcio, G. Strasser:
"Three-terminal mid-IR tunable emitters based on Wannier-Stark ladder transitions in semiconductor superlattices";
Semiconductor Science and Technology, **19** (2004), S. 87 - 88.

34. D Schneider, C Brink, A. Schlachetzki, G. Ploner, G. Strasser, E. Gornik:
"*Tuned transition from a quantum well to a quantum wire investigated by magnetophonon resonance*";
Japanese Journal of Applied Physics, **95** (2004), S. 2509 - 2517.

35. F. F. Schrey, G. Fasching, T. Müller, G. Strasser, K. Unterrainer:
"*Optically induced intraband electron transfer in self-assembled InAs quantum dots*";
Physica Status Solidi (c), **1** (2004), S. 434 - 437.

36. F. Schrey, T. Müller, G. Fasching, S. Anders, C. Pflügl, W. Schrenk, G. Strasser, K. Unterrainer:
"*Intersublevel dynamics of semiconductor nanostructures*";
Physica E, **25** (2004), S. 271 - 279.

37. A. Schröder, S. Harasek, M. Kupnik, M. Wiesinger, E. Gornik, E. Benes, M. Gröschl:
"*A Capacitance Ultrasonic Transducer for High-Temperature Applications*";
IEEE Transactions on Ultrasonics, Ferroelectrics, and Frequency Control, **51** (2004), 7; S. 896 - 907.

38. J. Smoliner, D. Rakoczy, M. Kast:
"*Hot electron spectroscopy and microscopy*";
Reports on Progress in Physics, **67** (2004), S. 1863 - 1914.

39. V. Spagnolo, G. Scamarcio, W. Schrenk, G. Strasser:
"*Influence of the band-offset on the electronic temperature of GaAs/Al(Ga)As superlattice quantum cascade lasers*";
Semiconductor Science and Technology, **19** (2004), S. 110 - 112.

40. V. Tamosiunas, R. Zobl, G. Fasching, J. Ulrich, G. Strasser, K. Unterrainer, R. Colombelli, C. Gmachl, K. West, L. Pfeiffer, F. Capasso:
"*Magnetic field effects in terahertz quantum-cascade lasers*";
Semiconductor, Science and Technology, **19** (2004), S. 348 - 350.

Conference Publications

1. M. Austerer, C. Pflügl, W. Schrenk, T. Roch, G. Strasser:
"*Surface Emitting Quantum Cascade Laser*";
in: "*GMe Annual Report 2003*", Gesellschaft für Mikro- und Nanoelektronik, 2004, 3-901578-12-9, S. 31.

2. M. Coquelin, R. Zobl, G. Strasser, E. Gornik:
"Plasmon Enhanced THz Emission";

in: “GMe Annual Report 2003”, Gesellschaft für Mikro- und Nanoelektronik, 2004, 3-901578-12-9, S. 49.

3. M. Coquelin, R. Zobl, G. Strasser, E. Gornik:
“Recent Structures for Plasma Instability Search”;
in: “GMe Annual Report 2003”, Gesellschaft für Mikro- und Nanoelektronik, 2004, 3-901578-12-9, S. 117 - 119.

4. J. Darmo, G. Strasser, J. Kröll, K. Unterrainer:
“Heterostructure-Based Photoconductive Terahertz Emitters”;
in: “GMe Annual Report 2003”, Gesellschaft für Mikro- und Nanoelektronik, 2004, 3-901578-12-9, S. 53.

5. G. Fasching, F. Schrey, G. Strasser, K. Unterrainer:
“Photocurrent and Photoluminescence Measurements of InAs Quantum Dots”;
in: “GMe Annual Report 2003”, Gesellschaft für Mikro- und Nanoelektronik, 2004, 3-901578-12-9, S. 65.

6. S. Golka, W. Schrenk, G. Strasser:
“Fabrication of Dry Etched Planar Photonic Crystals for THz Regime”;
in: “GMe Annual Report 2003”, Gesellschaft für Mikro- und Nanoelektronik, 2004, 3-901578-12-9, S. 45.

7. M. Kast, C Pacher, M. Coquelin, W Boxleitner, G. Strasser, E. Gornik:
“High-Resolution Hot -Electron Spectroscopy in Parallel Magnetic Fields”;
in: “GMe Annual Report 2003”, Gesellschaft für Mikro- und Nanoelektronik, 2004, 3-901578-12-9, S. 71.

8. T. Müller, F. Schrey, G. Fasching, G. Strasser, K. Unterrainer:
“Ultrafast Intraband Dynamics in InAs/GaAs Quantum Dots”;
in: “GMe Annual Report 2003”, Gesellschaft für Mikro- und Nanoelektronik, 2004, 3-901578-12-9, S. 59.

9. C. Pflügl, M. Litzenberger, W. Schrenk, D. Pogany, E. Gornik, G. Strasser:
“Interferometric Temperature Mapping of GaAs-based Quantum Cascade Laser”;
in: “GMe Annual Report 2003”, Gesellschaft für Mikro- und Nanoelektronik, 2004, 3-901578-12-9, S. 33.

10. G. Pillwein, G. Brunthaler, G. Strasser:
“Fabrication and Characterization of Lateral Quantum Dots in GaAs Heterostructures”;
in: “GMe Annual Report 2003”, Gesellschaft für Mikro- und Nanoelektronik, 2004, S. 67.

11. D. Rakoczy, G. Strasser, J. Smoliner:
“BEEM/BEES Investigations on AlAs/GaAs Single Barriers and RTDs”;
in: “GMe Annual Report 2003”, Gesellschaft für Mikro- und Nanoelektronik, 2004, 3-901578-12-9, S. 75.

12. T. Roch, W. Schrenk, S Anders, C. Pflügl, G. Strasser:
“X-Ray Investigatin of Interface Broadening by Rapid Thermal Processing”;
in: “GMe Annual Report 2003”, Gesellschaft für Mikro- und Nanoelektronik, 2004, 3-901578-12-9, S. 109.

13. W. Schrenk, S Anders, T. Roch, C. Pflügl, G. Strasser:
“Tuning Quantum-Cascade Lasers by Postgrowth Rapid Thermal Processing”;
in: “GMe Annual Report 2003”, Gesellschaft für Mikro- und Nanoelektronik, 2004, 3-901578-12-9, S. 37.

14. F. Schrey, G. Fasching, T. Müller, G. Strasser, K. Unterrainer:
“Confocal Micro-Photoluminescence and Micro-Photoluminescence Excitation

Spectroscopy on Single Self Assembled InAs Quantum Dots";
in: "GMe Annual Report 2003", Gesellschaft für Mikro- und Nanoelektronik, 2004, 3-901578-12-9, S. 61.

15. P Schwaha, S Anders, V Tamosiunas, W. Schrenk, G. Strasser:
"Light Field in Quantum Cascade Ring Lasers";
in: "GMe Annual Report 2003", Gesellschaft für Mikro- und Nanoelektronik, 2004, 3-901578-12-9, S. 39.

16. V Tamosiunas, R. Zobl, G. Fasching, J. Ulrich, G. Strasser, K. Unterrainer, R. Colombelli, C. Gmachl, L. Pfeiffer, K. West, F. Capasso:
"Terahertz Quantum-Cascade Lasers in a Magnetic Field";
in: "GMe Annual Report 2003", Gesellschaft für Mikro- und Nanoelektronik, 2004, 3-901578-12-9, S. 41.

Presentations with Proceedings

1. M. Austerer, C. Pflügl, W. Schrenk, T. Roch, G. Strasser:
"*Surface emitting quantum cascade laser*";
Talk: Workshop on Compound Semiconductor Devices and Integrated Circuits (WOCSDICE), Smolinice Castle, Slovakia; 17.05.2004 - 19.05.2004; in: "*Proceedings of WOCSDICE 2004*", (2004), S. 63 - 64.

2. S. Bychikhin, L.K.J. Vandamme, J. Kuzmik, G. Meneghesso, D. Pogany:
"*Low frequency noise characterization of the GaN LEDs*";
Talk: 5th International Conference on Advanced Semiconductor Devices and Microsystems, Smolenice Castle, Slovakia; 17.10.2004 - 21.10.2004; in: "*IEEE Proceedings of ASDAM 2004*", (2004), S. 85 - 86.

3. J. Darmo, J. Kröll, M. Hulman, K. Unterrainer, H. Kuzmany:
"*Terahertz time-domain linear spectroscopy of single-walled carbon nanotube film*";
Talk: International Conference on Advanced Semiconductor Devices and Microsystems (ASDAM), Smolenice, Slovakia; 17.10.2004 - 21.10.2004; in: "*IEEE Conference Proceedings of the 5th International Conference on Advanced Semiconductor Devices and Microsystems 2004 04 EX876*", (2004), ISBN 0-7803-8535-7; S. 239 - 242.

4. J. Darmo, J. Kröll, K. Unterrainer:
"*Time and frequency resolved THz spectroscopy of micro- and nano-systems*";
Talk: 12th International Symposium on Ultrafast Phenomena in Semiconductors, Vilnius, Lithuania (invited); 22.08.2004 - 25.08.2004; in: "*Book of Abstracts*", (2004), ISBN 9986-9284-4-3; S. 13.

5. J. Darmo, J. Kröll, K. Unterrainer, M. Hulman, H. Kuzmany:
"*Terahertz time-resolved linear spectroscopy of single-wall carbon nanotube films*";
Talk: CLEO/IQEC 2004, San Franisco, USA; 16.05.2004 - 21.05.2004; in: "*Technical Digest*", (2004), Paper-Nr. JMB7, 2 S.

6. J. Darmo, J. Kröll, K. Unterrainer, M. Hulman, H. Kuzmany:
"*Absorption of single-wall carbon nanotubes at Terahertz frequencies*";
Poster: 12th International Conference on Terahertz Electronics, Karlsruhe, Deutschland; 27.09.2004 - 01.10.2004; in: "*IEEE Conference Digest of the 2004 IRMMW 2004/THz 2004 04EX857*", (2004), ISBN 0-7803-8490-3; S. 409 - 410.

7. J. Darmo, V. Tamosiunas, J. Kröll, T. Müller, G. Strasser, K. Unterrainer, R. Colombelli, C. Gmachl, K. West, L. Pfeiffer:
"*THz quantum cascade lasers: magnetic field effects and waveguide properties*";

Talk: 2004 MRS Fall Meeting, Boston, USA; 29.11.2004 - 03.12.2004; in: "*Abstracts*", (2004), S. 46.

8. V. Dubec, S. Bychikhin, D. Pogany, E. Gornik, N. Jensen, M. Stecher, G. Groos: "*Error Analysis in Phase Extracton in a 2D Hologrphic Imaging of Semiconductor Devices*";
   Talk: SPIE Conference, San Jose, California, USA; 18.01.2004 - 21.01.2004; in: "*Proceedings of the SPIE Vol.5290*", (2004), S. 233 - 241.
9. G. Fasching, W. Brezna, J. Smoliner, G. Strasser, K. Unterrainer: "*Photocurrent spectroscopy of single InAs/GaAs quantum dots*";
   Talk: Int. Conf. on Superlattices, Nanostructures and Nanodevices (ICSNN), Cancun, Mexico; 19.07.2004 - 23.07.2004; in: "*Programm & Abstracts*", (2004), S. 119 - 120.
10. S. Golka, M. Austerer, C. Pflügl, W. Schrenk, G. Strasser: "*Processing of Deeply etched GaAs/AlGaAs quantum casdade lasers with grating structures*";
    Talk: 2004 MRS Fall Meeting, Boston, USA; 29.11.2004 - 03.12.2004; in: "*Mater. Res. Soc: Symp. Proc. Vol 829*", (2004), S. 1 - 5.
11. S. Golka, W. Schrenk, G. Strasser: "*High aspect ratio etching with SiCl4 plasma for THz Photonic Crystals in GaAs*";
    Talk: Workshop on Compound Semiconductor Devices and Integrated Circuits (WOCSDICE), Smolenice Castle, Slovakia; 17.05.2004 - 19.05.2004; in: "*Proceeding of WOCSDICE 2004*", (2004), S. 127 - 128.
12. G. Hobler: "*Simulation of Focused Ion Beam Milling*";
    Talk: SEM X Int. Congress & Exposition on Experimental and Applied Mechanics, Costa Mesa, CA; 07.06.2004 - 10.06.2004; in: "*Proc. 5th Int. Symp. MEMS and Nanotechnology*", (2004), S. 46 - 51.
13. G. Hobler, A. Lugstein, W. Brezna, E. Bertagnolli: "*Simulation of focused ion beam induced damage formation in crystalline silicon*";
    Poster: Materials Research Society Fall Meeting (MRS), Boston/MA, USA; 01.12.2003 - 05.12.2003; in: "*Proceedings of MRS Fall Meeting 2003*", (2004), 6 S.
14. J. Kröll, J. Darmo, K. Unterrainer: "*Properties of ultra thin metal layers in the THz region*";
    Poster: Terahertz Workshop 2004 Technology and Application, Freiburg, Germany; 17.02.2004; in: "*Book of Abstracts*", (2004), S. 16.
15. J. Kröll, J. Darmo, K. Unterrainer: "*Terahertz electrodynaics of ultra thin Cr layers*";
    Talk: The 28th Workshop on Compound Semiconductor Devices and Integrated Circuits held in Europe, Smolenice, Slovakia; 17.05.2004 - 19.05.2004; in: "*WOCSDICE 2004*", (2004), ISBN 80-227-2050-X; S. 125 - 126.
16. J. Kröll, J. Darmo, K. Unterrainer: "*Terahertz spectroscopy of vibrational modes of molecular crystal of sucrose*";
    Talk: 11th International Conference of Terahertz Electronics, Karlsruhe, Deutschland; 27.09.2004 - 01.10.2004; in: "*IEEE Conference Digest of the 2004 IRMMW 2004/THz 2004 04EX857*", (2004), ISBN 0-7803-8490-3; S. 89 - 90.
17. J. Kröll, J. Darmo, K. Unterrainer: "*Ultra-thin metallic layers studied by broadband Terahertz time-domain spectroscopy*";
    Talk: 12th International Conference on Terahertz Electronics, Karlsruhe, Deutschland; 27.09.2004 - 01.10.2004; in: "*Conference Digest of the 2004 Joint*

29th International Conference on Terahertz Electronics", (2004), ISBN 0-7803-8490-3; S. 465 - 466.

18. J. Kröll, J. Darmo, K. Unterrainer:
"*High resolution Terahertz time-domain spectroscopy*";
Talk: CLEO/IQEC 2004, San Francisco, USA; 16.05.2004 - 21.05.2004; in:
"*Technical Digest*", (2004), Paper-Nr. JMB5, 2 S.

19. J. Kuzmik, S. Harasek, G. Constantinidis, S. Hascik, D. Pogany, E. Bertagnolli, A. Georgakilas:
"*Zr02/GaN metal oxide semiconductor structures characterization and application*";
Talk: Workshop on Compound Semiconductor Devices and Integrated Circuits (WOCSDICE), Smolenice Castle, Slovakia; 17.05.2004 - 19.05.2004; in:
"*Wocsdice 2004*", (2004), S. 35 - 36.

20. P Moens, S. Bychikhin, K Reynders, D. Pogany, M Zubeidat:
"*Effects of Hot Spot Hopping and Drain Ballasting in Integrated Vertical DMOS Devices under TLP Stress*";
Talk: International Reliability Physics Symposium (IRPS), Phoenix, USA; 25.04.2004 - 29.04.2004; in: "*Proceedings of the IRPS 2004*", (2004), S. 241 - 246.

21. P Moens, K Reynders, S. Bychikhin, D. Pogany, M Zubeidat:
"Optimization of Integrated Vertical DMOS Transistors for ESD Robustness";
Talk: ISPSD, Kitakyushu, Japan; 24.05.2004 - 27.05.2004; in: "Proceeding of 2004 International Symposium on Power Semiconductor Devices & ICs", (2004), S. 221 - 224.

22. T. Müller, F. Schrey, C. Pflügl, G. Strasser, K. Unterrainer:
"*Ultrafast intraband dynamics in quantum dots*";
Talk: CLEO/IQEC 2004, San Francisco, USA; 16.05.2004 - 21.05.2004; in:
"*Technical Digest*", (2004), Paper-Nr. IThJ4, 2 S.

23. G. Otto, G. Hobler:
"Coupled kinetic Monte Carlo and molecular dynamics simulations of implant damage accumulation in silicon";
Poster: Materials Research Society Fall Meeting (MRS), Boston/MA, USA; 01.12.2003 - 05.12.2003; in: "Proceedings of MRS Fall Meeting 2003", (2004), S. 1 - 6.

24. C. Pflügl, S. Golka, M. Austerer, W. Schrenk, A. M. Andrews, G. Strasser:
"*Surface Emitting Quantum Cascade Lasers*";
Talk: International Conference on Infrared and Millimeter Waves, Karlsruhe, Deutschland (invited); 27.09.2004 - 01.10.2004; in: "*Conference Digest of the IRMMW 2004*", (2004), S. 157 - 158.

25. C. Pflügl, S. Golka, M. Austerer, W. Schrenk, G. Strasser:
"*High power surface emitting quantum cascade lasers*";
Talk: Int. Conf. on Superlattices, Nanostructures and Nanodevices (ICSNN), Cancun, Mexico; 19.07.2004 - 23.07.2004; in: "*Programm and Abstracts*", (2004), S. 33 - 34.

26. C. Pflügl, T. Müller, W. Schrenk, T. Roch, M. Kast, F. Schrey, K. Unterrainer, G. Strasser:
"*Intraband dynamics and transitions in quantum dot structures*";
Talk: Workshop on Compound Semiconductor Devices and Integrated Circuits (WOCSDICE), Smolenice Castle, Slovakia; 17.05.2004 - 19.05.2004; in:
"*Proceeding of the WOCSDICE 2004*", (2004), S. 59 - 61.

27. W. Schrenk, C. Pflügl, S. Golka, T. Roch, G. Strasser:
"*GaAs/AlGaAs based Quantum Cascade Lasers*";

Talk: International Conference on Infrared and Millimeter Waves, Karlsruhe, Deutschland; 27.09.2004 - 01.10.2004; in: "*Confernce Digest of the IRMMW 2004*", (2004), S. 281 - 282.

28. F. F. Schrey, T. Müller, G. Fasching, G. Strasser, K. Unterrainer:
"*Ultrafast intersublevel spectroscopy on InAs/GaAs Quantum dots*";
Talk: Quantum Dots 2004, Banff, Canada; 10.05.2004 - 13.05.2004; in: "*Program and Book of Abstracts*", (2004), S. 135.

29. F. Schrey, G. Fasching, T. Müller, C. Pflügl, T. Roch, K. Unterrainer, G. Strasser:
"*Quantum dot inter-sublevel devices*";
Poster: 13th International Winterschool on New Developments in Solid State Physics, Mauterndorf, Salzburg, Austria; 15.02.2004 - 20.02.2004; in: "*Book of Abstracts*", (2004), S. 119.

30. F. Schrey, D. Nguyen, T. Müller, L. Rebohle, N. Regnault, R. Ferreira, G. Bastard, G. Strasser, K. Unterrainer:
"*IR quantum dot detectors with miniband tunnel extraction*";
Talk: 12th International Conference on Terahertz Electronics, Karlsruhe, Deutschland; 27.09.2004 - 01.10.2004; in: "*IEEE Conference Digest of the 2004 IRMMW 2004/THz 2004 04EX857*", (2004), ISBN 0-7803-8490-3; S. 245 - 246.

31. V. Tamosiunas, S. Anders, T. Müller, W. Schrenk, G. Strasser, K. Unterrainer:
"*THz quantum cascade lasers: From quantum wells to quantum boxes*";
Talk: Colorado Meeting on Fundamental Optical Processes in Semiconductors (FOBS), Colorado, USA (invited); 08.08.2004 - 13.08.2004; in: "*Proceedings for the Colorado Meeting on Fundamental Optical Processes in Semiconductors*", (2004), S. 1.

32. V. Tamosiunas, G. Fasching, J. Darmo, J. Kröll, G. Strasser, K. Unterrainer, R. Colombelli, C. Gmachl, K. West, L. Pfeiffer, F. Capasso:
"*Magnetic quantization in terahertz Quantum cascade lasers*";
Poster: 13th International Winterschool on New Developments in Solid State Physics, Mauterndorf, Austria; 15.02.2004 - 20.02.2004; in: "*Book of Abstracts*", (2004), S. 120.

33. V. Tamosiunas, Z. Kancleris, M. Dagys, R. Simniskis, M. Tamosiuniene, G. Valusis, G. Strasser, K. Unterrainer:
"*Finite-difference time-domain simulation of mid- and far-infrared quantum cascade lasers*";
Talk: 12th International Symposium on Ultrafast Phenomena in Semiconductors, Vilnius, Lithuania; 22.08.2004 - 25.08.2004; in: "*Book of Abstracts*", (2004), ISBN 9986-9284-4-3; S. 24.

34. V. Tamosiunas, R. Zobl, G. Fasching, G. Strasser, K. Unterrainer, R. Colombelli, C. Gmachl, L. Pfeiffer, K. West, F. Capasso:
"*Magnetic modulation of THz quantum cascade lasers*";
Talk: 12th International Conference on Terahertz Electronics, Karlsruhe, Deutschland; 27.09.2004 - 01.10.2004; in: "*IEEE Conference Digest of the 2004 IRMMW 2004/THz 2004 04EX857*", (2004), ISBN 0-7803-8490-3; S. 541 - 542.

35. K. Unterrainer:
"*Few-cycle terahertz generation and spectroscopy of nanostructures*";
Talk: 12th International Symposium on Ultrafast Phenomena in Semiconductors, Vilinius, Lithuania (invited); 22.08.2004 - 25.08.2004; in: "*Book of Abstracts*", (2004), ISBN 9986-9284-4-3; S. 3.

36. K. Unterrainer:
"*Field control of quantum cascade lasers*";
Talk: 3rd Akasaki Research Center Symposium: 2004 International (To the New

Horizon of the Nitride Research), Nagoya, Japan; 05.03.2004; in: "*Book of Abstracts*", (2004), S. 28.

37. K. Unterrainer:
"*Field control of THz quantum cascade lasers*";
Talk: International Workshop on Quantum Cascade Lasers, Seville, Spain (invited); 04.01.2004 - 08.01.2004; in: "*Abstract Book*", (2004), S. 55.

38. K. Unterrainer, J. Darmo, J. Kröll, T. Müller, G. Strasser, T. Le, A. Stingl:
"*Cavity enhanced THz generation*";
Talk: Photonics West, San Jose, CAL, USA (invited); 24.01.2004 - 29.01.2004; in: "*Technical Summary Digest*", (2004), S. 401.

39. K. Unterrainer, T. Müller, J. Darmo, G. Strasser:
"*Few-cycle THz generation and spectroscopy of nanostructures*";
Talk: The 28th Workshop on Compound Semiconductor Devices and Integrated Circuits held in Europe, Smolenice, Slovakia (invited); 17.05.2004 - 19.05.2004; in: "*WOCSDICE 2004*", (2004), ISBN 80-227-2050-X; S. 117.

40. K. Unterrainer, T. Müller, F. Schrey, G. Fasching, C. Pflügl, G. Strasser:
"*Interlevel dynamics in semiconductor nanostructures*";
Talk: 13th International Winterschool on New Developments in Solid State Physics, Mauterndorf, Austria (invited); 15.02.2004 - 20.02.2004; in: "*Book of Abstracts*", (2004), S. 40.

41. L.R. Wilson, P. Green, A.B. Krysa, J.S. Roberts, H. Ng, D.G. Revin, C. Pflügl, W. Schrenk, G. Strasser, J.W. Cockburn:
"*High-performance quantum cascade lasers grown by metal-orgnic vapor phase epitaxy*";
Talk: SPIE Conference, Denver, USA; 01.08.2004 - 06.08.2004; in: "*Proc. SPIE Int. Soc. Opt. Eng.*", 5564 (2004), S. 156.

42. M. Wörner, F. Eickemeyer, K. Reimann, T. Elsaesser, S. Barbieri, C. Sirtori, T. Müller, R. Bratschitsch, K. Unterrainer, G. Strasser:
"*Coherent vs. incoherent charge transport in semiconductor quantum cascade structures*";
Talk: SPIE Conference, Denver, USA; 01.08.2004 - 06.08.2004; in: "*Proc. SPIE Int. Soc. Opt. Eng.*", 5352 (2004), S. 333.

43. R. Zobl, V. Tamosiunas, G. Fasching, J. Ulrich, G. Strasser, K. Unterrainer, R. Colombelli, C. Gmachl, L. Pfeiffer, K. West, F. Capasso:
"*Terahertz quantum cascade lasers operating in magnetic fields*";
Talk: The 16th International Conference on High Magnetic Fields in Semiconductor Physics, Tallahassee, Florida; 02.08.2004 - 06.08.2004; in: "*SemiMag- 16*", (2004), S. 7.

Presentations without Proceedings

1. A. M. Andrews, C. Pflügl, M. Austerer, T. Roch, W. Schrenk, M. Kast, G. Strasser:
"*High performance GaAs-based Quantum Cascade Lasers*";
Talk: North American Conf. on Molecular Beam Epitaxy (NAMBE), Banff, Canada; 10.10.2004 - 14.10.2004.

2. W. Brezna, S. Harasek, A. Lugstein, T Leitner, H Hoffmann, E. Bertagnolli, J. Smoliner:
"*Quantitative Scanning Capacitanc Spectroscopy*";
Talk: International Conference on Physics of Semiconductor (ICPS), Flagstaff, Arizona, USA (invited); 26.07.2004 - 30.07.2004.

3. W. Brezna, M. Schramböck, A. Lugstein, S. Harasek, H. Enichlmair, E. Bertagnolli, E. Gornik, J. Smoliner:
"*Quantitative Scanning Capacitance Sppecroscopy*";
Talk: 8th Int. Conference on Nanometer Scale Science and Technology, Venice, Italy; 29.06.2004 - 01.07.2004.

4. S. Bychikhin, V. Dubec, D. Pogany, E. Gornik, M. Graf, V. Dudek, W. Soppa:
"*Transient interferometric mapping of smart power SOI ESD protection devices under TLP and vf-TLP stress*";
Talk: European Symposium on Reliability of Electron Devices, Failure Physics and Analysis (ESREF), Zürich, Schweiz; 04.10.2004 - 08.10.2004.

5. M. Coquelin, C Pacher, M. Kast, G. Strasser, E. Gornik:
"*Interlevel crossing in double period superlattices*";
Poster: International Conference on Physics of Semiconductor (ICPS), Flagstaff, USA; 26.07.2004 - 30.07.2004.

6. J. Darmo, J. Kröll, T. Müller, G. Strasser, K. Unterrainer:
"*Cavity enhanced THz generation*";
Talk: Terahertz and Gigahertz Electronics and Photonics III, part of the Photoncs West Symposium Optoelectronics 2004: Integrated Optoelectronics Devices, San Jose, USA (invited); 24.01.2004 - 29.01.2004.

7. J. Darmo, J. Kröll, G. Strasser, K. Unterrainer:
"*Linear spectroscopy and imgaging with compact Terahertz sources*";
Talk: Terahertz Workshop 2004 Technology and Application, Freiburg, Germany (invited); 17.02.2004.

8. V. Dubec, S. Bychikhin, M. Blaho, M. Heer, D. Pogany, E. Gornik, M. Denison, N. Jensen, M. Stecher, G. Groos:
"*Multiple-time-instant 2D thermal mapping during a single ESD event*";
Talk: European Symposium on Reliability of Electron Devices, Failure Physics and Analysis (ESREF), Zürich, Schweiz; 04.10.2004 - 08.10.2004.

9. J.N. Heyman, N Coates, A Reinhardt, G. Strasser:
"*Ultrafast THz measurements of Hot Carrier Diffusion and Drift in Semiconductors*";
Poster: International Conference on Physics of Semiconductor (ICPS), Flagstaff, USA; 26.07.2004 - 30.07.2004.

10. M. Kast, W Boxleitner, G. Strasser, E. Gornik:
"*High-resolution ballistic electron spectroscopy in parallel magnetic fields*";
Poster: International Conference on Physics of Semiconductor (ICPS), Flagstaff, USA; 26.07.2004 - 30.07.2004.

11. C. Kranz, A. Kueng, A. Lugstein, E. Bertagnolli, B. Mizaikoff:
"*AFM Tip Integrated Electrochemical Biosensors for Simultaneous Topographical and Activity Mapping of Soft Samples*";
Talk: Annual Linz Winter Workshop on Scanning Probe Microscopy, Linz, Austria; 31.01.2004 - 02.02.2004.

12. C. Kranz, A. Kueng, A. Lugstein, E. Bertagnolli, B. Mizaikoff:
"*AFM-Tip Integrated Electrochmical Sensors - Simulaneous Electrochemical and AFM Imaging in Dynamic Mode Operation*";
Talk: 205th Meeting of the Electrochemical Society, San Antonio, TX; 09.05.2004 - 13.05.2004.

13. A. Lugstein, B. Basnar, E. Bertagnolli:
"*Metallic nanodots realized by a subtractive self organization process*";
Talk: European Materials Research Society (EMRS), Strassbourg, France; 24.05.2004 - 28.05.2004.

14. A. Lugstein, B. Basnar, W. Brezna, M. Weil, S. Golka, E. Bertagnolli:
"*Advanced nanopattern formation by a subtractive self organization process with Focused Ion Beams*";
Poster: International Conference on Ion Beam Modification of Materials (IBMM), Monterey, California, USA; 05.09.2004 - 10.09.2004.

15. A. Lugstein, B. Basnar, M. Weil, J. Smoliner, E. Bertagnolli:
"*Advanced nanoscale material processing with focused ion beams*";
Talk: International Conference on Electron, Ion and Photon Beam Technology and Nanofabrication (EIPBN), San Diego; 01.06.2004 - 04.06.2004.

16. A. Lugstein, M. Weil, E. Bertagnolli:
"*Advanced nanopattern formation by a subtractive self organization process with Focused Ion Beams*";
Poster: European FIB User Group Meeting, Dübendorf, Schweiz; 01.10.2004.

17. C. Pflügl:
"*Quantum Dot Intraband Emission*";
Talk: Workshop on THz Electronics and Quantum Heterostructures, Regensburg, Deutschland (invited); 05.02.2004.

18. C. Pflügl, M. Austerer, W. Schrenk, T. Roch, S. Anders, G. Strasser:
"*Surface emitting quantum cascade laser*";
Talk: International Conference on Physics of Semiconductor (ICPS), Flagstaff, USA; 26.07.2004 - 30.07.2004.

19. C. Pflügl, M. Austerer, W. Schrenk, T. Roch, G. Strasser:
"*Bound-to-Continuum GaAs/AlGaAs Quantum Cascade Laser*";
Poster: 13th Int. Winterschool on New Developments in Solid State Physics, Mauterndorf, Österreich; 15.02.2004 - 20.02.2004.

20. C. Pflügl, W. Schrenk, M. Kast, T. Roch, K. Unterrainer, G. Strasser:
"*Utilizing quantum dots in unipolar intraband emitters*";
Poster: International Conference on Physics of Semiconductor (ICPS), Flagstaff, USA; 26.07.2004 - 30.07.2004.

21. G. Pillwein, G. Brunthaler, G. Strasser:
"*Conductance Fluctuations in the Coulomb Blockade Regime in AlGaAs Quantum Dots*";
Poster: International Conference on Physics of Semiconductor (ICPS), Flagstaff, USA; 26.07.2004 - 30.07.2004.

22. G. Pillwein, G. Brunthaler, G. Strasser:
"*Fabrication and Characterisation of Lateral Quantum Dots in GaAs/AlGaAs Heterostructures*";
Poster: 13th Int. Winterschool on New Developments in Solid State Physics, Mauterndorf, Österreich; 15.02.2004 - 20.02.2004.

23. G. Pillwein, G. Brunthaler, G. Strasser:
"*Leitwertfluktuation im Coulomb Blockade Regime von AlGaAs Quantenpunkten*";
Poster: 54. Jahrestagung der Österreichischen Physikalischen Gesellschaft, Linz, Austria; 28.09.2004 - 30.09.2004.

24. T. Roch, W. Schrenk, F. Schrey, K. Unterrainer, G. Strasser:
"*X-ray investigation of quantum well intermixing after postgrowth rapid thermal processing*";
Poster: 7th Biennial Conference on High Resolution X-Ray Diffraction and Imaging (XTOP), Prag, Czech Republic; 07.09.2004 - 10.09.2004.

25. F. Schrey, G. Fasching, T. Müller, G. Strasser, K. Unterrainer:
"*Ultrafast intersublevel spectroscopy of a single quantum dot*";

Poster: International Conference on Physics of Semiconductor (ICPS), Flagstaff, USA; 26.07.2004 - 30.07.2004.

26. G. Strasser:
"*Design, growth and processing of GaAs-based Quantum Cascade Lasers*";
Talk: Int. Conf. on Solid State Crystals & 7th Polish Conf. on Crystal Growth, Zakopane, Poland (invited); 16.05.2004 - 20.05.2004.

27. G. Strasser:
"*High Power Single Mode Surface Emission of Quantum Cascade Lasers*";
Talk: Semiconductor Physics Institute, Vilnius, Germany (invited); 26.11.2004.

28. V Tamosiunas, S Anders, T. Müller, W. Schrenk, G. Strasser, K. Unterrainer:
"*THz Quantum Cascade Lasers: From quantum wells to quantum boxes*";
Talk: Fundamental Optical Prosesses in Semiconductors (FOPS), Estes Park, USA; 08.08.2004 - 13.08.2004.

29. V Tamosiunas, R. Zobl, G. Fasching, T. Müller, J. Darmo, J. Kröll, G. Strasser, K. Unterrainer, R. Colombelli, C. Gmachl, K. West, L. Pfeiffer, F. Capasso:
"*Field Control of THz Quantum Cascade Lasers*";
Talk: International Conference on Physics of Semiconductor (ICPS), Flagstaff, USA; 26.07.2004 - 30.07.2004.

30. H. D. Wanzenböck:
"*Electron beam systems - Nanotechnology and Applications in Semiconductor Technology*";
Talk: Leo GEMINI Meeting, Oberkochen, Germany (invited); 04.05.2004 - 05.05.2004.

31. K. Unterrainer:
"*Few cycle THz spectroscopy of semiconductor nanostructures*";
Talk: Seminar MSI Molecular Science Center Okazaki, Okazaki, Japan (invited); 27.02.2004.

32. K. Unterrainer:
"*Magnetic quantization in terahertz Quantum cascade lasers*";
Talk: Seminar University of Tokyo, Institute of Industrial Science, Tokyo, Japan (invited); 01.03.2004.

33. K. Unterrainer:
"*Materials - semiconductor and insulators*";
Talk: DOE-NSF-NIH, Washington, USA (invited); 12.02.2004 - 14.02.2004.

34. K. Unterrainer:
"*Quantum cascade structures*";
Talk: Colorado Meeting on Fundamental Optical Processes in Semiconductors (FOBS), Estes Park, COL, USA (invited); 08.08.2004 - 13.08.2004.

35. K. Unterrainer:
"*Quantum dots for infrared photonics*";
Talk: Pauli Colloquium of the Wolfgang Pauli Institute, TU Wien, Wien, Austria (invited); 12.09.2004.

36. K. Unterrainer:
"*Semiconductor nanostructures: THz spectroscopy - coherent control*";
Talk: SFB- Quanten-Interferenz-Kolloquium, Atominstitut Wien (invited); 10.12.2004.

37. K. Unterrainer:
"*Time resolved spectroscopy and control of semiconductor nanostructures*";
Talk: Applied Physics Colloquium, University Princeton, USA (invited); 29.11.2004.

38. R. Zobl, V Tamosiunas, G. Fasching, J. Ulrich, G. Strasser, K. Unterrainer: "*Terahertz Quantum Cascade Lasers Operating in Magnetic Fields*"; Talk: International Conference on High Magnetic Fields in Semiconductor Physics (SEMIMAG), Tallahassee, USA; 02.08.2004 - 06.08.2004.

Doctor's Theses

1. Doris Rakoczy, "Elektronentransport durch Gebiete unterschiedlicher Elektronenmasse", TU Wien, May 2004

Diploma Works

1. R. Pichler, "Untersuchung der Zündhomogenität von gg-nMOS ESD-Schutzstrukturen mittels optischer Interferometrie", TU Wien, June 2004
2. Philipp Schwaha, "*Quantum Cascade Ring Lasers*", TU Wien, March 2004
3. Karl Gruber, "Processing of Bragg Reflectors with Saturable Absorbers and LT-GaAs Emitter", TU Wien, April 2004
4. Maximilian Austerer, "*Surface Emitting Quantum Cascade Lasers*", TU Wien, May 2004
5. Matthias Schramböck, "Quantitative CV-Messungen mit dem Rasterkapazitäts–mikroskop", TU Wien, June 2004
6. Stefan Müller, "Elektronenstrahlinduzierte Abscheidung von Festkörperfilmen aus der Gasphase", TU Wien, October 2004
7. Thomas Zahel, "Investigation of the isotope effect in hydrogen-induced blistering of silicon using kinetic Monte Carlo simulation", TU Wien, December 2004

Cooperations

1. JKU Linz, G. Bauer, W. Heiss, W. Jantsch, L. Palmetshofer, F. Schäffler
2. Universität Wien, H. Kauffmann, G. Kresse
3. TU Wien, H. Rauch, H. Hutter, P. Pongratz, G. Lendl
4. Universität für Bodenkultur Wien, U.Sleytr, D. Pum
5. Montanuniversität Leoben, F. Kuchar
6. Austrian Research Centers, H. Brückl
7. AMS-Unterbremstätten, H. Enichlmair, K. Tschernay, F. Unterleitner
8. Femtolasers, Wien, A. Stingl
9. High Q Laser, Hohenems, Dr. D. Kopf
10. IMS, Wien, E. Fantner, E. Platzgummer
11. AMIS, Oudenaarde, P. Moens, Belgien
12. Interuniversity Microelectronics Center (IMEC), Leuven, N. Mahadeva, Belgien
13. Siemens AG, E. Wolfgang, G. Sölkner, W. Maurer, A. Felder, Deutschland
14. Infineon München, M. Stecher, W. Stadler, Deutschland
15. ATMEL, Heilbronn, M. Graaf, Deutschland

16. TU-München, G. Abstreiter, P. Vogl, Deutschland
17. Universität Regensburg, W. Wegscheider, Deutschland
18. Friedrich-Schiller-Universität Jena, K. Gärtner, Deutschland
19. TU Braunschweig, D. Schneider, Deutschland
20. Technische Universität Berlin, D. Bimberg, Deutschland
21. Heinrich Hertz Institut, Berlin, H. Künzel, Deutschland
22. Paul Drude Institut, Berlin, H. Grahn, Deutschland
23. Institut für Kriststallzucht, Berlin, M. Albrecht, Deutschland
24. Universität Bremen, D. Hommel, Deutschland
25. Forschungszentrum Rossendorf, Dresden, M. Helm, Deutschland
26. Bosch, Reutlingen, W. Wilkening, Deutschland
27. XFAB, Erfurt, C. Foss, Deutschland
28. IZM Frauenhofer Institut, München, H. Grieser, Deutschland
29. Max Born Institut, Berlin, K. Reimann, M. Wörner, Deutschland
30. University Ulm, E. Kohn, Deutschland
31. University Darmstadt, D. Pavlidis, Deutschland
32. IZM Fraunhofer Institute, Munich, H. Gieser, H. Wolf, Deutschland
33. University of Armed Forces, Neubiberg, G. Groos, Deutschland
34. Research Center Jülich, Jülich, P. Kordos, Deutschland
35. WITEC, Ulm, O. Hollricher, Deutschland
36. MPI, Halle, U. Gösele, Deutschland
37. Imperial College, London, C. Phillips, England
38. Univ. Leeds, G. Davis, England
39. University of Sheffield, M. Skolnick, J. Cockburn, England
40. University of Surrey, B.N. Murdin, England
41. University Limoges, J.-P. Teyssier, Frankreich
42. University Lille, IEMN, De Jaeger, Frankreich
43. Centre National de la Recherche Scientific, Laboratoire de Microstructures et de Microelectronique, B. Etienne, Cedex, Frankreich
44. CEA, Grenoble, E. Monroy, Frankreich
45. Thales, Orsay , H. Page, D. Corbin, S. Delage, Frankreich
46. Universite Paris Sud, F. Julien, Frankreich
47. Universite Paris 7, C. Sirtori, Frankreich
48. FORTH, Crete, Konstantinidis, G. Georgakilas, Griechenland
49. Technische Universität Delft, P. Planken, Holland
50. Philips Neimegen, T. Smedes, Holland
51. Sub-Micron Center, Weizmann Institute, Rehovot, M. Heiblum, Israel
52. INFM-SNS Pisa, F. Beltram, A. Tredicucci, Italien

53. TASC Trient, L. Sorba, Italien
54. Universita Bari, G. Scamarcio, Italien
55. STMicroelectronics, A. Andreini, Italien
56. University Bologna, Bologna, G. Baccarani, S. Reggiani, Italien
57. Univ. Osaka, C. Hamaguchi, Japan
58. Univ. Nagoya, N. Sawaki, Japan
59. RIKEN, K. Ishibashi, Japan
60. Universite de Quebec, Quebec, B. Terreault, Kanada
61. TopGaN, Warschau, C. Skierbiszewski, S. Porowski, Polen
62. UniPress, Warschau, T. Suski, P. Perlin, Polen
63. Ioffe Physico-Technical Institute, St. Petersburg, Y. Ivanov, P. Rodin, Rußland
64. Herriot Watt University, Edinburgh, C. Pidgeon, Schottland
65. Univ. Glasgow, C. Ironside, Schottland
66. University Neuchatel, J. Faist, Schweiz
67. EPFL Lausanne, M. Ilegems, N Grandjean, Schweiz
68. ETH Zürich, W. Fichtner, Schweiz
69. Alpes Lasers, Neuchatel, A. Müller, Schweiz
70. EMPA, Thun, J. Michler, Schweiz
71. Slovak Academy of Sciences, Bratislava, Slowakei
72. Univ. of California, Lawrence Berkeley Laboratories, E. E. Haller , USA
73. Univ. of California, Los Angeles, S. Prussin, USA
74. Univ. of California, Santa Barbara, J. Allen, A. Gossard, M. Sherwin, USA
75. Columbia University, New York, H. Störmer, USA
76. Princeton University, C. Gmachl, S. Lyon, USA
77. Boston College, Boston, MA, K. Kempa, P. Bakshi, USA
78. EPI MBE Components, St. Paul, Minnesota, USA

Terahertz Quantum Cascade Lasers Operating in Magnetic Fields

G. Fasching[1], R. Zobl[1], V. Tamošiunas[1], J. Ulrich[1], G. Strasser[1], K Unterrainer[1], R. Colombelli[2], C. Gmachl[2], L.N. Pfeiffer[2], K.W. West[2], and F. Capasso[3]

[1]Institute of Photonics and Center for Micro- and Nanostructures, Vienna University of Technology, A-1040 Vienna, Austria

[2]Bell Laboratories, Lucent Technologies, 600 Mountain Avenue, Murray Hill, NJ 07974

[3]Harvard University, Division of Engineering and Applied Sciences, Cambridge, MA 02138

We have measured the emission intensity and spectra of Terahertz Quantum Cascade Lasers in an external magnetic field applied normal to the epilayers. We have observed a reduction of the threshold current, an enhancement of laser emission intensity and shifts of the emission line. A wider operating range was predicted for the selected waveguide design according to our finite-difference time-domain simulation results. The intensity enhancement and the threshold current reduction are attributed to the suppression of nonradiative Auger-intersubband transitions by Landau-quantization of the in-plane electron motion, to the modulation of the injection rate via resonant inter-Landau-level transfer, and to the modulation of waveguide properties.

Introduction

The first Quantum Cascade-Laser (QCL) in the Terahertz range was recently demonstrated by Köhler et al [1] proving that QCL concept can be successfully implemented also in far-infrared region. The continuous wave operation of the THz QCL was also reported [2]. However, the further improvement of THz QCLs and lasing at even longer wavelengths is a challenge for different reasons related to the intersubband population dynamics and the waveguide properties. Electron-electron scattering and interface roughness are the main scattering mechanisms at low temperatures in this range of intersubband energies. They lead to fast carrier relaxation, counteracting population inversion. An external magnetic field applied normal to epilayers should lead to an additional quantization of the in-plane electron motion [3] and to the modification of the scattering. The recently observed enhancement of the luminescence intensity of GaAs/AlGaAs [4] and InGaAs/InAlAs [5] Terahertz quantum cascade structures confirms such effect.

Experimental

The system used in the emission experiments consists of a FTIR spectrometer (NICOLET Magna IR 850) equipped with a Si beamsplitter and a 4.2 K Si bolometer. For the magnetic field measurements, the THz QCL is mounted in a magnet cryostat with two superconducting magnets. In this cryostat, detection is possible by a magnetic field tunable InSb cyclotron resonance detector, by a broadband Ga doped Ge detector, or by the external FTIR (Fig. 1).

The magnetic field at the location of the sample (oriented perpendicular to the epitaxial layers) can be adjusted independently from 0 T to 6.7 T by a second magnet. A closed light pipe guides the radiation from the sample to the detector. This narrow band InSb detector [4] is tuned by the magnetic field of the second (detector) superconducting magnet. The whole spectrometer is immersed in liquid He, so that room temperature background radiation cannot distort the measurements.

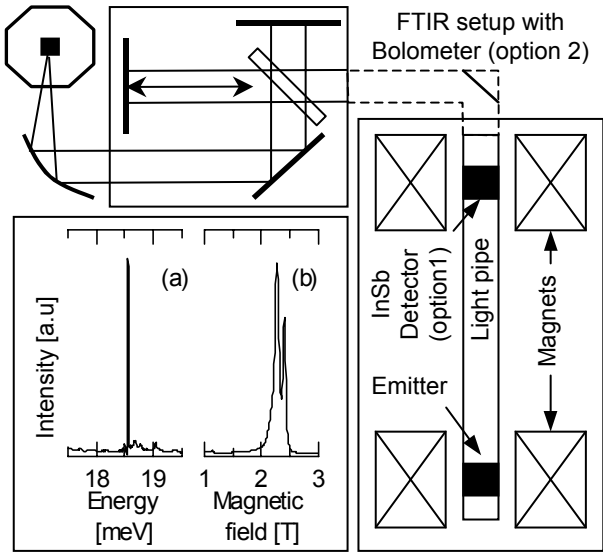

Fig. 1: Set-up for high resolution spectral measurements: cryostat with superconducting magnets, high resolution (0.0155 meV) Fourier spectrometer and Si bolometer. (a) High-resolution spectrum of the laser without applied magnetic field at the emitter sample. (b) Response of the InSb detector versus applied detector magnetic field when illuminated by the THz laser (one line corresponds to the free electron cyclotron resonance, the other one to the impurity bound resonance).

Measurements

A 4.5 THz Quantum Cascade Laser, based on the active structure design proposed in [1] was used for the measurements in a magnetic field. 100 periods of the active structure were sandwiched between two n^+-doped contact layers (the bottom layer was d = 500 nm thick with n = $4x10^{18}$ cm^{-3} doping, the top layer was d = 100 nm thick with n = $7x10^{18}$ cm^{-3} doping) grown on a semi insulating GaAs substrate using molecular beam epitaxy (MBE).

A 100 µm wide device was selected for the intensity measurements in magnetic field due to its broadest lasing range. The broadband Ge detector was used to obtain the laser intensity as a function of different sample magnetic fields which is presented in Fig. 2. The laser emission intensity increases substantially for certain values of the magnetic field when compared to B = 0 T. For increasing magnetic fields we observe oscillations with a larger period. The application of a magnetic field increases the laser intensity by a factor of more than five at B = 4.2 T (see Fig. 2). This effect is understood as a consequence of the discretization of the energy spectrum. In the parabolic dispersion relation in the absence of a magnetic field the energy conservation requirement for intersubband Auger-scattering processes is fulfilled for a continuum of energy changes ΔE (meaning one electron suffers an energy change of $+\Delta E$, the other one a change of $-\Delta E$). However, for a non-vanishing magnetic field the only allowed energy changes ΔE

are multiples of the cyclotron resonance energy $\hbar\omega_c$. Since the Auger-scattering rate scales inversely with the associated change in energy and momentum, it is more and more suppressed with increasing Landau-level splitting. The laser intensity is proportional to the inversion which is directly proportional to the injection rate and inversely proportional to the non-radiative relaxation rate.

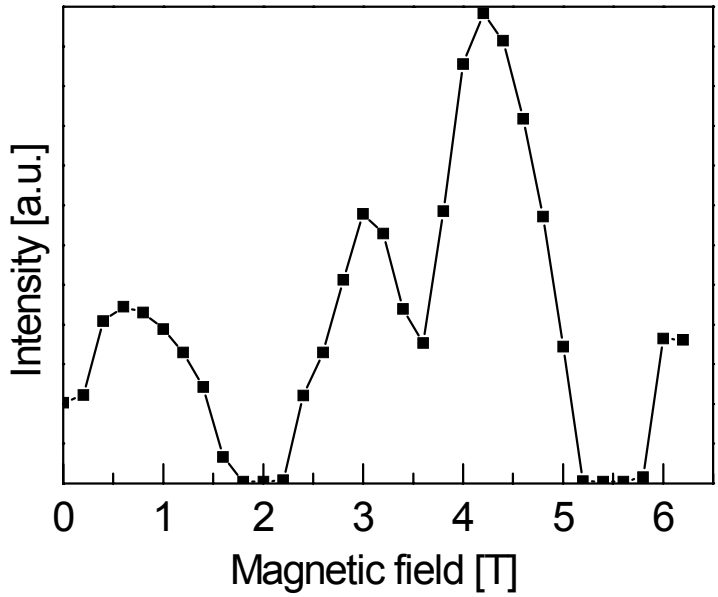

Fig. 2: Maximal laser emission intensity versus magnetic field. Laser emission intensity was recorded for every given magnetic field flux density value by adjusting pulse generator settings to obtain the maximum intensity. Clear emission intensity maxima are observed for N = 2.5 (4.2 T) and N = 3.5 (3 T).

We first assume that the injection rate is not influenced by the magnetic field. We would expect an oscillatory increase of the laser emission with minima where the magneto-intersubband resonance condition is met:

$$E_2 - E_1 = \frac{\hbar e B_N}{m^*} N$$

Here $E_2 - E_1$ is the energy difference between the lowest Landau-levels of the upper and lower laser transition, $\hbar$ - the Planck constant, e - the elementary charge, B_N - magnetic flux density , m^* - effective mass, N – an integer. Resonant tunneling between Landau levels opens up an additional non-radiative relaxation channel via the Landau ladder ($|1,N\rangle$, $|1,N\text{-}1\rangle$, ...$|1,0\rangle$) and by reducing the population inversion leads to the decrease of the laser emission intensity. It should be pointed out that a theoretical model proposed by Raikh and Shahbazyan [9] well describes a momentum transfer caused by interface roughness or impurities, which is required for resonant transfer between Landau levels of different subbands. It is clearly seen from the figure that the laser stops working at these magneto-intersubband resonances.

The energy difference between the injector states is small (~3.1 – 3.8 meV [10]) and the condition for complete magnetic quantization

$$\frac{\hbar e B}{m^*} > \Delta E_{injector}$$

is reached at relatively low magnetic fields. Optimum performance of the laser should be achieved for $\frac{\hbar eB}{m^*}M = \Delta E_{injector}$ and $\frac{\hbar eB}{m^*}N \neq \Delta E_{laser}$, where N and M are integers. The interplay between increased injector efficiency and reduced non-radiative relaxation determines the detailed dependence of the laser intensity on the magnetic field.

The laser intensity increase and oscillatory behavior was consistently observed for all lasing devices independently of device width.

Conclusion

In summary, we have observed a reduction of the threshold current, an enhancement of laser emission intensity and shifts of the emission line in an external magnetic field applied normal to epilayers. An operating range of the selected waveguide design is consistent with our finite-difference time-domain simulation results. The intensity enhancement and the threshold current reduction are attributed to the suppression of nonradiative Auger-intersubband transitions by Landau-quantization of the in-plane electron motion, to the modulation of the injection rate via resonant inter-Landau-level transfer and to the modulation of waveguide properties.

Acknowledgements

We acknowledge support by the Austrian Science Foundation (START, ADLIS SFB) and the European Community IST program (Teravison, Supersmile).

References

[1] R. Köhler, A. Tredicucci, F. Beltram, H.E. Beere, E.H. Linfield, A.G. Davies, D.A. Ritchie, R.C. Iotti, F. Rossi, Nature 417, 156 (2002).

[2] L. Ajili, G. Scalari, D. Hofstetter, M. Beck, J. Faist, H. Beere, G. Davis, E. Linfield, D. Ritchie, Elect. Lett. 38, 1675 (2002).

[3] A. Blank and S. Feng, J. Appl. Phys. 74, 4795 (1993).

[4] J. Ulrich, R. Zobl, K. Unterrainer, G. Strasser, and E. Gornik, Appl. Phys. Lett. 76, 19 (2000).

[5] S. Blaser, M. Rochat, M. Beck, D. Hofstetter and J. Faist, Appl. Phys. Lett. 81, 67 (2002).

[6] K. S. Yee, IEEE Trans. Antennas Propagat., vol. AP-14, pp. 302-307, May 1966.

[7] A. Taflove, Computational Electrodynamics: The Finite-Difference Time-Domain Method. Norwood, MA: Artech House, 1995.

[8] R. W. Ziolkowski, J. M. Arnold, D. M. Gogny, Phys. Rev. A, vol. 52, 4, pp. 3082-3094, 1995.

[9] M. E. Raikh and T. V. Shahbazyan, Phys. Rev. B 49, 5531 (1994).

[10] R. Köhler, R. C. Iotti, A. Tredicucci, F. Rossi, Appl. Phys. Lett. 79, 3920 (2001).

[11] V. Tamosiunas, R. Zobl, J. Ulrich, K. Unterrainer, R. Colombelli, C. Gmachl, K. West, L. Pfeiffer, F. Capasso, Appl. Phys. Lett. 83, 3873 (2003).

Surface-Emitting Single-Mode Quantum Cascade Lasers

M. Austerer, C. Pflügl, W. Schrenk, S. Golka, G. Strasser

Zentrum für Mikro- und Nanostrukturen, Technische Universität Wien, Floragasse 7, A-1040 Wien

We present high power surface-emitting single mode GaAs-based quantum cascade lasers (QCLs) in the mid-infrared. By using an air-AlGaAs waveguide combined with second-order distributed feedback processing, we obtained optical output via the surface above 3W. Surface-normal dual-lobe light emission exceeds the emission from one as-cleaved facet by a factor of six.

Introduction

Significant improvements during the last decade made quantum cascade lasers [1] (QCLs) interesting for many applications, where coherent light emitters in the mid- and far-infrared are required. An important step for the use of these devices was the achievement of single mode emission. This was first demonstrated by processing the lasers as first order distributed feedback (DFB) lasers, where a grating which is imposed on top of the laser selects a single mode within the gain spectrum of the device [2], [3]. Recently, tunable single mode emission was also achieved by grating-coupled external cavity QCLs [4].

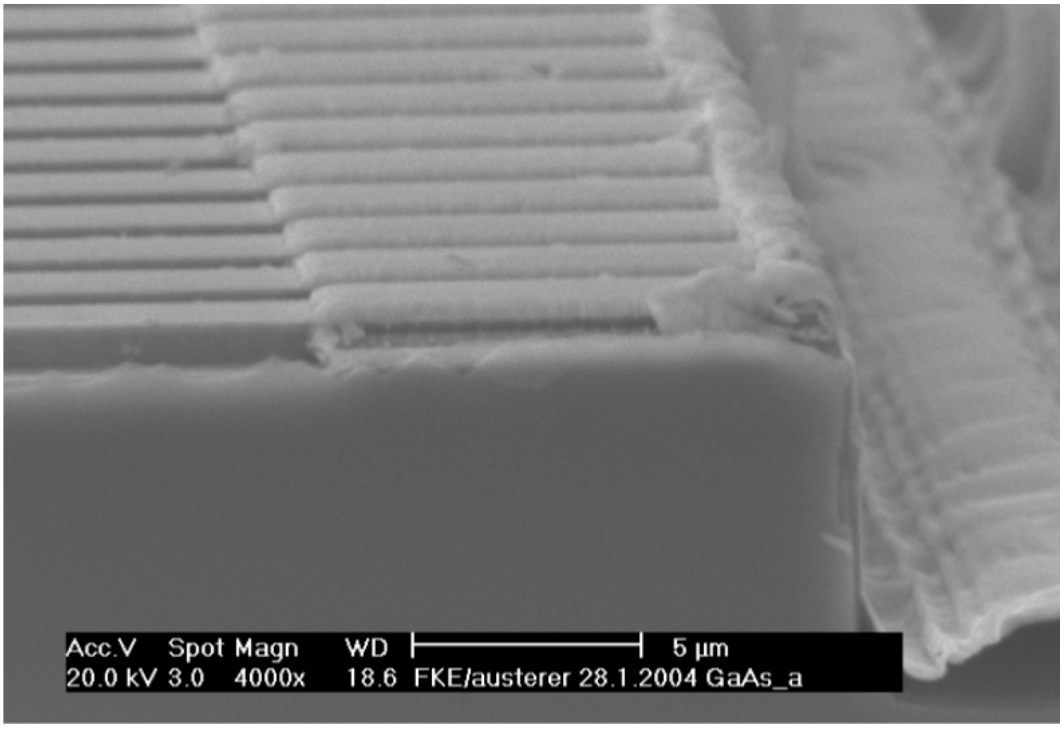

Fig. 1: REM image of the processed DFB laser ridges.

QCLs are based on intersubband transitions. Selection rules for transitions in quantum wells allow gain only for TM polarized electromagnetic waves. Therefore conventional vertical cavity surface emitting laser design is not suitable for QCLs. If one wants to exploit the advantages of surface normal emission another approach must be taken. One successful way to achieve surface emission is to use two-dimensional photonic crystals [5]. We have chosen a distributed feedback design where the feedback is given through a second-order Bragg grating etched into the surface of the laser ridge. Such surface emitting QCLs have been realized both in the InGaAs/InAlAs/InP and also in the GaAs/AlGaAs material system [6], [7]. Appropriate etch depths, a low loss top air cladding and metallization of the grating peaks only, lead to high power surface emission. Surface emitting QCLs have the big advantage that the radiation field could be increased significantly and the beam divergence is reduced.

Design and Characterization

The laser material is grown by molecular beam epitaxy on (100) GaAs substrates. The gain media is embedded in the most cases in a double plasmon enhanced waveguide. Such a waveguide consists of ~1 µm thick highly doped cladding layers (~$4x10^{18}$ cm^{-3}), and ~3.5 µm thick low doped spacer layers (~$4x10^{16}$ cm^{-3}). The highly doped layers are used for light confinement and the spacer layers reduce the penetration of the guided mode into the cladding layers as they show huge free carrier absorption. A surface plasmon waveguide is usually used for long wavelength material ($\lambda > 20$ µm) because of the reduced thickness, which is important for MBE growth.

Different cavity types such as Fabry Perot (FP), distributed feedback (DFB), and cylinder lasers were fabricated. Reactive ion etching was used for directional etching to obtain vertical etch profiles (Fig. 1). SiN is used for insulation and the extended contacts are sputtered. The grating for the DFB lasers was etched into the surface of the top cladding layer and covered with metal. The light is confined by total internal reflection in the case of cylinder shaped lasers. The lasers were soldered with In on Cu plates and wire bonded.

Our laser material is grown by solid source molecular beam epitaxy on n-doped GaAs (Si, $2x10^{18}$ cm^{-3}. The active region consists of 40 cascades of a GaAs/$Al_{0.45}Ga_{0.55}As$ three well design [8]. As a waveguide we have chosen an air/AlGaAs cladding in order to reduce absorption losses compared with a typical double-plasmon waveguide. Our calculations yield a waveguide loss coefficient of $\alpha = 3.8$ cm^{-1}, whereas the structure with a double-plasmon waveguide has α-values of 12 cm^{-1}. The significant reduction of the losses was investigated by comparing the threshold current density of this device with a device (both fabricated as Fabry-Perot lasers) with the same active region but a double plasmon waveguide. The threshold was reduced from 4.1 kA/cm^2 to 2.7 kA/cm^2 at 78 K and from 11.8 kA/cm^2 to 7.8 kA/cm^2 at 240 K, whereas we have comparable output powers and emission spectra. A reduction of the threshold current is favorable concerning the strong self-heating due to the applied current of electrically pumped lasers. In the case of 2nd order DFB lasers a low loss top waveguide is particularly important because the light is coupled out via the surface.

Taking the waveguide structure and the desired wavelength of 8.9 microns into account, a suitable grating period ($\Lambda = 2.8$ µm), duty cycle ($\sigma = 0.5$) and grating depth (1.1 µm) were calculated. The grating was exposed on top of the MBE grown material by means of optical lithography and reactive ion etching (RIE) (see Fig.1). The grating peaks were covered with a metal to provide a homogenous lateral current distribution even for wide ridges. Then the ridges (30 to 70 µm) were defined also by RIE (depth 10 µm). The metal on the grating peaks is actually contacted by side contacts with an overlap of about 8 µm on both sides, resulting in a width of the surface emission window w_{wind} between $w_{wind} = 14$ µm ($w = 30$ µm) and $w_{wind} = 54$ µm ($w = 70$ µm). The ex-

tended contacts are insulated with SiN. The cleaved laser facets are left uncoated and the laser bars are mounted epilayer up on a temperature controlled cold finger in a flow cryostat.

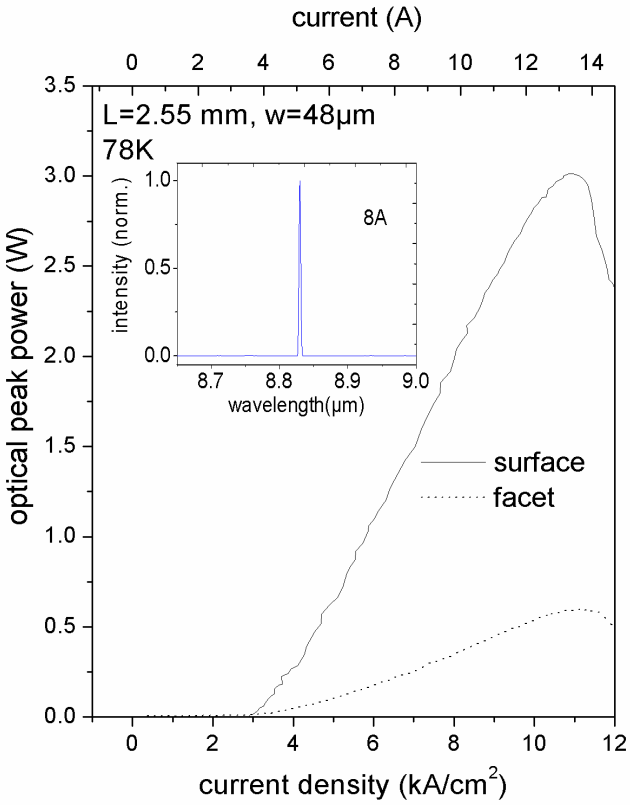

Fig. 2: Absolute light output power versus bias current density for a 2.55 mm long laser at 78 K. The inset shows the spectrum for an applied current of 8 A.

The laser ridges were cleaved to different lengths in order to investigate the critical DFB coupling length. Lasers that are shorter than 1.4 mm, thus having a product of DFB coupling coefficient κ = 7 cm^{-1} and length (cm) smaller than one, do not experience sufficient feedback from the surface grating and are showing typical Fabry-Perot modes. The samples were mounted substrate-down on a turnable cold finger and operated under pulsed bias (100 ns, 5 kHz) at 78 K. By turning the cold finger we could observe both edge and surface emission.

The far field of such lasers exhibits an asymmetric dual lobe pattern, because the near field close to the emitting surface also includes interference terms. An in-detail investigation shows that the relative position of the grating and the end mirrors determines the ratio of the two lobe intensities [9]. The single mode emission wavelength is continuously tunable by the heat sink temperature.

In Fig. 2 absolute light output power versus bias current density for a 2.55 mm long laser is plotted. Single mode emission is observed for all bias currents above threshold (inset of Fig. 2). Light power was measured using a calibrated thermopile detector. We obtained peak output power at 78 K above 3 W via the surface. In the case of edge emission an f/1 AR-coated ZnSe lens was used to collect the light from the highly divergent beam. In both cases the light power was focused onto the thermopile detector by means of a gold coated off-axis parabola. The ratio between surface emission and single-facet emission is determined to be six for this device.

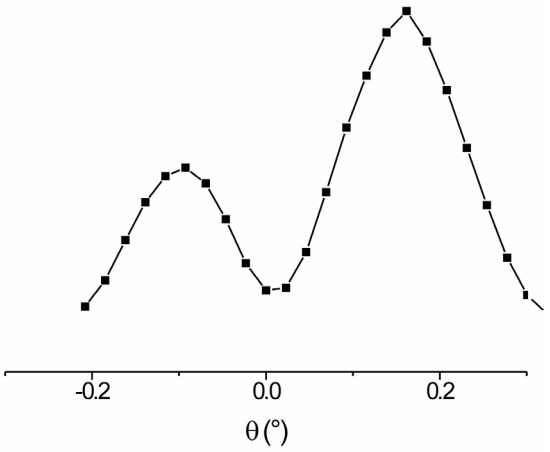

Fig. 3: Far field distribution of the laser emission.

The far field distribution (Fig. 3) of the laser emission was measured using a 1 mm x 1 mm sensitive area liquid-nitrogen cooled HgCdTe detector at a distance of 124 cm away from the laser chip. Lateral resolution of 1 mm results in an angular resolution of 0.046°. The two beam lobes are separated by 0.25° and have an FWHM beam divergence of 0.2° in laser ridge parallel direction. Beam divergence in ridge normal direction is determined by the ridge width, here FWHM beam divergences are in the range of 10° to 20°.

Conclusions

We have shown the high-power capabilities of surface emitting DFB quantum cascade lasers. Single lobe emission surface emission of second order DFB QCLs is proposed by introducing a phase shift into the surface grating. Such low divergence emission pattern would further improve practical usability. In contrary to facet emitters, for many applications no collimating lens would be necessary.

Acknowledgements

This work was supported by the EC (NMP-project) ANSWER, the Austrian FWF (SFB-ADLIS) and the Austrian Gesellschaft für Mikroelektronik (GMe).

References

[1] J. Faist, F. Capasso, D. L. Sivco, C. Sirtori, A. L. Hutchinson and A. Y. Cho, Science 264, 553 (1994)

[2] J. Faist, C. Gmachl, F. Capasso, C. Sirtori, D. L. Sivco, J. N. Baillargeon, A. Y. Cho, Appl. Phys. Lett. 70, 2670 (1997)

[3] W. Schrenk, N. Finger, S. Gianordoli, L. Hvozdara, G. Strasser, E. Gornik, Appl. Phys. Lett. 76, 253 (2000)

[4] R. Maulini, M. Beck, J. Faist, and E. Gini, Appl. Phys. Lett. 84, 1659 (2004)

[5] R. Colombelli, K. Srinivasan, M. Troccoli, O. Painter, C. F. Gmachl, D. M. Tennant, A. M. Sergent, D. L. Sivco, A. Y. Cho, F. Capasso, Science 302, 1374 (2003)

[6] D. Hofstetter, J. Faist, M. Beck, U. Oesterle, Appl. Phys. Lett. 75, 3769 (1999)

[7] W. Schrenk, N. Finger, S. Gianordoli, L. Hvozdara, G. Strasser, E. Gornik, Appl. Phys. Lett. 77, 2086 (2000)

[8] H. Page, C. Becker, A. Robertson, G. Glastre, V. Ortiz, and C. Sirtori Appl. Phys. Lett. 78, 3529 (2001)

[9] H. Kogelnik, C. V. Shank, J. Appl. Phys. 43, 2327 (1972)

Quantitative Scanning Capacitance Spectroscopy on GaAs and InAs Quantum Dots

W. Brezna, T. Roch, G. Strasser, J. Smoliner

Institute of Solid State Electronics
Vienna University of Technology, A-1040 Vienna, Austria

In this work, quantitative scanning capacitance spectroscopy studies on bulk GaAs and InAs quantum dots are carried out in ambient atmosphere. The experimental results are well described by a simple spherical capacitor model, and the corresponding barrier heights and sample dopings are determined from the measured data. We further find a strong dependence of the C(V) data on the applied tip force. The barrier height is decreasing significantly with increasing pressure.

Introduction

Scanning Capacitance Microscopy/Spectroscopy (SCM/SCS) is an extension of conventional Atomic Force Microscopy (AFM) and a promising tool for two-dimensional carrier profiling in semiconductor devices. In SCM/SCS, a conductive AFM tip is used to measure the local capacitance between the tip and the sample. The current state of the art of this technique can be found in the review articles [1] – [4].

In scanning capacitance spectroscopy (SCS), the tip-sample capacitance is recorded during a DC voltage sweep to obtain a capacitance versus voltage (C(V)) curve [5]. However, quantitative SCM/SCS measurements are still a major challenge for technical and physical reasons. First, the capacitance between the AFM tip and the sample is in the aF regime only. To obtain a reasonable signal size at reasonable data collection speed for imaging, lock-in techniques are normally used. Thus, commercial SCM systems usually yield qualitative dC/dV data only. To obtain quantitative results, these data have to be calibrated. This, however, is technically complicated due to large difficulties with the reproducibility of the reference sample preparation process. In addition, the currently commercially available SCM systems do not operate at small signal conditions, which further complicates the data evaluation and makes sophisticated simulation methods almost inevitable [1] – [4].

To circumvent at least the reproducibility problems with reference samples, quantitative scanning capacitance spectroscopy can be used. In our previous work [6] we have demonstrated that this method is e.g. useful for a nanoscale analysis of high-k dielectric materials such as ZrO_2 and a pointwise calibration of capacitance images obtained by commercial SCM systems.

While a large amount of literature exists on SCM measurements on silicon samples, significantly fewer publications can be found on SCM on GaAs and other III-V materials. Besides very innovative approaches such as X-ray absorption measurements by SCM [7] and local capacitance measurements on InAs dot-covered GaAs surfaces by scanning capacitance microscopy [8] under high vacuum conditions, most of the SCM work on GaAs was devoted to the SCM characterization of laser structures [9], [10]. Douheret, e.g., has shown that SCM can provide a complete 2D map of the device structure, including doping variations, the location of p-n junctions, and regrown interfaces.

In this paper, bulk GaAs and InAs quantum dots are studied by scanning capacitance spectroscopy in ambient atmosphere. It is found that the experimental data agree well with capacitance spectra calculated from a simple spherical capacitor model. The donor concentrations obtained from this model are in excellent agreement with the sample parameters and the measured Schottky barrier heights are consistent with data obtained by Ballistic Electron Emission Microscopy on similar samples [12]. The influence of illumination and tip force is found to be very critical.

Experimental Preliminaries

All samples we used for our experiments were MBE grown GaAs layers on semi insulating GaAs substrates. The layer thickness was 1 µm for all samples and the doping was N_d = 1x10^{16} cm^{-3} and N_d = 1x10^{17} cm^{-3} for the GaAs bulk samples, respectively. The "on surface" quantum dot sample we used had the same layer structure and was also doped at a level of N_d = 1x10^{16} cm^{-3}.

For all capacitance measurements, an ultrahigh precision, low frequency (1 kHz) capacitance bridge (*Andeen Hagerling* 2550) was used, which allows capacitance and loss measurements under well controlled, small signal conditions down to the aF regime. A (*Keithley*) source measure unit was used to provide the DC voltage component. External coax cables from the capacitance bridge were attached on both the sample and the AFM tip holder. The AFM was only used for tip positioning and for the tip-sample approach. As tips we used highly doped (p-type 1x10^{20} cm^{-3}) conductive diamond tips (*Nanosensors*, Germany). The spring constant of the cantilevers was 42 N/m and the typical tip radius was 100 nm according to the data sheet. Note that this type of cantilevers is normally used for scanning spreading resistance measurements only; the reasons for using these tips are described below.

In contrast to standard SCM/SCS measurements, where the applied frequencies are so high (≈1 GHz) that light induced charge carriers cannot follow the HF fields, our setup operates at a frequency of 1 kHz. Here, the measurement turned out to be extremely sensitive to the influence of light. Therefore, the AFM hardware was modified in order to switch off the laser and all other illumination and the feedback loop was controlled externally during the C(V) measurements [11]. To minimize vibrations and acoustic noise, the AFM system was placed on an air suspended table and put into an acoustic hood. This also allowed an operation under temperature stable conditions which turned out to be crucial. In detail, the temperature variations were kept below ±10 mK during the measurements. Due to improved shielding measures and larger signals compared to our earlier experiments [6], a reasonable signal to noise ratio was already obtained at moderate averaging times and a typical C(V) spectrum took 20 minutes.

Results and Discussion

Figure 1 (a) shows typical C(V) curves, which were obtained in complete darkness. The force we used for these measurements was 2.9 µN. Curve (1) was recorded on bulk GaAs with a doping of N_d = 1x10^{16} cm^{-3}. Curve (2) was bulk GaAs too, with N_d = 1x10^{17} cm^{-3}, and curve (3) was obtained on a InAs quantum dot on GaAs substrate with a doping of N_d = 1x10^{16} cm^{-3}. Obviously, the onset of these C(V) spectra is shifted to lower bias for higher substrate doping and the onset of the C(V) curve obtained on a quantum dot is even lower.

As already found by Yamamoto [8], a simple parallel plate capacitor model cannot be used to describe AFM based capacitance spectra on GaAs. The reason for this lies in the nature of the Schottky contact between the tip and the GaAs underneath. In a Schottky contact, the extent of the depleted space charge region determines the ca-

pacitance of the contact. As the depletion length easily reaches several hundred nanometers on low doped samples and the tip radius is much smaller, a simple parallel plate capacitor model is not appropriate for geometric reasons. In contrast to that, the active region in Metal-SiO_2-Silicon (MOS) junctions is always directly at the Si-SiO_2 interface directly underneath the tip, which is the reason why simple parallel plate capacitor models on Si samples normally yield results which are correct at least within an order of magnitude.

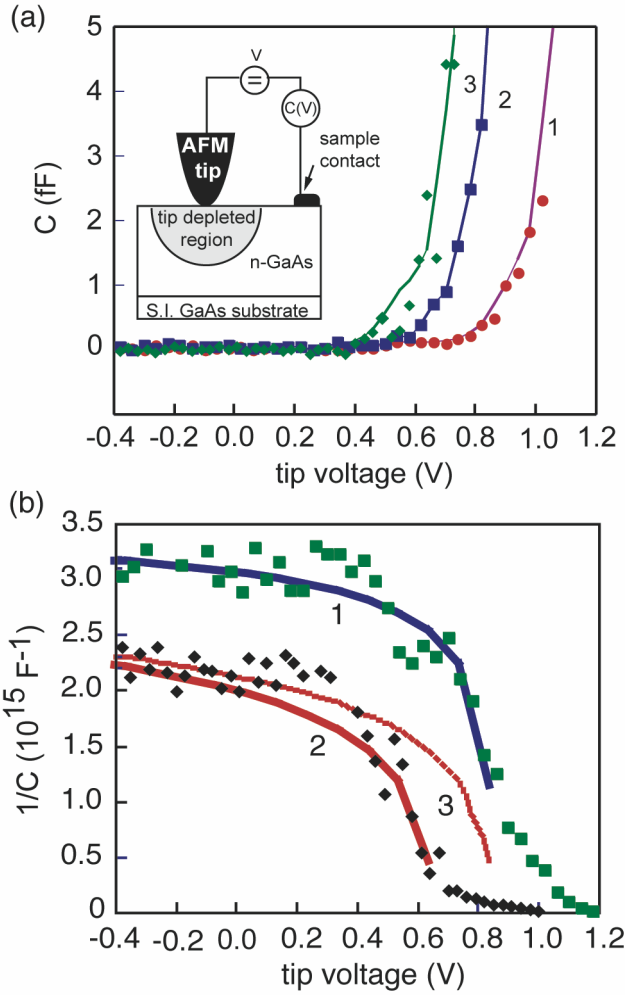

Fig. 1: (a) Capacitance – voltage (C(V)) spectra measured on three different samples (curves 1 – 3). (1): bulk GaAs with $N_d = 1x10^{16}$ cm^{-3}, (2): bulk GaAs with $N_d = 1x10^{17}$ cm^{-3}, (3): InAs dots on GaAs with $N_d = 1x10^{16}$ cm^{-3}. The solid lines connecting the data points are only a guide for the eye. A schematic view of the experimental setup is shown in the inset. (b) Capacitance data for the high and low doped bulk sample plotted as 1/C over bias. The solid lines were calculated using a spherical capacitor model. Details are found in the text.

To analyze our data, we therefore applied a simple model assuming a capacitor consisting of two concentric spheres. The capacitance of such a spherical capacitor is calculated as $C = 4\pi\varepsilon_r\varepsilon_0\left(\frac{r_1 r_2}{r_2 - r_1}\right)$, where ε_0 is the dielectric constant of vacuum, ε_r is the relative dielectric constant and r_1 and r_2 are the radii of the inner and outer sphere. To estimate the capacitance of our tip-semiconductor system we simply set $r_1 = r_{tip}$, where

r_{tip} is the tip radius and r_2 is set to $r_2 = (r_{tip} + d)$, where d is the depletion layer thickness in GaAs. We further assume that ε_r =13 and ignore all influence of the dielectric constant of the diamond tip and the surrounding air. For a given Schottky barrier height V_b, the depletion layer thickness d is calculated as: $d = \left(2(V - V_b)\varepsilon_r \varepsilon_0 / (eN_D)\right)^{1/2}$, where V is any applied external voltage, and N_D the doping concentration. Finally we take for the tip-sample capacitance C_{TS} a value of $C_{TS} = C/2$ only, because we just consider the lower half sphere of the capacitor. As long as $d > r_1$, which is easily achieved on low doped substrates, this will be a reasonably good approximation.

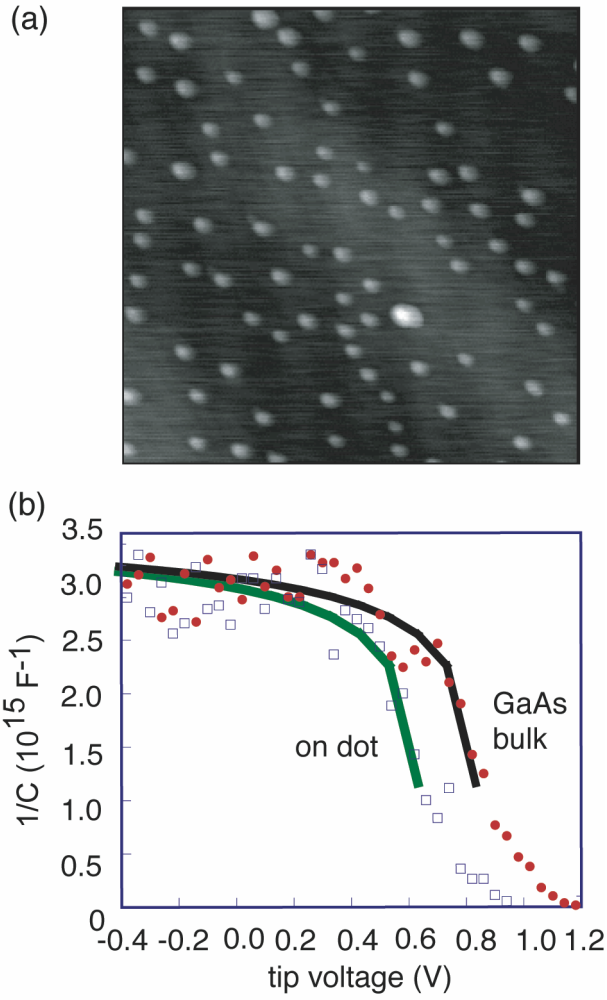

Fig. 2: (a): AFM image of the quantum dot sample. Scan size is 1µm x 1µm. The typical dot diameter is 40 nm. (b): 1/C(V) curves obtained on the low doped bulk sample and on quantum dot positions. The solid lines were calculated using a spherical capacitor model. Details are found in the text.

To compare the model with the experimental data, it is helpful to plot $1/C_{TS}$ versus tip-bias similar like the $1/C_2$ versus bias plots, which are usually made for C(V) curves on Schottky junctions assuming parallel plate capacitors. For the low doped sample, the agreement between the experimental data and the primitive model is amazing. Figure 1 (b) shows a comparison of the measured and calculated curves. Curve (1) shows the result for a substrate doping of $N_d = 1 \times 10^{16}$ cm^{-3}, a tip radius of 90 nm, and a Schottky barrier height of Vb = 0.9 eV. The background stray capacitance was also subtracted.

Below the barrier height, the agreement is really excellent. For bias values above the barrier height, the model can not be applied. Curve (2) shows the result for the sample with the higher doping (N_d = 1x10^{17} cm^{-3}). In agreement with our simulation, the reciprocal of the measured signal becomes smaller with increased doping level. To fit the shifted onset position, an "effective" barrier height of V_b = 0.7eV was assumed to account for the tunneling effects through the thinner Schottky barrier at higher doping levels. However, the overall agreement between the calculation and the experiment is still not as good as for the low doped substrate. In our opinion, this is due to the smaller extension of the depleted region, where the primitive spherical capacitor approximation becomes less accurate. For comparison, the result of an equivalent simulation assuming a barrier height of 0.9 eV is also shown in curve (3).

Motivated by the good agreement between theory and experiment on bulk GaAs, the same measurements were also carried out on InAs quantum dots. An AFM topography of our sample can be seen in Figure 2 (a). The dots have a typical diameter of 40 nm on this sample. Figure 2 (b) shows the corresponding capacitance data.

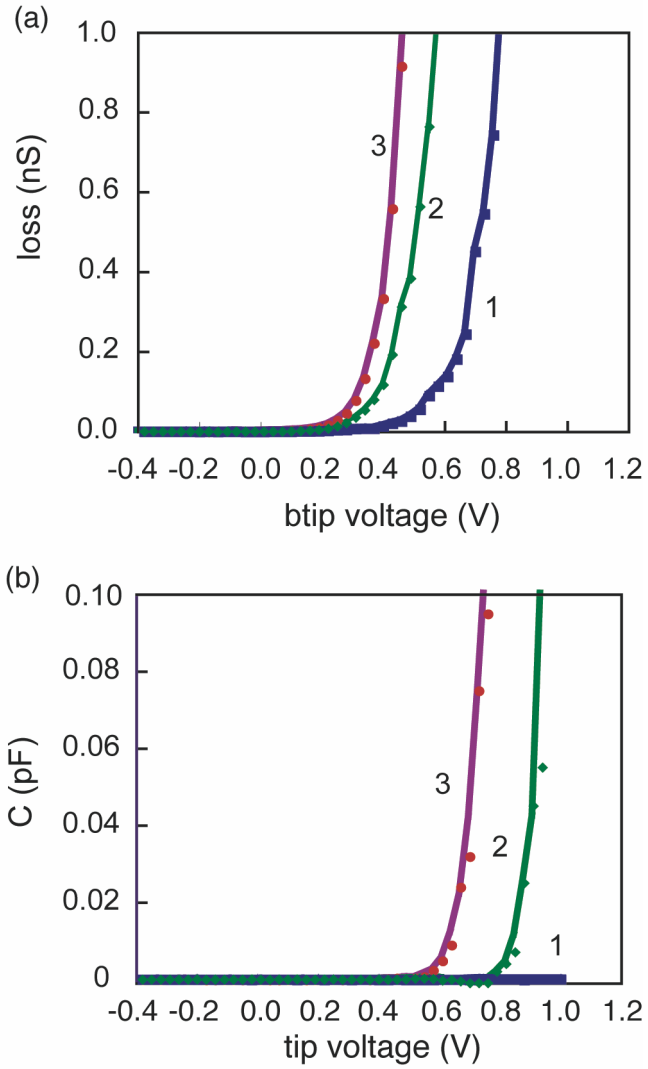

Fig. 3: (a) Loss curves recorded on bulk GaAs (N_d = 1x10^{16} cm^{-3}) using forces of 2.0 µN, 3.8 µN and 6.1 µN, for curves (1 – 3), respectively. (b) Simultaneously measured C(V)-spectra.

Compared to the GaAs bulk data, the “on dot” curve looks qualitatively the same and is just shifted to the left. The calculated “on-dot” curve was obtained using a barrier height of V_b = 0.65 eV, which is in excellent agreement with the band offset between InAs dots and GaAs determined earlier [12] by Ballistic Electron Emission Microscopy (BEEM). This indicates, that the InAs dot acts as intermediate contact to the tip and that the capacitance is dominated by the behavior of the InAs-GaAs system and not the tip. A similar behavior was already found by Yamamoto et al. [8].

As final point we want to discuss the influence of the tip-sample force, which turned out to have a significant influence on the results. Figure 3 (a) shows typical loss (differential conductance) spectra on the low doped GaAs bulk sample as a function of tip-force. Curves (1) – (3) were measured using tip forces of 2.0 µN, 3.8 µN and 6.1 µN, respectively. As in conventional spreading resistance measurements, the loss increases with increasing force between tip and sample. It must be pointed out, however, that the minimal force (F ≈ 1 µN) to obtain reproducible loss data is surprisingly high. For all our measurements we had to use diamond coated “scanning spreading resistance cantilevers” with a high spring constant (C = 42 N/m). With conductive diamond coated “contact mode cantilevers” (C = 1 N/m) the forces turned out to be too low to achieve reliable conductance data. The physical origin for this behavior is probably found in the ambient conditions where the measurements were carried out. Under ambient conditions, all samples are usually covered with a thin film of water. Especially on semiconductors, one can expect an additional native oxide, too. Thus, the existence of a force threshold to penetrate these films with an AFM tip is not that surprising, the rather high amount of force, however, is.

For local capacitance measurements, the situation is even worse. Even at tip forces where a clear local conductance via the tip is already observed (Figure 3 (a), curve (1)), no capacitance signal can be detected (Figure 3 (b), curve (1)). At a tip force of 3.8 µN, which turned out to be the minimum value for reproducible capacitance measurements on our sample, we obtain typical data as they are shown in curve (2). Under these conditions, we obtain a barrier height of V_b = 0.9 eV as discussed above. At a tip force of 6.1 µN (curve (3)), the capacitance curve is shifted to the left and the barrier height is reduced and our model yields a significantly reduced value of V_b = 0.55 eV. Going to higher pressures was impossible, since this normally led to tip destruction before further significant changes could be detected.

On the reasons why the threshold force for reproducible capacitance measurements is even higher than for conductance measurements, we can only speculate. Most probably, however, any intermediate layer (water, oxide) had to be penetrated completely by the tip before a reasonable Schottky contact is established. In contrast to that, thin oxide layers would show a finite conductance already much earlier due to tunneling effects.

On the quantum dot sample, systematic pressure studies were unfortunately impossible, since the dots were considerably damaged at higher tip forces. In addition, we noticed that tip forces greater than 4.7 µN had to be used before any capacitance signal could be recorded on off-dot positions on the wetting layer. Since the samples were not grown freshly, the wetting layer was probably oxidized completely. However, we have no explanation why an oxidized InAs wetting layer is significantly thicker or less conducting than native GaAs oxide and we also found no information in the literature on this topic.

Summary

In summary, quantitative AFM based capacitance studies were carried out in air on bulk GaAs and InAs quantum dots. All C(V) data were well described by a simple

spherical capacitor model on all samples, and substrate doping as well as the corresponding barrier heights were determined and in agreement with reference data. We also found a force threshold for reproducible capacitance measurements and a significant influence of the tip sample force on the obtained results.

Acknowledgements

This work was sponsored by “Fonds zur Förderung der wissenschaftlichen Forschung (FWF)” project No P16337-N08. The authors are grateful to J. Prinzinger for technical assistance.

References

[1] V.V. Zavyalov, J.S. McMurray, C.C. Williams, Rev. Sci. Instr. 7, 158 (1999)

[2] R. Stephenson, P. DeWolf, T. Trenkler, T. Hantschel, T. Clarysse, P. Jansen, W. Wandervorst, Vac. Sci. Technol. B18, 555 (2000)

[3] D.D. Bugg, P.J. King, J. Phys. E21 147 (1988)

[4] V.V. Zavyalov, J.S. McMurray, C.C. Williams, Rev. Sci. Instr. 7, 158 (1999)

[4] P. De Wolf, R. Stephenson, T. Trenkler, T. Clarysse, T. Hantschel, W. Vandervorst, J. Vac. Sci. Technol. B18, 361 (2000)

[5] E.H. Nicollian, J.R. Brews, MOS (metal oxide semiconductor) physics and technology, John Wiley & Sons Ltd, New York 1982

[6] W. Brezna, M. Schramboeck, A. Lugstein, S. Harasek, H. Enichlmair, E. Bertagnolli, E. Gornik, J. Smoliner, Appl. Phys. Lett. 83 4253 (2003)

[7] M. Ishii, T. Uchihashi, Physica B 340-342, 1142 (2003)

[8] H. Yamamoto, T. Takahashi, I. Kamiya, Appl. Phys. Lett. 77, 1994 (2000)

[9] O. Douheret, S. Anand, C. Angulo-Barrios, S. Lourdudoss, Appl. Phys. Lett. 81, 960 (2002)

[10] M.W. Xu, N. Duhayon, W. Vanderworst, 2002 GaAs MANTECH Conference Digest of Papers, 173 (2002)

[11] for more technical details please send email to: juergen.smoliner@tuwien.ac.at

[12] D. Rakoczy, G. Strasser, J. Smoliner, J. Vac. Sci. Technol. B20, 373 (2002)

Photocurrent Spectroscopy of Single InAs/GaAs Quantum Dots

G. Fasching, F.F. Schrey, T. Müller, and K. Unterrainer

Institute of Photonics, Vienna University of Technology, Floragasse 7, A-1040 Vienna, Austria

W. Brezna, M. Austerer, T. Roch, M.A. Andrews, J. Smoliner, and G. Strasser

Institute of Solid State Electronics, Vienna University of Technology, Floragasse 7, A-1040 Vienna, Austria

In this work, we present a carrier escape study from InAs/GaAs self assembled QD's by the use of photocurrent measurements. As a function of the applied field, we detect a shift of the exciton ground state transition due to the quantum-confined Stark shift. From the measured Stark shift S = 4.3 meV we deduce a exciton dipole moment of p = (4.3 ± 0.2)×10^{-29} Cm. The tunneling time, which is directly related to the observed photocurrent linewidth due to $\tau \sim \hbar/(2\Gamma)$, changes by a factor of five in the photocurrent regime. The measured linewidth dependency on the electric field is modeled by a simple 1D WKB approximation for the tunneling process, which shows that the energetic position of the wetting layer is important for the measured tunneling time out of the dot.

Introduction

Since the first proposal of quantum dots in 1982 [1] a great deal of research has been dedicated to the study of the optical and electrical properties of QD's. The improved understanding of the excellent properties of this quantum system made it already possible to implement QD's in devices like lasers [2], [3], MIR photodetectors [4], single-photon turnstile devices [5], [6] or single-electron turnstile devices [7]. In previous work [7], [8] a decay of the coherent excitation was observed due to competing mechanisms like carrier-carrier scattering, Coulomb scattering, phonon scattering and tunneling escape.

In this contribution we investigate the influence of these scattering processes on the scattering rate of the observed exciton ground state transition. In our experiments we resonantly excite the exciton interband ground state transition of single InAs/GaAs self-assembled QD's embedded in an *n-i*-Schottky photodiode. QD's provided with both electric contacts and optical access allow us to vary independently the electric field while measuring the electrical or optical response of a single QD. Complementary to the photoluminescence (PL), the collected photocurrent (PC) provides information about the absorption spectrum and the tunneling escape times of single QD's.

Experimental

Sample and Experimental Setup

The sample investigated was grown using molecular beam epitaxy on semi-insulating GaAs (100). Nominally, 1.55 ML of InAs are deposited at 500 °C on *i*-GaAs 40 nm

above an *n*-doped GaAs layer (10^{18} cm^{-3}) which forms the bottom contact. During the growth of the QD's the rotation of the wafer has been stopped to produce an InAs deposition gradient across the wafer, resulting in a variation of the corresponding InAs QD density. Atomic force microscopy (AFM) studies of a similar sample with uncapped dots could determine the density gradient from ~500 μm^{-2} to zero. The growth of the self-assembled QDs is followed by 80 nm *i*-GaAs, a 40 nm thick $Al_{0.3}Ga_{0.7}As$ barrier, and a 10 nm *i*-GaAs cap layer. After the growth the sample was processed by photolithographic methods into photodiodes. Ohmic contacts were established to the doped n^+ region and semitransparent Ti-Schottky contacts were deposited on the top surface to achieve a homogeneous electric field in the region of the investigated QD's. The Schottky contact was in addition covered with an opaque Au mask where 2 μm^{-2} apertures were opened to allow optical access to the QDs. The results reported in the present work were obtained from a region of the wafer where the QD density I < 1 μm^{-2}.

The PL and the PC measurements were performed at 4.2 K using the 760 nm line of a cw Ti:Sapphire laser for PL spectroscopy and a tunable Ti:Sapphire laser to resonantly excite the QD energy levels for PC spectroscopy. The sample was placed in a low drift Oxford LHe flow cryostat. The PL and PC excitation paths as well as the PL detection path lead through a confocal laser scanning microscope (LSM) with a lateral and axial resolution below 500 nm. The PL signal is filtered by an 850 nm long pass filter and dispersed in a 0.5 m spectrometer, which allows a spectral resolution better than 50 µeV with a liquid nitrogen cooled CCD detector. The PC signal is detected by a sensitive photodiode amplifier which is capable to bias the photodiode and standard lock-in technique. The spectral resolution of the PC measurements determined by the laser linewidth is ≈30 µeV.

Measurements

The band structure under negative bias condition is shown schematically in Fig. 1. Changing the bias voltage from positive to negative voltage reduces the tunneling barrier thickness in the direction of the applied field and therefore the tunneling time τ_t of the photoexcited carriers out of the dot. When τ_t becomes equal or even smaller than the radiative lifetime of the exciton τ_r ~ 1 ns one changes from the PL measurement regime to the PC measurement regime.

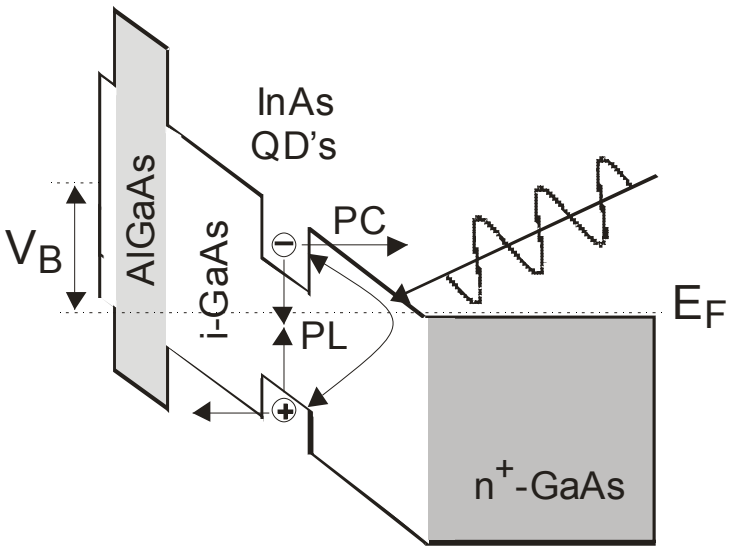

Fig. 1: Schematic band diagram of the investigated Schottky photodiode under negative bias voltage V_B

Figures 2 (a) and (b) show PL and PC spectra at the same aperture of the shadow mask under different bias conditions. In both cases sharp single peaks are observed attributed to single QD emission (PL) and absorption (PC). The PC line in Fig. 2 (b) is measured at higher electric field than the PL line in Fig. 2 (a) and is therefore shifted to a lower energy due to the QCSE. Under the measurement conditions shown in the inset of Fig. 2 (b) the observed PC peak magnitude is 2.5 pA. This current corresponds to a generation rate of 10^7 e-h pairs per second. The fact that no biexciton lines are observed, which have typically about 3 meV binding energies, leads to the conclusion that the used excitation power was low enough that occupation of the QD with more than one exciton can be excluded. The FWHM of the PL line corresponds (according to $\tau \sim \hbar/(2\Gamma)$) to an exciton lifetime τ of about 6 ps which is approx. three orders of magnitude smaller than the radiative lifetime of 1 ns mentioned above. This effective lifetime is given by $\tau^{-1} = \tau_r^{-1} + \tau_t^{-1} + \tau_c^{-1}$, where τ_r is the recombination time, τ_t is the tunneling time and τ_c^{-1} describes Coulomb scattering by free carries (due to the nonresonant excitation for PL), defects, impurities, and alloy fluctuations. The PC linewidth is limited to ~100 µeV for low electric fields where also PL can be measured. Due to these findings we claim that the FWHM of the measured PC and PL lines is limited due to the Coulomb interactions mentioned above. The PC signal can be observed in the electric field range of 30 kV/cm to 80 kV/cm.

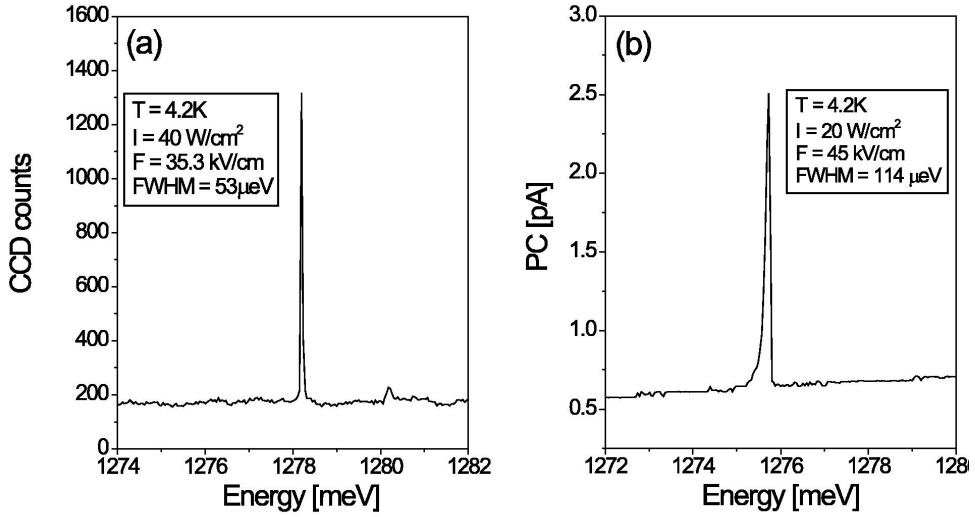

Fig. 2: Photoluminescence (a) and photocurrent (b) spectrum of a single QD. The energetic shift is due to the Stark shift and bias-controlled charging of the QD at low electric fields where the QD ground state level is shifted below the Fermi level [9].

Conclusion

In this contribution we report on field-dependent photocurrent measurements of the excitonic interband transitions of single InAs/GaAs self-assembled QD's. The application of an external electric field allows controlling the transition energy due to the QCSE. The measured Stark shift S = 4.3 meV/V of the exciton transition can be used for the realization of a single QD spectrometer. From the measured Stark shift we obtain a dipole moment $p = (4.3 \pm 0.2) \times 10^{-29}$ Cm. The decrease of the PC linewidth for low electric fields is limited to a value of $\Gamma \sim 100$ µeV, which is attributed to Coulomb interaction of the exciton with carriers surrounding the QD.

Acknowledgements

The authors acknowledge financial support by the Austrian Science Fund (FWF), SFB-ADLIS and START Y-47.

References

[1] Y. Arakawa and H. Sakaki, *Appl. Phys. Lett.* **40**, 939 (1982).

[2] G. Park, O.B. Shchekin, D.L. Huffaker, D.G. Deppe, *IEEE Photon. Tech. Lett.* **12**, 230 (2000).

[3] N.N. Ledentsov, A.R. Kovsh, A.E. Zhukov, N.A. Maleev, S.S. Mikhrin, A.P. Vasil'ev, E.S. Semenova, M.V. Maximov, Yu.M. Shernyakov, N.V., Kryzhanovskaya, V.M. Ustinov, D. Bimberg, *IEEE Electron. Lett.* **39**, 1126 (2003).

[4] L.Rebohle, F.F. Schrey, S. Hofer, G.Strasser, K. Unterrainer, *Appl. Phys. Lett.* **81**, 2079 (2002).

[5] P. Michler, A. Kiraz, C. Becher, W.V. Schoenfeld, P.M. Petroff, Lidong Zhang, E. Hu, A. Imamoglu, *Science* **290**, 2282 (2000).

[6] Z. Yuan, B.E. Kardynal, R.M. Stevenson, A.J. Shields, C.J. Lobo, K. Cooper, N.S. Beattie, D.A. Ritchie, M. Pepper, *Science* **295**, 102 (2002).

[7] A. Zrenner, E. Beham, S. Stufler, F. Findeis, M. Bichler, G. Abstreiter, *Nature* **418**, 612 (2002).

[8] X. Li, Y. Wu, D. Steel, D. Gammon, T.H. Stievater, D.S. Katzer, D. Park, C. Piermarocchi, and L.J. Sham, *Science* **301**, 809 (2003).

[9] F. Findeis, M. Baier, E. Beham, A. Zrenner, and G. Abstreiter, *Appl. Phys. Lett.* **78**, 2958 (2001).

Carrier Dynamics in Quantum Dots

T. Müller, F.F. Schrey, G. Fasching, L. Rebohle, G. Strasser, K. Unterrainer

Institut für Photonik & Zentrum für Mikro- und Nanostrukturen, TU-Wien
Floragasse 7, A-1040 Wien, Austria

The electron capture and relaxation dynamics in self-assembled InAs/GaAs quantum dots is investigated by means of interband pump – intraband probe spectroscopy. By tuning femtosecond infrared pulses into resonance with intraband transitions between confined quantum dot states and the wetting layer continuum, the electron population of the quantum dot ground state is determined as a function of time-delay after the interband pump.

Introduction

The capture and relaxation of carriers in semiconductor quantum dots (QDs) has attracted much attention during the last decade, since a profound understanding of these processes is essential for the development of novel optoelectronic devices. A drastic slow-down of the relaxation compared to higher-dimensional structures has been predicted because of the so-called phonon bottleneck effect [1], [2]. However, it has turned out that a number of scattering processes, including multi-phonon emission [3] – [7], electron-electron scattering [8] – [10] and electron-hole scattering [11], [12], can circumvent the phonon bottleneck, leading to capture and relaxation times from approximately one to several tens of picoseconds. Most of the experiments have been performed by using interband techniques, such as time-resolved photoluminescence (PL) spectroscopy [4], [5], [7], [9] and differential transmission spectroscopy [6], [11], where the signal reflects the combined electron-hole dynamics. In this letter we report an interband pump – intraband probe experiment, which is sensitive to the capture and relaxation of electrons only. The pump excites electrons and holes in the GaAs matrix surrounding the QDs, while the infrared (IR) probe is tuned into resonance with electronic intraband transitions [13] between the bound QD states and continuum states in the wetting layer (WL).

Results and Discussion

The investigated sample was grown by molecular beam epitaxy on a semi-insulating GaAs substrate. It consists of 30 layers of InAs QDs separated by 50 nm thick GaAs barriers and a 50 nm GaAs cap layer. The dot density was estimated from an atomic force microscopy study to be around 2×10^{10} cm^{-2} per layer. For IR absorption measurements, the sample was polished at 58° to the growth axis in order to form a single-pass waveguide for the IR radiation.

Room-temperature PL spectra for two different excitation densities were recorded using a continuous-wave Ti:sapphire laser (740 nm excitation wavelength) and are presented in Fig. 1. At low excitation density (25 W/cm^2) we observe two transitions corresponding to *e*1*h*1 luminescence at 1.081 eV and *e*2*h*2 luminescence at 1.137 eV. At higher excitation (1 kW/cm^2) the QD states are filled up and luminescence corresponding to the *e*3*h*3 transition at 1.194 eV is also observable, as well as luminescence at 1.333 eV from the underlying InAs WL. The inhomogeneous broadening of the transitions (~50 meV full width at half maximum (FWHM)) mainly reflects the size distribution

of the InAs QDs. At T = 5 K the PL shifts by ~90 meV towards higher energy which is due to the temperature-dependence of the GaAs and InAs bandgaps. The energy differences between the QD states, however, are not affected. From the PL we determine an energetic difference of 252 meV between the QD ground state *e*1*h*1 and the WL. Approximately two thirds of this energetic difference occur between the conduction band offsets [6]. Thus, we estimate the intraband transition energy between the QD ground state *e*1 and the WL to be ~160 meV.

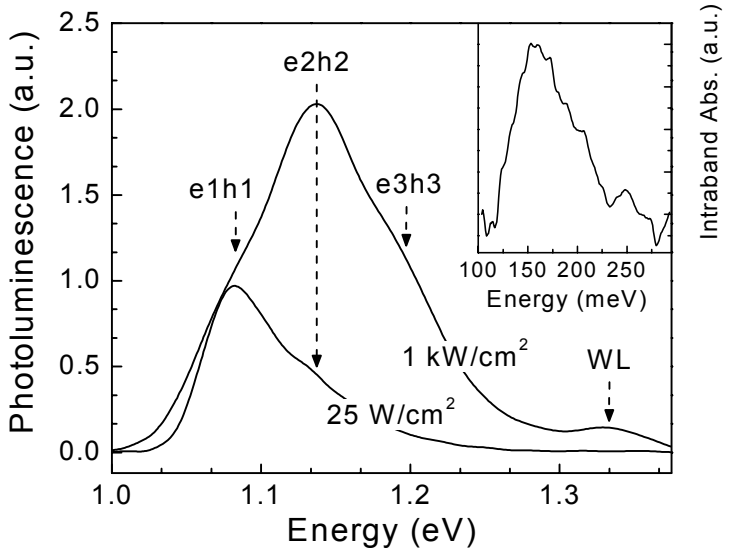

Fig. 1: Room-temperature photoluminescence spectra at two different excitation densities. Inset: Photoinduced intraband absorption spectrum at T = 5 K.

For time-resolved probing of the intraband transitions we used a mode-locked Ti:sapphire laser that delivers 12 fs pulses centered at a wavelength of 780 nm. Half of the laser intensity served as an interband pump to inject electrons and holes in the GaAs barriers. The other part was used to generate the linear polarized IR probe pulses by phase-matched difference frequency mixing in a 0.5 mm thick GaSe crystal [14]. The probe pulses are tunable in the E_{pr} = 75 – 155 meV range (10 – 20 meV FWHM) with pulse durations between ~100 and ~200 fs.

Figure 2 (a) shows typical pump-probe signals (E_{pr} = 155 meV, I_p = 25 W/cm^2) at room-temperature when the probe is tuned into resonance with the *e*1–WL transition. When the probe is polarized perpendicular to the growth direction (*s*-polarization) we observe a step-like increase of the absorption, which rises within the time resolution of the experiment and decays within several hundred picoseconds. This signal is attributed to free-carrier absorption in the substrate and barriers and its decay to free-carrier recombination. When the probe is polarized in growth direction (*p*-polarization) a slowly rising absorption superimposed on the free-carrier signal is observed. Relaxation and thermalization in the GaAs barriers and the InAs WL occur on a time scale <1 ps. Thus, the slow rise of the absorption reflects the effective electron capture into the QD, more precisely into the QD ground state. From the absorption data we deduce the capture time τ_c by an exponential fitting procedure.

The inset of Fig. 2 (a) displays the excitation density dependence of the capture time τ_c at room-temperature. We observe two regimes exhibiting a different density dependence of the capture time. τ_c decreases with increasing excitation density above 25 W/cm^2. In contrast, the capture time changes only slightly at low excitation densities. The high-power dependence can be explained by electron-electron scattering: An elec-

tron is scattered into the QD ground state by transferring its energy to a hot electron in the barrier or the WL. A sequence of scattering processes where the electron relaxes through excited QD states is even more probable [8]. Assuming that the electron-electron scattering rate is proportional to the excitation density and taking another density-independent scattering process (described by the scattering rate τ_i^{-1}) into account we can write for the overall capture rate [9] $\tau_c^{-1} = \tau_i^{-1} + \sigma \cdot I_p$, where σ is a fitting parameter. Using this simple expression we can fit the experimental results, as shown by the solid line in Fig. 2 (a).

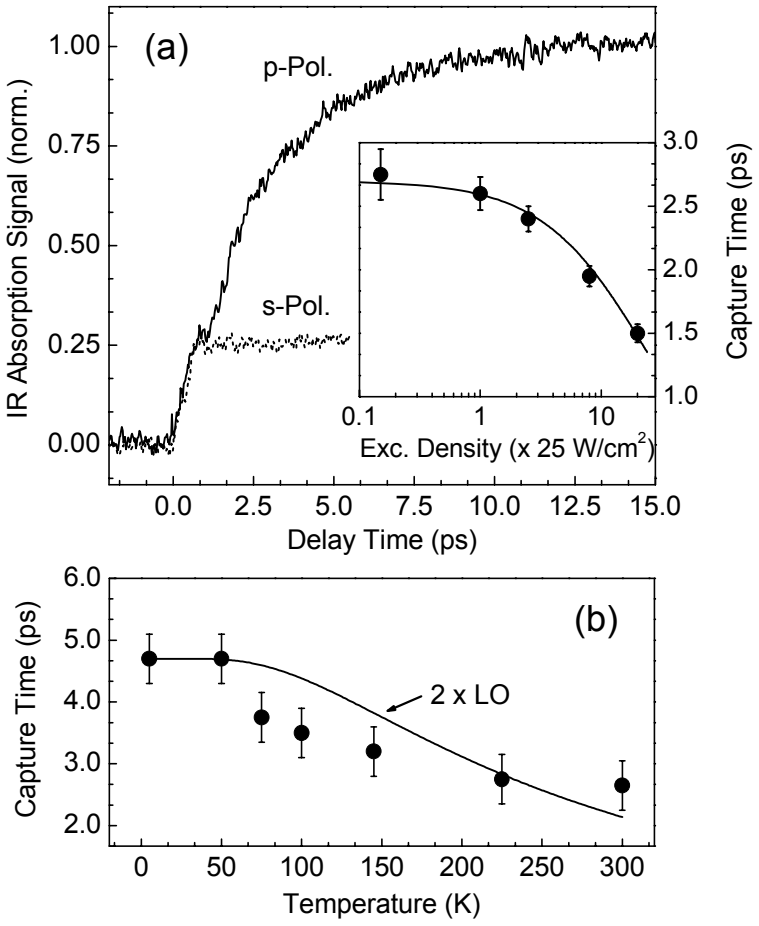

Fig. 2: (a) Photoinduced IR absorption signals of the QD sample as a function of pump-probe delay for a probe energy of 155 meV. Inset: excitation density dependence of the capture time at room-temperature. (b) Temperature-dependence of the capture time at an excitation density of 25 W/cm^2.

Let us now turn our attention to the low-density regime where electron-electron scattering can be ruled out as a relaxation mechanism. Figure 2 (b) shows the temperature-dependence of the capture time at I_p = 25 W/cm^2. We find an increase of τ_c from 2.7 ps to 4.7 ps upon decreasing the temperature from 300 K to 5 K. Two scattering mechanisms could explain such short capture times at low excitation density:

(i) Multi-phonon emission: One possible explanation for the observed short capture times could be that electrons scatter between subsequent QD states via repeated emission of two LO phonons. The corresponding two-phonon scattering rate for this process can be written as [7] $\tau_c^{-1} = \Gamma_0 \times [N_{LO}(T) + 1]^2$, where Γ_0 is the scattering rate at

T = 0 K and $N_{LO}(T)$ is the Bose-Einstein distribution function for LO phonons. The calculated curve can roughly account for the experimental temperature dependence, as shown in Fig. 2 (b) by the solid line. Although LO phonons can relax electrons in a QD only for a narrow range of dot sizes (because of their weak dispersion), emission of energetically different LO phonons (from the GaAs barriers, the WL, the QDs, and the respective interfaces) and also broadening of the phonons (due to strain and alloy inhomogeneities) could enlarge this energetic window [14].

(ii) Electron-hole scattering: Another fast relaxation mechanism in QDs is electron-hole scattering. Since this process involves only a single electron and a single hole in a QD it can occur even at very low excitation densities [11]. Due to the high effective hole mass the QD level separation in the valence band is in the range of a few meV. This allows holes to thermalize within several hundred femtoseconds. Electrons in the conduction band can transfer their energy to holes, which then lose their energy via phonons.

Acknowledgements

This work was sponsored by “Gesellschaft für Mikroelektronik (GMe)” and “Fonds zur Förderung der wissenschaftlichen Forschung (SFB-ADLIS)”.

References

[1] U. Bockelmann and G. Bastard, Phys Rev. B **42**, 8947 (1990).

[2] H. Benisty, C. M. Sotomayor-Torres, and C. Weisbuch, Phys Rev. B **44**, 10945 (1991).

[3] T. Inoshita and H. Sakaki, Phys. Rev. B **46**, 7260 (1992).

[4] B. Ohnesorge, M. Albrecht, J. Oshinowo, A. Forchel, and Y. Arakawa, Phys. Rev. B **54**, 11532 (1996).

[5] R. Heitz, M. Veit, N. N. Ledentsov, A. Hoffmann, D. Bimberg, V. M. Ustinov, P. S. Kopev, and Zh. I. Alferov, Phys. Rev. B **56**, 10435 (1997).

[6] J. Feldmann, S. T. Cundiff, M. Arzberger, G. Böhm, and G. Abstreiter, J. Appl. Phys. **89**, 1180 (2001).

[7] M. De Giorgi, C. Lingk, G. von Plessen, J. Feldmann, S. De Rinaldis, A. Passaseo, M. De Vittorio, R. Cingolani, and M. Lomascolo, Appl. Phys. Lett. **79**, 3968 (2001).

[8] U. Bockelmann and T. Egeler, Phys. Rev. B **46**, 15574 (1992).

[9] D. Morris, N. Perret, and S. Fafard, Appl. Phys. Lett. **75**, 3593 (1999).

[10] S. Sauvage, P. Boucaud, F. Glotin, R. Prazeres, J.-M. Ortega, A. Lemaître, J.-M. Gérard, and V. Thierry-Flieg, Appl. Phys. Lett. **73**, 3818 (1998).

[11] T. S. Sosnowski, T. B. Norris, H. Jiang, J. Singh, K. Kamath, and B. Bhattacharya, Phys. Rev. B **57**, R9423 (1998).

[12] R. Ferreira and G. Bastard, Appl. Phys. Lett. **74**, 2818 (1999).

[13] S. Sauvage, P. Boucaud, F. H. Julien, J.-M. Gérard, and V. Thierry-Mieg, Appl. Phys. Lett. **71**, 2785 (1997).

[14] R. A. Kaindl, D. C. Smith, and T. Elsaesser, Opt. Lett. **23**, 861 (1998).

Ultrafast Intersublevel Spectroscopy of Quantum Dot Ensembles and Single Quantum Dots

F.F. Schrey, G. Fasching, T. Müller, G. Strasser, and K. Unterrainer

Zentrum für Mikro- und Nanostrukturen, Technische Universität Wien, Floragasse 7, A-1040 Wien

Based on ultrafast interband pump intraband probe spectroscopy we measure electron capture and relaxation times into the discrete dot energy levels within a few picoseconds and discuss possible relaxation mechanisms. Further we present an approach to rule out dot ensemble related effects within the time resolved measurements by combining interband micro-photoluminescence measurements with the intersublevel pump and probe spectroscopy. We show preliminary results for time-resolved, mid infrared induced direct electron transfer between electron intersublevels, which is monitored by changes in the interband luminescence of a single quantum dot.

Introduction

The strong interest in semiconductor quantum dots (QD) is based on their macroscopic quantum mechanical properties. Their low dimensionality within the surrounding 3D semiconductor matrix reduces phase scattering within the quantum mechanical wavefunctions of the QDs and leads to atomlike eigenstates in their energetic structure. Within the last decade, many attempts were made to exploit these properties in order to optimize the performance of optoelectronic devices like mid- and far-infrared photodetectors [1] or QD based near-infrared band-gap lasers [2]. Furthermore, it became possible to directly address single QDs, which led to optically and electrically driven single photon turnstile devices [3]. QDs can even be regarded as candidates for quantum-bit operations since its eigenstates could be entangled and basic q-bit operations have been carried out [4].

However many questions concerning carrier dynamics in QDs still remain open. Especially where only the electrons within the dots contribute to the device performance, the existing interband techniques to study exciton dynamics within these nanostructures deliver only ambiguous results, which complicate or even prevent the correct design of the device. Hence, getting access to the electron properties separated from hole contributions and ensemble related effects will allow accurate predictions how far QDs can improve devices working in the MIR and FIR regions.

We will demonstrate how ultrafast interband pump intraband probe spectroscopy will access these informations.

Experiments

Both samples were grown by MBE on semi-insulating GaAs substrates. The first one, for QD ensemble experiments, consists of 30 layers of InAs QDs separated by 50 nm thick GaAs barriers and a 50 nm GaAs cap layer. The dot density was estimated from an atomic force microscopy study to be around 2×10^{10} cm^{-2} per layer. For IR absorption measurements, the sample was polished at 58° to the growth axis in order to form a

single-pass waveguide for the IR radiation and to enable a considerable electric field component along the growth axis. The second sample for single dot (SQD) experiments contains only one QD layer with a density gradient between 10^7 dots/cm^2 and 5×10^{10} cm^{-2}. In the low-density area, the sample was processed into 8.5 µm tall micropillars with diameters between 1 and 10 µm. This assures the illumination and detection of one QD only in the micro-photoluminescence (µPL) experiments below.

For the first sample room-temperature photoluminescence (PL) spectra for two different excitation densities were recorded using a continuous-wave Ti:sapphire laser (740 nm excitation wavelength). From the PL we determine an energetic difference of 252 meV between the QD ground state e1h1 and the wetting layer (WL). Approximately two thirds of this energetic difference occur between the conduction band offsets [5]. Thus, we estimate the intraband transition energy between the QD ground state e1 and the WL to be ~160 meV. Accordingly, we expect intraband transitions from the excited states e2 and e3 to the WL at energies of ~105 meV and ~50 meV, respectively. Thus, the intraband absorption into the WL at probe energies of 160, 105 and 50 meV can be interpreted in terms of e1, e2 and e3 QD level electron populations, respectively.

For time-resolved probing of the intraband transitions, we used a mode-locked Ti:sapphire laser that delivers 12 fs pulses centered at a wavelength of 780 nm. Half of the laser intensity I_p served as an interband pump to inject electrons and holes in the GaAs barriers. The other part was used to generate the linear polarized IR probe pulses by phase-matched difference frequency mixing in a 0.5 mm thick GaSe crystal [6]. The probe pulses are tunable in the 75 – 155 meV range with pulse durations between ~100 and ~200 fs.

Absorption signals were measured at two different IR probe beam polarizations: When the probe is polarized perpendicular to the growth direction (s-polarization) we observe a step-like increase of the absorption, which rises within the time resolution of the experiment and decays within several hundred picoseconds. This signal is attributed to free-carrier absorption in the substrate and barriers and its decay to free-carrier recombination. When the probe is polarized in growth direction (p-polarization) a slowly rising absorption superimposed on the free-carrier signal is observed. Relaxation and thermalization in the GaAs barriers and the InAs WL occur on a time scale <1 ps. Thus, the slow rise of the absorption reflects the effective electron capture into the QD, more precisely into the QD ground state. From the absorption data, we deduce the capture time τ_c by an exponential fitting procedure.

Let us turn our attention to an excitation regime where electron-electron scattering can be ruled out as a relaxation mechanism [7]. Recording the temperature-dependence of the capture time at I_p = 25 W/cm^2 we find an increase of τ_c from 2.7 ps to 4.7 ps upon decreasing the temperature from 300 K to 5 K. Two scattering mechanisms could explain such short capture times: (i) multi-phonon emission and (ii) electron-hole scattering.

(i) Multi-phonon emission: The most efficient capture pathway in our sample is the step-wise relaxation through the excited QD states. The longitudinal optical (LO) phonon energy in InAs amounts to E_{LO} = 29 meV and the average electron level separation in our QDs is ~55 meV. Thus, one possible explanation for the observed short capture times could be that electrons scatter between subsequent QD states via repeated emission of two LO phonons [7], [8]. Although LO phonons can relax electrons in a QD only for a narrow range of dot sizes (because of their weak dispersion), emission of energetically different LO phonons (from the GaAs barriers, the WL, the QDs, and the respective interfaces) and also broadening of the phonons (due to strain and alloy inhomogeneities) could enlarge this energetic window [6]. This “continuum” of LO phonons could relax the entire distribution very efficiently.

(ii) Electron-hole scattering: since this process involves only a single electron and a single hole in a QD, it can occur even at very low excitation densities [9]. Due to the high effective hole mass, the QD level separation in the valence band is in the range of a few meV. This allows holes to thermalize within several hundred femtoseconds. Electrons in the conduction band can transfer their energy to holes, which then lose their energy via phonons. Holes can be scattered depending on their initial energy either into higher QD hole states or into the WL.

Our understanding of the capture process is the following: Electrons are generated by the pump pulse in the GaAs barrier and are then transferred very fast into the WL. This process, which is mediated by LO phonons, occurs on a sub-picosecond timescale [10]. Afterwards the electrons relax between subsequent QD states either via repeated emission of two LO phonons or via subsequent electron-hole scattering processes.

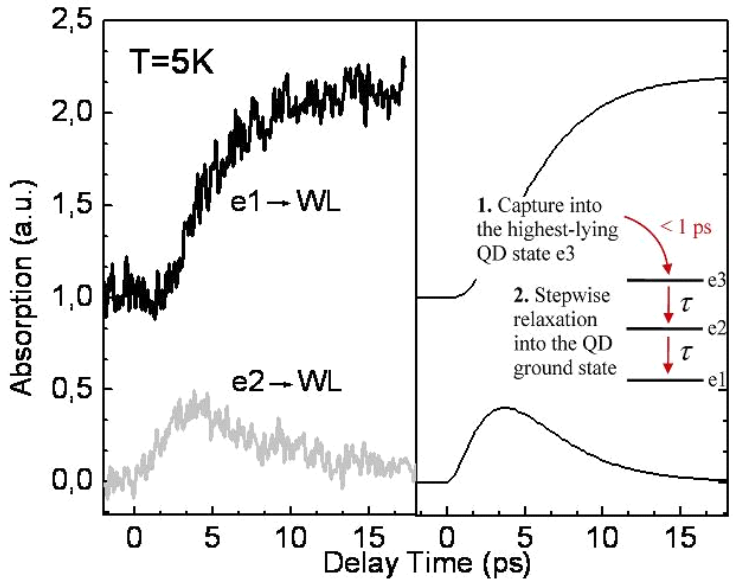

Fig. 1: (a) Photoinduced IR absorption signals for the E1-WL transition at 155 meV and the E2-WL transition at 105 meV (lower curve) as a function of pump-probe delay at 5K. (b) Results from the three level model sketched between the curves.

In order to support this interpretation we compare in Fig. 1 (a) the IR absorption at energies of 155 meV and 105 meV, corresponding to the e1-WL and e2-WL intraband transitions, respectively (T = 5 K). Note that in this figure the free-carrier absorption signals have been subtracted for better clarity. Since the absorption signals can be interpreted in terms of QD level populations it is clear that the QD ground state e1 gets populated via the excited state e2, because the electrons leave e2 with the same time constant as they arrive in e1. In Fig. 1 (b) we present results obtained by solving the rate equations for a simple three-level model, shown in the inset. In this model it is assumed that electrons populate the highest-lying QD state e3 within 1 ps after the pump and relax afterwards via e2 to the ground state e1. Good agreement with the experimental data is obtained for τ = 2.5 ps. These results suggest that not only the capture, but also the relaxation of electrons in our QDs occurs on a picosecond timescale [7].

However, these experiments cannot completely satisfy question concerning the relaxation processes. The ensemble broadening in PL as well as in the absorption signal might cover important aspects within the dynamic behavior of the dots. To rule out ensemble related processes or contributions from the surrounding material these time

resolved studies have to be extended into the SQD regime. Since direct MIR pump and probe measurements on SQDs are impossible due to the small sensitivity of absorption measurements, another radiative process has to be used to monitor the intersublevel dynamic. We suggest using the recombination NIR radiation of excitons and excited excitons within the SQD for this purpose. By combining P&P with the µPL setup, we obtain all necessary tools for our time resolved investigation.

Preliminary results from NIR excitation of a SQD within a micromesa structure superimposed with cw MIR radiation indicate a direct electron transfer between the s- and p-levels of the SQD [11], [12]. Corresponding to the electron occupation the photon count rate of the exciton lines is changed if MIR excitation is superimposed on the NIR excitation.

In case of a time resolved experiment we expect changes in the photon count rate in dependence of the NIR-pump-MIR-probe delay. Such an experiment is depicted in Fig. 2 (a) where we recorded the delay dependent count rate for an exciton ground state in a SQD within a 5 µm micropillar.

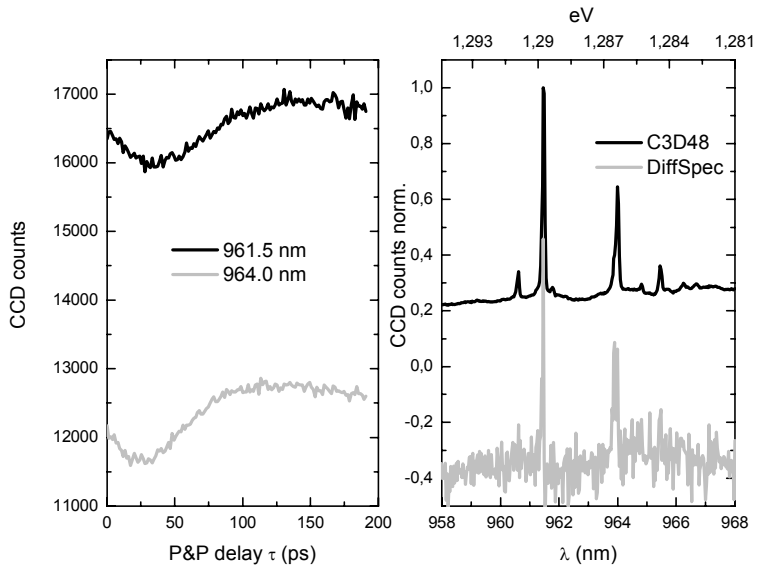

Fig. 2: Intersublevel dynamics in a SQD: (a) Photon count rate in dependence of P&P time delay τ. (b) Spectrum of QD ground state (upper curve) and difference spectrum after NIR/MIR superposition at τ = 30 ps.

In this case, the electron is transferred via the 95 meV MIR probe pulse from the ground state into the WL continuum and thus removed from the recombination channel of the SQD. Consequently, the PL count rate decreases for the observed transitions at 961.5 nm and 964 nm. As control experiment we recorded the SQD spectrum for NIR excitation with and without superimposed MIR radiation at delay τ = 30 ps. Afterwards we subtracted both spectra from each other as depicted in the lower curve of Fig. 2 (b). Again the count rate was decreased if an appropriate delay interval was chosen while no effect could be monitored if a very large time delay (>400 ps) was chosen. Further investigations of these MIR induced electron transfers will follow and new insights into the relaxation effects within SQDs are expected in the near future.

Conclusions

We suggest exploiting the capacity of ultrafast interband pump intraband probe spectroscopy combined with μPL tools for the investigation of QD dynamics. We could monitor the electron capture and relaxation dynamics of a QD ensemble on a low picosecond timescale. In addition, we could demonstrate a P&P procedure that allows studying electron dynamics in a single QD.

Acknowledgements

This work was supported by the EC (NMP-project) ANSWER, the Austrian FWF (SFB-ADLIS) and the Austrian Gesellschaft für Mikro- und Nanoelektronik (GMe).

References

[1] L. Rebohle, F. F. Schrey, S. Hofer, G. Strasser, and K. Unterrainer, Appl. Phys. Lett. 81, 2079 (2002).

[2] D. Bimberg, N. N. Ledentsov, N. Grundmann, N. Kirstaedter, O. G. Schmidt, M. H. Mao, V. M. Ustinov, A. Y. Egorof, A. E. Zhukov, P. S. Kopev, Z. I. Alferov, S. S. Ruvimov, U. Goesele, and J. Heydenreich, Phys. stat. sol. (b) 194, 159 (1996).

[3] P. Michler, A. Kiraz, C. Becher, W. V. Schoenfeld, P. M. Petroff, Lidong Zhang, E. Hu, A. Imamoglu, Science 290, 2282 (2000)

[4] Xiaoqin Li, Yanwen Wu, Duncan Steel, D. Gammon, T. H. Stievater, D. S. Katzer, D. Park, C. Piermarocchi, and L. J. Sham, Science 301, 809 (2003)

[5] D. Wasserman and S. A. Lyon, Appl. Phys. Lett. 81, 2848 (2002).

[6] R. A. Kaindl, D. C. Smith, and T. Elsaesser, Opt. Lett. 23, 861 (1998).

[7] T. Müller, F.F. Schrey, G. Strasser, and K. Unterrainer, Appl. Phys. Lett. 83, 3572 (2003)

[8] M. De Giorgi, C. Lingk, G. von Plessen, J. Feldmann, S. De Rinaldis, A. Passaseo, M. De Vittorio, R. Cingolani, and M. Lomascolo, Appl. Phys. Lett. 79, 3968 (2001).

[9] T. S. Sosnowski, T. B. Norris, H. Jiang, J. Singh, K. Kamath, and B. Bhattacharya, Phys. Rev. B 57, R9423 (1998).

[10] R. Ferreira and G. Bastard, Appl. Phys. Lett. 74, 2818 (1999).

[11] F.F. Schrey, G. Fasching, T. Müller, G. Strasser, and K. Unterrainer, phys. stat. sol. (c) 1, 434 (2004)

[12] F.F. Schrey, T. Müller, G. Fasching, S. Anders, C. Pflügl, W. Schrenk, G. Strasser, and K. Unterrainer, Physica E 25, 271 (2004)

Cross-Sectional Ballistic Electron Emission Microscopy for Schottky Barrier Height Profiling on Heterostructures

D. Rakoczy, G. Strasser, J. Smoliner

Institut für Festkörperelektronik & Mikrostukturzentrum der TU-Wien
Floragasse 7, A-1040 Wien, Austria

In this work, Cross-Sectional Ballistic Electron Emission Microscopy (= ”XBEEM”) is introduced to determine a Schottky barrier height profile of a GaAs-AlGaAs multi heterostructure in cross-sectional geometry. Ballistic electron spectra measured across the heterostructure with nm resolution indicate that the measured Schottky barrier height profile is smeared out compared to the conduction band profile calculated from the sample growth parameters. We attribute this behavior to lateral band bending effects along the heterojunction. In addition, we have evidence that the barrier height profile is influenced by single impurities in the AlGaAs layers.

Introduction

Ballistic Electron Emission Microscopy (BEEM) [1], [2] is a three terminal extension of Scanning Tunneling Microscopy (STM) [3] – [5] where the STM tip is used to inject hot electrons into a semiconductor via a thin metallic base layer evaporated onto a semiconductor surface. If the electron energy is high enough to overcome the Schottky barrier height at the metal-semiconductor interface, the electrons can penetrate into the semiconductor. The corresponding current, measured vs. the tunneling bias using a backside collector contact, is called BEEM spectrum. By mapping the BEEM current for a constant tip bias while scanning the sample surface, images can be taken with a spatial resolution of about 1 nm. Presently, BEEM is a well established technique to determine Schottky barrier heights (SBH) and subsurface band offsets. An overview of this technique can be found in several review articles [6] – [8].

Cross-sectional STM techniques are widely used in surface physics. During the last years, it was found that cross-sectional STM techniques (XSTM) are especially helpful for the characterization of MBE (Molecular Beam Epitaxy) grown heterostructures. XSTM measurements, e.g. have resolved atomic features of segregated interfaces [9], [10]. More recently, special attention was given to XSTM on InAs-GaAs heterostructures, since they are the base material for self assembled quantum dots. On such samples, the local composition of the InAs dots and the wetting layer [11], [12] was studied by XSTM.

Surprisingly, and although it is a quite straightforward idea to combine cross-sectional STM techniques and BEEM, no cross-sectional BEEM (XBEEM) experiments have been reported in the literature until now. In our opinion, the reason for this is not a lack of application possibilities, but notable technical difficulties, e.g. the precise sample positioning and, especially for profile measurements, a state of the art compensation of piezo creep. Once these problems are overcome, XBEEM turns out to be a very useful technique to determine profiles of various band structure related features, e.g. the conduction band offsets of GaAs-AlGaAs multi heterostructures.

Experimental

In this paper, cross-sectional BEEM measurements are reported on the cleaved [011] surface of a GaAs-AlGaAs multi-heterostructure covered with gold. To test XBEEM as a new method for cross-sectional SBH profile measurements, we used an MBE grown GaAs-AlGaAs multiple barrier structure with relatively thick layers: On a semi insulating substrate (GaAs [100]), a 3 µm thick layer of n-type GaAs (silicon doped, N_D = $8x10^{16}$ cm^{-3}) was grown as a spacer. On top of this layer we grew 6 periods of an AlGaAs-GaAs heterostructure (d_{AlGaAs} = 20 nm, d_{GaAs} = 50 nm) followed by a 200 nm thick GaAs spacer. This layer sequence was repeated three times, however, with layer thicknesses of (d_{AlGaAs} = 50 nm, d_{GaAs} = 20 nm) and (d_{AlGaAs} = 50 nm, d_{GaAs} = 50 nm), respectively. The aluminum content was 30% for all AlGaAs layers. In order to use the sample in a BEEM configuration one has to provide means to collect the injected ballistic current. This was achieved by doping all GaAs layers with silicon (N_D = $8x10^{16}$ cm^{-3}) and the AlGaAs layers with N_D = $5.6x10^{16}$ cm^{-3}, which guarantees a sufficient collector conductance as well as a good Schottky contact.

To prepare the samples for BEEM, InSn pellets were alloyed into the sample to establish the collector contact. After that, the samples were cleaved in air and immediately transferred into a vacuum chamber. As base layer, a 7 nm thick gold film was evaporated onto the cleaved [011] surface at base pressures $<1x10^{-7}$ mbar using shadow evaporation techniques. After the evaporation process, the samples were glued on edge onto a sample transfer plate with conductive silver, which also provides the contact to the InSn pellets. An indium covered gold wire was attached to the gold covered [011] surface as a base contact. Finally, the sample was transferred as fast as possible into an Omicron Cryo SFM head. The scanning head is operated in helium atmosphere in a variable temperature inset of a cryostat. In this way, an undesired oxidation of the AlGaAs layers is suppressed. For all STM and BEEM measurements presented here, Au-coated ($d_{AU} \approx$ 10 nm) non-contact AFM-tips were used. All measurements were carried out at a temperature of T = 200 K. This temperature is a very good compromise in meeting the requirements of minimizing piezo drift and sample degradation on the one hand and of a sufficiently large scan field and an optimal duty cycle of the bath cryostat on the other hand.

Results

The left hand side of Fig. 1 (a) shows a topographic image of the active region of our sample. The image was recorded at a tunneling current of I_T = 2 nA and a bias of V_T = 1.6 V. Underneath the Au covered surface, the AlGaAs barriers are slightly visible as horizontal lines. The AlGaAs regions appear a little bit higher (≈ 0.5 nm) than the GaAs regions, which is due to weak strain effects between the GaAs and the AlGaAs layers. The right hand side of Fig. 1 (a) shows the corresponding BEEM image. Here, the AlGaAs barriers are clearly visible as dark horizontal lines. Note that the samples are not stable and start to degrade after being stored in air for some days. A typical example for this can be seen in Fig. 1 (b): Here, the Au layer appears to be broken into fragments and in the corresponding BEEM image (Fig. 1 (b), right), the AlGaAs barriers are no longer clearly resolved and appear to have intermixed with the GaAs layers. In addition, the overall transmission is reduced approximately by a factor of 5 compared to a fresh sample. We attribute this behavior to an oxidation of the AlGaAs layers.

Figure 2 shows typical BEEM spectra acquired on a GaAs (curve (1)) and an AlGaAs region (curve (2)) on the cross-section of our sample. To show the onsets more clearly, we zoomed into the interesting data range. As common practice in BEEM, the current onsets were determined by a Bell Kaiser fit and are at $V_{b,GaAs}$= 0.97 V and $V_{b,AlGaAs}$ = 1.235 V, respectively. The difference $e\Delta V_b$ = 265 meV is larger than the conduction band offset between GaAs and AlGaAs, which is ΔE_c =230 meV for x = 30% according

to the literature. Further note that these onset positions are about 50 meV higher compared to values commonly reported for conventional BEEM on [100] GaAs and AlGaAs samples. Possible explanations for this lie in the properties of the cleaved [011] surface and in the fact that the surface was not treated with HCl as it is usually done in conventional BEEM for oxide removal.

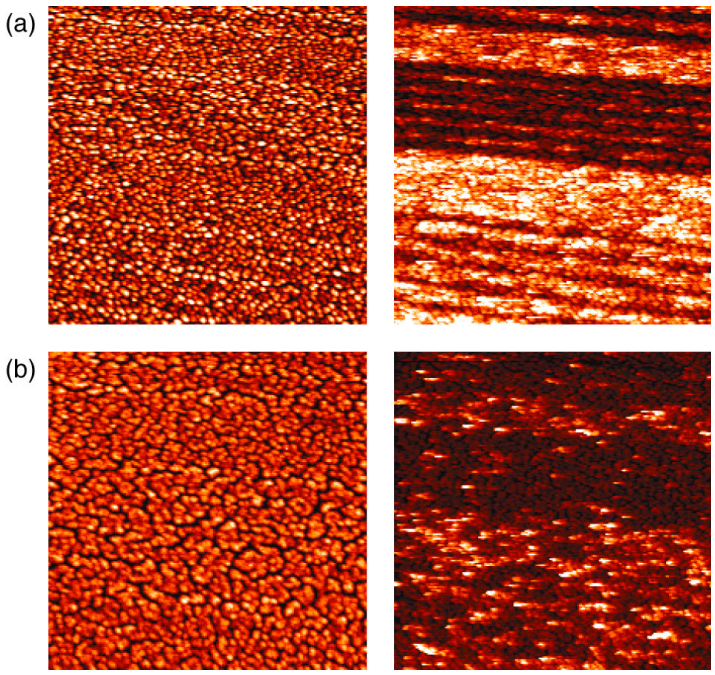

Fig. 1: (a), Left: Topographic STM image of the active region of our sample. Scan size is 1400 nm x 1400 nm. The z-scale is 4 nm. Tunneling current: I_T = 2nA, bias V_T = 1.6 V. Right: Simultaneously recorded BEEM image. The color scale corresponds to BEEM currents of 0…2.5 pA. (b), Images of a degraded sample, same scan size as in (a). I_T = 5nA, V_T = 1.6 V. Left: STM topography. The z-scale is 8 nm. Right: Simultaneously recorded BEEM image. The color scale corresponds to BEEM currents of 0…1.25 pA.

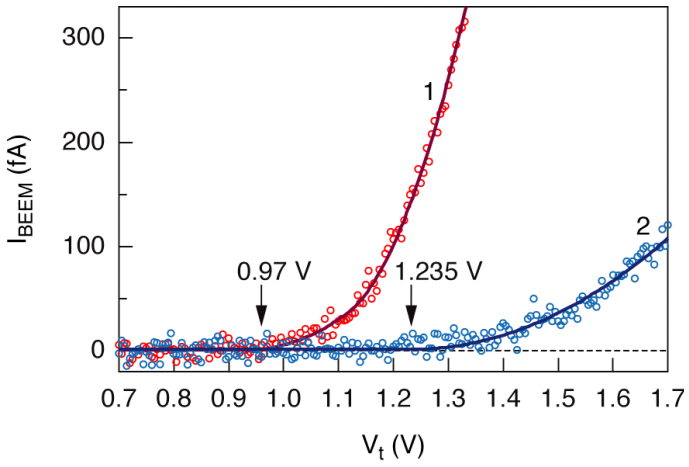

Fig. 2: Typical BEEM spectra acquired on a GaAs (curve (1)) and an AlGaAs region (curve (2)). The tunneling current was I_T = 2nA and the temperature was T = 200K. The onset bias is at 0.97 V and 1.235 V, respectively.

Figure 3 (top) shows a 143 nm x 45 nm large BEEM image taken in the area of an AlGaAs barrier. The barrier region is visible as dark area in this image, embedded by two brighter regions of GaAs. As typical for BEEM, the Au grains have a significant influence on the transmission. The total transmission is a convolution of the transmission of the granular Au layer and the barrier underneath, which makes it difficult to depict the sharp MBE grown GaAs-AlGaAs interface precisely. However, a different Au-coverage of the base layer does not influence the onset of the BEEM spectra, which is merely determined by the Schottky barrier height.

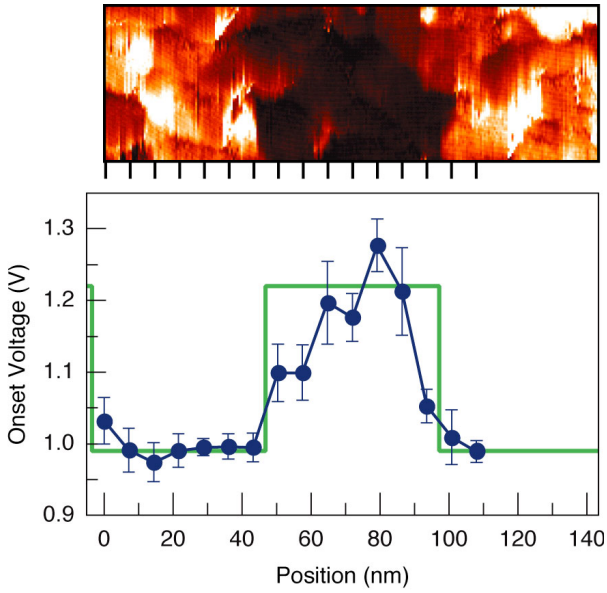

Fig. 3: Top: BEEM image of a AlGaAs barrier region, Scan size: 143 nm x 45 nm. I_T = 2 nA, V_T = 1.7 V. The color scale corresponds to current values from 0 pA … 4 pA. Along the bottom line of this image, a series of BEEM spectra was recorded. The distance between the single points is 7.2 nm. Bottom: Measured Schottky barrier height profile determined from the BEEM spectra and the conduction band profile of the sample as calculated from the MBE growth parameters.

For a quantitative profile of the SBH across the heterostructure, a number of BEEM spectra (I_T = 2nA) were recorded at the marked spots along the bottom line of the image in Fig. 3. From the onset of these spectra, the local barrier heights were determined using a Bell-Kaiser fit. The result of this procedure can be seen in the lower part of Fig. 3 together with a conduction band profile based on the heterostructure design parameters. For comparison with the GaAs-AlGaAs band offsets, this band profile was aligned with the measured SBH in the GaAs regions. Each data point of the measured curve represents an average over the onsets of several spectra taken at the same position. The error bars indicate the standard deviation in the measured onset at each position. The lateral distance between the single data points is 7.2 nm.

As one can see, the barrier is depicted clearly in the profile. The barrier width is consistent with the BEEM image as well as with the growth parameters. However, the barrier height profile is not rectangular, as it would be expected from a conduction band profile obtained from the MBE growth parameters, and also exhibits a certain asymmetry. In addition, the maximum barrier height difference between GaAs and AlGaAs differs notably from the expected conduction band offset between GaAs and AlGaAs. Furthermore, the noise in the barrier height profile is significantly larger in the AlGaAs regions than in the GaAs areas on our sample.

Before the origins of the above features are discussed, we would like to point out that we can definitely exclude two possible experimental artifacts: First of all, the smeared out barrier height profile is not due to the limited lateral resolution of BEEM. As already confirmed in previous measurements, the typical resolution of BEEM is about 1nm. This is also verified by Fig. 3 (a), where BEEM contrast is achieved on such length scales. In contrast to that, the smeared out region in the barrier height profile is significantly larger.

Second, the higher noise in the barrier height profile in the AlGaAs regions is definitely not due to improper tunneling conditions. As one can see in Fig. 1 (a), the sample is very flat and the image quality is good everywhere. Also the noise in the BEEM spectra is equal for all regions (see Fig. 2) and the noise in the barrier height profile in the GaAs regions is comparable to what we are used from earlier measurements on reference samples. Thus, we conclude, that this effect is a genuine feature of the local properties of the AlGaAs layer.

In our opinion, the smeared out barrier height profile is most likely due to lateral band bending effects across the heterojunctions based on the following arguments: In general it can not be expected that the GaAs-AlGaAs conduction band offset is exactly mirrored by the difference in the SBH of the two materials. This is confirmed by our data, where the SBH on some points of the AlGaAs layers is notably larger than the SBH on GaAs plus the band offset between GaAs and AlGaAs. On the other hand, the Fermi level must be constant all over the sample surface and thus lateral band bending effects are unavoidable. A quantitative analysis of this behavior, however, requires extensive simulation as well as additional systematic measurements and is beyond the scope of this paper.

While lateral band bending can explain the amount of broadening on the right edge of the barrier profile seen in Fig. 3, it does not explain the rather gradual increase on the left edge of the profile. Also the increased noise in the AlGaAs regions is still an open issue. However, a look on earlier measurements, where we investigated the local influence of single impurities in AlAs barriers in BEEM [13], can shed light on this behavior. In that work we found that in the vicinity of an impurity the onset of the BEEM current was reduced from the Schottky barrier height of AlGaAs to the energetic level of the impurity.

Considering the design of our present sample, the AlGaAs barriers are doped with $N_D = 5.6 \times 10^{16}$ cm^{-3}, which means that the average distance between two impurities is ≈33 nm. Thus, on average, one to four impurities are present in the vicinity of any cross-section through a 50 nm thick AlGaAs barrier.

While in GaAs silicon impurity levels are close to the conduction band edge, they act as deep donors in AlGaAs. As shown in our previous work, the local influence of these impurities on the current onset position is quite dominant, which probably is the reason why the corresponding AlGaAs barrier height depends so strongly on the position on our sample. In contrast to that, the donor levels on GaAs are just 5 meV below the conduction band edge and therefore have almost no influence on the local barrier height. This is consistent with our experimental observation that the barrier height shows just little variations throughout the GaAs regions of our sample.

Summary

In summary, cross-sectional BEEM measurements were introduced to determine a Schottky barrier height profile on the cleaved [011] surface of a GaAs-AlGaAs multiheterostructure. The measured data exhibit indications of lateral band bending effects at the GaAs-AlGaAs interfaces. Furthermore, an influence of deep impurity levels in the AlGaAs barriers on the measurements was observed.

Acknowledgements

This work was sponsored by “Fonds zur Förderung der wissenschaftlichen Forschung (FWF)” project No P16337-N08 and “Gesellschaft für Mikro- und Nanoelektronik (GMe)”

References

[1] W.J. Kaiser and L.D. Bell, Phys. Rev. Lett. 60, 1406 (1988)

[2] L.D. Bell and W.J. Kaiser, Phys. Rev. Lett. 61, 2368 (1988)

[3] G.Binnig, G.Rohrer, Ch.Gerber, E.Weibel, Phys. Rev. Lett. 49, 57 (1982)

[4] R.Wiesendanger, Scanning Probe Microscopy and Spectroscopy, Cambridge University Press (1994)

[5] C. Julian Chen, Introduction into Scanning Tunneling Microscopy, Oxford Series in Optical and Imaging Sciences, Oxford University Press (1993)

[6] M.Prietsch, Physics Reports 253, 163 (1995)

[7] V.Narayanamurti and M.Kozhevnikov, Physics Reports 349, 447 (2001)

[8] J.Smoliner, D.Rakoczy, M.Kast, Rep. Prog. Phys. 67, 1863 (2004)

[9] J.Harper, M.Weimer, D.Zhang, C.H.Lin, S.S.Pei, J.Vac. Sci. Technol. B16, 1389 (1998).

[10] R.Magri, A.Zunger, Phys. Rev. B64, 081305/1-4 (2001)

[11] D.M.Bruls, P.M.Koenraad, M.Hopkinson, J.H.Wolter, H.W.M.Salemink, Appl. Surf. Sci. 190, 258 (2002)

[12] S.L.Zuo, E.T.Yu, A.A.Allerman, R.M.Biefeld, J.Vac. Sci. Technol. B17, 1781 (1999)

[13] D.Rakoczy, G.Strasser, J.Smoliner, Phys. Rev. B68, 073304 (2003)

Thermal Imaging at Multiple Time Instants for Study of Self-Heating and ESD Phenomena

V. Dubec, S. Bychikhin, M. Blaho, M. Heer, D. Pogany, E. Gornik
Institute of Solid State Electronics, Vienna University of Technology, A-1040 Vienna, Austria

M. Denison, M. Stecher
Infineon Technologies, D-81617 Münich, Germany

G. Groos
University of Federal Armed Forces, D-85577 Neubiberg, Germany

A 2D backside transient interferometric mapping (TIM) method for nanosecond thermal energy imaging at multiple time instants during a single stress event is introduced. The method is based on fringe interferometry and the interferograms are analyzed using the Fast Fourier Transform technique. The method is applied to investigate moving current filaments in smart power DMOS transistors and in electrostatic discharge (ESD) protection devices exhibiting non-repeatable triggering behavior under ESD-like stress. The method additionally allows the extraction of instantaneous 2D power dissipation density (P_{2D}), which represents the current density distribution in the devices.

Introduction

Protection against electrostatic discharge (ESD) is an important requirement in automotive electronics [1]. For optimization of ESD protection devices (PDs) and for verification of device simulation models it is important to have an experimental access to the internal device behavior. Since self-heating is the main device failure cause [2], the temperature monitoring is especially important in device inspection.

Recently a 2D backside transient interferometric mapping (TIM) technique based on fringe interferometry has been introduced for ns thermal energy imaging at single time instants during a single stress event [3]. However, measurements of devices with complex unrepeatable current filament dynamics are time consuming to perform. An extended version of the 2D TIM method suitable for imaging at two time instants during a single stress event has been therefore developed [4], which overcomes the above limitation. In this article, smart power technology high power DMOS [5] and ESD protection devices [6] developed for automotive applications are investigated by this method. In addition, the current density distribution in the devices is extracted from the measurements.

Experimental Setup and Theory

The backside 2D TIM technique is based on the thermo-optical and plasma-optical effect. During the electrical pulse, the temperature and the free carrier density variation cause a change in the optical length of the laser beam. The optical path difference is measured in a Michelson interferometer, see Fig. 1. For imaging at two time instants, two orthogonally polarized laser beams produced by two high energy pulsed laser

sources (λ = 1.3 µm, 5 ns pulses), combined by a polarizing beam splitter cube (PBS1) are led into the Michelson interferometer. The parallel beams reflected from the device (DUT) (see detail on the right in Fig. 1) and from the reference mirror (M) are split according to their polarization (PBS2) and create the interference fringe patterns on two infrared (IR) cameras. The laser pulse positions relative to the stress pulse can be chosen independently. The image and waveform acquisition is synchronized and computer controlled.

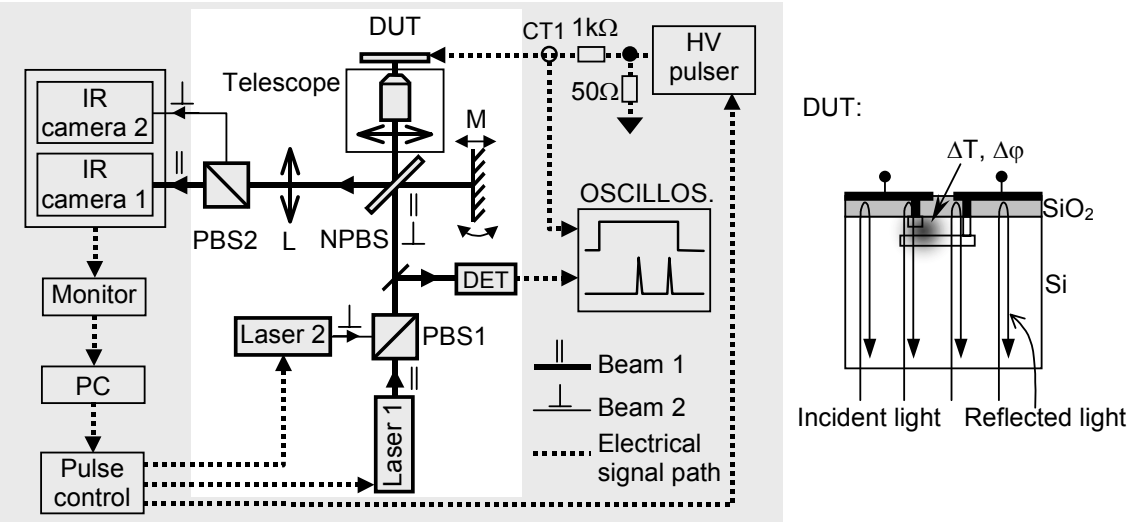

Fig. 1: Schematic drawing of the setup: PBS – polarizing beam splitter, NPBS – non-polarizing beam splitter, M – mirror, L – lens, DET – optical detector, CT1 – current probe, DUT – device under test (after [4]). On the right side the cross section of a DUT, the probe laser beam and the heat source ΔT is depicted.

The temperature-related phase distribution in the device at a particular time instant is extracted using a FFT-based method [7]. For elimination of the phase profile arising from the device the reference phase related to the interferogram without heating is subtracted. This removes also the phase tilt introduced by the reference mirror. The phase calculation results in phase modulo 2π, and the unwrapping is necessary. For unwrapping the pixel queue method or the minimum spanning three method are performed [8], [9]. Before the unwrapping is done, a pre-processing procedure is developed [7].

As two images during a single pulse are possible to record, the method allows extraction of the instantaneous 2D power dissipation density P_{2D}, which represents the current density distribution in the devices. Neglecting the heat transfer to the top device layers (normal component of the heat flow vector), P_{2D} is given by [6]:

$$P_{2D}(x,y,t) = \lambda\left(4\pi\frac{dn}{dT}\right)^{-1}\left(c_V\frac{\partial\varphi(x,y,t)}{\partial t} - \kappa\frac{\partial^2\varphi(x,y,t)}{\partial x^2} - \kappa\frac{\partial^2\varphi(x,y,t)}{\partial y^2}\right) \quad (1)$$

where λ is the laser beam wavelength, *dn/dT* is the temperature coefficient of the refractive index, c_V is the volume specific heat, $\varphi(x,y,t)$ is the measured phase shift, κ is the thermal conductivity, *x, y* and *t* are the spatial coordinates and time, respectively. The time derivative in Eq. (1) is approximated using the phase difference between two images $\varphi(x,y,t)$ and $\varphi(x,y,t-\Delta t)$ recorded during the same ESD pulse at times *t* and $t-\Delta t$, respectively. The value of Δt = 30 ns is a good compromise taking into account the phase and space resolution of the setup.

Results

The method is applied to the study of moving current filaments in ESD protection devices and DMOSes during a bipolar snapback mode where the current distribution in the device is strongly inhomogeneous. The backside IR image of the ESD PD is shown in Fig. 2 (a) and its cross section in Fig. 2 (f). Figures 2 (b) – (e) and (g) – (j) show the measured phase images and the extracted P_{2D} at four time instants, respectively. Due to the negative differential resistance a current filament, represented by a spatially localized P_{2D}, is formed in the middle of the device, see Fig. 2 (g). Later, due to the reduction of the impact ionization coefficient with increasing temperature, the filament starts to move towards a cooler region (to the corner) of the device, see Fig. 2 (h). When the filament reaches the corner, it is "reflected" back (Fig. 2 (i)) and moves again to the middle and toward the opposite corner of the device (Fig. 2 (j)). The initial direction (right or left) of the movement is random. The current filament amplitude is about 30 mW/μm^2, which is consistent with the results obtained previously using the time-consuming scanning TIM method [10].

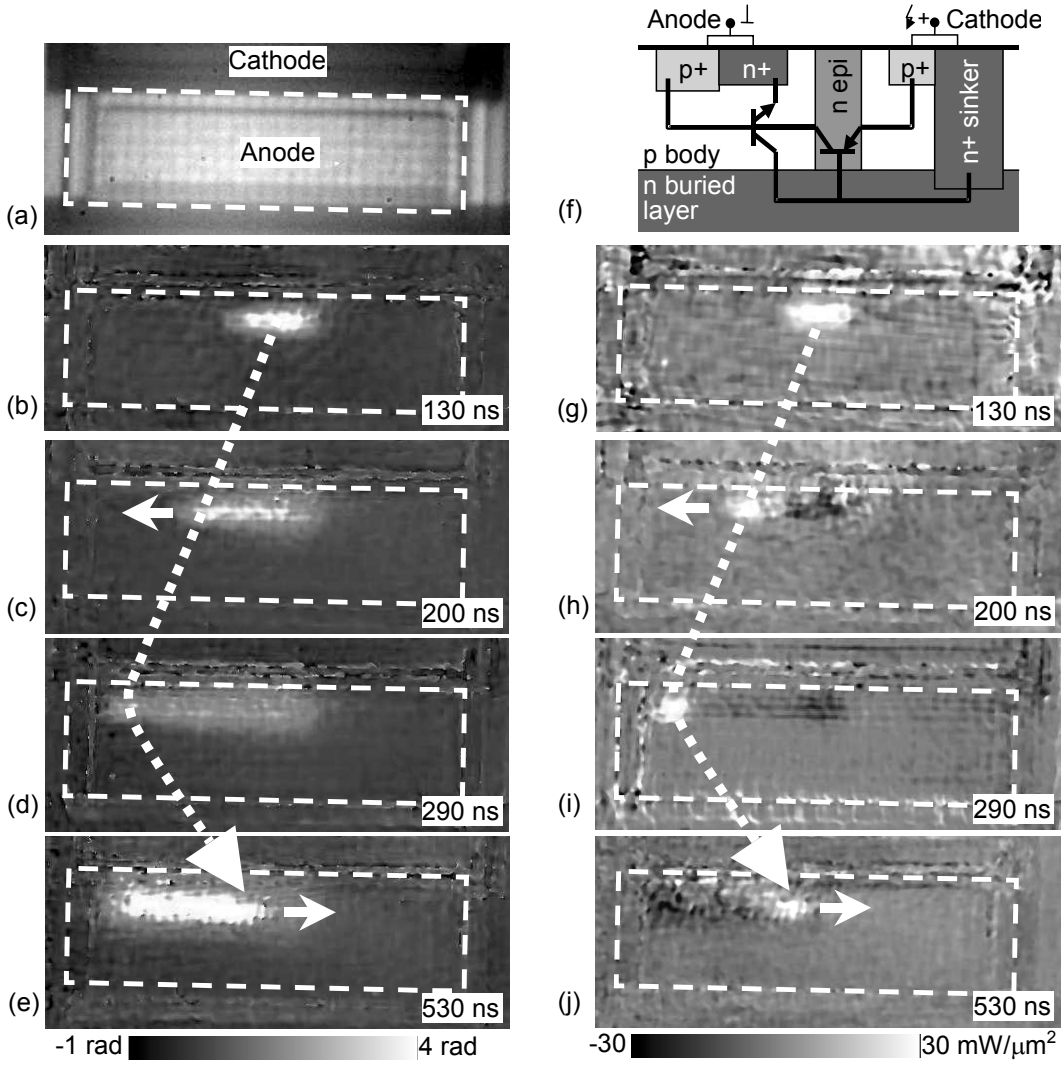

Fig. 2: (a) Backside IR image of the ESD PD and (f) device cross section. (b) – (e) Phase shift distribution $\varphi(x,y,t)$ in the ESD PD at four time instants during current pulses of 0.25 A, 600 ns duration. The heating is displayed by light color. (g) – (j) show the P_{2D}, representing the current filament position. The dashed arrow and the small white arrows denote the movement direction (after [4]).

The backside IR image of the DMOS device is shown in Fig. 3 (a) and its cross section in Fig. 3 (b). At snap back, when the parasitic bipolar transistor (see Fig. 3 (b)) of the DMOS turns on, a few cells take over the current and localized current filaments are formed along the source field termination. With time the filaments penetrate into cooler regions. The trigger position, number of the filaments, and direction of their movement vary randomly and non-repeatedly from pulse to pulse [4], [5].

In order to localize the active cell at a particular time instant in the DMOS, the P_{2D} is necessary to extract. For this the two imaging laser beams were positioned at time instants 120 ns and 150 ns, see Figs. 3 (c), (d). The P_{2D} calculated by Eq. (1) corresponding to t = 150 ns is shown in Fig. 3 (e). At this particular case, DMOS cells marked by the circles inside of the source field are active and there are no more active cells along the termination line.

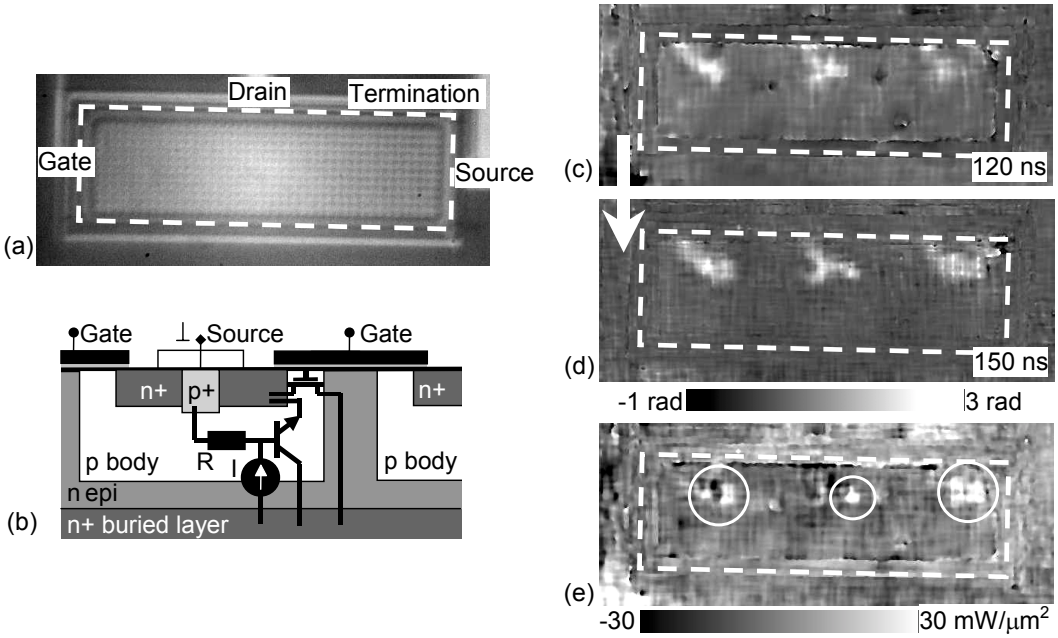

Fig. 3: (a) Backside IR image of the vertical DMOS, (b) device cross section. (c, d) Phase shift distribution in the DMOS at 120 ns and 150 ns during a 3 A, 250 ns stress pulse and (e) corresponding P_{2D} (after [4]).

Conclusion

With the presented method, the position and direction of the filament movement can unambiguously be extracted from few single-shot measurements. Using the two-time-instant measurement the instantaneous power dissipation density can be obtained. This allows investigation of current dynamics in devices exhibiting complex unrepeatable behavior, which is not possible by any other method. The method has a potential for time-efficient studies of destructive phenomena in semiconductor devices including thermal run-away effects in the ns to ms time range and study of surface displacement of MEMS, bio-membranes, sensors and microfuidics.

Acknowledgements

The project was supported by European Community project DEMAND IST2000-30033 and Wittgenstein award.

References

[1] B. J. Baliga: “Modern power devices”, John Wiley, New York, 1987.

[2] V. M. Dwyer, A. J. Franklin, D. S. Campbell: “Thermal failure in semiconductor devices”, Solid-St. Electron., Vol. 33, 1990, pp. 553-560.

[3] D. Pogany, V. Dubec, S. Bychikhin, C. Fürböck, M. Litzenberger, G. Groos, S. Stecher, E. Gornik: “Single-shot thermal energy mapping of semiconductor devices with the nanosecond resolution using holographic interferometry”, IEEE Electron Dev. Lett., Vol. 23, 2002, pp. 606-608.

[4] V. Dubec, S. Bychikhin, M. Blaho, M. Heer, D. Pogany, M. Denison, N. Jensen, M. Stecher, G. Groos, E. Gornik: “Multiple-time-instant 2D thermal mapping during a single ESD event”, (ESREF 2004), Microel. Reliab. 44, 2004, pp.1793-1798.

[5] M. Denison, M. Blaho, P. Rodin, V. Dubec, D. Pogany, D. Silber, E. Gornik, M. Stecher: “Moving current filaments in integrated DMOS transistors under short-duration current stress”, IEEE Trans. Electron Dev., Vol. 51, 2004, pp. 1695-1703.

[6] D. Pogany, S. Bychikhin, M. Litzenberger, E. Gornik, G. Groos, M. Stecher: “Extraction of spatio-temporal distribution of power dissipation in semiconductor devices using nanosecond interferometric mapping technique”, Appl. Phys. Lett., Vol. 81, 2002, pp. 2881-2883.

[7] V. Dubec, S. Bychikhin, D. Pogany, E. Gornik, G. Groos, M. Stecher: “Error analysis in phase extraction in a 2D holographic imaging of semiconductor devices”, Proc. SPIE: Practical Holography XVIII: Materials and Applications, Vol. 5290, 2004, p. 233-242.

[8] T. Kreis: “Holographic interferometry”, Berlin, 1996.

[9] H. A. Vrooman: “Quaint: quantitative analyses of interferograms”, Delft Univ. Pr., 1991.

[10] D. Pogany, S. Bychikhin, M. Denison, P. Rodin, N. Jensen, G. Groos, M. Stecher, E. Gornik: “Thermally-driven motion of current filaments in ESD protection devices”, Solid-St. Electron., Vol. 49, 2005, pp. 421-429.

Degradation Mechanisms in AlGaN/GaN HEMTs under Electrostatic Overstress

J. Kuzmík, M. Blaho, S. Bychikhin, D. Pogany, E. Gornik

Institute of Solid State Electronics
Vienna University of Technology, A-1040 Vienna

P. Javorka, P. Kordoš

Institute of Thin Films and Interfaces, Research Centre Jülich, Jülich D-52425, Germany

We study degradation mechanism in AlGaN/GaN HEMTs under 100 ns long rectangular current pulses applied on the drain contact. Devices were dc characterized after consecutive current stresses. We observed a sudden increase of source and drain resistances after the stress of 1.65 A. We used a backside transient interferometric mapping technique to localize the current path in the device during stresses. We revealed a current filamentation during stresses and dark spots formation in the position corresponding to filaments occurrence. We assume electron injection into the device buffer layer and an electromigration on contacts.

Introduction

Devices may face electrical overstress events (EOS) during manufacturing, handling or device operation. Typical current pulses are in the ampere range with duration between nanoseconds and microseconds. The importance of a failure mechanism study in III-nitride transistors is given by their potential usage as power devices in many defense and commercial applications where harsh environment conditions can be expected. It was previously suggested that the electrical conduction mechanism in AlGaN/GaN HEMTs during EOS might be linked to the avalanche-injection processes in the GaN buffer layer [1]. On the other hand, the device's ohmic and Schottky barrier contacts degradation was revealed as the main mechanism responsible for the failure of AlGaN/GaN HEMTs after EOS [2].

Experimental

The AlGaN/GaN HEMT structures used in this study were grown on both-sides polished sapphire wafer by MO-VPE. The device processing included e-beam lithography [2], the gate geometry was 50 μm width, 450 nm length. We used a transmission line pulser (TLP) to stress the device. In the TLP technique a coaxial cable (TL) with a 50 Ω characteristic impedance is charged by a voltage source and afterwards is discharged by closing a relay, providing rectangular current pulses for our devices. Devices were characterized after consecutive current stresses of increasing level. Ohmic contact and open channel resistances were extrapolated from the functional dependence of the source-drain resistance on gate voltage [3]. We used backside interferometric mapping (TIM) technique [4] to localize the current path (dissipated power) in HEMTs during TLP stresses. The mapping was performed using an infrared laser beam scanning the device from the backside. The measured phase shift, caused by the temperature-induced change in the refractive index, is directly proportional to a local 2D energy density in the device [4].

Results and Discussion

The HEMT drain-source high-current pulsed *I-V* characteristics exhibit S-shape with three regions (see Fig. 1): A low-current / high-impedance region A, a NDC region B, and a high-current / low-voltage region C. A parasitic bipolar effect [1] may be linked to the S-shape.

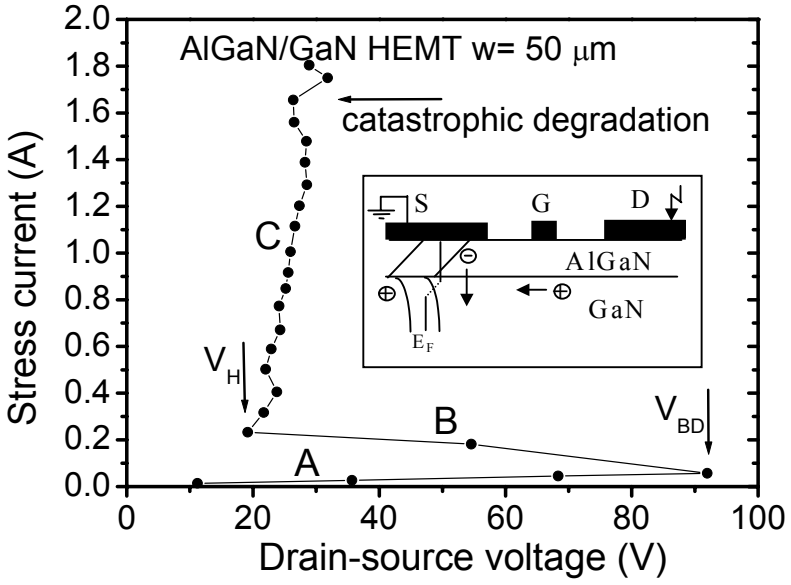

Fig. 1: Typical drain-source high-current pulsed *I-V* curve of the HEMT. The inset illustrates the band diagram and assumed process of the hole accumulation and electron injection into the GaN buffer (after [1]).

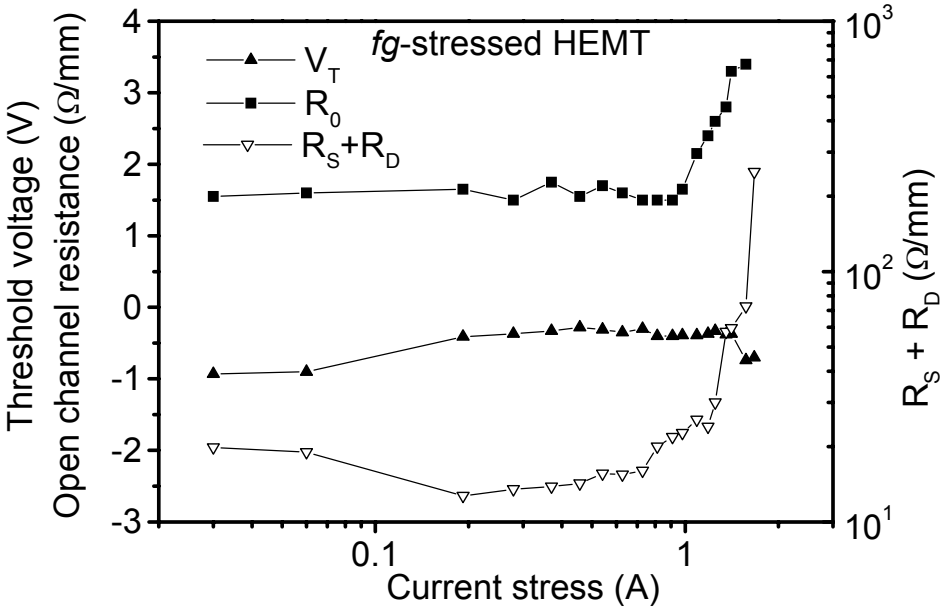

Fig. 2: Evolution of the AlGaN/GaN HEMT threshold voltage, open channel resistance and source + drain resistances values in dependence of previous current stress level (after [2]).

Transistor threshold voltage V_T, open channel resistance R_0, and the sum of the source R_S and drain R_D ohmic contact resistances as a function of the current stress level are shown in Fig. 2. The ohmic contacts' catastrophic degradation (ten-fold increase from the nominal value) was recorded at I_{stress} = 1.65 A. The abrupt R_S + R_D increase is accompanied with a partial increase of the open channel resistance R_0. However, R_0 becomes marginal in comparison to R_S + R_D at this point.

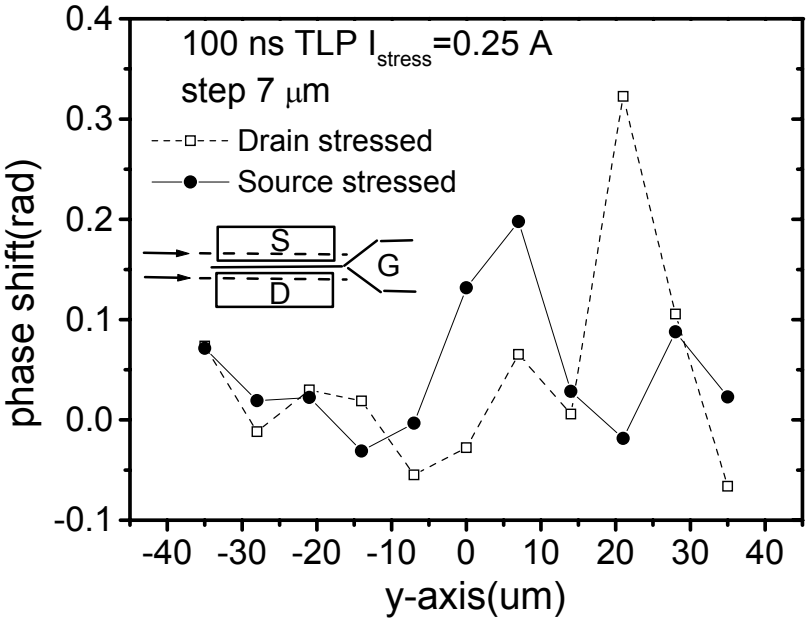

Fig. 3: Phase shift distributions of the AlGaN/GaN HEMT along the drain and source at I_{stress} = 0.25 A at the end of the pulse. Source was grounded for a scan along the drain and vice versa. Inset: Schematic device layout with indicated scan lines (after [2]).

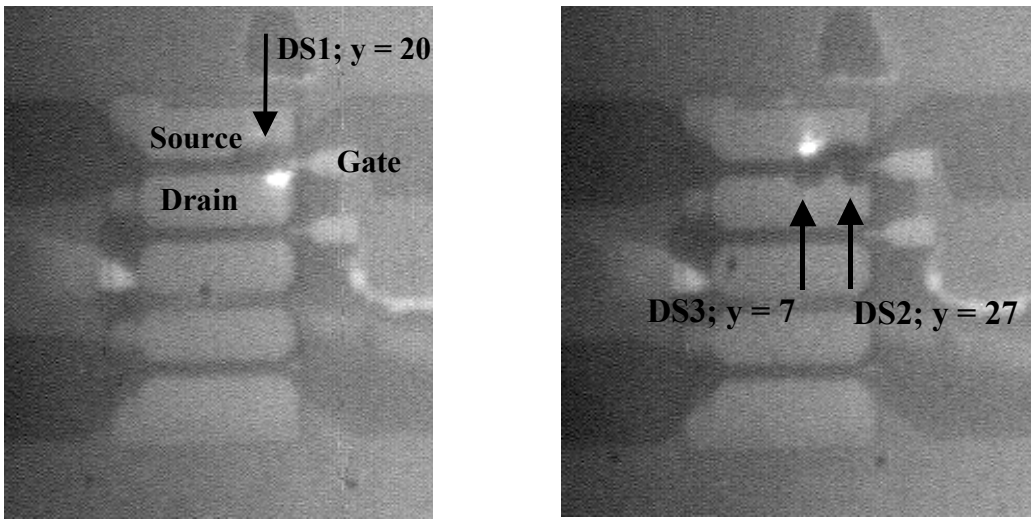

(a) (b)

Fig. 4: Backside infrared camera view of the AlGaN/GaN HEMT after I_{stress} = 0.25 A on the (a) drain, (b) source. Arrows mark dark spot (DS1 – 3) appearance, laser beam indicates the position of the maximal phase shift signal (after [2]).

Results of the TIM technique are presented in Fig. 3. The device was scanned along the stressed contact with a step of 7 μm. First, the source was grounded and the drain was stressed with a positive pulse. The phase shift characteristics show a fair local maximum at the right edge of the HEMT. Following the change of the stress polarity (drain grounded, source stressed), two new maxima appeared in new positions close to the previous one. These observation correlates with the backside infrared images of the device (Figs. 4 (a), (b)) where dark spot positions correspond to the phase shift maxima on the grounded (opposite) contact.

Conclusion

The AlGaN/GaN HEMT behavior and degradation mechanisms under pulsed overstress conditions have been investigated. The current filament formation and the electromigration effect were shown to be responsible for the *ohmic* contact dark spot formation. Dark spots may be considered as a precursor of the *ohmic* contact degradation. Semiconductor material parameters are not changed substantially during the EOS event.

References

[1] Kuzmík J., Pogany D., Gornik E., Javorka P., Kordoš P., “Electrostatic discharge effects in AlGaN/GaN HEMTs”, Applied Physics Letters, Vol. 83, 2003, pp. 4655 – 4657.

[2] Kuzmík J., Pogany D., Gornik E., Javorka P., Kordoš P., “Electrical overstress in AlGaN/GaN HEMTs: study of degradation processes”, Solid-State Electronics, Vol. 48, 2004, pp. 271-276.

[3] Shur M., GaAs Devices and Circuits, New York and London: Plenum Press, 1987. p.369-372.

[4] Pogany D., Bychikhin S., Fürböck C., Litzenberger M., Gornik E., Groos G., Esmark K., Stecher M., “Quantitative internal thermal energy mapping of semiconductor devices under short current stress using backside laser interferometry”, IEEE Trans. Electron Dev Vol.49, 2002 pp. 2070-2079.

Direct-Write Deposition Utilizing a Focused Electron Beam

M. Fischer, J. Gottsbachner, S. Müller, W. Brezna, and H.D. Wanzenboeck

Institute of Solid State Electronics, Vienna University of Technology, A-1040 Vienna, Austria

Local deposition of material can be induced by a focused electron beam delivering materials with a high purity and a clear interface to the substrate. Based on a commercial variable-pressure scanning electron microscope custom-tailored equipment was developed that allows introducing precursor gases through a nozzle system directly to the spot of deposition. For the deposition of material tetraethylorthosilicate (TEOS) was chosen, yielding a silicon oxide based material. The deposition process was investigated and optimized for high deposition rates. Variation of acceleration voltage and dwell time was performed, by depositing the material with a univariat parameter change. A higher deposition rate was obtained for lower electron energies. This result suggests a deposition mechanism based on the interaction with secondary electrons. Also effects of dwell time were discussed.

Introduction

The locally confined direct-write deposition is a new, maskless nanostructuring technique that is capable of fabricating 3-D structures within a single process step. The conventional fabrication of nanostructured devices with cutting-edge optical lithography requires the use of cost-intensive phase-shift masks and the processing time for several process steps including blanket deposition of the material, lithographic structuring and etch-back to obtain the desired structures. For prototyping a novel approach using direct-write deposition has been acknowledged as a promising alternative. The energy of a focused particle beam is used to locally induce a chemical vapor deposition. No mask is required and the structures can be deposited within a single process step. A frequently used approach is the deposition of a focused ion beam (FIB) [1], [2]. However, the ion contamination originating from the ion source and the atomic mixing of deposited material put a serious constraint on this method. An alternative technique could be the focused electron beam induced deposition. This technology delivers materials with a higher purity and a clear interface to the substrate.

In this article, tetraethoxysilane (TEOS) was used as a precursor for electron beam insulator deposition. The effects of several process parameters were studied. The variation of parameters was performed by depositing arrays of material with a univariat parameter change. The aim of the present work is to investigate the deposition process and to optimize the deposition parameters.

Experimental

Experiments have been performed using a variable-pressure scanning electron microscope LEO 1530 VP with a sophisticated gas inlet system. With a nozzle system the gas was introduced directly to the focus point of the electron beam. The energy of the electrons could be adjusted via the acceleration voltage in a range from 0.1 to 30 kV. The scanning operation of the electron beam could be controlled with a RAITH ELPHY PLUS pattern generator. The pattern generator allowed varying the pixel spacing of the

scan array, the dwell time of the beam on a single spot, and the number of scan repetitions.

For the deposition of material, tetraethylorthosilicate (TEOS) was chosen as exemplary precursor. The vapor pressure of TEOS is about 2 mbar at 20 °C and is sufficient for an accurate control of the gas flux via a dosing valve of the gas injection system. The acceleration voltage was varied in arrange from 5 to 30 kV. The maximum beam current was 3 to 4.3 nA (depending on the acceleration voltage), results of the use of the 120 µm aperture. In order to investigate the deposition process 50 x 20 µm SiO*x* pads were deposited. The height of the deposition was determined by a DEKTAK profilometer. The surface morphology of the deposited material patches was investigated by atomic force microscopy in tapping mode.

Results and Discussion

For the deposition of silicon oxide a focused electron beam was used. The electron beam was scanned in a rectangular area.

First experiments should demonstrate that depositions of silicon oxide are feasible with the used set-up. Figure 1 shows an AFM-image of a deposited 6 x 6 µm area of silicon oxide. For this deposition an acceleration voltage of 5 kV, a pixel spacing of 46 nm, and a dwell time of 0.5 µs were adjusted.

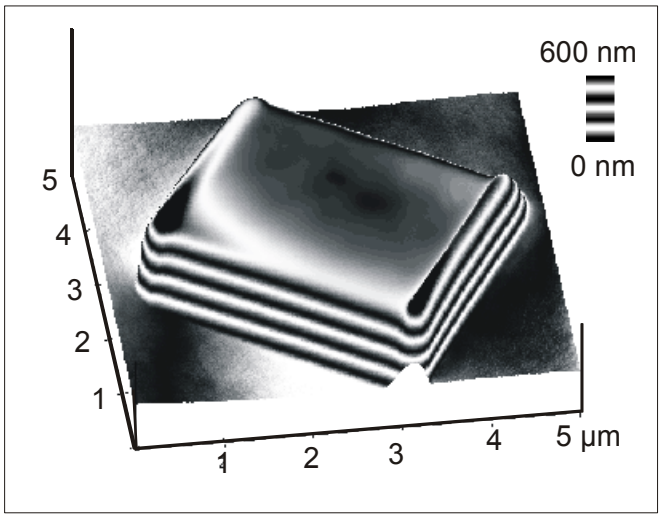

Fig. 1: AFM – image of a silicon oxide deposition on a 6x6 µm area

In the AFM-image (Fig. 1) a 6 x 6 µm deposition is seen. The deposited field has a total height of about 630 nm. The thicker material at the rim results from the longer dwell time at the left and right edge of the scan pattern, which is generated by the pattern generator. In the area between the rims the roughness of the surface is very low. This is of special interest in combination with optical applications. These findings prove that an electron beam may be used as a local probe for the deposition of well-defined structures. Investigations of the correlation between acceleration voltages and deposition thickness were performed with acceleration voltages from 30 kV down to 5 kV. All other process parameters were kept constant. The thickness of the deposited material was measured with a Dektak profilometer.

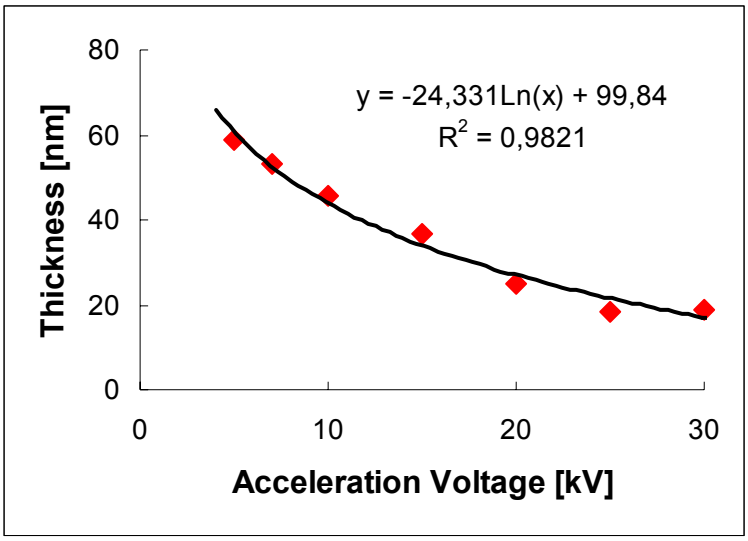

Fig. 2: Deposited thickness to acceleration voltage

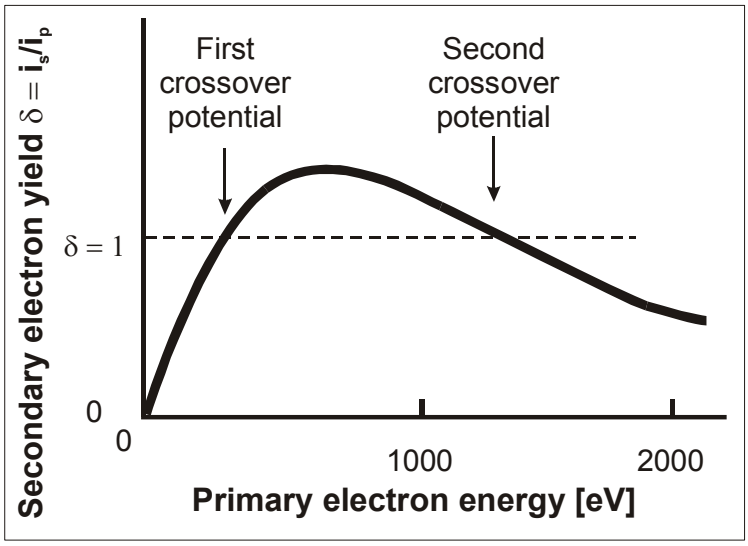

Fig. 3: Secondary electron yield correlated depending on the acceleration voltage from Hearle [4]

The dependence of the deposited thickness against the acceleration voltage is illustrated in Fig. 2. The graph indicates that the deposition rate increases at lower beam energies. This result correlates with the hypothesis that the deposition reaction is potentially induced by interaction of the adsorbed precursor with the secondary electrons [3], [4]. The yield of the secondary electrons (SE) depends on the energy of the primary electrons as it is illustrated in Fig. 3. Towards lower beam energies down to 600 V the penetration depth of electrons is reduced and the secondary electrons yield increases. The problem with low primary electron energy is the loss of beam stability.

The effect of the dwell time on the deposition thickness was analyzed by fabricating an array of 50 x 20 µm areas in a 3 x 6 matrix (Fig. 4) with increasing dwell times. The default value for the shortest dwell time was set at 0,375 µs. Other dwell times were obtained with a multiplier (= 1 + 2n) resulting in a 3-, 5-, 7-, …- fold longer dwell time.

Within the array (Fig. 4) the dose for every deposited field was different. The thickness was measured by Dektak profilometer. To compare the deposited thickness the measured values were calibrated against the exposure dose. The deposited structures in Fig. 4 are well defined with sharp edges and excellently aligned. This array demonstrates that electron beam lithography is a serious technique for maskless direct-write lithography and for prototyping in the sub µm microelectronic technology.

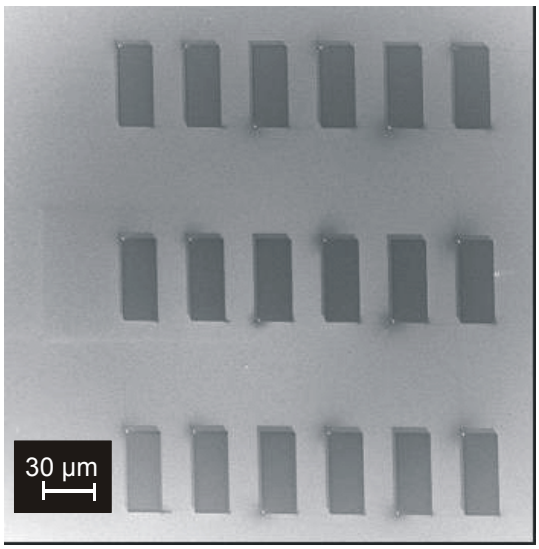

Fig. 4: Array of deposited material by electron beam induced deposition

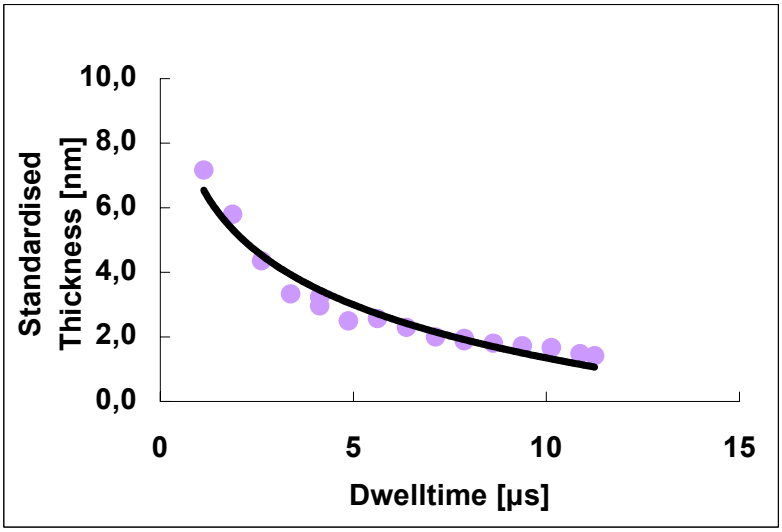

Fig. 5: Standardized thickness against dwell time

The evaluation of the dwell time influence is shown in Fig. 5. It is shown that the deposition thickness increased at lower dwell times. This indicates that the deposition reaction is faster than the surface saturation. A further decrease of the dwell time will result in a rise of the deposition rate.

Conclusions

It has been successfully demonstrated that an electron beam may be used as a local probe for the deposition of well-defined structures. This technique is an essential technology for repairing and preparing sub-µm feature sized structures. It has been shown that a higher deposition rate was obtained for lower electron energies. A deposition mechanism based on the interaction of the adsorbed precursor molecules with secondary electrons is leads to the assumption. These findings are considered a solid bias for the better understanding of electron-induced surface reactions and path the way to a further process optimization of this innovative nanofabrication technique.

Acknowledgement

This work was performed with financial support of the Austrian Society for Microelectronics (Gesellschaft für Mikro- und Nanoelektronik). Erich Gornik (Vienna University of Technology) is thanked for providing the cleanroom of the center of micro- and nanostructures (ZMNS) for the fabrication of devices.

References

[1] H.D. Wanzenboeck, M. Verbeek, W. Maurer, E. Bertagnolli, Proceedings of the SPIE – The international Society for Optical Engineering, 4186, 148-57 (2001)

[2] S. Lipp, L. Frey, C. Lehrer, B. Frank, E. Demm, S. Pauthner, H. Ryssel, J. Vac. Sci. Technol. B 14(6), 3920-3, (1996)

[3] R. R. Kunz and T. M. Mayer, Appl. Phys. Lett. 50, 962 (1987)

[4] J.W.S. Hearle, J.T Sparrow, and P.M. Cross, The Use of the Scanning Electron Microscope, Pergamon Press, Oxford, New York, Toronto, Sidney, Braunschweig (1972)

A New Approach for the Formation of Size and Site Controlled Metallic Nano Dots Seeded by Focused Ion Beams

A. Lugstein, E. Bertagnolli

Institute of Solid State Electronics
Vienna University of Technology, A-1040 Vienna, Austria

We present a new approach for the generation of metallic nano pattern, which in contrast to conventional bottom up or top down processes is based on a subtractive self organization process relying on material decomposition induced by focused ion beam (FIB) exposure. Two dimensional ordered arrays of embedded as well as freestanding nanometer sized Ga dots were fabricated by a site control technique relying on preformed craters and an irradiation mediated migration and agglomeration. The formation of these dots is discussed in terms of selective etching of arsenic due to the local energy injection by the gallium ions and further minimization of the excess free energy of the surfaces.

Further we have shown that FIB bombardment of InAs produces indium crystallites. The influence of the ion dose, the beam energy, the sample temperature and the dose rate on the surface evolution has been investigated for further III/V compound semiconductors by atomic force microscopy, scanning electron microscopy, auger electron spectroscopy and X-ray diffraction measurements.

In summary, the surface topography resulting from FIB bombardment is being investigated for possible use in nano-technology applications. This technique, based on a subtractive self organization process, may lead to a new fabrication process for three dimensional metallic nanostructures.

Introduction

Nanoscale structuring opportunities are prerequisites for any nanoscale engineering. The main bottleneck in the application of nano dots for quantum devices [1] – [3] is the difficulty of creating ordered arrays of size controlled dots in the nanometer range with a high uniformity in size. Low-dimensional nanostructures are usually fabricated using either a top down or a bottom up strategy. The former technique is extremely flexible, but suffers from limitations in minimum feature size and uniformity. The latter one, utilizing spontaneous self-ordering effects, is limited by the broad size distribution and the lack of control of the positioning of the self-organized nanostructures. In this context the discovery of the appearance of periodic structures with dimensions in the nanometer regime induced by ion bombardment [4] – [7] has attracted growing interest due to the possibility of obtaining a self-organized formation of nanostructures. In particular resistless focused ion beam techniques are most suited for the combination of top-down structuring with selective bottom-up self-assembling techniques. To keep up with the trend of structures to shrink in dimensions, the response of ion induced material modifications will have to be controlled on a nanometer scale. A prerequisite thereof is a deep understanding of the ion beam interaction with the processed substrate material. In this paper, we present a new approach for the generation of metallic nano dots based on a subtractive self organization process, relying on compound semiconductor decomposition induced by FIB exposure.

Experimental

The samples exposed to the FIB were cleaved from mirror polished (100) InAs and (100) GaAs wafers. All machining experiments were carried out using the Micrion twin lens FIB system equipped with a Ga liquid metal ion source. The FIB system was operated with a 200 µm beam-limiting aperture corresponding to a nominal beam diameter of 120 nm and a beam current of 4.7 nA at an acceleration voltage of 50 kV. To investigate the morphological evolution, the samples were irradiated in a single scan with ion fluences between 6.25×10^{15} ions/cm^2 and 7.25×10^{16} ions/cm^2. After FIB irradiation, post-exposure annealing is performed at 200 °C in forming gas. For the formation of the regular Ga dot structures we generated an array consisting of 50 x 50 nominally identical 80 nm deep holes. The pattern evolution was observed by FIB-Secondary Electron Microscopy (FIB-SEM), Atomic Force Microscopy (AFM), Auger Electron Spectroscopy (AES) and X-ray diffraction (XRD).

Results and Discussion

Our FIB system enables the in-situ monitoring of the pattern evolution of the GaAs surface during FIB bombardment. Figure 1(a) shows a FIB-SEM image of a (50 x 50) µm^2 box on the GaAs surface after FIB exposure with 50 keV Ga+ ions and an ion fluence of 3.75x1016 ions/cm^2. Droplet like features appears on the GaAs surface and the diameter of the dots varies between 120 nm and 640 nm. The AFM image in Fig. 1(b) reveals a perfect calotte shape of one single dot with a diameter of 190 nm and a height of 75 nm, resulting in an aspect ratio of about 0.4 and the smooth surface surrounding of the dot.

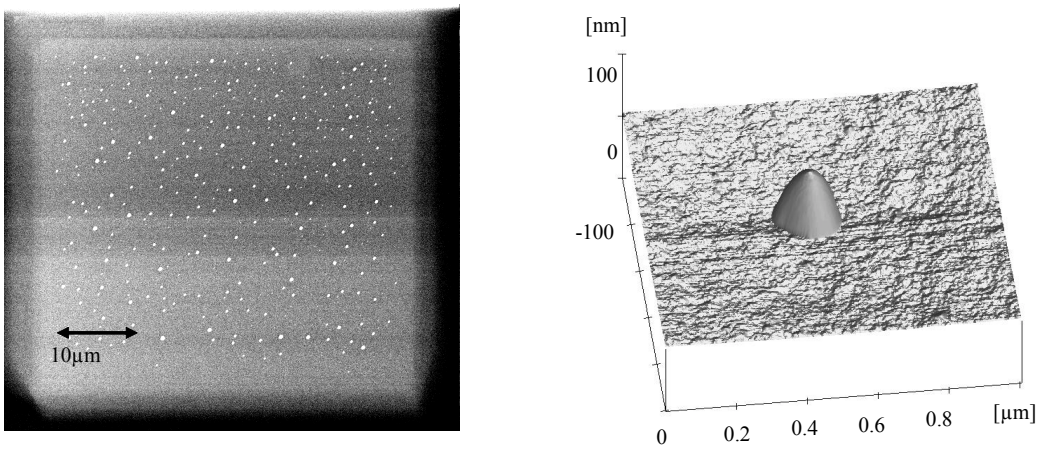

(a) (b)

Fig. 1: FIB-SEM image of a GaAs surface after 50 keV Ga^+ FIB exposure with an ion dose of 3.75×10^{16} ions/cm^2 (a) and the topographic AFM image of one single dot (b).

AES investigations point toward Ga enrichment in the protrusion after FIB exposure and reveal the formation of nearly pure gallium dots after a moderate annealing. We assume that the irradiation leads to decomposition of GaAs and selective etching of arsenic due to the local energy injection by the gallium ions [8]. The excess Ga atoms are produced by preferential sputtering of the arsenic atoms, and because of enhanced diffusion, the Ga atoms agglomerate into the observed Ga-rich precipitates. The development of the new heterogeneous phase leads to an increase in the total surface energy of the system. Thus, in case of preferential FIB sputtering of GaAs, the minimiza-

tion of surface energy calls for a spherical shape of the small Ga dots, as we did observe. After formation of Ga dots the most crucial issue is to locate dots at predicted sites. In case of pre-patterning of the surface by milling holes in the GaAs surface the Ga-rich dots are formed at designated sites. The AFM image in Fig. 2 shows a part of the FIB generated array consisting of 50 x 50 nominally identical 80 nm deep holes, with the Ga droplets at the center of the craters.

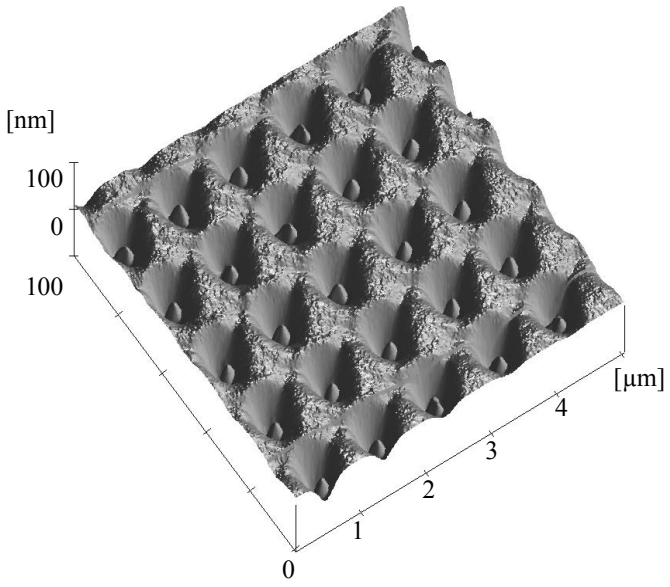

Fig. 2: AFM image of an array of embedded Ga dots generated by FIB milling of nominally identical 80 nm deep holes with a spacing of 1 µm between them.

From a section analysis of the AFM image we have measured an average diameter of the dots of 250 nm and a height of 55 nm. Besides the site controllability, the size uniformity is also improved, as each potential well in which the migrating Ga atoms are collected is uniform.

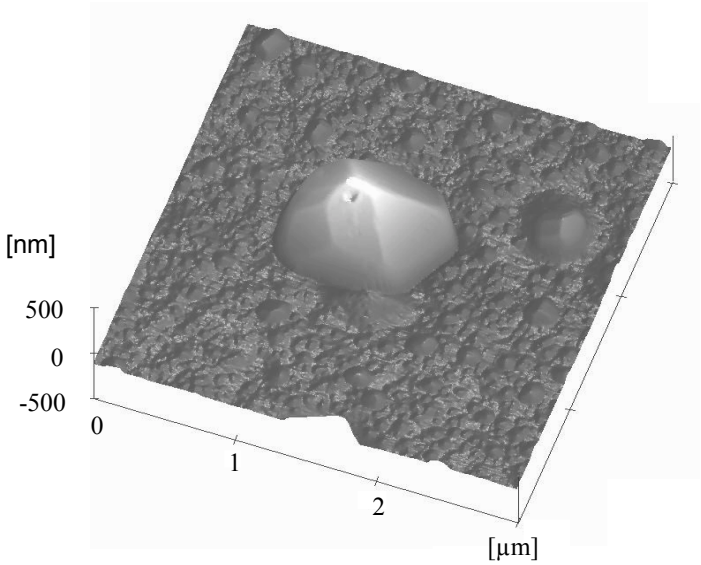

Fig. 3: AFM image of an indium crystallite on the InAs surface after FIB exposure with an ion dose of $5x10^{16}$ ions/cm^2

In case of InAs randomly distributed micro-protrusions are formed due to FIB exposure with diameters ranging from 30 nm to 2 µm. The AFM image in Fig. 3 indicates that the protrusions are nearby perfect crystallites with obvious facets, in close contact with the substrate. A two-dimensional AES mapping points towards the enrichment of indium in the crystallites, whereby the calculated composition of the ion bombarded neighborhood aside the crystallites is very close to the ratio of the undisturbed InAs surface. The XRD measurements shown in Fig. 4 prove the assumption of indium crystallite formation, as the three most intense reflections of crystalline indium are clearly visible in the X-ray diffractograms after FIB treatment. Relative intensities and *d* spacings of these reflections are in perfect agreement with reference material [8].

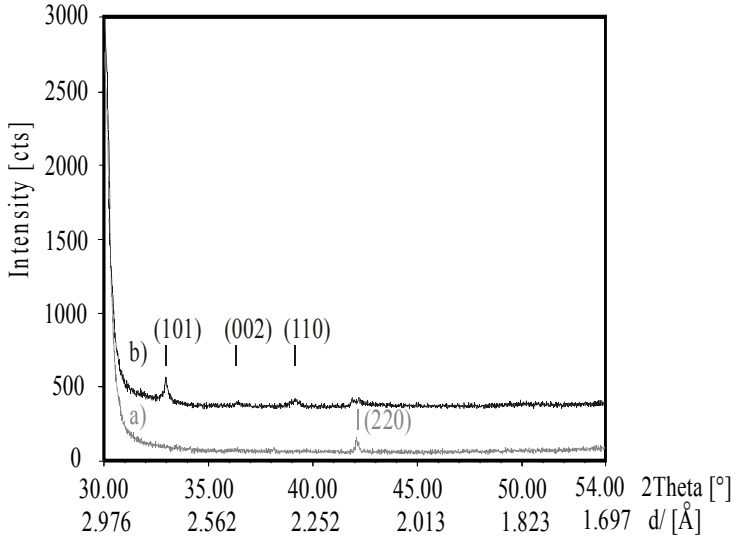

Fig 4: X-ray diffractograms of an InAs wafer before (a) and after (b) Ga^+ ion beam irradiation.

Conclusions

Concluding, we have shown that 50 keV FIB-Ga^+ ion bombardment at normal incidence produces droplet like Ga dots on a GaAs substrate and indium crystallites on the InAs surface. The formation of these dots is discussed in terms of selective etching of arsenic due to the local energy injection by the gallium ions and further agglomeration because of enhanced diffusion of the remaining species. In case of GaAs, regular patterns can be obtained by a new site control technique using ion beam surface potential modification. This technique is a promising way to obtain three dimensional metallic nanostructures with uniform dot sizes and high packaging densities. Furthermore, this method is expected to apply to various metals apart from gallium and indium.

Acknowledgement

This work was performed with financial support of the Austrian Society for Micro- and Nanoelectronics (Gesellschaft für Mikro- und Nanoelektronik). Matthias Weil (Vienna University of Technology) is acknowledged for performing the XRD investigations.

References

[1] K. Mukai, N. Nishioka, M. Sugawara, S. Yamazaki, Jpn. J. Appl. Phys. 33, L1710 (1994)

[2] J.N. Randall, Nanotechnology, 4, 41 (1993)

[3] P.D. Dresselhaus, L. Ji, S. Han, J.E. Lukens. K.K. Likharev, Phys. Rev. Lett. 72 3226 (1994)

[4] G. Carter, V. Vishnyakov, Phys. Rev. B 54, 17647 (1996)

[5] J. Erlebacher, M.J. Aziz, E. Chason, M.B. Sinclair, J.A. Floro, Phys. Rev. Lett. 82, 2330 (1999)

[6] S. Rusponi, G. Constantini, C. Boragno, U. Valbusa, Phys. Rev. Lett. 81, 4184 (1998)

[7] S. Habenicht, W. Bolse, K.P. Lieb, K. Reimann, U. Geyer, Phys. Rev. B 60, R2200 (1999)

[8] J. G. Pellerin, D. P. Griggis, P. E. Russel, J. Vac. Sci. Technol. B8, 1945 (1990).

Inductively Coupled Plasma Reactive Ion Etching of GaN

S. Golka, W. Schrenk, G. Strasser

Zentrum für Mikro- und Nanostrukturen, Technische Universität Wien, Floragasse 7, A-1040 Wien

We investigate in deep etching recipes for GaN based compound semiconductors. For nitride semiconductors wet chemistry does not work, therefore plasma etching is required. For deep structures of wavelength scale in GaN, a good etchant to mask selectivity and vertical etch profiles is needed. We present an inductively coupled plasma recipe that can etch 6 µm deep with smooth sidewalls with a SiNx hard mask.

Introduction

Since etching of GaN [1] cannot be accomplished by wet chemistry to a satisfactory degree, reactive ion etching (RIE) becomes very important, as it is the only means of obtaining vertical structuring. The only practical wet etch [2] is KOH at 50 …100 °C. The inability to find a mask that will hold up to such aggressive chemistry makes it more or less useless for accurate transfer of patterns. Unlike for other III-V semiconductors this is also valid for shallow structures for electronics. Demands on etch quality become even more stringent for deeper optically waveguided structures; especially where lithographic resolution needs to be on the micrometer scale. In that mask thickness will be limited by some lithographic technique; here selectivity plays a significant role.

With respect to the demands in optically integrated circuits a RIE recipe is needed to produce vertical or at least overcut sidewalls. Undercut would not be compatible with subsequent metallization steps. Preferably this sample preparation technique should be fast and reliable, which is not a matter of course for the nitrides, since etch rates are generally slow [1]. Smoothness of sidewalls becomes a crucial issue for optoelectronic devices operating at 1.55 µm or less. In rough sidewalls scattering will take place and hence will boost the waveguide losses. Additionally cleavage of waveguide facets is difficult or even impossible in the GaN/InGaAlN system if grown on commonly used sapphire substrate; therefore cleaved facets for in-plane fiber coupling are no option. Etched facets [3] are an excellent solution but this again demands vertical and smooth etches, in this case even in excess of 5 µm in order to make space for fiber tapers.

So far most groups used chlorine based RIE techniques, mainly because these provide the highest etch rates for GaN in the order of 50 nm/min for capacitively coupled plasma (CCP) RIE [4]. Going to higher plasma densities with inductively coupled plasma (ICP) RIE [5] enhances rates to the order of 600 nm/min. In this work we are mainly concerned with developing such an ICP process for very large etch depths.

Sample preparation

For advanced structures like tightly guiding rib waveguides a better mask to etchant selectivity is needed than the one obtained for GaN versus photo resist, which was smaller then 1:1 in favor of the photo resist. The use of an intermediate mask does not only enhance selectivity but also improves the sidewall smoothness which will be im-

portant for etched mirrors. Since SiN_X is available in almost any processing lab and has very good adhesive properties to GaN/AlN it is a good choice. Remaining SiN_X can easily be removed by HF after etching. We used a two step fabrication scheme as outlined in Fig. 1. The photo resist to SiN_X selectivity is only slightly better than 1:1, but the expected selectivity of GaN to SiN_X in an ICP RIE process step is well above 1:1 as will be shown later. Also, the process utilizing SiNx masks has the advantage of being totally free of organic substances during the deep etch process. Remaining photo resist is stripped by plasma oxidizing and KOH. By this additional cleaning procedure we avoid any micro masking [6] effects and wall roughening by contaminants.

Experiment

In ICP-RIE a $N_2/SiCl_4$ based chemistry, as compared to commonly used Ar/Cl_2, has proved itself due to two reasons: Nitrogen has less than half the atomic weight than Argon and therefore does much less damage the masking material. Concerning the acceleration voltage acting on the inert gas atoms normally there is an onset voltage where sputter removal of the mask just starts to be efficient. If one manages to stay below that only very slightly, etch selectivity is very much improved. This fine tuning works especially nice with nitrogen. Second, the $SiCl_4$ [7] is split in the plasma and provides silicon compounds that are again not reluctant to react with chlorine; these compounds can serve as passivation layers that stick on sidewalls were sputtering does not take place. So at the end it can act as a chemical underetch inhibitor. This inhibitor is still efficient at very high chlorine flow. Furthermore, $SiCl_4$ is much more compatible with residual water in the etch chamber. In contrary, the use of Cl_2 gas causes major troubles with residual water vapors and needs additional cleaning steps to prevent hydrogen-chlorine based erosion.

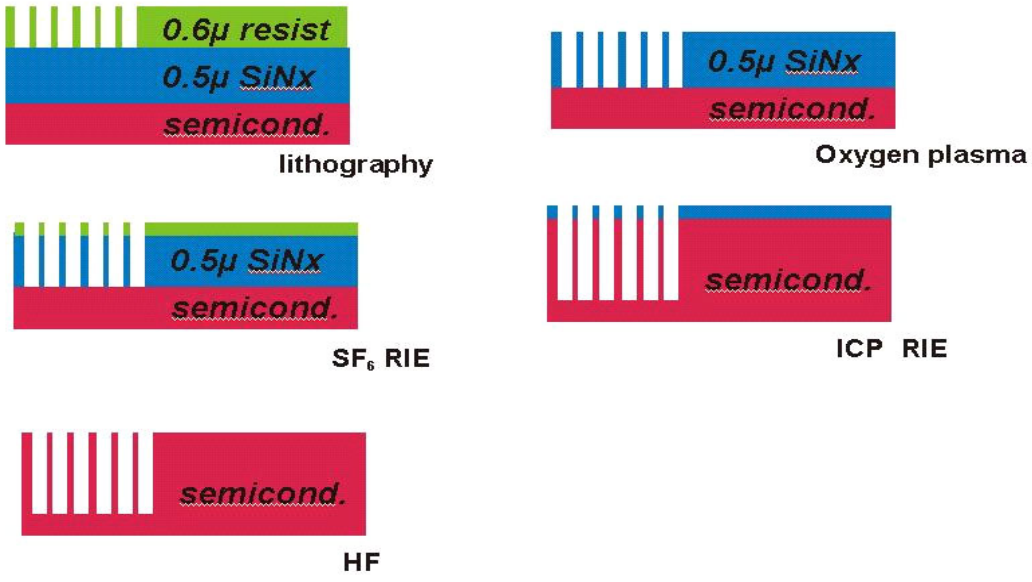

Fig. 1: Fabrication scheme for deep GaN/AlN structures

Initially processes with high flow of chemically reactive gas species have been tried assuming that this will enhance selectivity in any case. Unlike in, e.g., GaAs etching, where it represents an annoying problem, apparently chemical underetching of sidewalls is unlikely in GaN at least in the parameter range investigated within this study. Therefore it was thought that more $SiCl_4$ than N_2 flow would be advantageous. This

resulted in an ultimate etch depth of about 2 µm (Fig. 2). But surprisingly the opposite ratio, namely 20:10 N_2:$SiCl_4$ had almost double the selectivity, which we believe to be due to better etch product sputter removal, since the etch process is not flow limited at all, if in excess of 10 sccm $SiCl_4$. There is an additional argument supporting this gas mixture that was mentioned already: the $SiCl_4$ sputter rate of the SiN_x mask is about 50% higher than the mask sputter rate achieved by using N2 only.

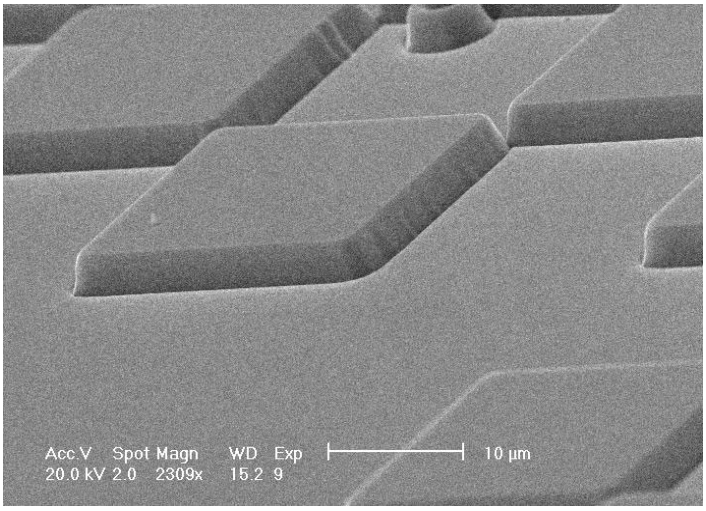

Fig. 2: Typical result of the first set of process testing obtained by etching thick intentionally undoped C-GaN layers on sapphire susbstrates. DC bias set to 200 V, $SiCl_4$:N_2 ratio was 20:10.

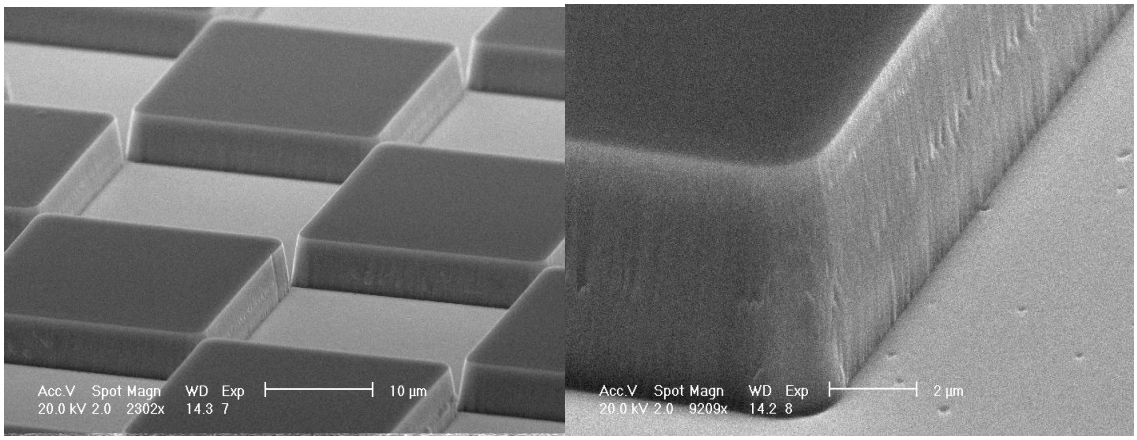

Fig. 3: SEM picture of the 20:10 N_2:$SiCl_4$ process with magnified sidewalls in the picture on the right. The surface roughness is well below a critical roughness for 1.55 µm light. Note that deviations from the verticality are well below 5°.

During optimization it also turned out that very low DC bias does give much better selectivity as well. This might seem somewhat contradictory to the above assumption about sputter removal, but even at room temperature the energy typical $GaCl_X$ compounds need for removal are very low. Thus, there is no additional enhancement in the sputter rate by increasing the ion energy via the applied DC bias. Higher ion energy on the other hand sputters the mask faster and, therefore, reduces the total achievable thickness for a given mask thickness. More reactive species are much more effectively

supplied by high powers to the ICP coil, which should break up the $SiCl_4$ in larger amounts. The resulting etch rates we found in our optimized process are about 106 nm/min for GaN and 13 nm/min for the SiN_X mask. This should be sufficient selectivity to prepare waveguides as well as deep etched mirrors. As can be seen in Fig. 3 the sidewall roughness is low and verticality <5° sufficient not to refract light off plane. This small angle deviation from rectangular sidewalls originates from mask erosion, which is always a little bit faster at the edges than in the center of large areas. The etch rate of both, the SiN_X mask and the GaN epilayers did not scale with temperature notably in the investigated temperature range spanning from 150 °C to 300 °C. This is exactly the temperature window in which $InCl_3$ evaporates at pressures around 10 mtorr. The consequence of this particular finding is that it will be easy to obtain smooth but still not underetched profiles of InGaN of any Indium content.

Conclusions

We developed and optimized an etch recipe to perform deep etching of GaN-based materials with a low surface roughness. The process employing inductively coupled plasma reactive ion etching (ICP-RIE) with N_2 and $SiCl_4$ allows an etch depth exceeding 5 µm, sidewalls deviate <5° from verticality. A SiN_X mask gives a selectivity of about 7:1. No trenching occurs at the bottom or into Al containing layers. This process can be readily used for processing of rib waveguides for 1.55 µm wavelength as well as etched reflecting facets.

This work was supported by the European project NITWAVE and the Austrian Gesellschaft für Mikro- und Nanoelektronik (GMe).

References

[1] S. J. Pearton, J. C. Zolper, R. J. Shul, and F. Ren, J. Appl. Phys. 86(1) Appl. Phys. Reviews 1-78 (1999)

[2] C.B. Vartuli, S.J. Pearton, J.W. Lee, C.R. Abernathy, J.D. Mackenzie, J.C. Zolper, R.J. Shul, and F. Ren, J. Electrochem. Soc. 143, 3681 (1996)

[3] F.A. Khan, L. Zhou, A.T. Ping, and I. Adesida, , J. Vac. Sci. Techn. B 17(6), 2750-2754 (1999)

[4] I. Adesida, A. Mahajan, E. Andideh M. Asif Khan, D. T. Olsen, and J. N. Kuznia, Appl. Phys. Lett. 63(20), 2777-2779 (1993)

[5] R. J. Shul, G. B. McClellan, S. A. Casalnuovo, D. J. Rieger, S. J. Pearton, C. Constantine, C. Barratt, R. F. Karlicek, Jr., C. Tran, and M. Schurman, Appl. Phys. Lett. 69(8), 1119-1121 (1996)

[6] Y. B. Hahn, Y. H. Im, J. S. Park, K. S. Nahm, and Y. S. Lee, J. Vac. Sci. Techn. A, 19(4), 1277-1281 (2001)

[7] E. Zhirnov, S. Stepanov, W.N. Wang, Y. G. Shreter, D. V. Takhin, and N. I. Bochkareva, J. Vac. Sci. Techn. A, 22(6), 2336-2341 (2004)

Microelectronics Technology — Cleanroom Linz

Micro- and Nanostructure Research: Cleanroom Linz

G. Bauer, W. Jantsch, G. Brunthaler

Institut für Halbleiter- und Festkörperphysik
Johannes Kepler Universität Linz, A-4040 Linz, Austria

The research in the cleanrooms of the "*Institut für Halbleiter-und Festkörperphysik*" is strongly supported by the Society for Microelectronics (GMe). In 2003, the central research focus was on semiconductor hetero- and nanostructures, thus forming a strong building block of the "Nanoscience and Technology" research activities of the Johannes Kepler University Linz. The research work encompasses all aspects of semiconductor nanostructures, ranging from nanofabrication, to fundamental investigations and modeling of physical properties, up to the realization of novel nanostructure devices. Nanostructures are fabricated using advanced lithography and processing techniques such as electron beam lithography as well as by self-assembly based on molecular beam epitaxy. In the Christian-Doppler Lab, which is also situated at the institute, the simulation and fabrication of photonic crystals for various optical applications is performed. The class 100 clean room facility forms the base for the processing equipment at the institute.

The funding of the activities in the cleanrooms at the University of Linz which are jointly used by several groups is of vital importance for our micro- and nanostructure research activities. This basic funding allows for investigations which are made possible through additional funding coming from the FWF, the FFF, the Christian-Doppler society, the European Commission, as well as through cooperations with industrial groups as listed in the report.

The fundamental structural, electronic, optical and magnetic properties of nanostructures and semiconducting layers are studied using a large variety of techniques. These range from advanced x-ray scattering techniques using synchrotron radiation, high-resolution electron microscopy, scanning force and scanning tunneling microscopy, optical spectroscopy, magnetic Squid investigations as well as low temperature magnetotransport measurements. The focus of research is to correlate the electronic properties of nanostructures with the fabrication processes and structural properties, taking advantage of the complementarity of information gained by the different techniques and modeling tools. A strong emphasis is put on infrared spectroscopy of the interband and intersubband electronic transitions in SiGe and narrow band gap semiconductors heterostructures, as well as on ballistic and quantum transport studies of SiGe and III-V hetero- and nanostructures in the milli-Kelvin temperature regime. In addition, the magnetic properties of magnetic semiconductor hetero- and nanostructures are investigated and novel tools for nanostructure investigations based on synchrotron light sources are developed.

Several research activities are devoted to the fabrication of semiconductor hetero- and nanostructure devices. In the optical area, mid-infrared intersubband and interband detectors, quantum cascade structures, mid-infrared vertical cavity surface emitting lasers and resonant cavity detectors are modeled, fabricated and investigated. The Christian-Doppler Laboratory at the institute is devoted to theoretical and practical aspects of photonic crystals for e.g. waveguide applications and polarization splitting in the near-infrared telecommunication spectral range and three patents were applied in this field in the last year. In the electric/electronic application field, devices such as

quantum dot and single electron transistors were formed in the Si/SiGe and AlGaAs material systems and investigated in the milli-Kelvin regime. Novel spintronic devices that take advantage of the spin degree of freedom in order to produce new functionalities are developed as well in the Si/SiGe system. And finally in the device area high-mobility n-channel organic field-effect transistors based on epitaxially grown C_{60} films were produced and characterized by electrical I-V curve measurements.

From the materials side, a strong focus is on Si/SiGe/SiGeC based hetero- and nanostructures for which a large molecular beam epitaxy system is operated in the clean room of the institute. There is also extensive work on narrow gap IV-VI compound semiconductors, which includes PbSe as well as PbTe based materials and magnetic europium chalcogenide semiconductors. For these materials another two molecular beam epitaxy systems are available at the institute. Gallium-Nitride material layers are as well being fabricated at the institute by a metal-organic chemical vapor deposition (MOCVD) system, where the layers are doped with iron and manganese in order to test the electrical and magnetic properties. The fabricated structures from the institute in Linz are supplied also to external research groups outside in the framework of long term international collaborations. On the other hand, also materials and structures including SiGe as well as GaAs/GaAlAs based structures are supplied from outside groups for further processing and analysis with techniques developed at our institute.

The research activities are embedded in several large research initiatives and project clusters such as the IRON special research program, the NIS Nanostructured Surface and Interface project cluster, as well as the SANDiE European network of excellence and several other EU funded research projects.

A detailed presentation of the mentioned physical investigation methods, devices fabrication and characterization and material systems is given in the separate, individual reports below.

Project Information for 2004

Project Manager

Associate Prof. Dr. Gerhard Brunthaler

Institut für Halbleiter-und Festkörperphysik,
Johannes Kepler Universität Linz,
A-4040 Linz, Austria

Project Group

Last Name	First Name	Status	Remarks
Bauer	Günther	University professor	
Heinrich	Helmuth	University professor	
Jantsch	Wolfgang	University professor	
Schäffler	Friedrich	University professor	
Brunthaler	Gerhard	Associate professor	
Palmetshofer	Leopold	Associate professor	
Springholz	Gunther	Associate professor	
Sitter	Helmut	Associate professor	
Bonanni	Alberta	Assistant professor	
Heiss	Wolfgang	Assistant professor	
Fromherz	Thomas	Assistant professor	
Stangl	Julian	Assistant professor	
Andreev	Andrej	Assistant professor	
Binder	Fritz	Technician	
Bräuer	Stephan	Technician	
Fuchs	Othmar	Technician	
Jägermüller	Josef	Technician	
Nusko	Ekkehard	Electronics Engineer	
Vorhauer	Ernst	Electronics engineer	
Andreeva	Svetlana	Lab Technician	FWF-START
Halilovic	Alma	Lab Technician	½ paid by GME
Hasenfuss	Christine	Lab Technician	CD Lab
Haslgrübler	Klaus	Lab Technician	½ paid by GME, till 31.3.2004
Kainz	Ursula	Lab Technician	½ position, till Oct. 2004
Praus	Antonia	Lab Technician	½ position, since Nov. 2004
Wirtl	Elisabeth	Phys. Lab. Assistent	
Firmberger	Johanna	Apprentice	
Hingerl	Kurt	Head of CD Lab	
Holy	Vaclav	Guest Researcher	Charles Univ. Prag

Last Name	First Name	Status	Remarks
Andreev	Andrej	Post Doc	FWF
Chen	Gang	Post Doc	FWF
Kocher	Gudrun	Post Doc	CDG
Lechner	Rainer	Post Doc	FWF
Montaigne-R.	Alberto	Post Doc	FWF
Schwarzl	Thomas	Post Doc	FWF
Abtin	Laurel	Ph.D. student	FWF
Achleitner	Joachim	Ph.D. student	
Baumgartner	Eugen	Ph.D. student	FWF
Berer	Thomas	Ph.D. student	FWF, Uni Linz
Böberl	Michaela	Ph.D. student	FWF
Glinsner	Thomas	Ph.D. student	EGV
Gruber	Daniel	Ph.D. student	FWF, Uni Start
Heisl	Elke	Ph.D. student	CDG, till Sept. 2004
Holy	Roman	Ph.D. student	CDT, since Sept. 2004
Kaufmann	Erich	Ph.D. student	FWF
Kovalenko	Maksym	Ph.D. student	FWF
Lichtenberger	Herbert	Ph.D. student	FWF
Lugovyy	Dmytro	Ph.D. student	FWF
Malissa	Hans	Ph.D. student	WIMI
Mundboth	Rajivshing	Ph.D. student	
Novak	Jri	Ph.D. student	EC (SiGeNET, SHINE)
Pachinger	Dietmar	Ph.D. student	FWF
Pillwein	Georg	Ph.D. student	FWF
Rauter	Patrick	Ph.D. student	EC (SHINE)
Rehman-Khan	Aaliya	Ph.D. student	ÖAD
Roither	Jörgen	Ph.D. student	FWF
Schmidegg	Klaus	Ph.D. student	EU ISCE-MOCVD, FWF
Schwinger	Wolfgang	Ph.D. student	FFF
Simbrunner	Clemens	Ph.D. student	EU ISCE-MOCVD
Simma	Matthias	Ph.D. student	FWF
Söllinger	Walter	Ph.D. student	FWF
Wintersberger	Eugen	Ph.D. student	EC (SHINE), FWF
Zarbakhsh	Javad	Ph.D. student	CDG
Anzengruber	Johannes	Diploma student	
Aynul	Islam	Diploma student	CD Lab
Grydlik	Martyna	Diploma student	stipendiat
Hörmann	Thomas	Diploma student	
Huber	Martin	Diploma student	CD Lab
Isfahani	Farnaz	Diploma student	CD Lab
Janecek	Stefan	Diploma student	finished July 2004
Kirchschlager	Raimund	Diploma student	

Last Name	First Name	Status	Remarks
Lindner	Benjamin	Diploma student	finished Nov. 2004
Pichler	Stefan	Diploma student	
Wegscheider	Matthias	Diploma student	

Publications in Reviewed Journals

published 2004

1. C. Schelling, J. Myslivecek, M. Mühlberger, H. Lichtenberger, Z. Zhong, B. Voigtländer, G. Bauer, F. Schäffler, "*Kinetic and strain-driven growth phenomena on Si(001)",* phys. stat. sol. (a) 201, 324-328 (2004) / DOI 10.1002/pssa.2003093966.
2. G. Grabecki, J. Wrobel, T. Dietl, E. Papis, E. Kaminska, A. Piotrowska, A. Ratuszna, G. Sprinholz, G. Bauer, "*Ballistic transport in PbTe-based nanostructures",* Physica E 20, 236 - 245 (2004).
3. R.T. Lechner, T.U. Schülli, V. Holy, G. Springholz, J. Stangl, A. Raab, G. Bauer, T.H. Metzger, "*Ordering parameters of self-organized three-dimensional quantum-dot lattices determined from anomalous x-ray diffraction",* Appl. Phys. Lett. 84, 885-887 (2004).
4. Zhenyang Zhong, Gang Chen, J. Stangl, T. Fromherz, F. Schäffler, G. Bauer, "*Two-dimensional lateral ordering of self-assembled Ge islands on patterned substrates",* Physica E 21, 588-591 (2004).
5. R. T. Lechner, T. Schülli, V. Holy, J. Stangl, A. Raab, G. Springholz, G. Bauer, "*3D hexagonal versus trigonal ordering in self-organized PbSe quantum dot superlattices",* Physica E 21, 611-614 (2004).
6. Zhenyang Zhong and G. Bauer, "*Site-controlled and size-homogeneous Ge islands on prepatterned Si (001) substrates",* Appl. Phys. Lett. 84, 1922-1924 (2004).
7. M. Meduna, J. Novak, G. Bauer, V. Holy, C.V. Falub, E. Müller, D. Grützmacher, Y. Campidelli, O. Kermarrec, D. Bensahel, "*Annealing studies of high Ge composition Si/SiGe multilayers",* Z. Kristallogr. 219, 195-200 (2004).
8. S.D. Tsujino, C.V. Falub, E. Müller, M. Scheinert, L. Diehl, U. Gennser, T. Fromherz, A. Borak, H. Sigg, D. Grützmacher, Y. Campidelli, O. Kermarrec, D. Bensahel, "*Hall mobility of narrow Si0.2Ge0.8-Si quantum wells on Si0.5Ge0.5 relaxed buffer substrates",* Appl. Phys. Lett. 84, 2829-2831 (2004).
9. J. Fürst, H. Pascher, T. Schwarzl, M. Böberl, G. Springholz, G. Bauer, W. Heiss, "*Continuous-wave emission from midinfrared IV-VI vertical-cavity surface-emitting lasers",* Appl. Phys. Lett. 84, 3268-3270 (2004).
10. T. U. Schülli, R. T. Lechner, J. Stangl, G. Springholz, and G. Bauer, "*Soft x-ray magnetic scattering from ordered EuSe nanoislands",* Appl. Phys. Lett. 84, 2661-2663 (2004).
11. V. M. Pudalov, M. E. Gershenson, H. Kojima, G. Brunthaler, G. Bauer, "*Are the interaction effects responsible for the temperature and magnetic field dependent conductivity in Si-MOSFETs?",* Phys. Stat. Sol. (b) 241, 47-53 (2004).
12. G. Brunthaler, B. Lindner, G. Pillwein, S. Griesser, M. Prunnila, J. Ahopelto, "*Two-Dimensional Metallic State in Silicon-on-Insulator Structures",* Physica E **22**, 252 – 255 (2004).

13. J. Stangl, T. Schülli, H. Metzger, G. Bauer, "*Im Inneren von Halbleiternano-strukturen",* Physik Journal 3, 33-39 (2004).

14. R. Kirchschlager, W. Heiss, R. T. Lechner, G. Bauer, G. Springholz, "*Hysteresis loops of the energy band gap and effective g factor up to 18 000 for metamagnetic EuSe epilayers",* Appl. Phys. Lett. 85, 67-69 (2004).

15. Zhenyang Zhong, A. Halilovic, H. Lichtenberger, F. Schäffler, G. Bauer, "*Growth of Ge islands on prepatterned Si (001) substrates",* Physica E 23, 243-247 (2004).

16. H. Lichtenberger, M. Mühlberger, C. Schelling, W. Schwinger, S. Senz, F. Schäffler, *Transient-enhanced Si diffusion on natural-oxide-covered Si(0 0 1) nano-structures during vacuum annealing,* Physica E 23, 442-448 (2004).

17. J. Stangl, V. Holy, G. Bauer, "*Structural properties of self-organized semiconductor nanostructures",* Rev. Mod. Phys. 76, 725-783 (2004).

18. H. Malissa, W. Jantsch, M. Mühlberger, F. Schäffler, Z. Wilamowski, M. Draxler, P. Bauer, "*Anisotropy of g-factor and electron spin resonance linewidth in modulation doped SiGe quantum wells",* Appl. Phys. Lett. 85, 1739-1741 (2004).

19. K. Lai, W. Pan, D.C. Tsui, S. Lyon, M. Mühlberger, F. Schäffler, "*Two-flux composite fermion series of the fractional quantum hall states in strained Si",* Phys. Rev. Lett. 93, 156805-1/4 (2004).

20. S. Danis, V. Holy, Z. Zhong, G. Bauer, O. Ambacher, "*High-resolution diffuse x-ray scattering from threading dislocations in heteroepitaxial layers",* Appl Phys Lett. 85, 3065-3067 (2004).

21. J. Stangl, T. Schülli, A. Hesse, V. Holy, G. Bauer, M. Stoffel, O.G. Schmidt, "*Structural properties of semiconductor nanostructures from x-ray scattering",* Adv. in Solid State Phys. 44, 227-237 (2004).

22. W. Heiss, R. Kirchschlager, G. Springholz, Z. Chen, M. Debnatz, Y. Oka, "*Magnetic polaron induced near-band-gap luminescence in epitaxial EuTe",* Phys. Rev. B 70, 035209 035209-1 - 035209-8 (2004).

23. K. Wiesauer, G. Springholz, "*Critical thickness and strain relaxation in high-misfit heteroepitaxial systems: $PbTe_{1-x}Se_x$ on PbSe (001)",* Phys. Rev. B 69, 245313-1 - 245313-9 (2004).

24. O. Kirfel, E. Müller, D. Grützmacher, K. Kern, A. Hesse, J. Stangl, V. Holý, G. Bauer, "*Shape and composition change of Ge dots due to Si capping",* Appl. Surf. Sci. 224, 139-142 (2004).

25. J. Fürst, T. Schwarzl, M. Böberl, H. Pascher, G. Springholz, W. Heiss, "*Vertical-cavity surface-emitting lasers in the 8-mm midinfrared spectral range with continuous-wave and pulsed emission",* IEEE Journal of Quantum Electronics Vol. 40, 966-969 (2004).

26. T. U. Schülli, R. T. Lechner, J. Stangl, G. Springholz, G. Bauer, M. Sztucki, T. H. Metzger, "*Strain determination in multilayers by complementary anomalous x-ray diffraction",* Phys. Rev. B 69, 195307-1/8 (2004).

27. T. U. Schülli, R. T. Lechner, J. Stangl, G. Springholz, G. Bauer, M. Sztucki, T. H. Metzger, "*Strain determination in multilayers by complementary anomalous x-ray diffraction"*, European Synchrotron Radiation Facility (ESRF) Highlíghts 2004, 80-81 (2004).

28. K. Koike, I. Makabe, M. Yano, E. Kaufmann, W. Heiss, G. Springholz and M. Böberl, "*Molecular Beam Epitaxial Growth and Photoluminescence Characterization of PbTe/CdTe Quantum Wells for Mid-Infrared Optical Devices",* Journal of the Society of Materials Science 53, 1328 – 1333 (2004).

29. M. Böberl, T. Fromherz, T. Schwarzl, G. Springholz, W. Heiss, "*IV-VI resonant-cavity enhanced photodetectors for the mid-infrared", S*emicond. Sci. Technol. 19, L115-L117 (2004).

30. G. Bauer and G. Springholz, "Lead Salts" in "*Encyclopedia of Modern Optics"*, edited by Robert D. Guenther, Duncan G. Steel and Leopold Bayvel, Elsevier, Oxford, 2004, ISBN 0-12-227600-0, p 641.

31. A. Kadashchuk, A. Andreev, H. Sitter, N.S. Sariciftci, Yu. Skryshevski, Yu. Piryatinski, I. Blonsky, D. Meissner
Aggregate states and energetic disorder in highly-ordered nanostructures of para-sexiphenyl grown by Hot-Wall Epitaxy
Advanced Functional Mat. **14**, 970 (2004),

32. A. Yu. Andreev, C. Teichert, G. Hlawacek, H. Hoppe, R. Resel, D.-M. Smilgies, H. Sitter, N. S. Sariciftci
Morphology and growth kinetics of organic thin films deposited by hot wall Epitaxy
Organic Electronics **5**, 23-27 (2004)

33. A. Montaigne, K. Schmidegg, A. Bonanni, H. Sitter, D. Stifter, Li Shunfeng, D. J. As, K. Lischka
In-situ growth monitoring by spectroscopic ellipsometry of MOCVD cubic - GaN (001)
Thin Sol. Films **455-456**, 684-687 (2004)

34. F. Quochi, F. Cordella, R. Orru, J. E. Communal, P. Verzeroli, A. Mura, G. Bongiovanni, A. Andreev, H. Sitter, N. S. Sariciftci
Random laser action in self-organized para-sexiphenyl nano-fibers grown by Hot Wall Epitaxy
Appl. Phys. Lett. **84**, 4454-4456 (2004)

35. Z. Wilamowski, W. Jantsch
Spin Relaxation of 2D electron in Si/SiGe quantum well suppressed by an applied magnetic field
Semicond. Sci. Technol. **19**, 390-391 (2004)

36. W. Jantsch, Z. Wilamowski
Spin Coherence and Manipulation in Si/SiGe Quantum Wells
in: Frontiers in Molecular-Scale Science and Technology of Nanocarbon, nanoSilicon and Biopolymer Multifunctional Nanosystems, Proc. NATO ARW, ed. by E. Buzaneva and P. Scharff, 379-390, Kluwer Academic Publishers (2004)

37. K. Schmidegg, A. Kharchenko, A. Bonanni, H. Sitter, J. Bethke, K. Lischka
Characterization of MOCVD growth of cubic GaN by in situ X-ray diffraction
J. Vac. Sci. Technol. B **22** (2004)

38. A. Andreev, T. Haber, D.-M. Smilgies, R. Resel, H. Sitter, N. S. Sariciftci, L. Valek
Morphology and growth kinetics of organic thin films deposited by Hot Wall Epitaxy on KCl substrates
J. Cryst. Growth (Proceedings Grenoble) (2004)

39. A. Bonanni, K. Schmidegg, A. Montaigne Ramil, A. Kharchenko, J. Bethke, K. Lischka, H. Sitter
On-line growth control of MOCVD deposited GaN and related ternary compounds via spectroscopic ellipsometry and x-ray diffraction
Phys. Stat. Sol (a), **201**, 2259-2264 (2004)

40. A. Andreev, F. Quochi, A. Kadaschuk, H. Sitter, C. Winder, H. Hoppe, S. Sariciftci, A. Mura, G. Bongiovanni
Blue emitting self-assembled nano-fibers of para-sexiphenyl grown by Hot Wall Epitaxy

Phys. Stat. Sol. (a), **201**, 2288-2293 (2004)
Conference on Photo-Responsive Materials, Kariega, South Africa, Febr. 25-29 (2004)

41. E. Belas, P. Moravec, R. Grill, J. Franc, A. L. Toth, H. Sitter, P. Höschl
Silver diffusion in p-type CdTe and (CdZn)Te near room temperature
Phys. Stat. Sol. (c) **1**, 929-932 (2004)

42. M.Svaluto Moreolo, K.Hingerl, G. Cincotti
"Ultra compact 2-D photonic crystal add-drop multiplexer"
ICTON conference proceedings

43. J.Zarbakhsh. F. Hagmann, S. F. Mingaleev, K. Busch,-K, K. Hingerl
"Arbitrary angle waveguiding applications of two-dimensional curvilinear-lattice photonic crystals"
Appl. Phys. Lett., **84**, 4687

44. Javad Zarbakhsh, Kurt Hingerl, Frank Hagmann, Sergei F. Mingaleev, Kurt Busch
"Curvilinear Photonic Crystals"
Proceedings of the Opt, Soc. Meeting, Rochester, NY.

45. V.Rinnerbauer, J. Schermer, K. Hingerl
"Polarization demultiplexer with Photonic Crystals"
Proceedings of European Conference on Optical Communication, ECOC 2004 Stockholm

Submitted 2004 / in print

1. G. Springholz, T. Schwarzl and W. Heiss, "Mid-infrared Vertical Cavity Surface Emitting Lasers based on the Lead Salt Compounds", in: Mid-infrared Semiconductor Optoelectronics, ed. A. Krier (Springer-Verlag London, in print).
2. A.M. Tyryshkin, S.A. Lyon, W. Jantsch, F. Schäffler, "Spin Manipulation of Free Two-Dimensional Electrons in Si/SiGe Quantum Wells", Phys. Rev. Letters, in print.
3. V. Holy, T.U. Schülli, R.T. Lechner, G. Springholz, G. Bauer, *"Anomalous x-ray diffraction from self-assembled PbSe/PbTe quantum dots"*, J. Alloys and Compounds, in print.
4. M. Meduna, J. Novak, C.V. Falub, G. Chen, G. Bauer, S. Tsujino, D. Grützmacher, E. Müller, Y. Campidelli, O. Kermarrec, D. Bensahel, N. Schell, *"High temperature investigations of Si/SiGe based cascade structures using x-ray scattering methods"*, J. Phys. D: Appl. Phys., to be published.
5. J. Fürst, H. Pascher, T. Schwarzl, G. Springholz, M. Böberl, G. Bauer, W. Heiss, *"Magnetic field tunable circularly polarized emission form midinfrared IV-VI vertical emitting layers"*, Appl. Phys. Lett., in print.
6. G. Springholz, *"Three-dimensional stacking of self-assembled quantum dots in multilayer structures"*, C. R. Physique, in print.
7. D. Grützmacher, S. Tsujino, C. Falub, A. Borak, L. Diehl, E. Müller, H. Sigg, U. Genser, T. Fromherz, M. Meduna, G. Bauer, J. Faist, O. Kermarrec, *"Transport and absorption in strain-compensated Si/$Si_{1-x}Ge_x$ multiple quantum well and cascade structures deposited on $Si_{0.5}Ge_{0.5}$ pseudosubstrates"*, Materials Science in Semiconductor Processing, in print.
8. R. T. Lechner, G. Springholz, T. U. Schülli, J. Stangl, T. Schwarzl, G. Bauer, *"Strain induced changes in the magnetic phase diagram of metamagnetic heteroepitaxial Eu/Se/PbSe1-xTex multilayers"*, Phys. Rev. Lett., in print.

9. T. Schwarzl, M. Böberl, G. Springholz, E. Kaufmann, J. Roither, W. Heiss, J. Fürst, H. Pascher, *"Molecular beam epitaxy of vertical-emitting microcaviyt lasers for the 6-8 micron spectral range operating in continuous-wave mode"*, J. Crystal Growth, in print.

10. J. A. H. Coaquira, V. A. Chitta, N. F. Oliveira Jr., P. H. O. Rappl, A. Y. Ueta, E. Abramof, G. Bauer, *"Electrical Characterization of p-Type Pb1-xEuxTe"*, Journal of Superconductivity: Incorporating Novel Magnetism, in print.

11. T. Schwarzl, G. Springholz, M. Böberl, E. Kaufmann, J. Roither, W. Heiss, J. Fürst, H. Pascher, *"Emission properties of 6.7 mm continuous-wave PbSe-based vertical-emitting microcavity lasers operating up to 100 K"*, Appl. Phys. Lett., in print.

12. H. Lichtenberger, M. Mühlberger, C. Schelling, F. Schäffler, *"Ordering of self-assembled Si0.55Ge0.45 islands on vicinal Si(001) substrates"*, J. Crystal Growth, submitted.

13. J. Novák, V. Holý, J. Stangl, T. Fromherz, Z. Zhong, G. Chen, G. Bauer, B. Struth, *"Ge/Si islands in a 3D island crystal studied by x-ray diffraction"*, J. Appl. Phys., submitted.

14. T. M. Burbaev, V. A. Kurbatov, M. M. Rzaev, A. O. Pogosov, N. N. Sibel'din, V. A. Tsvetkov, H. Lichtenberger, F. Schäffler, J. P. Leitao, N. A. Sobolev, and M. C. Carmo, *"Morphological transformation of a Germanium layer grown on a Silicon surface by Molecular-Beam Epitaxy at low temperatures"*, Phys. Solid State, submitted.

15. J.P. Leitão, A. Fonseca, N.A. Sobolev, M.C. Carmo, N. Franco, A.D. Sequeira, T.M. Burbaev,V.A. Kurbatov, M.M. Rzaev, A.O. Pogosov, N.N. Sibeldin, V.A. Tsvetkov, H. Lichtenberger, and F. Schäffler, *"Low-temperature molecular beam epitaxy of Ge on Si"*, Materials Science in Semiconductor Processing, in print.

16. M. Rzaev, F. Schäffler, V. Vdovin and T. Yugova, *"Misfit dislocation nucleation and multiplication in fully strained SiGe/Si heterostructures under thermal annealing"*, Materials Science in Semiconductor Processing, in print.

17. M. Draxler, M. Mühlberger, F. Schäffler and P. Bauer, *"Non-destructive quantitative analysis of the Ge concentration in SiGe quantum wells by means of low energy RBS"*, Nucl. Inst. Meth., in print 2005.

18. H. Lichtenberger, M. Mühlberger and F. Schäffler, "*Ordering of $Si_{0.55}Ge_{0.45}$ Islands on Vicinal Si(001) Substrates: The Interplay between Kinetic Step Bunching and Strain-Driven Island Growth*", Appl. Phys. Lett., in print.

19. G. Chen, H. Lichtenberger, F. Schäffler, G. Bauer, W. Jantsch, "*Geometry dependence of nucleation mechanism for SiGe islands grown on pitpatterned Si(001) substrates",*
Mat. Science Engineering C, ELSEVIER, in print.

20. K. Schmidegg, G. Neuwirt, H. Sitter, A. Bonanni
Simultaneous determination of composition and growth rate of MOCVD-growth ternary nitride compounds by multiple wavelength spectroscopic ellipsometry
J. Cryst. Growth (Proceedings Grenoble), in print

21. D. Franta, I. Ohlidal, P. Klapetek, A. Montaigne-Ramil, A. Bonanni, D. Stifter, H. Sitter
Optical properties of ZnTe films prepared by molecular beam epitaxy
Thin Sol. Films, in print

22. M. Siler, I. Ohlidal, D. Franta, A. Montaigne-Ramil, A. Bonanni, D. Stifter, H. Sitter
Optical characterization of double layers containing epitaxial ZnSe and ZnTe films
Journ. of Mod. Optics, in print

23. H. Malissa, D. Gruber, D. Pachinger, F. Schäffler, W. Jantsch, Z. Wilamowski
Demonstration of g-factor tuning in a SiGe double quantum well device
superlattices and microstructures, submitted

24. H. Przybylínska, G. Kocher, W. Jantsch, D. As, K. Lischka
Photoconductivity study of Mg and C acceptors in cubic GaN
Proc. ICPS-27, in print

25. K. Schmidegg, H. Sitter, A. Bonanni
In-situ optical analysis of low temperature MOVCD GaN nucleation layer formation via multiple wavelength ellipsometry
J.Cryst.Growth, in print

26. J. Roither, M. V. Kovalenko, S. Pichler, T. Schwarzl, W. Heiss
Nanocrystal based microcavity light emitting devices operating in the telecommunication wavelength range
Appl. Phys. Lett.

27. H. Przybylínska, A. Bonanni, A. Wolos, M. Kiecana, M. Sawicki, T. Dietl, H. Malissa, C. Simbrunner, M. Wegscheider, H. Sitter, K. Rumpf, P. Granitzer, H. Krenn, W. Jantsch
Magnetic properties of a new spintronic material – GaN:Fe
Mat. Science Engineering C (ELSEVIER publisher) in print

28. J. Chaloupka, J. Zarbakhsh, K. Hingerl
"Local density of states and modes in circular photonic crystal cavities"
Phys. Rev. B

Presentations

Invited Talks:

1. F. Schäffler, "Nanostructured Semiconductors: Top-Down and Bottom-Up Techniques", IIR Nano-Seminar, Vienna, 29.09.2004
2. F. Schäffler, "*Growth Instabilities on Si(001):from Kinetic Step Bunching to Perfectly Ordered SiGe Islands*", MRS Fall Meeting, Boston, USA, 29.11. - 03.12.2004
3. J. Stangl, "*Structural Properties of Semiconductor Nanostructures from X-Ray Scattering*", DPG-Frühjahrstagung Regensburg, March 8, 2004.
4. J. Stangl, "*Influence of growth parameters on the composition of SiGe islands: an x-ray diffraction study*", Summerschool "Jaszowiec 2004", Jaszowiec, Poland, June 3, 2004.
5. J. Stangl, "*High resolution x-ray diffractometry: Determination of strain and composition*", XTOP Prague, Czech Republic, Sept. 8, 2004.
6. G. Bauer, "*Growth and characterization of semiconductor nanostructures*", 20th General Conference of the Condensed Matter Division of the European Physical Society (EPS), Prague, July 19-20, 2004.
7. G. Bauer, Z. Zhong, G. Springholz, R. T. Lechner, J. Stangl, T. Schüllli, T. H. Metzger, V. Holy, "*Nanostructure growth and self-assembly*", ESRF Workshop on Surfaces and Interfaces, Grenoble, Sept. 29 - Oct. 02, 2004.
8. G. Bauer, "*Nanostructure growth and self-assembly*", ALBA Workshop Universidad Autonoma de Madrid, Nov. 3-4, 2004.

9. H. Sitter, A. Andreev, C. Teichert, G. Hlawacek, T. Haber, D. Smilgies, R. Resel, A. Montaigne-Ramil, S. Sariciftci, *Organic thin films grown by Hot Wall Epitaxy on inorganic substrates,* XVII Latin American Symposium on Solid State Physics, 06.-09.12.2004, Habana, Cuba
10. W. Jantsch, Z. Wilamowski, *Spin properties of conduction electrons in Si/SiGe quantum wells,* SiGeNET Final Meeting- Research Training Network Contract HPRN-CT-1999-00123, 02.-03.02.2004, University of Linz, Austria
11. W. Jantsch, Z. Wilamowski, *Properties and manipulation of electron spins in low dimensional SiGe structures,* International Workshop Spintronics: Spin injection, Transport and Manipulation, 11.-12.10.2004, Ruhr-Universität Bochum, Germany

Seminar Talks:

1. G. Bauer, "*Strukturelle Untersuchungen an Halbleiter-Nanostrukturen*", Kolloquiumsvortrag Universität Jena, July 5, 2004.
2. F. Fromherz, P. Rauter, G. Bauer, "*SiSiGe cascade structures: structural characterization and optical properties*", Kolloquiumsvortrag Universität Prag, May 20-21, 2004.
3. J. Stangl, "*Investigation of semiconductor nanostructures by x-ray diffraction techniques*", Symposium on the Use of Synchrotron Radiation, Vienna, 15 March 2004.
4. Z. Zhong, "*Site-controlled Ge islands grown on the patterned Si substrates*", Seminar Talk, Max Planck Institut für Festkörperforschung Stuttgart (Abt. Von Klitzing), Dec. 13, 2004.
5. F.Schäffler, "*Si-based Heterostructures*"; SiGe-Net project meeting, Linz 02.02.2004
6. F. Schäffler, ***"****Presentation of the NanoScience/Technology Center Linz",* Annual Meeting of the Austrian Physical Society, Linz, 28. - 30.10.2004
7. G. Springholz, *"Strain relaxation and dislocation formation in strained-layer heteroepitaxy",* Forschungszentrum Jülich, Germany, 4.11.2004.
8. G. Springholz, "*Surface and Interface Structure in Heteroepitaxial Systems*", Montanuniversität Leoben, Austria 26.2.2004.

Conference presentations (talks and posters):

1. H. Lichtenberger, M. Mühlberger, C. Schelling and F. Schäffler, "*Ordering of Self-Assembled Si0.55Ge0.45 Islands on Vicinal Si(001) Substrates*", 13th Int. Conf. on Molecular Beam Epitaxy, Edinburgh, UK, 23. - 27.08.2004
2. G. Pillwein und G. Brunthaler, "*Leitwertfluktuationen im Coulomb Blockade Regime von AlGaAs Quantenpunkten*", Annual Meeting of the Austrian Physical Society, Linz, 28. - 30.10.2004.
3. H. Lichtenberger, M. Mühlberger, C. Schelling, F. Schäffler, ***"****Ordering of Self-Assembled* $Si_{0.55}Ge_{0.45}$ *Islands on Vicinal Si(001) Substrates",* Annual Meeting of the Austrian Physical Society, Linz, 28. - 30.10.2004
4. G. Pillwein, G. Brunthaler, G. Strasser, "Fabrication and Characterization of lateral quantum dots in GaAs/AlGaAs Heterostructures", Poster, 13th Int. Winterschool on New Developments in Solid State Physics, 15. - 20. Feb. 2004, Mauterndorf, Salzburg.

5. M. Böberl, W. Heiss, T. Schwarzl, and G. Springholz, Z. Wang, K. Reimann, and M. Woerner (Poster),*"Dynamics of lead-salt microcavity lasers after femtosecond optical excitation",* 13th International Winterschool on New Developments in Solid State Physics: "Low-Dimensional Systems", Mauterndorf, Austria, February 15 – February 20, 2004.
6. E. Kaufmann, W. Heiss, G. Springholz, M. Böberl, T. Schwarzl, M. Yano, I. Makabe, K. Koike, (Poster), *"Continuous-wave midinfrared photoluminescence of IV-VI and IV-VI/II-VI heterostructures",* 13th International Winterschool on New Developments in Solid State Physics: "Low-Dimensional Systems", Mauterndorf, Austria, February 15 – February 20, 2004
7. R. T. Lechner, T. U. Schuelli, V. Holy, G. Springholz, J. Stangl, A. Raab, T. H. Metzger, G. Bauer (Talk), "*Fabrication and characterization of three dimensional ordered quantum dot lattices using self assembled epitaxy*", Spring Meeting of the Materials Research Society, San Francisco, USA, 12.4.-16.4.2004.
8. R. T. Lechner, T. U. Schuelli, S. Dhesi, P. Bencok, J. Stangl, G. Springholz and G. Bauer (Talk), "*Laterally ordered magnetic EuSe quantum dots*", Spring Meeting of the Materials Research Society, San Francisco, USA, 12.4.-16.4.2004.
9. M. Böberl, T. Schwarzl, G. Springholz und W. Heiss, J. Fürst, H. Pascher (Talk), Bleisalzverbindungen für optische Bauelemente im mittleren Infraroten, Infrarot-Kolloquium, Feiburg, Germany, 20-21.4.2004.
10. K. Rumpf, P. Granitzer, S. Janecek, G. Springholz , H. Krenn, "*Ideal and real behaviour of the magnetic phase transitions of low-dimensional antiferromagnetic EuTe/PbTe-superlattices*", Joint European Magnetic Symposia JEMS'04, Dresden, Germany, 05-10, 2004.
11. K. Rumpf, P. Granitzer, S. Janecek, G. Springholz , H. Krenn, "*Magnetic Phase Diagram of low-dimensional EuTe/PbTe-Multi-quantum Wells Measured by SQUID-magnetometry*", 8th Int. Conf. on Nanometer-Scale Science and Technology, Venice, Italy, 28.6.-2.7.2004.
12. T. Schwarzl, J. Fürst, M. Böberl, H. Pascher, G. Springholz, W. Heiss (Talk), "*Continuous-wave emission from vertical-cavity surface-emitting lasers at long wavelengths of 8 microns*", 6th International Conference on Mid-Infrared Optoelectronic Materials and Devices, 28.6-1.7.2004, St. Petersburg, Russia.
13. E. Kaufmann, W. Heiss, G. Springholz, M. Böberl, T. Schwarzl, M. Yano, I. Makabe, K. Koike (Poster), "*Continuous-wave light emission from PbTe based heterostructures with CdTe or PbEuTe barriers*", 6th International Conference on Mid-Infrared Optoelectronic Materials and Devices, 28.6-1.7.2004, St. Petersburg, Russia.
14. E. Baumgartner, T. Schwarzl, G. Springholz, W. Heiss (Poster), "*Omnidirectional laser-quality Bragg mirrors with broad stop bands in the mid-infrared*", 6th International Conference on Mid-Infrared Optoelectronic Materials and Devices, 28.6-1.7.2004, St. Petersburg, Russia.
15. M. Simma, T. Fromherz, G. Springholz and G. Bauer (Poster), "*Mid-infrared photocurrent spectroscopy on self-organized PbSe quantum dots*", 6th International Conference on Mid-Infrared Optoelectronic Materials and Devices, 28.6-1.7.2004, St. Petersburg, Russia.
16. G. Springholz, D. Lugovy, R. T. Lechner, A. Raab, L. Abtin, V. Holy, G. Bauer (Talk), "*Size effects and shape transitions in self-organized ordering of PbSe/PbEuTe quantum dot superlattices*", 14th International Conference on Crystal Growth and 12th International Conference on Vapor Growth and Epitaxy, 9.-13.8.2004, Grenoble, France.

17. R Kirchschlager, W. Heiss, R. T. Lechner, G. Bauer, G. Springholz, "*Hysteresis loops of the energy band gap and effective g-factor up to 18000 for metamagnetic EuSe epilayers*", 27th International Conference on the Physics of Semiconductors, 26.7.-31.7.2004, Flagstaff, USA.
18. G. Springholz, T. Schwarzl, E. Baumgartner, W. Heiss (Talk), "Molecular beam epitaxy of wide/narrow band gap semiconductors for mid-infrared broad-band Bragg mirrors and high finesse microcavities", 13th International Conference on Molecular Beam Epitaxy, 22.-27.8.2004, Edinburgh, UK.
19. R. T. Lechner, G. Springholz, T. U. Schülli, L. Abtin, H. Krenn, and G. Bauer (Talk), "*In and ex situ characterisation of magnetic EuSe/PbSe$_{1-x}$Te$_x$ superlattices grown by molecular beam epitaxy*", 13th International Conference on Molecular Beam Epitaxy, 22.-27.8.2004, Edinburgh, UK.
20. D. Lugovyy, G. Springholz, P. Simiceck and V. Holy (Poster), "*Monte Carlo simulation and growth of vertical and lateral ordering in self-assembled PbSe quantum dot superlattices*", 13th International Conference on Molecular Beam Epitaxy, 22.-27.8.2004, Edinburgh, UK.
21. T. Schwarzl, J. Fürst, M. Böberl, H. Pascher, G. Springholz, W. Heiss (Talk), *"MBE growth of vertical-emitting microcavity lasers for the 6 - 8 micron spectral range operating in continuous-wave mode",* 13th International Conference on Molecular Beam Epitaxy, 22.-27.8.2004, Edinburgh, UK.
22. L. Abtin, A. Raab, G. Springholz and V. Holy (Talk), *"Surface evolution and shape transitions of self-assembled PbSe quantum dots during overgrowth",* 13th International Conference on Molecular Beam Epitaxy, 22.-27.8.2004, Edinburgh, UK.
23. G. Springholz and K. Wiesauer (Talk), "Quasi-Periodic Nanopatterning of Strain-Relaxed Heteroepitaxial Layers by Misfit Dislocation Arrays as Demonstrated for PbTe on PbSe (001)", Fall Meeting of the Materials Research Society, 29.11.-3.12.2004, Boston, USA.
24. G. Springholz, T. Schwarzl, J. Fürst, M. Böberl, H. Pascher, W. Heiss (Talk), *"Vertical-Cavity Surface-Emitting Lasers with cw-Emission at Long Wavelengths of 6-8 Microns",* Fall Meeting of the Materials Research Society, 29.11.-3.12.2004, Boston, USA.
25. S. Tsujino, A. Borak, C. V. Falub, E. Müller, L. Diehl, M. Scheinert, H. Sigg, D. Grützmacher, T Fromherz, U. Gennser, Y. Campidelli, O. Kermarrec, D. Bensahel, J. Faist, *"Quantum transport of s quasi-two-dimensional hole gas in strain compensated SiGe wells and superlattices"*, 13th International Winterschool on New Developments in Solid State Physics, Low-Dimensional Systems, Mauterndorf, Austria, 15-20 Feb. 2004.
26. D. Grützmacher, C. Falub, S. Tsujino, A. Borak, M. Scheinert, E. Müller, H. Sigg, M. Meduna, T. Fromherz, G. Bauer, *"Achievements and challenges on the road to a SiGe quantum cascade laser"*, 12th International Symposium Nanostructures: Physics and Technology St Petersburg, Russia, 21–25 June 2004
27. T. Fromherz, M. Grydlik, P. Rauter, M. Meduna, C. Falub, L. Diehl, G Dehlinger, H. Sigg,, D. Grützmacher, H. Schneider, G. Bauer, *"Si/SiGe QWIPs for voltage-tuneable, resonator-enhanced, two-colour detection in the MIR"*, 3rd International Workshop on Quantum Well Infrared Photodetectors (QWIP 2004), Kananaskis, Alberta, Canada, August 7-13, 2004.
28. A. Andreev, F. Quochi, H. Hope, H. Sitter, S. Sariciftci, A. Mura, G. Bongiovanni, *Blue emitting self-assembled nanocrystals of para-sexiphenyl grown by Hot Wall*

Epitaxy, 5th Int.Conf. on Low Dimensional Structures and Devices, 12.-17.12. 2004, Cancun – Mexico

29. M. Oehzelt, T. Haber, A. Andreev, H. Sitter, D. Smilgies, J. Kecks, R. Resel, *Epitaxial growth of sexiphenyl on KCl(100)-performance of reciprocal space maps,* 7th Biennial Conference on High-Resolution X-ray Diffraction, 07.-10.09.2004, Prag, Czech Republic
30. R. Resel, O. Lengyel, T. Haber, M. Oehzelt, S. Mülleger, A. Winkler, B. Winter, G. Koller, M. Ramsey, G. Hlawacek, C. Teichert, A. Andreev, H. Sitter, *Formation and Structure of oligo-phenyl thin films for organic opto-electronics,* Workshop on Compound Semiconductor Devices and Integrated Circuits, 17.-19.05.2004, Smolenice, Slovakia
31. T. Haber, M. Oehzelt, D. Smilgies, W. Grogger, B. Schaffer, H. Sitter, A. Andreev, R. Resel, *Epitaxial Growth of sexiphenyl Thin Films on KCl(100),* International Conference on Surface Science, 28.06.-02.07.2004, Venice, Italy
32. R. Resel, M. Ramsey, G. Koller, C. Teichert, A. Andreev, H. Sitter, *Foramtion of Sexiphenyl Nanofibers by Epitaxial Growth on Dielectric Substrates,* 324th WE-Heraeus Seminar, Exploring the nanostructures of Soft Materials with X-rays, 10-12.05.2004, Bad Honnef, Germany
33. F. Quochi, A. Andreev, F. Cordella, R. Orru, A. Mura, G. Bongiovanni, H. Hope, H. Sitter, S. Sariciftci, *Low-threshold blue lasering in nanocrystals of para-sexiphenyl grown by Hot-Wall Epitaxy,* International Conference on Synthetic Metals, 28.06.-2.07.2004, Wollongang, Australia
34. K. Schmidegg, A. Kharchenko, A. Bonanni, K. Lischka, H. Sitter, J. Bethke, *In-Situ determination of growth-rate and concentration of ternary MOCVD nitrides via multiple wave-length ellipsometry,* 12th International Conference on Metal Organic Vapor Phase Epitaxy, 30.05.-04.06.2004, Lahaina, Maui, Hawaii, USA
35. A. Bonanni, K. Schmidegg, A. Montaigne-Ramil, A. Kharchenko, J. Bethke, K. Lischka, H. Sitter, *On- line growth control of MOCVD deposited GaN and related ternary compounds via spectroscopic ellipsometry and x-ray diffraction,* Conference on Photo-Responsive Materials, 25.-29.02.2004, Kariega, South Africa
36. A. Andreev, F. Quochi, H. Hope, H. Sitter, S. Sariciftci, A.Mura, G. Bongiovanni, *Blue emitting self-assembled nanocrystals of para-sexiphenyl grown by Hot Wall Epitaxy,* Conference on Photo-Responsive Materials, 25.-29.02.2004, Kariega, South Africa
37. A. Andreev, H. Hope, T. Haber, D. Smilgies, H. Sitter, S. Sariciftci, R. Resel, *Highly Oriented Organic Semiconductor Thin Films Grown by Hot Wall Epitaxy on Different Substrates,* 5th International Conference "Electronic Processes in Organic Materials" (ICEPOM-5), 24.-29.05.2004, Kiew, Ukraine
38. A. Andreev, F. Quochi, T. Haber, H. Hope, D. Smilgies, H. Sitter, S. Sariciftci, R. Resel, A. Mura, G. Bongiovanni, *Morphology and growth kinetics of organic thin films deposited by Hot Wall Epitaxy on KCl and NaCl substrates,* 14th International Conference on Crystal Growth, 09.-13.08.2004, Grenoble, France
39. A. Andreev, F. Quochi, H. Hope, H. Sitter, S. Sariciftci, A. Mura, G. Bongiovanni, *Blue emitting self-assembled nanocrystals of para-sexiphenyl grown by Hot Wall Epitaxy,* 5th Int.Conf. on Low Dimensional Structures and Devices, 12.-17.12. 2004, Cancun – Mexico
40. M. Oehzelt, T. Haber, A. Andreev, H. Sitter, D. Smilgies, J. Kecks, R. Resel, *Epitaxial growth of sexiphenyl on KCl(100)-performance of reciprocal space maps,*

7th Biennial Conference on High-Resolution X-ray Diffraction, 07.-10.09.2004, Prag, Czech Republic

41. R. Resel, O. Lengyel, T. Haber, M. Oehzelt, S. Mülleger, A. Winkler, B. Winter, G. Koller, M. Ramsey, G. Hlawacek, C. Teichert, A. Andreev, H. Sitter, *Formation and Structure of oligo-phenyl thin films for organic opto-electronics,* Workshop on Compound Semiconductor Devices and Integrated Circuits, 17.-19.05.2004, Smolenice, Slovakia
42. T. Haber, M. Oehzelt, D. Smilgies, W. Grogger, B. Schaffer, H. Sitter, A. Andreev, R. Resel, *Epitaxial Growth of sexiphenyl Thin Films on KCl(100),* International Conference on Surface Science, 28.06.-02.07.2004, Venice, Italy
43. R. Resel, M. Ramsey, G. Koller, C. Teichert, A. Andreev, H. Sitter, *Foramtion of Sexiphenyl Nanofibers by Epitaxial Growth on Dielectric Substrates,* 324th WE-Heraeus Seminar, Exploring the nanostructures of Soft Materials with X-rays, 10-12.05.2004, Bad Honnef, Germany
44. F. Quochi, A. Andreev, F. Cordella, R. Orru, A. Mura, G. Bongiovanni, H. Hope, H. Sitter, S.Sariciftci, *Low-threshold blue lasering in nanocrystals of para-sexiphenyl grown by Hot-Wall Epitaxy,* International Conference on Synthetic Metals, 28.06.-2.07.2004, Wollongang, Australia
45. K. Schmidegg, A. Kharchenko, A. Bonanni, K. Lischka, H. Sitter, J. Bethke, *In-Situ determination of growth-rate and concentration of ternary MOCVD nitrides via multiple wave-length ellipsometry,* 12th International Conference on Metal Organic Vapor Phase Epitaxy, 30.05.-04.06.2004, Lahaina, Maui, Hawaii, USA
46. A. Bonanni, K. Schmidegg, A. Montaigne-Ramil, A. Kharchenko, J. Bethke, K. Lischka, H. Sitter, *On-line growth control of MOCVD deposited GaN and related ternary compounds via spectroscopic ellipsometry and x-ray diffraction,* Conference on Photo-Responsive Materials, 25.-29.02.2004, Kariega, South Africa
47. A. Andreev, F. Quochi, H. Hope, H. Sitter, S. Sariciftci, A. Mura, G. Bongiovanni, *Blue emitting self-assembled nanocrystals of para-sexiphenyl grown by Hot Wall Epitaxy,* Conference on Photo-Responsive Materials, 25.-29.02.2004, Kariega, South Africa
48. A. Andreev, H. Hope, T. Haber, D. Smilgies, H. Sitter, S. Sariciftci, R. Resel, *Highly Oriented Organic Semiconductor Thin Films Grown by Hot Wall Epitaxy on Different Substrates,* 5th International Conference “Electronic Processes in Organic Materials” (ICEPOM-5), 24.-29.05.2004, Kiew, Ukraine
49. A. Andreev, F. Quochi, T. Haber, H. Hope, D. Smilgies, H. Sitter, S. Sariciftci, R. Resel, A. Mura, G. Bongiovanni, *Morphology and growth kinetics of organic thin films deposited by Hot Wall Epitaxy on KCl and NaCl substrates,* 14th International Conference on Crystal Growth, 09.-13.08.2004, Grenoble, France
50. H. Malissa, W. Jantsch, M. Muehlberger, F. Schaeffler, Z. Wilamowski,, *Bychkov-Rasba Effect in low dimensional SiGe structures,* 26.-30.07.2004, 27th Int. Conference on the Physics of Semiconductors, Flagstaff Arizona, USA
51. Z. Wilamowski, H. Malissa, W. Jantsch, *Cyclotron resonance revisited: the effect of carrier heating,* 26.-30.07.2004, 27th Int. Conference on the Physics of Semiconductors, Flagstaff Arizona, USA
52. H. Przybylinska, R. Buczko, G. Kocher, W. Jantsch, D. As, K. Lischka,, *Photoconductivity study of Mg and C acceptors in cubic GaN,* 26.-30.07.2004, 27th Int. Conference on the Physics of Semiconductors, Flagstaff Arizona, USA
53. H. Przybylinska, G. Kocher, W. Jantsch, D. As, K. Lischka, R. Buczko, *Mg and C acceptors in cubic GaN studied by photothermal ionization spectroscopy,* 28.-

30.09.2004, 54. Jahrestagung der Österreichischen Physikalischen Gesellschaft, Linz, Austria

54. H. Malissa, Z. Wilamowski, W. Jantsch, *Cyclotron resonance in high mobility Si: the effect of carrier heating,* 28.-30.09.2004, 54. Jahrestagung der Österreichischen Physikalischen Gesellschaft, Linz, Austria

55. O. M. Fedorych, Z. Wilamowski, W. Jantsch, J. Sadowski, *Electrically detected magnetic resonance,* 28.05.-04.06.2004, XXXIII International School on the Physics of Semiconducting , Compounds, Jaszowiec, Poland

56. A. Andreev, T. Haber, D. M. Smilgies, L. Valek, R. Resel, H. Hope, H. Sitter, S. Sariciftci, *Mophology and growth kinetics of organic thin films deposited by Hot Wall Epitaxy on different substrates*, poster at the Jahrestaung der ÖPG, 01.06.2004, Linz, Austria

57. A. Bonanni, K. Schmidegg, H. Sitter,, *In-situ multiple wave-length ellipsometry: virtual-interface approximation model for simultaneous determination of growth-rate and composition in MOCVD nitrides,* poster at the 14th International Conference on Crystal Growth, 09.-13.08.2004, Grenoble, France

58. J. Liday, I. Hotovy, H. Sitter, K. Schmidegg, A. Bonanni, P. Vogrincic, *NiO-based contacts for blue emitting diodes,* poster at the International Conference on Inorganic New Materials, September 2004, Antwerp, Belgium

59. A. Andreev, F. Quochi, T. Haber, H. Hope, D. Smilgies, H. Sitter, S. Sariciftci, R. Resel, A. Mura, G. Bongiovanni, *Epitaxial Growth of Blue Emitting Organic Nano-Wires*, poster at the 13th International Conference on Molecular Beam Epitaxy, 22.-27.08.2004, Edingburgh, England

60. A. Bonanni, D. Stifter, K. Hingerl, H. Sitter, K. Schmidegg, *In-situ multipel wavelength ellipsometry for real time process characterization of nitride MOCVD,* 27th International Conference on the Physics of Semiconductors (ICPS27), July 2004, Flagstaff

61. K. Schmidegg, H. Sitter, K. Hingerl, A. Bonanni, *In-Situ optical analysis of low-temperature MOCVD GaN nucleation layer formation via multiple-wavelength ellipsometry,* 12th Intenational Conference on Metal Organic Chemical Vapor Deposition (ICMOVPE12), June 2004, Lahaina (Hawaii)

62. W. Heiss, J. Roither, K. Hingerl, S. Andreeva, *Waveguiding effects in layer by layer deposited films of chemically synthesized CdTe nanocrystals,* E-MRS 2004 Spring Meeting, 24.-28.05.2004, Strasbourg, France

63. J. Roither, W. Heiss, V. Talapin, N. Gaponik, A. Eychmüller,, *Highly directional emission from colloidally synthesized nanocrystals in vertical cavities with small mode spacing,* E-MRS 2004 Spring Meeting, 24.-28.05.2004, Strasbourg, France

64. Veronika Rinnerbauer: European Conference of Optical Communication, 8. 9. 2004, Stockholm, *"Polarization Splitting realized with Photonic Crystals*

65. Javad Zarbakhsh: Bad Honnef, 28. 4. 2004, Workshop on Photonic Crystals, poster presented by *"Arbitrary angle waveguiding applications of two-dimensional curvilinear-lattice photonic crystals"*

66. K. Hingerl, *"Reflectance modulated spectroscopy of cubic semiconductors under stress: a tool for piezo optical characterization"*, A. L. Martinez, L. F. Martinez, R. Balderas Navarro, ICPS, Flaggstaff, Arizona, 2 posters, 30. 7. 2004

67. R. Buczko, G. Kocher-Oberlehner, W. Jantsch, D. As, K. Lischka, *"Photoconductivity study of Mg and C acceptors in cubic GaN"* H. Przybylinska, ICPS, Flaggstaff, Arizona, 2 posters, 30. 7. 2004

Patents

1. K. Hingerl, R. Holly, T. Glinsner, H. Seyringer,
   "Process to produce a light coupling device between a glass fibre and a waveguide of a high refractive index" ("Verfahren zum Herstellen einer Lichtkopplungseinrichtung zwischen einer Glasfaser und einem Lichtwellenleiter höheren Brechungsindexes"),
   "Prägeverfahren", 33 049 A Österreich; 33 049 2004 3C 1550/2004.
2. K. Hingerl,
   "*Process to produce a light coupling device between a glass fibre and a waveguide of a high refractive index*" ("*Verfahren zum Herstellen einer Lichtkopplungseinrichtung zwischen einer Glasfaser und einem Lichtwellenleiter höheren Brechungsindexes*",
   "Einkopplung Glasfaser", 33 215 A Österreich; 33 215 2004 3C 1551/2004.
3. K Hingerl J Zarbakhsh,
   "*Photonic crystal structure*" ("*Photonischer Kristallstruktur*"),
   Photonic crystal structure P911 DE Deutschland 18064.3-P911 2004 10 2004 054 505.7.

Diploma Theses

Finished in 2004:

1. Eugen Wintersberger
   "Röntgenbeugung und –reflexion an Si/SiGe/GaAs Hetero- und Nanostrukturen"
2. Mathias Simma
   "*Photoleitungsuntersuchungen an Quantenpunkten*"
3. Stefan Janecek
   "*Simulation of the magnetic order of few-monolayer-(111)-EuTe in oblique magnetic fields*"
4. Benjamin Lindner
   "*Metall-Isolator-Übergang in zweidimensionalen Siliziumstrukturen*"

Current works:

1. Martyna Grydlik
   "Si/SiGe resonant cavity enhanced, tunable mid-infrared quantum well detectors."
2. Thomas Hörmann
   "*Modellrechnungen und Auswertungen zum Metall-Isolator-Übergang in zwei-dimensionalen Halbleiterstrukturen*"
3. Bernhard Mandl
   "*Au-free growth and characterization of semiconductor nanostructures*"
4. Anzengruber Johannes
   "*Optische Resonatoren für die Molekülspektroskopie*"
5. Isfahani Farnaz
   "*Fabrication of stamp for nanoimprint lithography using reactive ion etching – Study and optimization of the process parameters*"

6. Kirchschlager Raimund
   "*Magnetooptische Eigenschaften von Eu-Chalcogeniden*"
7. Pichler Stefan
   "*Nanokristall basierende elektrooptische Bauteile*"
8. Matthias Wegscheider
   "*Growth and optical characterization of nitride-based diluted magnetic semiconductors*"

Doctor's Theses

Finished in 2004:

1. Mag. Rainer T. Lechner
   "Herstellung und Charakterisierung von EuSe- Nanostrukturen"

Current works:

1. M.Sc. Laurel Abtin
   "STM investigation on self-assembled IV-VI semiconductor nanostructures"
2. Dipl.Ing. Thomas Berer
   "*Electronic and spin properties of Si/SiGe heterostructures*"
3. Dipl.Ing. Daniel Gruber
   "*Si/SiGe Heterostructure Devices for Spintronic Applications*"
4. Dipl. Phys. Anke Hesse
   "*Strukturelle Untersuchungen an Halbleiternanostrukturen*"
5. Dipl.Ing. Herbert Lichtenberger
   "*Kinetic and strain-induced self-organization of SiGe heterostructures*"
6. M.Sc. Dmytro Lugovyy
   "*Investigation of vertical and lateral ordering in self-organized PbSe quantum dot superlattices*"
7. Mag. Jiri Novak
   "*Untersuchung der strukturellen Eigenschaften von Quantenpunkten*"
8. Dipl.Ing. Dietmar Pachinger
   "Fabrication of SiGe Nanostructures for infrared Devices"
9. Dipl.Ing. Georg Pillwein
   "*Elektrische Untersuchungen von Quanteneffekten an Nanostrukturen*"
10. Dipl.Ing. Patrick Rauter
    "*SiGe nanostructures for next generation infrared detectors*"
11. M.Sc. Aaliya Rehman Khan
    "*Growth and structural characterisation of Si/SiGe hetero- and nanostructures*"
12. Dipl.Ing. Mathias Simma
    "Photoleitungsuntersuchungen an Quantenpunkten"
13. Dipl.Ing. Eugen Wintersberger
    "Röntgenbeugung und –reflexion an Si/SiGe/GaAs Hetero- und Nanostrukturen "
14. Dipl.Ing. Joachim Achleitner
    "*Simulation magnetooptischer Effekte in EuTe*"
15. Eugen Baumgartner
    "*Optoelectronic devices based on nanocrystals*"

16. Dipl.Ing. Michaela Böberl
    "*Electro-optical IV-VI devices for the mid-infrared*"
17. Dipl.Ing. Thomas Glinsner
    "*Herstellung von 3D photonischen Kristallen mittels nanoimprint Lithographie*"
18. M.Sc. Roman Holly
    "Fabrication and characterization of fiber to chip light couplers"
19. Mag. Erich Kaufmann
    "*Lateral emitting lead-salt microlasers*"
20. Maksym Kovalenko
    "*Synthesis and characterization of nanocrystals for the mid infrared*"
21. Dipl.Ing. Hans Malissa
    "*Spin properties of low-dimensional systems*"
22. Dipl.Ing. Jürgen Roither
    "*Light emitting nanodevices: Novel concepts and their realization*"
23. Dipl.Ing. Klaus Schmidegg
    "Growth and optical characterisation of GaN and its ternary compounds"
24. Dipl.Ing. Clemens Simbrunner
    "*MOCVD growth and In-situ characterization of ferromagnetic nitride semiconductors*"
25. Dipl.Ing Walter Söllinger
    "*Monte Carlo simulations of spin-related phenomena in magnetic semiconductor structures*"
26. M.Sc. Javad Zarbakhsh
    "*Designing photonic devices in silicon*"
27. Dipl.Ing. Gernot G. Fattinger
    "*Acoustic Wave Phenomena in Multilayered Thin Film Layer Stacks*"

Cooperations

1. Academy of Sciences, Bratislava, Slovakia
2. Aixtron, Aachen, Deutschland
3. Akademie der Wissenschaften, Warschau, Polen
4. AMS Unterpremstätten, Österreich
5. Balzers (Unaxis), Trübach, Schweiz
6. Bosch (Stefan Holl), Linz
7. CENG Grenoble, France
8. CNRS-CRMC2-Marseille, France
9. Daimler Benz Reserach Laboratories, Dr. Presting, Dr. König, Ulm
10. DESY, Hasylab, Hamburg, Deutschland
11. E+E Electronic GmbH, Engerwitzdorf, Österreich
12. ELETTRA, Triest, Italy
13. ESRF Grenoble, France
14. ETH, Zürich, Swiss

15. FORTH, Crete, Greece
16. Politecnico Milano
17. Fraunhofer-Institut (IAF) Freiburg (Chiptechnologie), Deutschland
18. Fraunhofer-Institut für Physikalische Meßtechnik (Freiburg, Deutschland)
19. Heriot Watt University, Edinburgh, Scotland
20. High Magnetic Field Lab., Grenoble, France
21. InfraTec GmbH, Infrarotsensorik und Messtechnik, Dresden, Germany
22. INFINEON Villach, Österreich
23. INSA, Lyon, France
24. Inst. f. Experimentalphysik I, Universität Bayreuth, Deutschland
25. Institut für Festkörperelektronik, TU Wien
26. Institute for Physics of Microstructures RAS, 603600 Nizhny Novgorod, Russland
27. Institute of Physics, Polish Academy of Sciences, Warschau, POLEN
28. Ioffe Physico-Technical Institute RAS, 194021 St.Petersburg, Russland
29. Lebedev Institut, Russian Academy of Sciences, Moskau, Russland
30. Masaryk University, Brno, Czech Republic
31. Charles University, Prague, Czech Republic
32. Max-Born Institut für Nichtlineare Optik, Berlin, Germany
33. Max-Planck Institut für Festkörperpforschung, Stuttgart
34. MIT, Cambridge, MA, USA
35. Nanoelectronics Research Center, University of Glasgow, Scotland
36. NIST, Gaithersburg, MD, USA
37. North Carolina State University, NC, USA
38. Ørsted Institut, Kopenhagen, Dänemark
39. Paul Scherrer Institut, Villigen, Schweiz
40. Philips Analytics, Almelo, Niederlande
41. Physics Department, Cornell University
42. Profactor, Steyr, Upper Austria
43. Purdue University, Lafayette, IN, USA
44. Sektion Physik, Ludwig-Maximilians Universität München
45. Sentech, Berlin
46. Siemens AG, Corporate Technology, Materials & Manufacturing, Innovative Electronics, Erlangen, Germany
47. Siemens München, Zentrale Technik, Bereich Halbleiter
48. ST Microelectronics, Crolles, Grenoble
49. TASC Triest, Italy
50. Teraview Limited, Cambridge, UK, and Thales, Orsay, France
51. Thomson, Paris, France

52. Tohoku University, Sendai, Japan
53. TU Berlin, Institut für Festkörperphysik, Deutschland
54. TU-München (Mikrowellentechnik), Deutschland
55. Unipress, High Pressure Research Center, Polish Academy of Sciences, Warschau
56. Universita Padova, Italia
57. Universität Bayreuth, Experimentalphysik I, Bayreuth, Germany
58. Universität Bremen, Deutschland
59. Universität Graz, Institut für Experimentalphysik
60. Universität Paderborn, Deutschland
61. Universität Potsdam, Deutschland
62. Universität Würzburg, Deutschland
63. Université de Montpellier, France
64. University of Erlangen-Nürnberg, D-91058 Erlangen, Deutschland
65. University of Lund, Solid State Physics, Lund, Sweden
66. University of Maryland, MD, USA
67. University of Southampton, England
68. University of Warwick, Coventry, England
69. Van der Waals-Zeeman Institute, University of Amsterdam, NL
70. VOEST ALPINE, Dr.Angerer, Linz
71. Walter Schottky Institut, TU München, Deutschland
72. W.L. Gor & Associates GmbH, Putzbrunn, Germany

Epitaxial Bragg Mirrors with Broad Omnidirectional Stop Band in the Mid-Infrared

E. Baumgartner, T. Schwarzl, G. Springholz, W. Heiss

Institut für Halbleiter und Festkörperphysik, Universität Linz, Altenbergerstraße 69, 4040 Linz, Austria

We present laser-quality low-loss Bragg mirrors exhibiting a broad omnidirectional stop band in the mid-infrared around 6.9 µm. Due to the high refractive index contrast of 80%, Bragg mirrors made from only three layer pairs of PbTe and EuTe are demonstrated to achieve reflectances higher than 99 % for angles of incidence up to 40° and higher than 98% for angles of incidence up to 70°. The relative omnidirectional stop band width is 50%.

Introduction

Similar to metallic mirrors, omnidirectional Bragg reflectors offer high reflectivity independent of the angle of incidence, but combined with the low-loss behavior and transparency of dielectric multilayer stacks. Such devices are advantageous for applications in laser resonators where light is incident from oblique directions, as in low-loss ring resonators or in two-dimensional planar-mirror resonators. They enable also the realization of highly-efficient corner-cube retro reflectors. Bragg mirrors exhibiting omnidirectional stop bands in the mid-infrared were demonstrated both theoretically and experimentally with relative stop band widths up to 45 % [1].

In our work, a high-finesse microcavity formed by two omnidirectional PbTe/EuTe Bragg mirrors for the mid-infrared was used for detailed optical analysis of the mirror properties. The appearance of a cavity resonance facilitates the accurate determination of the mirror reflectance from the quality factor of the resonator [2]. Similar mirrors have successfully been used for cw operating mid-infrared vertical-cavity surface-emitting lasers with divergence angles of 1° [3].

Theory

In modeling the transmittance behavior of a half wavelength microcavity enclosed between Bragg mirrors the characteristic matrix description is preferred [4], because it provides insight into the energetic position and extent of the photonic band gap.

An omnidirectional Bragg mirror will remain reflective throughout all angles of incidence, whenever the refractive indices of the environment and the mirror dielectrics are such that light impinging at grazing incidence will be refracted strong enough to avoid the Brewster angle on all subsequent refractions (Fig. 1 (d)). For a given microcavity structure (Fig. 1 (b)), the simulated angular dependence of the transmittance spectra (Fig. 1 (e), (f)) displays the stopband of almost vanishing transmission, lined by the Fabry-Perot interference fringes of the microcavity structure as a whole. Figs. 1 (c), (d) show the calculated photonic band structure of the Bragg mirrors forming the cavity.

The finesse F_m of a Fabry-Perot resonator of order m can be expressed as (Fig. 1 (a); R is the geometrical mean of the reflectances of the enclosing mirrors):

$$\frac{1}{m}\frac{k_0}{FWHM(k_0)} = F_m \approx \pi\frac{\sqrt{R}}{1-R}$$

Therefore, reflectances that are derived from the resonance line width FWHM (k_0) will always provide a worst-case estimate for the reflectance of one mirror.

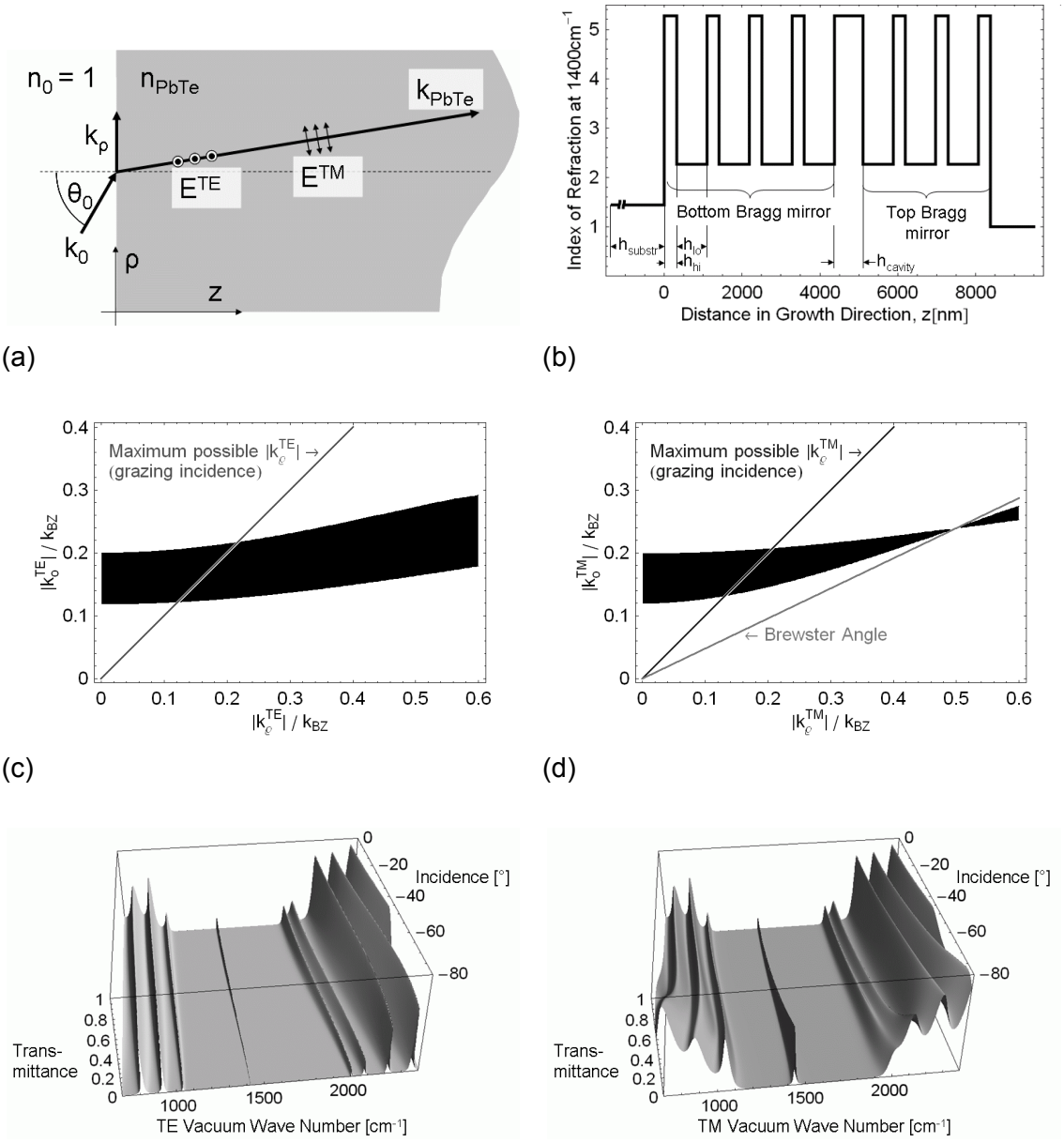

Fig. 1: (a) Terminology and coordinate system used; (b) target microcavity structure by index of refraction of its components; (c) and (d): Calculated angular dependence of the stopband width (black) for one of the mirrors as described in Fig. 1(b). By expressing the angle of incidence in terms of the in-plane wave vector component kρ (Fig. 1(a)) the angle dependence is transformed into a dispersion relation $\omega(k_\rho) = c_0 k_0(k_\rho)$. $k_{BZ} \equiv 2\pi/(h_{lo}+h_{hi})$. The region below the light line (grazing incidence) corresponds to unphysical system states. (e), (f): Angular dependence of calculated transmittance spectra for the model structure (b).

Experimental

Sample Preparation

On a ‹111› BaF_2 substrate the half wave cavity structure targeted at a wavelength of 6.9 µm was grown by molecular beam epitaxy. As indicated in Fig. 1 (b), the overall structure consisted of four PbTe/EuTe mirror layer pairs of width h_{hi} = 317 nm and h_{lo} = 777 nm respectively, a PbTe cavity layer of width h_{cavity} = 732 nm and three top mirror layer pairs. With the special choice of materials, even at grazing incidence all angles of refraction within the mirror structure will remain smaller than the Brewster angle for TM polarized light (Fig. 1 (d)).

Measurements and Results

The angular dependence of the transmittance spectrum was determined by Fourier transform infrared (FTIR) spectroscopy. Probing the sample through a 2 mm aperture made a compromise over the need for a large aperture to proceed to high angles of incidence and the desire to measure the true resonance line width by avoiding the influence of lateral sample inhomogeneities. From the Lorentzian shaped resonance of the 0° spectrum through a pinhole aperture and through the 2 mm aperture an apparatus function was calculated, which afterwards was used to deconvolve the resonance line shapes of the angle scan with the 2 mm aperture (see insert in Fig. 2 (b)).

In Fig. 2 (a) the angular dependence of the stop band edges (triangles) and the resonance position (squares) are plotted. Theoretical predictions made by matrix methods (lines) are evidently in good agreement to the experimental findings. At 3% transmittance level a broad omnidirectional stopband of 727 cm^{-1} width around a center frequency of 1440 cm^{-1} could be found. This corresponds to a relative omnidirectional stopband width of 50%.

In Fig. 2(b) the angular dependence of the halfwidth of the resonance linewidth is plotted for TE, TM polarization. Taking into account the penetration of the light into the mirrors, an effective cavity finesse (Fig. 2 (c)) of well over 100 for angles of incidence up to 70° can be deduced from this. The lower limit mirror reflectance data in Fig. 2 (d) clearly show reflectances higher than 99% for angles of incidence up to 40° and higher than 98% for angles of incidence up to 70°.

Conclusion

By means of an epitaxially fabricated half-wave microcavity for the mid-infrared formed by Bragg mirror layers made from PbTe and EuTe, we have experimentally and theoretically demonstrated the omnidirectionality of these Bragg mirrors for angles of incidence up to 70°. Around 6.9 µm, we have achieved a relative stopband width of 50% and have demonstrated effective reflectances higher than 99% for angles up to 40° and higher than 98% for angles of incidence up to 70°, indicating the suitability for laser applications.

Acknowledgements

This work was supported by the Austrian Science Fund FWF-P15583, Y179.

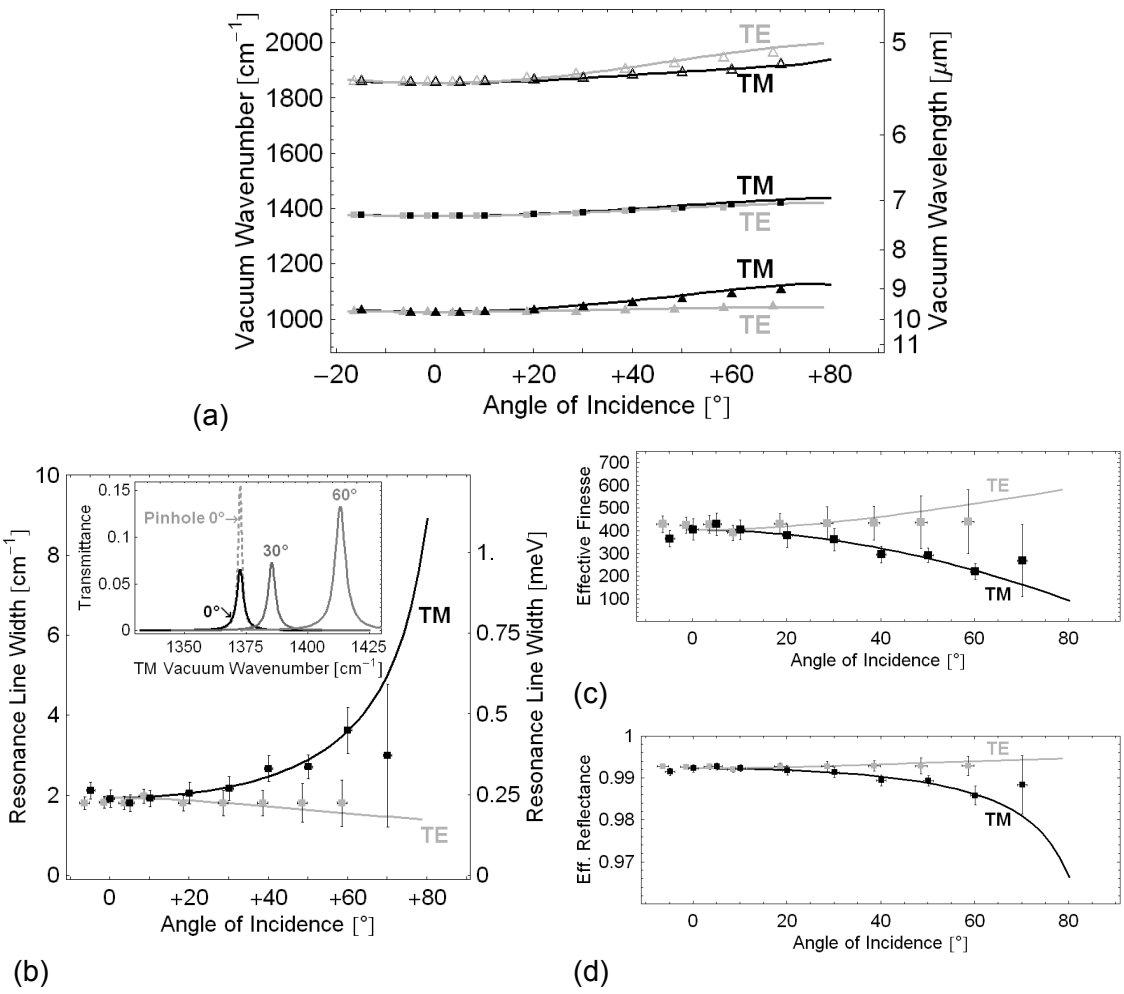

Fig. 2: (a) Angular dependence of Bragg mirror stopband edge (triangles) and cavity resonance (squares) position, compared to model prediction (lines). (b) Experimentally determined TE, TM resonance line widths. Insert: Angle scan TM resonance line shapes compared to that measured through a pinhole aperture (dashed line). (c) Effective finesse of the microcavity, as derived from the effective order of the cavity resonance and its line width. (d) Angular dependence of the lower limit of the effective Bragg mirror reflectance, as deduced from (c).

References

[1] Y. Fink, J. N. Winn, S. Fan, C. Chen, J. Michel, J. D. Joannopoulos, E. L.Thomas: “A Dielectric Omnidirectional Reflector”, Science 282, 1998, pp. 1679-1682

[2] T. Schwarzl, W. Heiss, G. Springholz: “Ultra-high-finesse IV-VI microcavities for the midinfrared”, Appl. Phys. Lett. 75 (9), 1999, pp. 1246-1248

[3] T.Schwarzl, G.Springholz, M.Böberl, E.Kaufmann, J.Roither, W.Heiss, J.Fürst, H.Pascher: “Emission properties of 6.7 µm continuous-wave PbSe-based vertical-emitting microcavity lasers operating up to 100 K”, Appl. Phys. Lett. 86, 2005, pp. 31102

[4] A. D. Rakic, M. L. Majewski in H. Li, K. Iga (Eds.): “Vertical-Cavity Surface-Emitting Laser Devices”, Springer-Verlag, Berlin 2003, pp. 259 – 301

Electronic and Magnetic Properties of GaN:Fe

A. Bonanni [1], H. Przybylinska [1,2], A. Wolos [1], C. Simbrunner [1], H. Sitter [1], W. Jantsch [1], M. Kiecana [2], M. Sawicki [2], T. Dietl [2], P. Granitzer [3], K. Rumpf [3], and H. Krenn [3]

[1] Institut für Halbleiter- und Festkörperphysik, Johannes Kepler Universität, Linz, Austria

[2] Institute of Physics, Polish Academy of Sciences, Warsaw, Poland

[3] Karl Franzens Universität, Graz, Austria

Here we report on metal-organic chemical vapor deposition growth of GaN:Fe and its characterization by means of high-resolution X-ray diffraction, secondary ion mass spectroscopy, photoluminescence, electron spin resonance, and magnetization measurements. Both electron spin resonance and photoluminescence demonstrate the existence of Fe in the isolated $3d^5$ (Fe^{3+}) state. The magnetization measurements show, apart from Curie paramagnetism due to Fe^{3+}, a temperature independent contribution which we attribute tentatively to van Vleck paramagnetism of Fe in the 2+ state. We conclude that the Fe ions coexist in two charge states in the investigated samples. The fraction of Fe^{3+} ions was found to increase upon additional co-doping with Mg acceptors, both in ESR as well as in magnetization. In the latter one a significant reduction of the temperature independent magnetic moment was simultaneously observed. High field magnetization data yield Fe concentration in the $x \approx 10^{-3}$ range, which compares well with secondary ion mass spectroscopy results.

Introduction

Transition metal doped GaN is one of the predicted candidates for obtaining Zener-type ferromagnetism with T_c > 300K. As a necessary condition, the transition metal ion should be incorporated on isolated (*i.e.* not clustered) substitutional sites and exhibit a high-spin ground state. So far, the Mn dopant in GaN has been investigated thoroughly, as it was expected to act as an acceptor providing besides the S = 5/2 spin also the high hole concentration necessary to mediate the exchange coupling among the Mn ions. More recently it has been shown, however, that unlike Mn in GaAs the 3+/2+ acceptor level of Mn in GaN is deep (>1.7 eV above the valence band edge) and the hole is localized on Mn, leaving it in the $3d^4$ state. Hence, Zener magnetism is not expected for the GaN:Mn system. In this respect the GaN:Fe seems to be more promising, especially with p-type co-doping.

Experimental

Sample Preparation

All samples have been fabricated in an AIXTRON 200RF horizontal tube metal-organic chemical vapor deposition (MOCVD) reactor. The growth of the device quality layers was carried out on c-plane sapphire substrates by using TMGa, NH, Cp Fe, Cp Mg and SiH as precursors and H as carrier gas. The deposition process has been performed according to a well established procedure consisting of substrate nitridation, low temperature (540 °C) GaN nucleation layer growth, annealing of the nucleation layer under

NH leading to re-crystallization and GaN buffer growth (1 µm). On top, iron doped GaN layers (1 µm) were grown at different temperatures (800 – 1050°C) and Cp_2Fe fluxes (50 – 200 scams).

Measurements

Crystal Quality

High-resolution x-ray diffraction measurements were performed routinely on the grown samples. Rocking curves showed a full width at half maximum (FWHM) of the order of 260 up to 320 deg, which is comparable to the state-of-the-art device material. Increasing the iron flux resulted in a broadening of the GaN (0002) reflex.

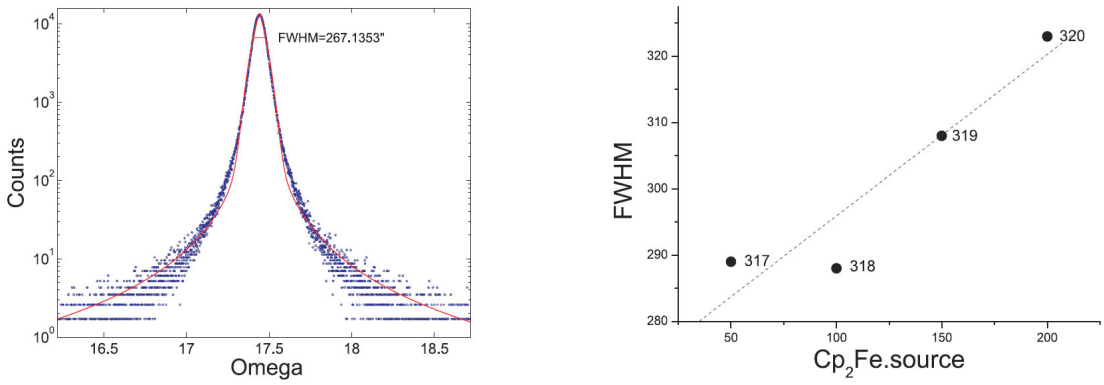

Fig. 1: Rocking curve of the GaN (0002) reflex measured for GaN:Fe epilayers (left panel) and the FWHM as a function of Fe flux (Cp_2Fe) (right panel).

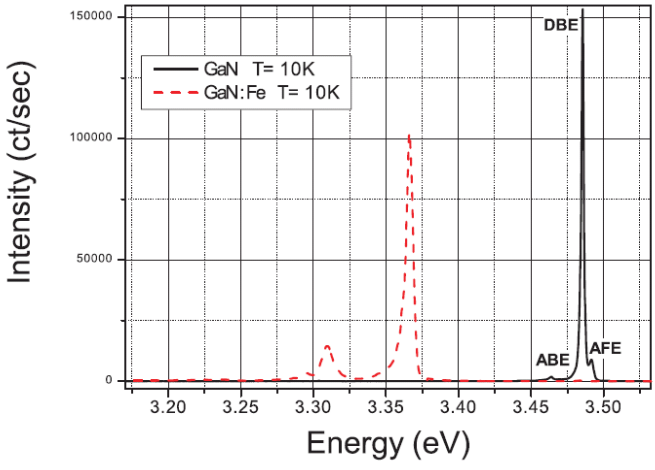

Fig. 2: Photoluminescence spectra of GaN and GaN:Fe samples showing excitonic transitions: AFE, DBE, ABE, as well as unidentified lines due to the Fe dopant.

Photoluminescence Measurements

Figure 2 shows a comparative photoluminescence (PL) study of pure GaN and GaN:Fe. The peaks were identified as an acceptor-free exciton (AFE), a donor bound exciton (DBE) as well as an acceptor bound exciton (ABE). The DBE may be bound to Si or O, which lead to the unintentional n-type behavior of pure GaN, the ABE may be bound to Mg [1]. The peaks assigned to iron have not been identified so far.

Figure 3 shows an infrared PL band at 1.289 eV, that is assigned to a $^4T_1(G)$ - $^6A_1(S)$ crystal field transition of Fe^{3+} (d^5 configuration) [2]. The strong crystal field is typical for GaN due to its small lattice constant and the high electronegativity of nitrogen.

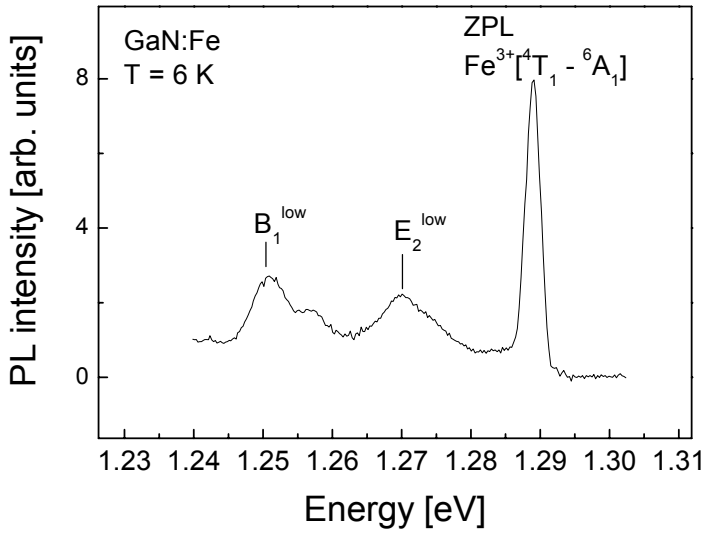

Fig. 3: Photoluminescence spectrum of an intracenter transition $^4T_1(G)$ - $^6A_1(S)$ within $Fe^{3+}(d^5)$ configuration of iron in GaN. The zero-phonon line at 1.289 is accompanied by GaN phonon replicas. E_2^{low} and B_1^{low} GaN phonons are marked.

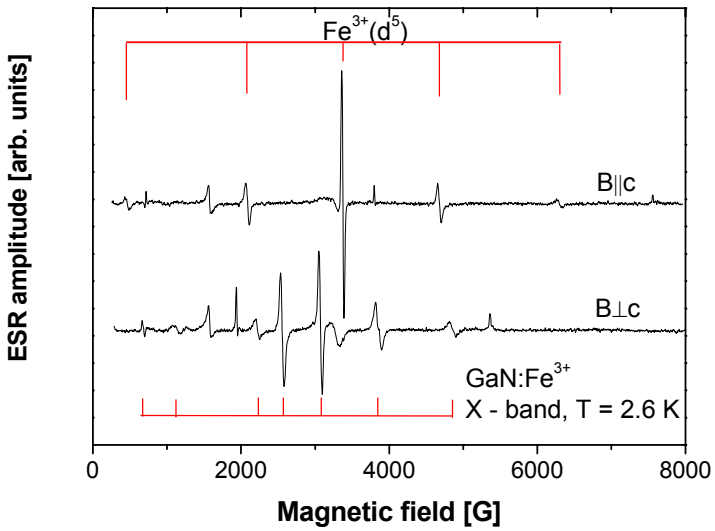

Fig. 4: ESR spectra of $Fe^{3+}(d^5)$ in wurtzite GaN epilayers collected in B || c and B ⊥ c configuration.

Electron Spin Resonance Measurements

Electron spin resonance (ESR) experiments show the presence of $Fe^{3+}(d^5)$ substituting Ga in all studied GaN samples. The examples of ESR spectra collected at the magnetic field parallel or perpendicular to the GaN c-axis are shown in Fig. 4. The amplitude of the ESR signal (proportional to the number of Fe^{3+} centers), increases after co-doping with Mg acceptors. This is the indication of a mixed valence state of the Fe impurity in GaN samples – *i.e.*, the co-existence of the $Fe^{3+}(d^5)$ and most probably the $Fe^{2+}(d^6)$ charge states.

Magnetic Properties

Magnetization measurements of GaN:Fe epilayers were performed by a superconducting quantum interference device magnetometer (SQUID). Figure 5 shows the temperature dependence of the magnetization as obtained from measurements at constant magnetic field on GaN:Fe with different Fe content. In addition to a Curie type of magnetism due to $Fe^{3+}(d^5)$ there is clearly a temperature independent contribution which we attribute to Van-Vleck magnetism, most possibly originating from $Fe^{2+}(d^6)$ configuration of iron. In some of the measured samples an additional ferromagnetic contribution to the magnetization was observed. However, there is no experimental evidence so far that this fraction originates from the homogeneously doped GaFeN layer.

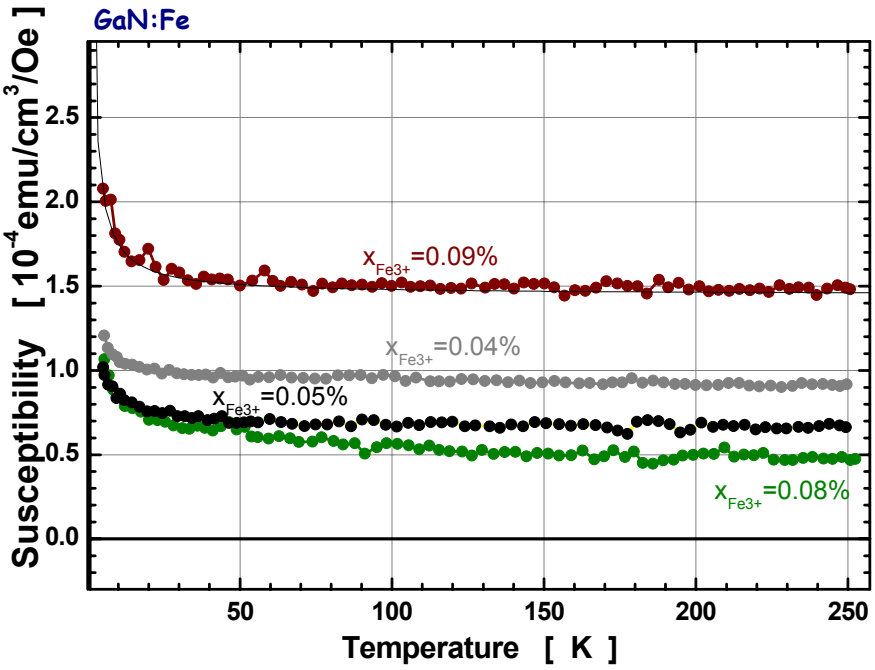

Fig. 5: Susceptibility (M/H) of GaN:Fe as a function of temperature measured at 10000 Oe. The paramagnetic contribution due to Fe^{3+} and the Van Vleck paramagnetism due to Fe^{2+} may be distinguished.

Conclusion

Both ESR and PL demonstrate the existence of Fe in the isolated $3d^5$ (Fe^{3+}) state. The magnetization measurements show, apart from Curie paramagnetism due to Fe^{3+}, a temperature independent contribution which we attribute tentatively to van Vleck para-

magnetism of Fe in the 2+ state. The fraction of Fe^{3+} ions was found to increase upon additional co-doping with Mg acceptors, both in ESR as well as in magnetization. In the latter one a significant reduction of the temperature independent magnetic moment was simultaneously observed. High field SQUID data yield Fe concentration in the $x \cong 10^{-3}$ range, in agreement with SIMS results. A small ferromagnetic contribution to magnetization was also observed, but as far there is no evidence that this fraction originates from homogeneous GaFeN.

References

[1] B. Monemar: “Bound excitons in GaN”, J. Phys: Condens. Matter, Vol. 13, 2001, pp. 7011-7026.

[2] R. Heitz, P. Maxim, L. Eckey, P. Thurian, A. Hoffmann, I. Broser, K. Pressel, and B. K. Meyer: “Excited states of Fe^{3+} in GaN”, Phys. Rev. B, Vol. 55, 1997, pp. 4382–4387.

Self-Organization of Ripples and Islands with SiGe-MBE

G. Chen, H. Lichtenberger, G. Bauer, and F. Schäffler

Institute of Semiconductor and Solid State Physics, Johannes Kepler University, A-4040 Linz, Austria

We explored two methods to obtain laterally ordered Ge/Si quantum dot arrays. For the first we exploit the two independent growth instabilities of the SiGe/Si(001) hetero-system, namely kinetic step bunching and Stranski-Krastanov (SK) island growth, to implement a two-stage growth scheme for the fabrication of long-range ordered SiGe islands. The second approach is to deposit Ge/SiGe onto prepatterned Si substrates, which are prepared via lithography and subsequent reactive ion etching (RIE). It results in perfectly ordered, 2D dot arrays that can be extended into 3D by strain-ordering of a Ge-dot superlattice.

Introduction

The self-organized growth of Ge/Si quantum dot hetero-structures has attracted considerable interest because of its potential for electronic and optoelectronics devices, and its compatibility with the well-explored Si-technology. Recently, laterally ordered Ge/Si quantum dots have also been suggested for the implementation of quantum computing functions, as well as quantum information storage, which both require the separate identification and external addressability of each quantum dot. To obtain laterally ordered Ge/Si quantum dot arrays, we explored two methods. (i) A route which is only based on self-organization to achieve ordering is based on a slightly vicinal Si(001) surface, which is intrinsically unstable against kinetic-step-bunching during homoepitaxial growth. The resulting ripple morphology serves as a one-dimensional template for preferential Ge dot nucleation. (ii) Another approach is to deposit Ge/SiGe onto two-dimensionally prepatterned Si-substrates, which are prepared via lithography and subsequent reactive ion etching (RIE).

Results and Discussion

The Si(001) surface is intrinsically unstable against kinetic step bunching during Si homo- and SiGe heteroepitaxy [1] – [4]. This phenomenon was originally attributed to lattice-mismatch strain [5], but it is now clear that it is of purely kinetic origin. Recent kinetic Monte Carlo simulations in connection with a basic stability analysis provide strong evidence for step bunching being caused by the interplay between the adsorption/desorption kinetics at single atomic height steps and the pronounced diffusion anisotropy on the reconstructed Si(001) surface [6], [7]. The simulations show excellent agreement with STM experiments, and qualitatively reproduce the pronounced temperature dependence of the step bunching phenomena.

The detailed understanding of homoepitaxial step bunching on Si(001) allowed us to tailor the period and height of the bunches by controlling substrate miscut, growth temperature, deposition rate and layer thickness (Fig. 1). This way, homoepitaxial layers with ripple periods of 100 ± 10 nm were prepared on Si(001) substrates with 4° miscut along [110] (Fig. 2).

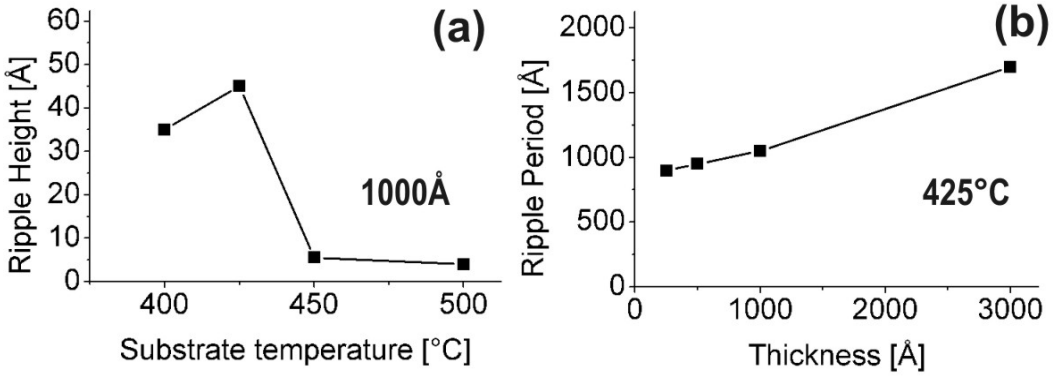

Fig. 1: (a) Dependence of the step-bunching ripple height on substrate temperature for a 1000Å Si-buffer. The maximum of the instability for 4° miscut and a Si-rate of 0.2Å/s occurs around 425°C; (b) Increase of the ripple period with thickness for the optimum Si-buffer temperature at 425°C.

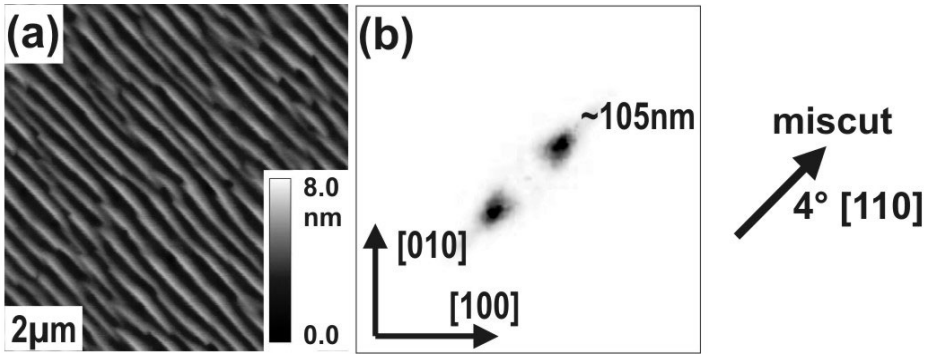

Fig. 2: (a) Kinetic step bunching of a homoepitaxial Si layer on a vicinal Si(001) substrate with 4° miscut along [110]. (b) Fast Fourier Transform showing a spacing for the step bunches of 100 ± 10 nm.

These were then employed as templates for the ordering of SiGe or Ge dots grown in the strain-driven Stranski-Krastanov mode. When the period length of the template complies with the mean spacing of the dots, only one dot row fits into one period (Fig. 3).

We could show that the dots then nucleate at the step bunches, where the energetically favorable {1 0 5} facets of the dots are most easily created by step-meandering [8] – [11]. Considering growth further away from thermal equilibrium, the $Si_{0.55}Ge_{0.45}$ film deposited at 425 °C does not completely disintegrate into individual islands, but reveals how and where island nucleation commences: Upon SiGe deposition the flanks of the step bunches are converted into a zigzag train of adjacent (1 0 5) and (0 1 5) facets.

The originally smooth flanks match quite well the slope of the [5 5 1] intersection line between two adjacent {1 0 5} facets and thus can easily be converted into a {1 0 5} faceted SiGe ridge structure, which is perpendicular to the step-bunches. This is a step-meandering instability induced by strain and the low-energy {1 0 5} facets of SiGe on Si(001). It marks the transition (Fig. 4) from conformal Si/SiGe epilayer growth to strain-driven, ordered 3D-growth which is observed at 625°C for the $Si_{0.55}Ge_{0.45}$ epilayer. This leads to a fair degree of 2D rectangular, face-centered ordering of the SiGe dots (Fig. 3 (d)) in an approach that employs self-organization mechanisms only [9] – [12].

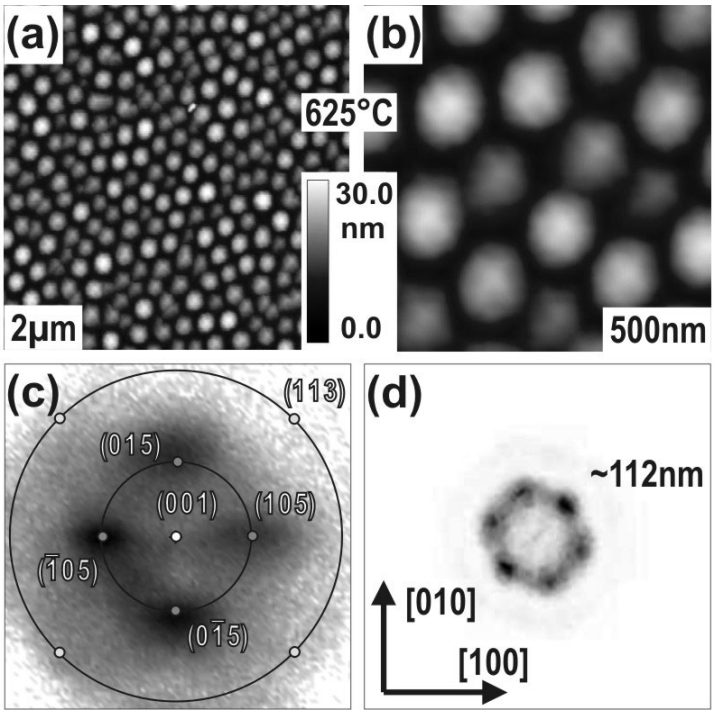

Fig. 3: (a), (b) Self-organized SiGe dots on the Si template from Fig. 2 with the 50 Å $Si_{0.55}Ge_{0.45}$ epilayer deposited @ 625°C; (c) Surface orientation maps derived from Fig. 2 (a). The dots show preferentially {1 0 5} facets (inner circle). (d) Fast Fourier Transform of Fig. 3 (a), revealing rectangular, face-centered ordering of the dots.

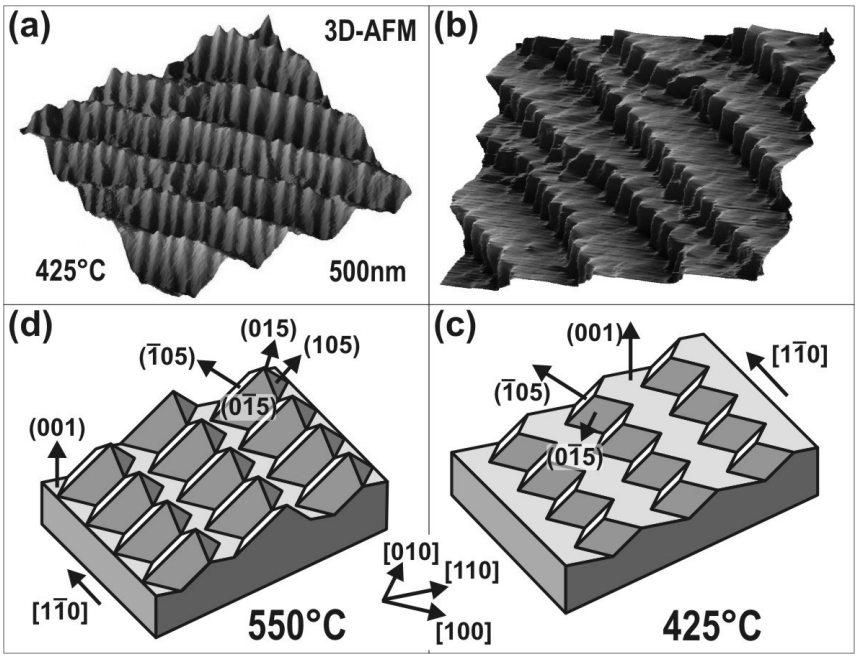

Fig. 4: (a), (b) 3D-AFM representations of a 50 Å $Si_{0.55}Ge_{0.45}$-layer grown @ 425 °C showing a strain-induced {1 0 5} zigzag structure decorating the bunch flanks. The dominant facets for SiGe layers deposited at 425 and 550 °C are depicted schematically in (c) and (d) respectively. At 550 °C also retrograde {1 0 5} facets appear which are necessary to form 3D-islands as depicted in Fig. 3.

To realize perfectly ordered SiGe and Ge dots in 2D and 3D, we used lithographically defined pit arrays. For small enough periods, only one dot per unit cell is created, which nucleates at the lowest point of the pit (Fig. 5).

XTEM images reveal that the nucleation site is defined by the intersection of neighboring facets, which form during Si buffer layer deposition on the nano-structured templates [13]. Thus, by combining nano-structuring with self-organized growth, arbitrarily large areas of perfectly ordered 2D SiGe and Ge dot arrays can be implemented [14] – [16]. On this base we also realized perfect 3D Ge dot arrays by additionally exploiting the strain-driven vertical ordering of Ge dots in a Si/Ge dot super-lattice [17].

Lithographically defined ordering of SiGe and Ge dots fulfills an essential precondition for all but the most elemental applications of self-organized dots, namely their addressability. Vertical stacking of such arrays provides the option to use the topmost dot layer as a self-aligned mask for selective ion implantation.

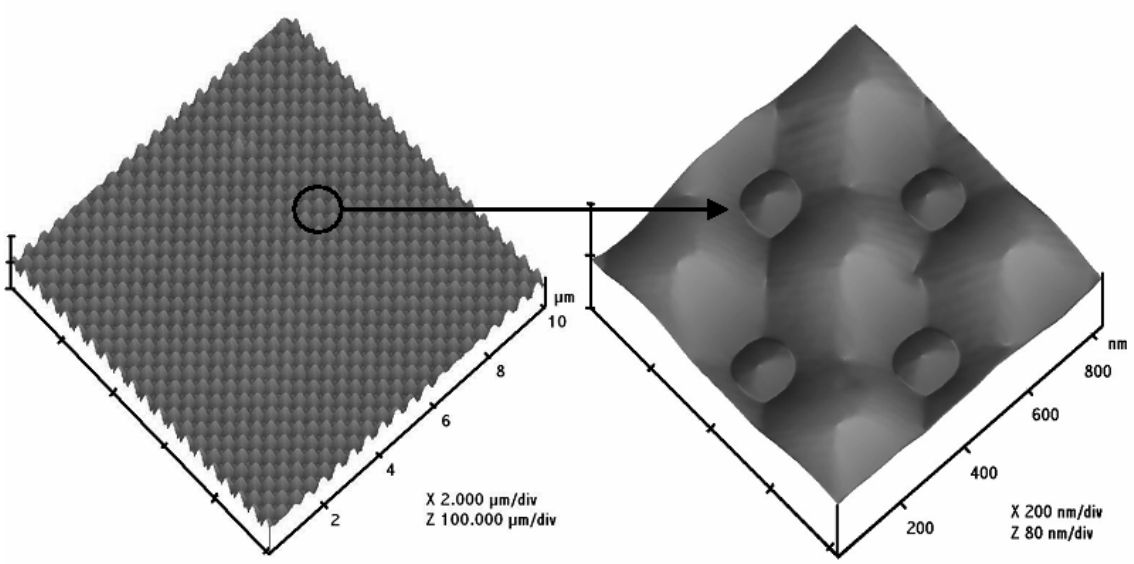

Fig. 5: 3D-AFM representations of a perfect 2D array of self-organized Ge with a periodicity of 350 nm on a Si template defined by lithography and reactive ion etching.

Acknowledgements

This work was supported by FWF P16223-N08 and INTAS 03-51-5015.

References

[1] C. Schelling *et al* , *Phys. Rev. Lett.* **83**, 995 (1999).

[2] C. Schelling *et al* , *Phys. Rev. B* **64**, 041301(R) (2001).

[3] M. Mühlberger *et al* , *Surf. Sci.* **721**, 532 (2003).

[4] A. Ronda *et al* , *Physica E* **23**, 370 (2004).

[5] J. Tersoff *et al* , *Phys. Rev. Lett.* **75**, 2730 (1995).

[6] J. Myslivecek *et al* , *Surf. Sci.* **520**, 193 (2002).

[7] J. Myslivecek *et al* , *cond-mat/* 021231.

[8] H. Lichtenberger *et al* , *J. Cryst. Growth*, in print.

[9] H. Lichtenberger *et al* , *Appl. Phys. Lett.* **86**, 131919 (2005)

[10] C. Teichert et al , Appl. Phys. A: Mater. Sci. Process. **67**, 675 (1998).

[11] J.-H. Zhu et al , Appl. Phys. Lett. **33**, 620 (1998).

[12] C. Teichert et al , Phys. Rep. **365**, 335 (2002).

[13] Z. Zhong et al , J. Appl. Phys. **93**, 6258 (2003).

[14] Z. Zhong et al , Appl. Phys. Lett. **82**, 445 (2003).

[15] Z. Zhong et al , Appl. Phys. Lett. **82**, 4779 (2003).

[16] Z. Zhong et al , Appl. Phys. Lett. **83**, 3695 (2003).

[17] Z. Zhong et al , Physica E **21**, 588 (2004).

High Mobility Si/SiGe Heterostructures for Spintronics Applications

D. Gruber [1], H. Malissa [1], G. Chen [1], D. Pachinger [1], H. Lichtenberger [1], T. Fromherz [1], F. Schäffler [1], G. Bauer [1], W. Jantsch [1], A. M. Tyryshkin [2], and S. A. Lyon [2]

[1] Institute of Semiconductor and Solid State Physics Johannes Kepler University Linz, A-4040 Linz

[2] Department of Electrical Engineering, Princeton University, Princeton, NJ 08544 USA

We investigate techniques for using Silicon-Germanium as material for solid-state quantum computing. Two topics are presented: First, the use of quantum well structures with different Ge content which can be used to shift the g-factor of conduction band electrons via voltages applied to gates above and below the structure. The change in g-factor allows then to put the electrons in and out of resonance in an Electron Spin Resonance experiment. Second, measurement of spin relaxation times of electrons confined in the strain field above Ge dots in a SiGe heterostructure. Photoluminescence (PL) shows indirect transitions from the VB of the Ge dots to the confined Si CB states. A single line is seen in ESR with g ≈ 2.0000 during illumination.

Introduction

The Silicon Germanium (SiGe) material system is a promising candidate for solid-state spintronics applications due to its very long spin relaxation times and its compatibility to standard Si process technology. There are proposals (*e.g.* [1]) for spin transistors in the SiGe material system which could be used for Quantum Computing. For this application very long spin coherence times and the ability to control and to read spin orientation is necessary. We address the topic with two different experiments: One is to demonstrate the ability to control the g-factor of electron spins in SiGe Quantum well structures by applying electrical fields, which can be used for selective spin manipulation. The second is the measurement of spin relaxation times of electrons confined in the strain fields above Ge dots in a SiGe matrix.

g-Factor Tuning in SiGe Quantum Wells

Our samples are grown in a Molecular Beam Epitaxy (MBE) system with electron beam evaporators for Si and Ge. The channels are n-type modulation-doped with Sb. High mobilities of up to μ_e = 250,000 cm^2/Vs have been reached in pure Si channels without back gate. The spin lifetimes are extremely long as well: Spin-echo measurements give T_1 = 2.3 µs and T_2= 3 µs for a magnetic field perpendicular to the 2DEG plane [2]. The high quality of our samples was also shown in recent magneto-transport experiments, where the ν = 1/3, 4/7 and 4/9 composite fermion states in the fractional quantum Hall effect were seen for the first time in the SiGe material system [3].The samples are either pure Si wells or double quantum well (QW) structures with a pure Si well and one with 5% Ge, which are separated by a barrier with 15% Ge content. The second structure is designed in a way that by applying electrical fields relative to the quantum wells one can completely shift the electronic wave function from one well to the other as depicted in a self-consistent band structure simulation in Fig. 1. Hand in hand with the

change in the surrounding material goes a change in g-factor of the electrons [4] and hence a change in resonance frequency in an Electron Spin Resonance (ESR) experiment. Spin manipulation via pulsed ESR techniques is then possible on the spins which have been shifted into resonance.

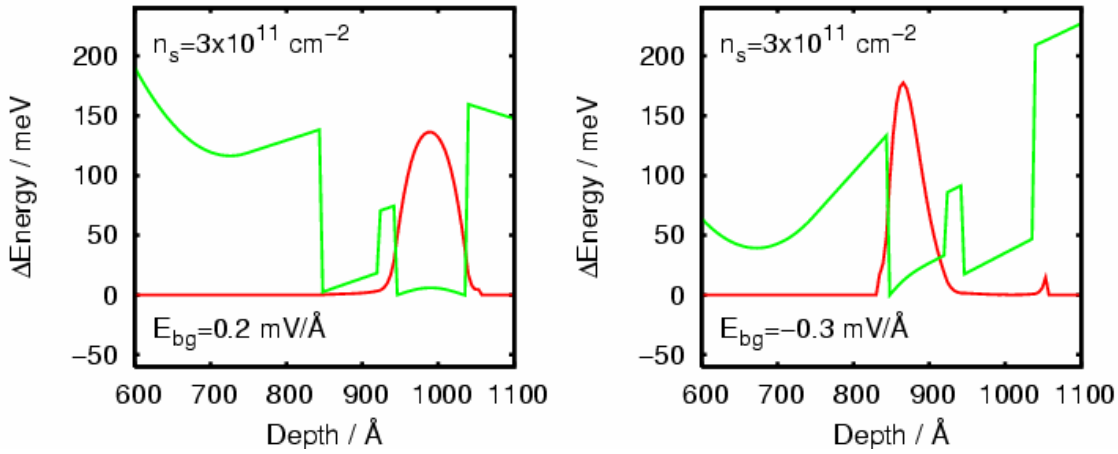

Fig. 1: Self-consistent band structure calculation of the double quantum well structure (as shown above and right) with different applied backgate fields: A front gate was used to keep the carrier concentration at a constant density of n_s = 3x10^{11} cm^{-2}. The calculated change in g-factor can be estimated as Δg = 2.5x10^{-4}, which is enough to separate the resonances and allow spin manipulation.

The required electrical fields are created by applying voltages to a Schottky-type topgate and either a grown-in n-type backgate or an evaporated Al backgate on the backside of the sample. Figure 2 shows how the carrier density and the mobility can be changed in a pure Si channel with Schottky topgate and evaporated Al backgate. Our next goal is the combination of front- and backgate and the double QW structure.

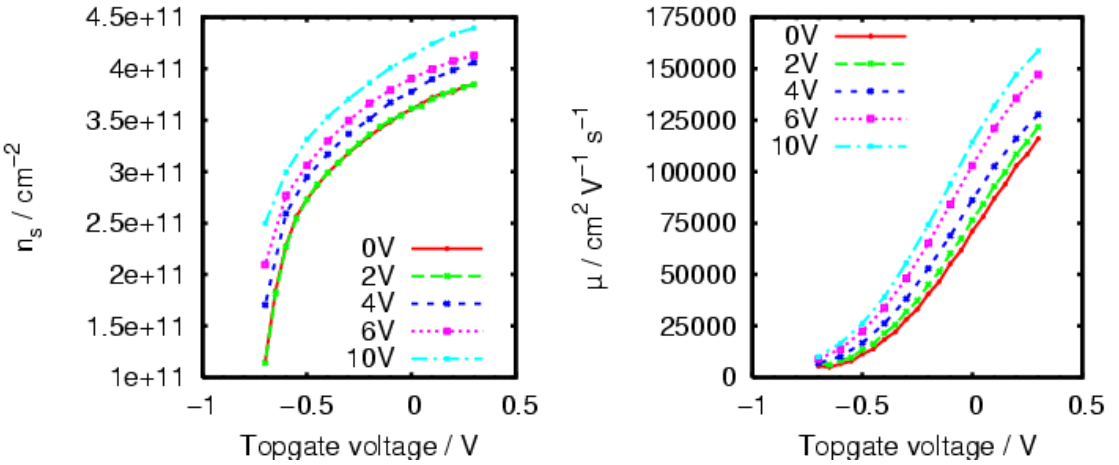

Fig. 2: Carrier density and mobility of a sample with pure Si channel with a Pd Schottky gate on top and an evaporated Al backgate on the back side plotted as a function of the topgate voltage for different backgate voltages. Both mobility and carrier density can be influenced by shifting the wave function away from the interface (higher backgate voltages).

In summary, we report about a SiGe double QW structure designed for tuning the electronic g-factor of electrons. Simulations show that it is possible to completely shift the electronic wave function between two wells with different Ge content and hence the g-factor which is a requirement for quantum computing in SiGe. The process for top- and backgate electrodes is established, and demonstrated on a single Si well sample. The next step will be the combination of double QW structure and front- and backgate.

Spin Relaxation Times in SiGe Islands

In III-V compounds it was shown that the confinement in low dimensional structures such as dots leads to a significant increase of spin lifetimes [5]. In order to achieve confinement in the SiGe material system, we grow Ge islands on Si(100) substrates (i) in a self-organized Stranski-Krastanov growth mode, which leads to an inhomogeneous distribution of island sizes and locations, and (ii) by prepatterning the substrate by either electron beam or holographic lithography. In the first type of samples (i) the density of dots is about 5 times higher than in the prestructured samples (ii), which we estimate from AFM measurements. The Ge dots were overgrown with Si which is locally strained due to the buried Ge dots. The strain causes an attractive potential for electrons. Repeating this procedure, Ge dots grow exactly on top of the strained Si areas. Up to 12 periods of dots were grown in that way which yielded a total of $>10^{10}$ dots.

In photoluminescence experiments a wide band appears around 0.8 eV which corresponds to transitions from the valence band of the Ge dots to conduction band states in the strained silicon (Fig. 3 (a)). This feature is much stronger in the samples with inhomogeneous size distribution (i), which can be attributed to the higher dot density. In EPR experiments a sharp line at g = 1.998 with a line-width of 0.25 G appears under illumination with sub-bandgap light (Fig. 3 (b)). The amplitude of this signal scales with the estimated total number of spins in the sample and also with the PL signal, and is very weak in the structured samples.

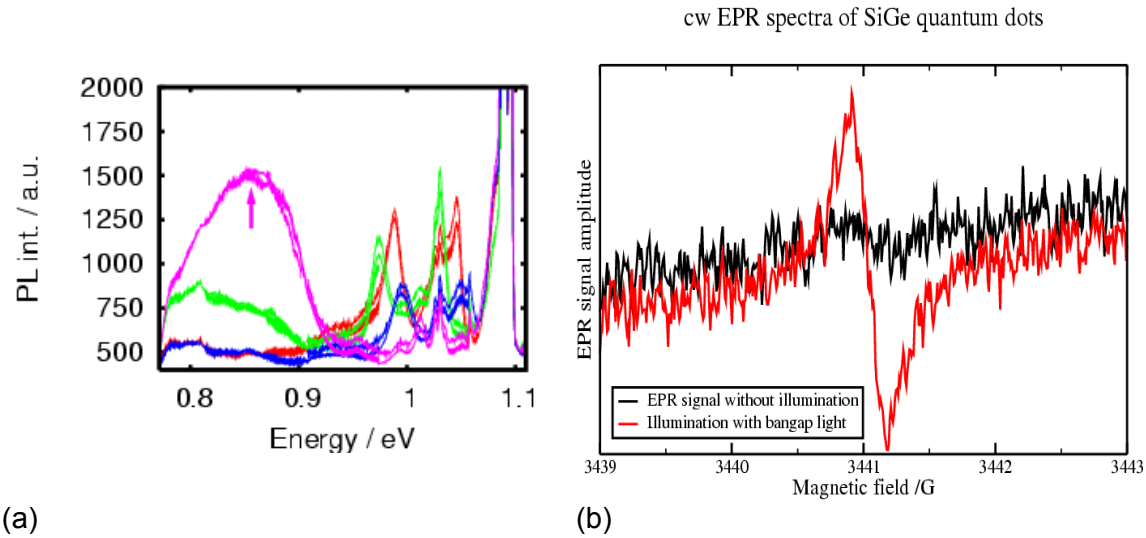

(a) (b)

Fig. 3: (a) photoluminescence data from structured and unstructured (marked) samples; (b) EPR line at g = 1.998 with and without illumination with bandgap light.

The spin relaxation times were measured in time-resolved EPR experiments. In such experiments, the sample is not continuously irradiated by microwaves (MW). Instead, short high power MW pulses are applied. At resonance, these pulses cause the spins to rotate out of their thermal equilibrium orientation parallel to the direction of the static external magnetic field H_0 by an angle that is proportional to the pulse duration around

the direction of H_1, where H_1 the value of magnetic component of the MW field. Applying a π/2 pulse causes the spins to rotate into the plane perpendicular to the H_0, and a π pulse rotates the spins by 180°, thus inverting the spin orientation. Interaction with the surrounding lattice (longitudinal relaxation) and with other spins (transverse relaxation) causes the spins to dephase and to return to their thermal equilibrium value.

Specific pulse sequences are applied in order to observe longitudinal (T_1) and transverse (T_2) relaxation [6]. A π/2 pulse puts the overall magnetization in a plane perpendicular to H_0 where it decays due to spin-spin interaction (transverse relaxation) which is observed as free induction decay (FID). Some time τ after the first pulse a π pulse is applied to rotate the spins by 180°. As a consequence, a second FID appears after a time τ, 2τ after the initial π/2 pulse (Hahn echo). By varying τ, T_2 results from:

$$M = M_0 e^{-2t/T_2},$$

where M is the echo amplitude at time τ and M_0 at τ = 0.

When a π pulse is applied, the magnetization is rotated opposite to its thermal equilibrium orientation. Due to interaction with the environment the spins will relax back to their initial orientation parallel to H_0 (longitudinal spin relaxation). After a time T, a π/2 pulse is applied to put the magnetization into the plane perpendicular to H_0, and a π pulse is used to observe the Hahn echo as described above. T_1 results from:

$$M = M_0 \left(1 - 2e^{-T/T_1}\right).$$

Only the sample containing self-organized dots could be measured with time resolved EPR. We obtain a value of 0.8 µs for T_2 which is isotropic, whereas T_1 depends on sample orientation: in the case where H_0 is perpendicular to the sample plane, T_1 is 0.7 µs; in the case where H_0 is oriented in-plane, T_1 is 1.2 µs which is roughly what one expects for spin orbit coupling. Expressed in terms of line width, the homogeneous transverse line width is 0.082 G (isotropic) and the longitudinal line width is 0.070 G for perpendicular H_0 and 0.022 G for in-plane H_0. For comparison, the inhomogeneously broadened line width from cw EPR is 0.220 G for perpendicular and 0.350 G for in-plane H_0, which is considerably larger than the homogeneous contributions. The large inhomogeneous line width is attributed (i) to a fluctuation of the g-factor for different dot sizes and (ii) the hyperfine interaction with ^{29}Si.

References

[1] R. Vrijen, E. Yablonovitch, K. Wang, H.W. Jiang et al.: “Electron-spin-resonance transistors for quantum computing in silicon-germanium heterostructures”, Phys.Rev.A, Vol. 62, 2000, pp. 012306

[2] A. M. Tyryshkin, S. A. Lyon, W. Jantsch, and F. Schäffler: “Spin Manipulation of Free Two-Dimensional Electrons in Si/SiGe”, Phys. Rev. Lett. 94, 2005, 12802

[3] K. Lai, W. Pan, D.C.Tsui, S. Lyon, et al.: “Two-Flux Composite Fermion Series of the Fractional Quantum Hall States in Strained Si”, Phys. Rev. Lett. 93,2004,156805

[4] H. Malissa, W. Jantsch, M. Mühlberger, F. Schäffler, Z. Wilamowski, M. Draxler, and “Anisotropy of g-factor and electron spin resonance linewidth in modulation doped SiGe quantum wells”, Apl. Phys. Lett. 85, 2004, 1739

[5] M. Kroutvar, Y. Ducommun, D. Heiss, M. Bichler, et al.: “Optically programmable electron spin memory using semiconductor quantum dots”, Nature 432, 2004, 81

[6] A. Schweiger and G. Jeschke: “Principles of Pulse Electron Paramagnetic Resonance” (Oxford University Press, Oxford, 2001)

Resonator Fabrication for Cavity Enhanced, Tunable Si/Ge Quantum Cascade Detectors

M. Grydlik[1], P. Rauter[1], T. Fromherz[1], G. Bauer[1], L. Diehl[2], C. Falub[2], G. Dehlinger[2], H. Sigg[2], D. Grützmacher[2]

[1] Institute for Semiconductor and Solid State Physics, University of Linz, Altenbergerstraße 69, A-4040 Linz

[2] Laboratory for Micro- and Nanotechnology, Paul-Scherrer Institute, CH-5232 Villigen PSI

A process for integrating SiGe quantum well infrared photodetectors (QWIPs) grown on SOI substrates into a vertical cavity resonator has been developed. The process is based on a low temperature (T < 250°C) etch mask deposition and, therefore, is applicable for novel QWIP structures grown by low temperature Si MBE.

Introduction

Infrared detection employing optical transitions in quantum wells has attracted a lot of research interest in the past several years. Due to the design freedom a variety of detector figures like for example the spectral region of sensitivity, the response time, the detector noise etc. can be adjusted over a large parameter range [1], [2] and optimized detector performance can be achieved for several areas of applications. In a recent work on Si/Ge QWIPs, we have demonstrated that in addition a large wavelength tunability can be achieved by employing the injector concept originally developed for quantum cascade electro-luminescence and laser structures [3]. The detectivity of these tunable SiGe QWIPs at 77K is approximately 1.5 x 10^9 cmHz$^{0.5}$/W, typically 1 – 2 orders of magnitude smaller than the detectivity of group III-V based devices. One concept to increase the detectivity of SiGe QWIPs in a narrow detection bandwidth consists of integrating the QWIP into a resonator. In Si/Ge QWIPs, typically the absorption of valence band quantum wells (QWs) is the basis for photocurrent generation. Since for valence band QWs, absorption is also allowed for radiation propagating parallel to the growth direction, vertical cavities can be used to enhance the absorption efficiency of these devices. Moreover, since for QWIPs based on SiGe cascade structures, an extremely large tuning range from for example 200 meV to 400 meV was demonstrated [3], the integration of this novel detectors into a properly designed vertical cavity will allow resonator enhanced detection for 2 narrow bands at wavelengths λ and 2λ that can be addressed by the externally applied voltage.

Experimental

For integrating a tunable QWIP into a vertical cavity resonator, 15 periods of nominally the same QW sequence as described in Ref. [3] (5 SiGe valence band quantum wells with 39, 26, 24, 23, and 35 Å well width and 0.42, 0.42, 0.40, 0.37, and 0.28 Ge concentration, respectively, separated by 30, 25, 25, and 25 Å Si barriers) have been grown on a SOI substrate by low temperature (T = 300 °C) solid source MBE. Detector mesas (typically 300 x 300 µm^2) with bottom and top contacts were formed by reactive ion etching and Al:Si metallization. A schematic sketch of the detector structure is shown in the inset of Fig.1. The photocurrent spectra shown in Fig. 1 clearly demon-

strate that the detectors grown on SOI substrate show a similar tunability as reported previously [3] for detectors grown on Si substrate.

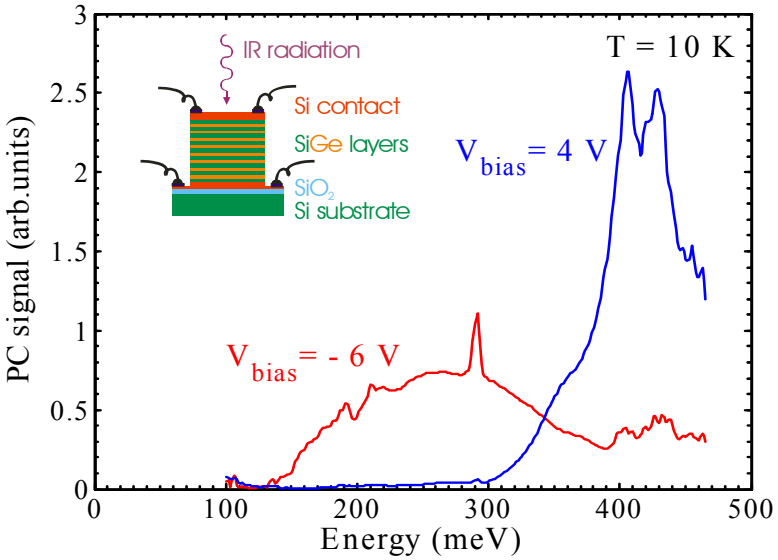

Fig. 1: Photocurrent spectra of SiGe cascade QWIPs measured at the bias voltages indicated in the plot.

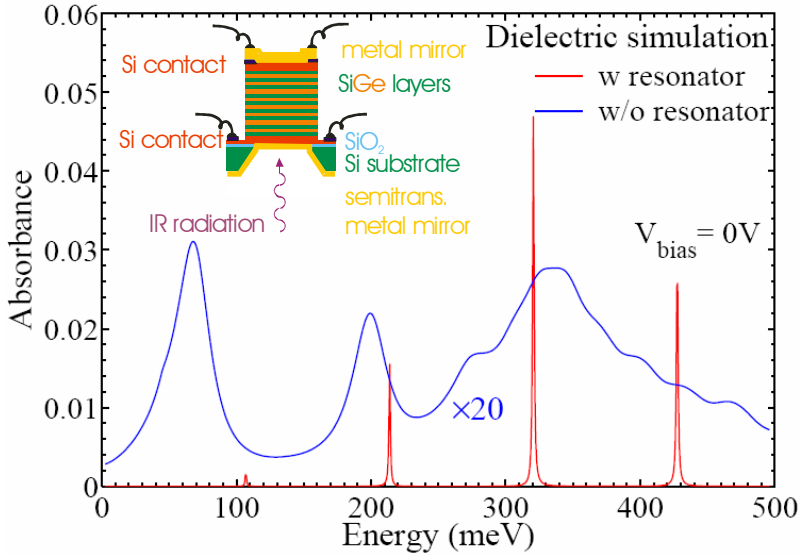

Fig. 2: Simulation of the QWIP absorbance with (red line) and without (blue line) resonator mirrors. Note that the result obtained for the case without mirrors is multiplied by 20.

In Fig. 2 a simulation of the effect of a resonator on the absorption efficiency is shown. Using the absorption spectrum calculated for the QWIP structure by k.p band structure simulations [3], the sample transmission, reflection and absorption including multireflections at all interfaces in the sample was calculated for radiation propagating perpendicular to the sample surface by the transfer matrix method [4]. The intensity absorbed by the QWIP layer sequences is shown by the blue line in Fig. 2. Using the same band

stucture for the QWIP and assuming a free standing membrane consisting of the QWIP layers coated with a thick gold layer on top of the membrane and a thin (for example 20 nm), semitransparent gold layer at the opposite side of the membrane through that radiation can be coupled into the QWIP (for a sketch, see inset of Fig. 2), the QWIP absorption was simulated by the transfer-matrix method [4] for comparison. In this simulation, the dielectric function of the gold was described by a Drude dispersion according to [5]. The simulated QWIP absorbance is shown by the red line in Fig. 2. It is evident from this plot that at the resonance wavelengths the QWIP absorption is enhanced by at least an order of magnitude.

For fabricating vertical cavity resonator as sketched in the inset of Fig. 2, openings aligned to the detector mesas have to be etched from the backside of the sample through the substrate. The buried oxide layer of the SOI substrate is used as an etch-stop. After removing the remaining SiO_2 layer by an HF etch, a free standing film consisting of the detector QW sequences results. On the top and bottom side of this detector film, broadband, high-reflectivity metal or Bragg mirrors will be deposited that finally form the resonator.

From the previous paragraph it is clear that the choice of a proper etchant is crucial for successful resonator fabrication. In our work, TMAH (Tetramethylammonium Hydroxide) at 90 °C was used as etchant for the following reasons: (a) TMAH has reasonably large etch rate (30 µm/h) for the Si (001) lattice plane that allows to etch free the buried oxide layer of a thinned SOI substrate (200 µm) in approximately 7 h. (b) In addition, the TMAH etch rate for Si (111) lattice planes is approximately an order of magnitude smaller than in (001) direction. Therefore, TMAH etch grooves are bound by (111) planes and negligible underetching of the etch mask occurs. (c) The etch rate of TMAH for thermally grown oxide is virtually vanishing. Therefore the etching process is effectively stopped by the 200 nm thick buried oxide of the SOI substrate. Even after a 2 h long over-etching the exposed SiO_2 layer showed no indication of an etch attack and remained optically flat. (d) TMAH is compatible with the standard Si technology as it is contained in most of the photoresist developers.

For the long etch times required to etch from the wafer backside to the buried SiO_2, an etch mask with high resistance against TMAH is required. In standard Si MEM technology, a structured Si_3N_4 layer deposited by LPCVD at approximately 900 °C is commonly used as mask for long TMAH etches. However, due to the high deposition temperature necessary for the LPCVD process, this mask material can not be used for samples with QWIP structures grown on the wafer front side. On the other hand, a 300 nm thick Si_3N_4 deposited at lower temperatures (250 °C) in a plasma enhanced CVD (PECVD) process was destroyed by the TMAH etch after approximately 100 nm etch depth. Increasing the thickness of the Si_3N_4 to 400 nm and 500 nm did not improve the results most probably due to increased number of strain induced cracks in the thicker Si_3N_4 layers.

The best results were obtained by a mask consisting of a double layer of Si_3N_4 (200 nm) and the spin-on polymer BCB (Bencocyclobutene, Dow Chemicals brand name: “Cyclotene” [6]) with a thickness of 6 – 8 µm. BCB can be structured by reactive ion etching in a mixed O_2 and CF_4 plasma. The Si_3N_4 layer acts as an adhesion promoter for the BCB film. With this mask and a 10 h long TMAH etch, free standing Si membranes could be produced on a test wafer consisting of a Si layer grown on an SOI substrate instead of the Si/Ge QWIP structure. Electron and optical microscope pictures of the membrane are shown in Figs. 3 (a) – (d). In the optical microscope (Figs. 3 (a), (b)) no surface roughness of the membrane and the (111) sidewalls are visible. The sample shown in Figs. 3 (a), (b) was illuminated from the backside resulting in a bright appearance of the Si membranes, indicating that the membranes are transparent in the visible spectral region due to their small thicknesses. Also the electron microscope pictures (Figs. 3 (c), (d)) do not show significant surface roughness of

the membranes and the sidewalls. The etch mask shown in Fig. 3 (d) is evidently not attacked by the TMAH etch and only a small underetching due to the non-vanishing etch rate in (111) direction is shown. Infrared transmission through a Si membrane was measured with an infrared microscope. The transmission spectrum plotted in Fig. 3 (e) shows strong Fabry-Perot oscillations with a periodicity corresponding to a membrane thickness of 1.42 µm. In future work, the line width of these oscillations will be decreased by increasing the cavity Q-factor with high-reflectivity broadband mirrors deposited on the membrane surfaces.

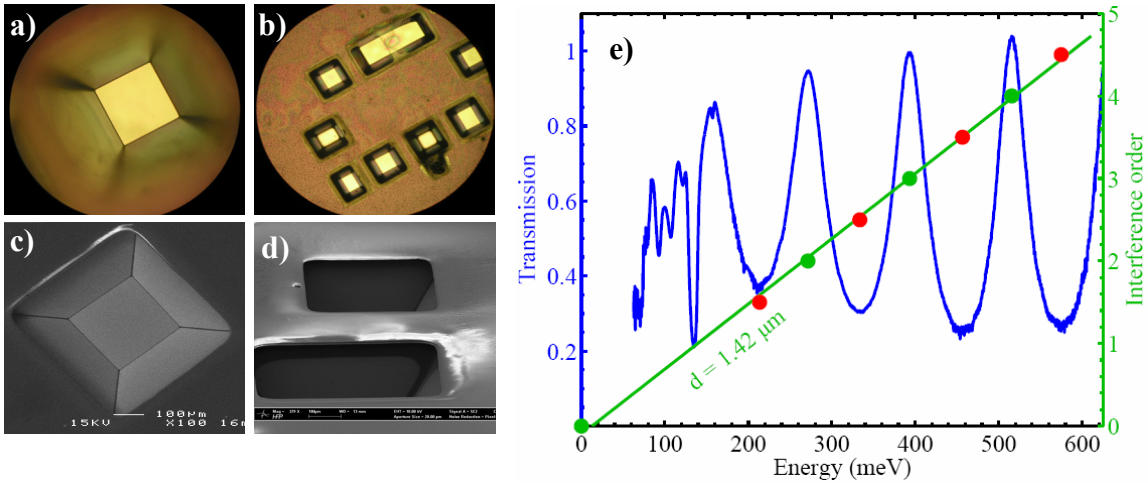

Fig. 3: Results obtained by visible ((a), (b)), electron ((c), (d)) and infrared microscope (e) experiments revealing an optically flat Si membrane with thickness of 1.42 µm fabricated by the process described in the text.

Conclusions

A process for fabricating a thin, free standing Si membrane by etching grooves from the backside of an SOI wafer has been developed, where the buried SiO_2 layer acts as an effective etch stop. Since only low temperature (T< 250°C) process steps are involved, the process is perfectly suited for integrating Si/Ge based QWIPs grown on SOI substrates into vertical cavity resonators.

Acknowledgements

Work was supported by BMVIT (Proj. Nr. GZ 604000/14-III/I5/2003) and the EC project SHINE (IST-2001-38035).

References

[1] B. F. Levine, “Quantum-well infrared photodetectors”, J. Appl. Phys. **74**, R1-R81 (1993).

[2] H. Schneider, P.Koidl, M. Walther, J. Fleissner, R. Rehm, E. Diwo, K. Schwarz, G. Weimann, “Ten years of QWIP development at Fraunhofer IAF”, Infrared Phys. Technol**. 42**, 283-289 (2001).

[3] P. Rauter, T.Fromherz, G. Bauer,L. Diehl, G. Dehlinger, H. Sigg, D. Grützmacher, H. Schneider, “Voltage tuneable, two-band MIR detection based on Si/SiGe quantum cascade injector structures”, Appl. Phys. Lett. **83**, 3879-3881 (2003).

[4] see for example: B. Harbecke,” Coherent and Incoherent Reflection and Transmission of Multilayer Structures”, Appl. Phys. B **39**, 165 (1986).

[5] M.A. Ordal, et. al, “Optical properties of fourteen metals in the infrared and far infrared..”, Appl. Optics **24**, 4493 (1985).

[6] http://www.dow.com/cyclotene/

Lateral Quantum Dots in High Mobility Heterostructures

G. Pillwein [1], T. Berer [1], G. Brunthaler [1], F. Schäffler [1], and G. Strasser [2]

[1] Institute for Semiconductor Physics, University Linz, Austria

[2] Institut für Festkörperelektronik TU Vienna, Austria

We have fabricated single lateral quantum dots in the two-dimensional electron gas (2DEG) of modulation doped GaAs/AlGaAs and Si/SiGe heterostructures, which are basic elements for more sophisticated devices. Electrical measurements were carried out at temperatures down to 30 mK. The technology of the GaAs structures has been adapted to Si/SiGe-based lateral quantum dots. We report Coulomb blockade measurements of lateral quantum dots formed by the split-gate technique on MBE grown modulation doped GaAs/AlGaAs and Si/$Si_{0.75}Ge_{0.25}$ heterostructures.

Introduction

In several recent proposals [1] – [3] lateral quantum dots were discussed as a promising option to realize the quantum entanglement necessary for quantum computation. As an approach to this topic we have chosen to fabricate single quantum dot devices in the two-dimensional electron gas (2DEG) of GaAs/AlGaAs and Si/SiGe heterojunctions. These dots are the basic building blocks of more complex structures (e.g. [4]), which we plan to investigate in the near future.

The technology of the GaAs structures has been adapted to Si/SiGe based lateral quantum dots. Recently, several lateral quantum dots in silicon/silicon-germanium heterostructures have been reported [5], [6]. However, none of these were achieved by the classical split-gate technique that is necessary for the coupling of quantum dots and for high integration.

Sample Preparation

GaAs/AlGaAs

High mobility modulation doped GaAs/AlGaAs heterostructures were grown by MBE at TU Vienna. The 2DEG in these samples is typically situated 70 – 100 nm below the surface. Further processing of the samples was done in the cleanroom in Linz. Hall bars were structured by optical lithography. Ohmic contacts to the 2DEG were made by depositing Cr, Au, Ge, Ni, Au and annealing at 450 °C. The mesa was wet chemically etched.

The electrical properties of the 2DEG were determined by quantum Hall effect and SdH measurements. Typical carrier densities were in the range from 2 to $4x10^{11}$ cm^{-2} with mobilities between 0.3 and $2x10^6$ cm^2/Vs.

The area of the quantum dot is defined by Cr/Au gates on top of the Hall bar mesa, which were written by e-beam lithography. The top center gate electrode acts as a plunger gate. Gold connections from the bond pads to the small gates are structured by optical lithography.

Si/SiGe

High mobility modulation doped Si/SiGe heterostructures were grown by MBE in Linz. The 2DEG in these samples is situated about 85 nm below the surface. Hall bars were structured by optical lithography. Ohmic contacts were formed by deposition of Au/Sb and subsequent annealing at 350 ºC. A Hall bar structure was prepared by reactive ion etching (RIE) with SF_6.

Electrical measurements (SdH and QHE) at 1.5 K showed an electron mobility of 150,000 cm²/Vs at an electron density of 3.2 x 10^{11} cm^{-2}

The split gate structures were written by e-beam lithography and defined by lift-off of the Schottky-gate metal Pd. The top center gate electrode acts as a plunger gate. Connections from the bond pads to the small gates are made of Palladium.

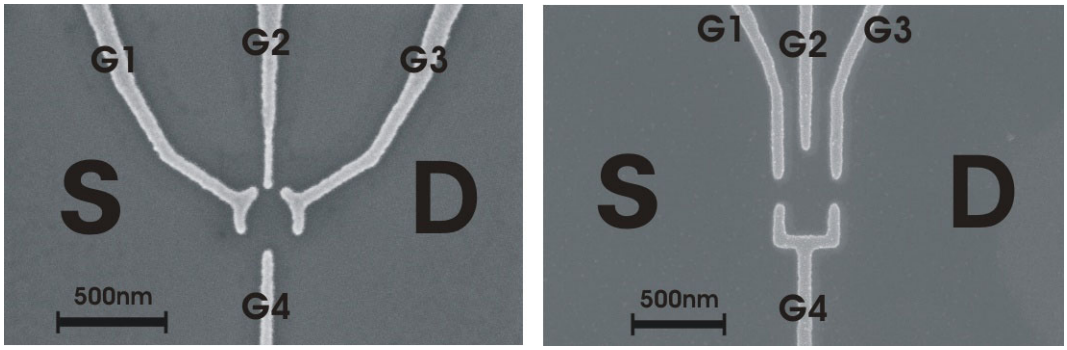

Fig. 1: Scanning electron micrograph of (a) the Cr/Au top gates on a GaAs/AlGaAs sample and (b) the Pd split gates on a Si/SiGe sample. The pitch between the upper gates is 185nm.

Measurements

When applying a negative voltage to the gates the underlying 2DEG is depleted and the dot area is defined in the center. By varying the plunger gate voltage, the energy levels inside the quantum dot can be moved into and out of resonance with the Fermi level in the leads. The conductance will increase whenever the energies are aligned and decrease in between, forming the so called Coulomb oscillations. If a large DC bias is applied at the source drain contacts the transport blockade can be overcome and excited energy states of the quantum dot can be probed.

GaAs Quantum Dots

By measuring the conductance versus both the plunger gate voltage V_G and the source drain voltage V_{SD}, we obtain the so-called quantum dot spectrum. It gives access to a lot of information about the quantum dot. Such a measurement is shown in Fig. 2 (a) below.

From the size and shape of the rhombic regions indicated by lines we obtain electrical properties such as capacitances of the gates and leads with respect to the dot. It is also possible to estimate the electrically active size of the dots from these data. This will differ from the actual geometrical size of the dot because of a depletion region, which extends around the gates. The difference between structural diameter and electrically active diameter indicates that the depletion region extends about 80 – 90 nm around the gates.

By changing the plunger gate voltage the tunnel barriers are also influenced, which limits the number of measurable Coulomb oscillations. Counteractive changing of the voltage on the outer gates allows us to stabilize the tunnel barriers and therefore increase the range of occupation numbers accessible by measurement.

In a few of the investigated samples we have observed conductance fluctuations superimposed upon the usual Coulomb oscillations. What at a first glance looked like random noise, turned out to be a reproducible fluctuation on a very small gate voltage scale, which was preserved over several sweeps in both directions (see Fig. 2 (b)).

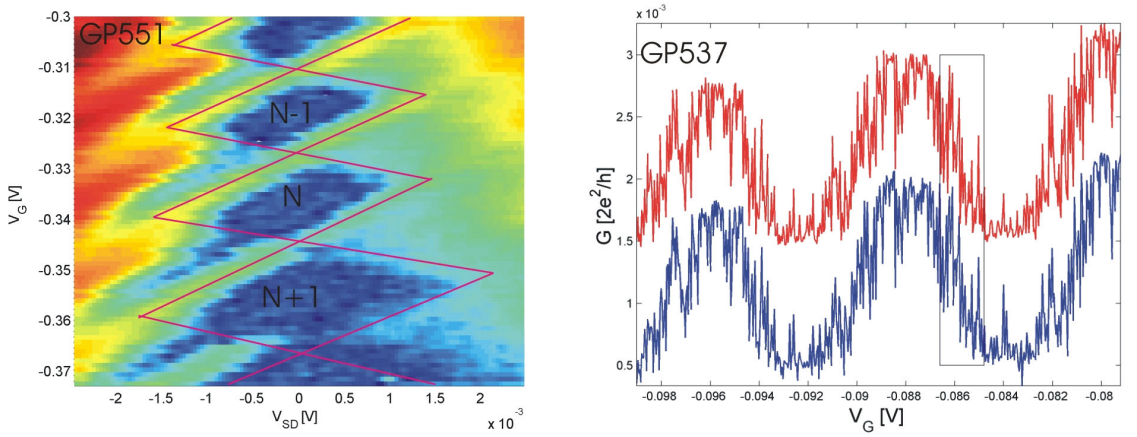

Fig. 2: (a) Differential Conductance of the AlGaAs quantum dot as a function of gate voltage and applied dc source-drain voltage; (b) reproducible conductance fluctuations.

Interestingly, these fluctuations still occur on an energy scale smaller than 3 μeV, which is an order of magnitude smaller than the thermal energy at 300 mK (k_{BT} = 26 μeV), and would therefore be assumed to be smeared out.

Further measurements will be required to investigate the exact origin of these fluctuations.

Si/SiGe Quantum Dots

A lateral quantum dot formed by a split-gate technique was realized on a modulation doped Si/$Si_{0.75}Ge_{0.25}$ heterostructure and Coulomb blockade was measured up to 1 K. Figure 3 shows the quantum dot spectrum (”Coulomb diamond”) taken at 30 mK and 1 K.

By analyzing the measured Coulomb diamonds we estimated the gate and the source capacity to be 6.4 aF and 30 aF respectively and the total dot capacity to be 65 aF. Therefore the dot diameter is approximately 160 nm resulting in less than 70 electrons in the dot.

These results show that SET functionality can be achieved in modulation-doped Si/SiGe heterostructures with a standard split-gate approach that can easily be integrated into an array of coupled SETs as suggested in Ref. [3].

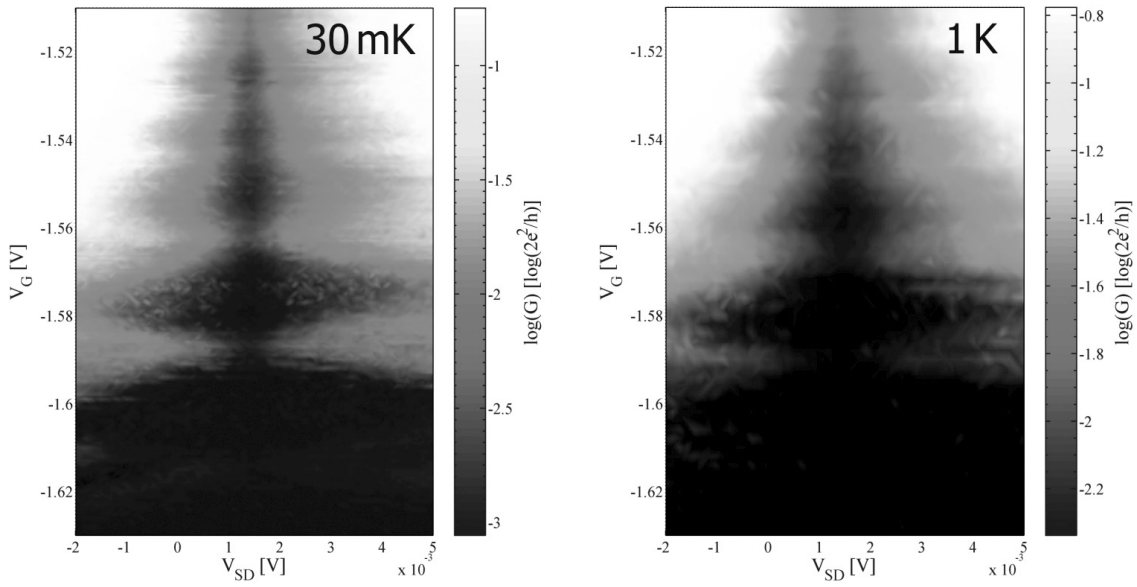

Fig. 3: Differential Conductance of the Si/SiGe quantum dot as a function of gate voltage and applied dc source-drain voltage at a) 30mK and b) 1K. Coulomb blockade diamonds are clearly visible.

Conclusion and Outlook

Single lateral quantum dots in the 2DEG of modulation doped GaAs/AlGaAs and Si/SiGe heterostructures have been realized with a split-gate technique. Coulomb blockade measurements, which prove the functionality of our devices, were performed down to a temperature of 30 mK. Based on these results we will fabricate quantum dot circuits consisting of two or more dots, which may be combined with quantum point contacts for charge readout.

Acknowledgements

This work was financially supported by FWF (P16160 and P16223-N08)

References

[1] D. Loss, D.P. DiVincenzo: “Quantum computation with quantum dots”, Phys. Rev. A 57, 1998, 120 – 126

[2] L.M.K. Vandersypen et al., quant ph/0207059 (unpublished)

[3] M. Friesen et al: ” Practical design and simulation of silicon-based quantum-dot qubits”, Phys. Rev. B, 67, 2004, 1213010-1 – 1213010-4

[4] J. Elzerman et al.: “Few-electron quantum dot circuit with integrated charge read out”, Phys. Rev. B 67, 2003, 161308-1 – 161308-4

[5] A. Notargiacomo et al: “Single-electron transistor based on modulation-doped SiGe heterostructures”, APL, 83, 2003, 302 – 304

[6] L. J. Klein et al: “Coulomb blockade in a silicon/silicon–germanium two-dimensional electron gas quantum dot”, APL, 84, 2004, 4047 – 4049

Polarization Splitting Based on Planar Photonic Crystals

V. Rinnerbauer[1,2], J. Schermer[2], and K. Hingerl[1]

[1]Christian Doppler Labor für oberflächenoptische Methoden, Johannes-Kepler-Universität Linz, A-4040 Linz
[2]Photeon Technologies, A-6900 Bregenz

Planar polarization splitting devices based on photonic crystal slabs have been developed, their main advantages being the planar design and their possible integration into PLCs. Three different principles are demonstrated and results from numerical simulations shown.

Introduction

The use of polarization multiplexing to double the existing fibre capacity has been demonstrated successfully in a recent field trial on an installed DWDM metropolitan area network in Berlin, Germany [1]. Together with the growing number of polarization preserving devices, in particular photonic crystal (PhC) devices, this experiment shows us the importance of effective polarization demultiplexers.

Due to their inherent polarization sensitivity, photonic crystals offer convenient solutions on a length scale of several tens of micrometers in silicon-based or other high index material systems. In a 2D photonic crystal slab, the presence of a horizontal symmetry plane allows us to decompose the guided modes into TE-like and TM-like polarization states, which are even and odd with respect to reflections through this plane [2]. In this paper, we will show three different principles that exploit the polarization dependency of these guided modes.

Polarization spitter design

Reflection at a photonic crystal interface

At the interface of a photonic crystal, an impinging wave is either transmitted or reflected, depending on whether there are allowed states for its frequency. The absence of allowed states can result either from a bandgap for this frequency, or else for symmetry reasons, which prohibit the excitation of the photonic crystal modes. Therefore reflection and transmission depend on the photonic crystal structure and the wavelength, the polarization and the incident angle of the impinging wave.

For this polarization splitter we have designed a photonic crystal structure that reflects one polarization while transmitting the other. The reflection and transmission spectra of a photonic crystal have been calculated using a plane wave expansion technique [3] based on a method proposed by K. Sakoda [4]. The results for a hexagonal lattice with 16 rows of air holes in silicon with a radius to period ratio r/a = 0.29 are shown in figure 1.

The effective refractive index of the silicon background was set to n_{eff} = 2.76, which corresponds to a slab height h of h/a = 0.6. This effective index was derived using the scaling laws, preserving the position of the bandgap for the transition from 2D to 3D

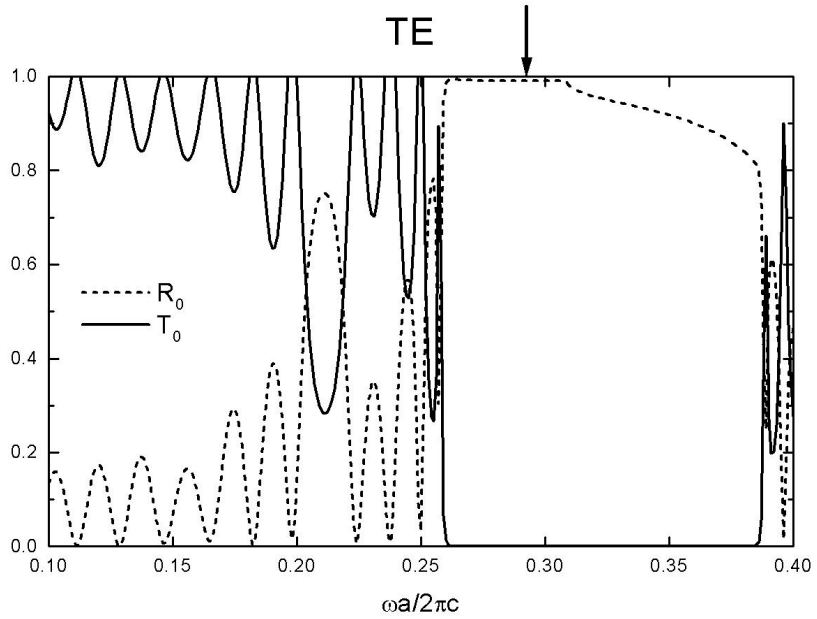

Fig. 1: Reflection at and transmission through a photonic crystal for TE (above) and TM polarization (below) as a function of normalized frequency

cases. The angle of incidence in this example is 10 degrees. It can be seen that for these parameters there are frequency regions where one polarization is transmitted but the other is reflected. We use the parameter ωa/2πc = 0.293. In figure 1 this parameter, whereby the power reflection is 0.990 for TE and the power transmission for TM is 0.998, is indicated by an arrow. The plane wave calculations were performed with 5 plane waves (n) parallel to the interface and 50 plane waves (m) perpendicular to it [notation of 4]. The results have been verified with 2D and 3D FDTD simulations of PhC slabs.

Guided modes and free propagation

In this example, a defect waveguide is introduced into a photonic crystal structure exhibiting a bandgap for TE polarization only. Because the bandgap prohibits propagation in the bulk, a bend in this photonic crystal waveguide redirects TE light with frequencies in the bandgap. However, the other polarization is not guided around the bend by the defect waveguide, and continues propagating straight through the crystal.

Once again, a hexagonal lattice of air holes in silicon with r/a = 0.29 is used. The period a is 415 nm and the height of the slab is 320 nm. This lattice has a bandgap for TE polarization for normalized frequencies of about 0.24 ≤ ωa/2πc ≤ 0.31.

The results of 3D FDTD simulations with a wavelength of 1.55 µm for such a structure are shown in figure 2. The time evolution of power is monitored at positions 1, 2 and the results shown below the picture of the field are a measure of the output power at the waveguide output on the right (position 1, dark gray) and at the top edge of the

photonic crystal (position 2, light gray). The power output for TE polarization is about 90% (insertion loss of 0.45 dB), and 75% (1.25 dB) for TM.

The geometry of the bend was then optimised to obtain maximum output for both polarizations for a broad bandwidth. Simulations of the optimised bend show an output power of 93% (insertion loss of 0.3dB) for both polarizations at 1.55 mm, with a crosstalk below 16 dB for TM and below 24 dB for TE. The non-uniformity in the C-band is less than 0.5 dB for both polarizations.

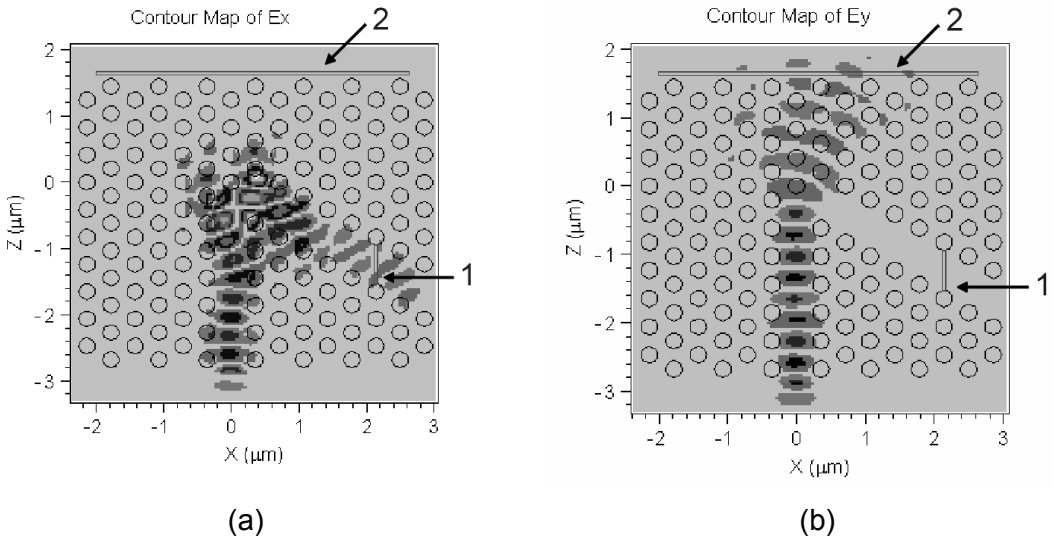

(a) (b)

Fig. 2: FDTD simulation of a PhC bend for (a) TE and (b) TM polarization

Polarization-dependent defect modes

In this case the polarizations are separated at a Y branch in a photonic crystal connecting three defect waveguides with polarization-dependent modes. The defect modes of the photonic crystal waveguides are designed in such a way that each output waveguide of the Y-branch supports only one polarization whilst the input waveguide supports both.

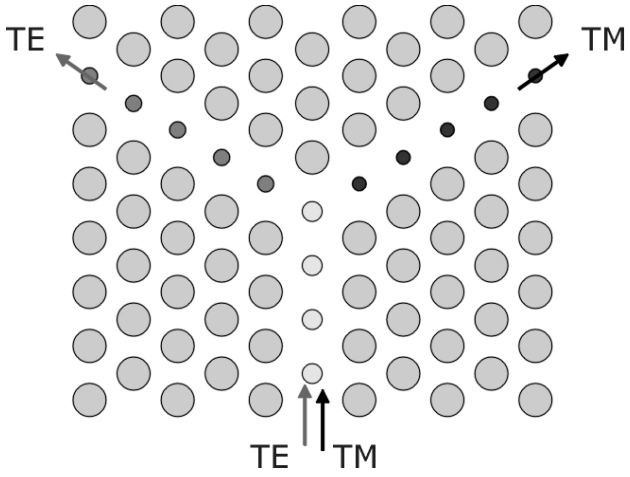

Fig. 3: Y-branch structure with polarization-dependent defect modes in the branches

In a 2D example we use a hexagonal lattice of air holes in silicon with r/a = 0.45. The lattice exhibits a bandgap for both polarizations for normalized frequencies of about $0.41 \leq \omega a/2\pi c \leq 0.45$.

Line defect waveguides are formed in this lattice by reducing the radius of the holes in one row. The input waveguide has a defect radius r/a = 0.33, which supports modes of both polarizations in the bandgap, whereas one output waveguide with a defect radius of r/a = 0. 2365 supports only TE modes (figure 3a) in a frequency region of about $0.430 \leq \omega a/2\pi c \leq 0.434$, and the other output waveguide with r/a = 0.1925 supports only TM modes in this frequency region (figure 3b).

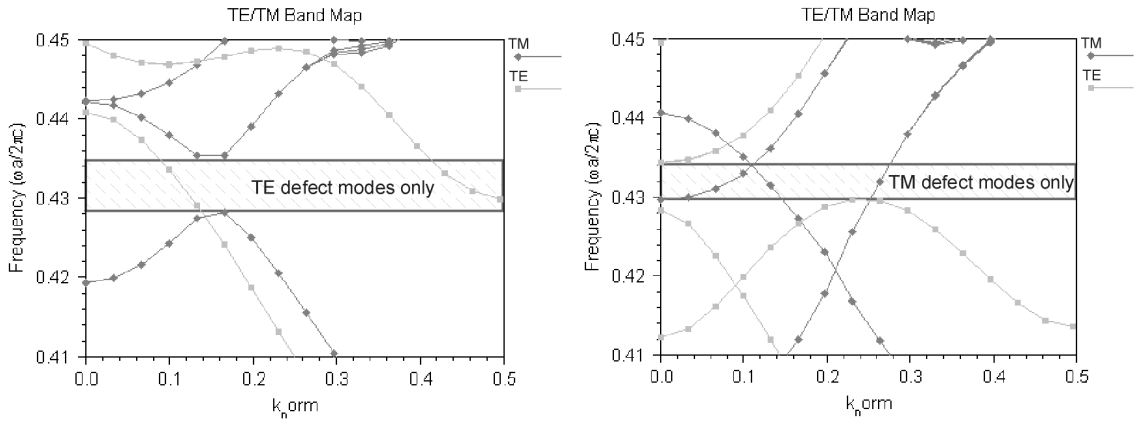

(a) (b)

Fig. 3: Defect bands for (a) r/a = 0. 2365 and (b) r/a = 0.1925, parameters as explained in the text

In this example, the design of the Y-branch junction is of crucial importance for good transmission.

Conclusion

We have demonstrated three different designs of polarization splitting devices in photonic crystal slabs, exploiting the inherent polarization sensitivity of 2D photonic crystal slabs. The main advantages of all designs are the planar geometry and the ability to be integrated into PLCs with high integration density.

References

[1] N.E.Hecker-Denschlag, W. Schairer, W. Fischler, A. Richter, T. Auernhammer, B. Lankl: “Polarization multiplexing in a remotely-configureable photonic network”, ECOC 2002, Vol.3, 6.4.5

[2] S.G. Johnson, Shanhui-Fan, P.R. Villeneuve, J.D. Joannopoulos, L.A. Kolodziejski: “Guided modes in photonic crystal slabs”, Phys. Rev. B, Vol. 60(8), 1999, pp 5751-8

[3] K. Hingerl, L. Mao, V. Holy,V. Rinnerbauer, J. Schermer: “Reflection and Transmission of Finite 2D Photonic Crystals”, ECOC 2003, Vol.3, pp 672-3

[4] K. Sakoda: “Optical Properties of Photonic Crystals”, Springer, Berlin 2001, Chapter 4

Nanocrystal Based Microcavity Light Emitting Devices

J. Roither, M. V. Kovalenko, S. Pichler, T. Schwarzl, W. Heiss

Institut für Halbleiter- und Festkörperphysik, Universität Linz, Altenbergerstraße 69, 4040 Linz, Austria

D. V. Talapin, N. Gaponik, A. Eychmuller

Institut für Physikalische Chemie, Universität Hamburg, D-20146 Hamburg, Germany

Highly luminescent, colloidally synthesized semiconductor nanocrystals are used to fabricate microcavity light emitting devices operating around 650 and 1540 nm. They consist of a Bragg interference mirror from standard optical materials, an active layer consisting of either CdSe nanocrystals for operation in the visible or HgTe nanocrystals with a strong emission in the telecommunication wavelength range, a spacer layer to achieve the desired cavity length, and a metallic top mirror. Both types of devices give highly directional, narrow mode emission with a beam divergence below 2° clearly evidencing that the nanocrystal emission couples to the microcavity resonances. Furthermore, operation up to 75°C is demonstrated without degradation of the nanocrystals, which is promising for potential applications.

Introduction

Semiconductor nanocrystals (NCs) synthesized by wet-chemical methods have been investigated because of their strongly size-dependent electrical and optical properties. The high flexibility of the synthesis processes allows one to obtain NCs with different shapes and with energy band gaps ranging from the mid-infrared to the UV depending on both the elemental composition and the size of the particles. Moreover, the very high photoluminescence (PL) quantum efficiencies close to unity achieved at room temperature make NCs ideal candidates to improve the performance of light emitting devices. Therefore, NCs have been used to increase the efficiency of plastic light emitting diodes and to obtain single photon sources operating at room temperature. In addition, the operation of NC-based laser devices such as distributed feedback- and microring lasers has been demonstrated. Recently, NCs have not only been used to realize spherical resonators with tremendously high quality factors but also to achieve ultra-low threshold continuous wave lasing at room temperature. While the emission of single NCs, films of NCs and spherical resonators is evenly distributed over all directions in space, in the present work we investigated microcavity light emitting devices, giving strongly directional emission from NCs in continuous wave operation mode. The microcavity devices contain as active material either CdSe NCs for operation in the visible at wavelengths around the damping minimum in plastic optical fibers or HgTe NCs with a strong emission in the telecommunication wavelength range.

Design and Fabrication

In the microcavity structures either CdSe or HgTe NCs are placed between a Bragg interference mirror and a metallic mirror. The devices were designed by transfer matrix calculations using the optical constants of the individual layer materials, determined by transmission spectroscopy of single reference layers.

Primarily, for the HgTe based microcavity devices (MC-HT), dielectric Bragg interference mirrors consisting of five pairs of TiO_2 and SiO_2 layers with a thickness of a quarter of the design wavelength of 1540 nm were deposited on a glass substrate by ion assisted electron beam evaporation. This results in mirror reflectivities of 95.5% in the center of the stop band. On top of the reflector ending up with a SiO_2 Bragg layer, a densely packed film of HgTe NCs was deposited by the layer-by-layer assembly method. A sequence of 20 bilayers of poly(diallyldimethylammonium chloride) and HgTe NCs results in a smooth and closely packed film with a thickness of 50 nm. The NC-film was covered by a spacer layer of SiO_2 to achieve (a) the desired cavity length for a single resonance right at the center of the Bragg mirror stop band as well as (b) a small refractive index at the interface to the metallic mirror on top of the structures to obtain a high overall reflectivity. The thickness of the spacer layer is varied to tune the wavelength of the cavity resonance. On top of the structures a 200 nm thick silver mirror was deposited by DC magnetron sputtering.

For the CdSe based devices (MC-CS), Bragg mirrors also consisting of five pairs of TiO_2 and SiO_2 layers but designed for a wavelength of 650 nm were deposited on a 22 microns thick, freshly cleaved sheet of pristine mica, whose surfaces are parallel to each other. On the other side of the mica substrate a film of CdSe NCs acting as the optical active material in our devices was deposited and covered by PMMA to protect them during deposition of the metallic top mirror.

Results

All devices were characterized by reflectivity measurements clearly showing a broad Bragg mirror stop band with a maximum reflectivity at the stop band center of 95.5% in perfect agreement with the expected value from our design simulations.

For the MC-HT devices a SiO_2 spacer layer thickness of 170 nm results in single resonator mode right at the center of the Bragg mirror stop band at 1540 nm with a full width at half maximum (FWHM) of only 19.5 meV. By increasing the spacer layer thickness and thus the cavity length, the resonance can be deliberately detuned to lower photon energies [1].

In contrast to that, more than 30 narrow modes are found within the stop band around 650 nm in the MC-CS devices due to the mica sheet thickness of 22 microns [2]. Each resonator mode consists of a double peak structure with a width of 8.5 meV and a spacing of 5.8 meV whose energy splitting is found to scale with the thickness of the mica sheets [2], [3], indicating that it is solely caused by the birefringent properties of the used mica sheets.

For PL experiments, the samples were optically excited by commercially available laser diodes in cw operation mode at wavelengths of 980 and 532 nm at room temperature. For the MC-HT devices a single peak is found, with a FWHM close to 20 meV, which is about eight times smaller than the emission of a NC reference sample (Fig. 1 (a) (solid curves)). The peak energy coincides with the resonance energy deduced from the reflectivity experiments, clearly evidencing that the NC emission couples to the microcavity mode. By increasing the cavity length from 170 nm to 220, 270 and 320 nm SiO_2 spacer layer thickness, the emission of the microcavity can be spectrally tuned over a large range of nearly 90 meV towards lower energies, as shown in Fig. 1 (a).

Decreasing the cavity length results in the same tuning range but towards higher energies (not shown here). Thus, the microcavity emission can be tuned over a total range of 177 meV (1400-1750 nm), only limited by the width of the NC PL (Fig. 1 (a) (dashed curve)) which is comparable to that of the Bragg mirror stop band. Furthermore, temperature dependent PL experiments reveal only a moderate decrease of the device emission, so that at 75 °C still one third of the intensity at 25 °C is observed [1]. This

decrease is solely caused by an increase of nonradiative recombination and not by decomposition of the NCs, because after cycling the temperature several times up and down the same PL intensities are obtained.

The PL spectrum of a MC-CS device is presented in Fig. 1 (b) (solid curve) together with that of a NC reference layer (dashed curve). Obviously, the envelope of the device emission matches well to that of the reference layer, both exhibiting its maximum around 1.9 eV (650 nm).

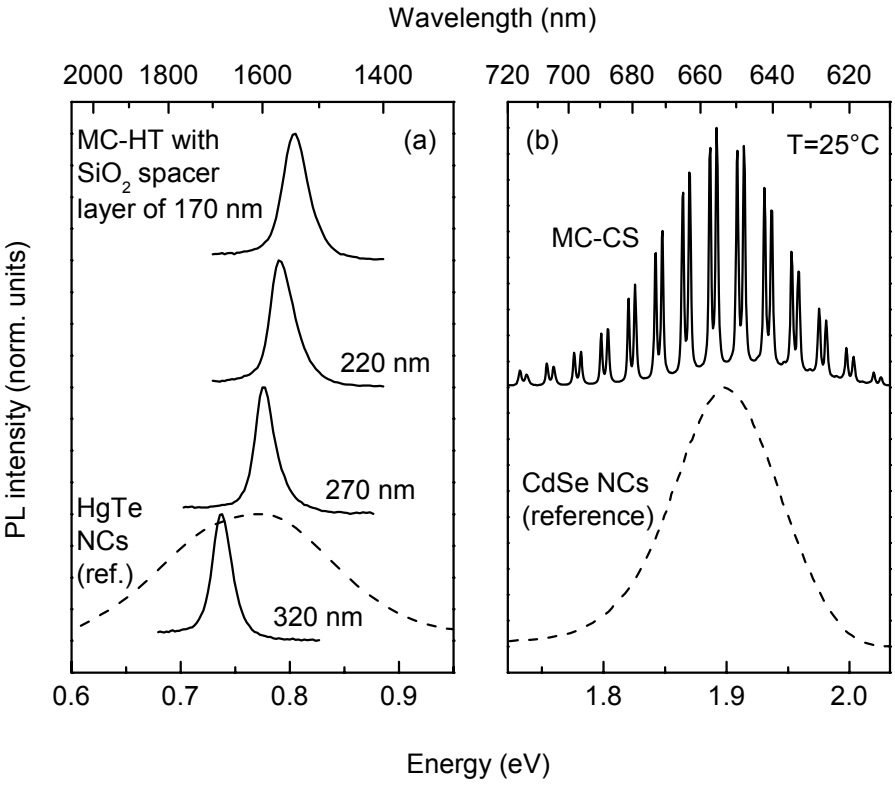

Fig. 1: Room temperature PL spectra of (a) four HgTe based devices (MC-HT) with different cavity lengths (SiO_2 spacer layer thicknesses of 170, 220, 270 and 320 nm, respectively) and (b) a CdSe based device (MC-CS) with a cavity length of approximately 22 microns. For clarity the spectra are shifted in vertical direction with respect to each other. In (a) as well as in (b) the PL spectrum of a NC reference layer is shown as a dashed curve.

The device spectrum, however, shows 30 pronounced resonator modes with a spacing of only 19 meV and a width of each double peak of 8.5 meV so that almost 50 % of the NC PL spectrum is covered by the modes. Therefore, a large fraction of the NC PL is extracted from the device.

As a final point we discuss the angular dependence of the spontaneous emission which was determined in the same way as described in Ref. [2]. As depicted in Fig. 2, the experimental angular dependence can be well fitted by a Gaussian function with a half width at half maximum of 0.65° for the MC-CS device (MC-HT devices show similar results). For emission angles of only 2° off from the surface normal (see sketch in the inset), the emission intensities essentially drop to zero. Therefore, the narrow forward directed emission in combination with the symmetric beam profile and the narrow spectral width, resulting from the geometry of our cavities, is very promising for future applications of such devices.

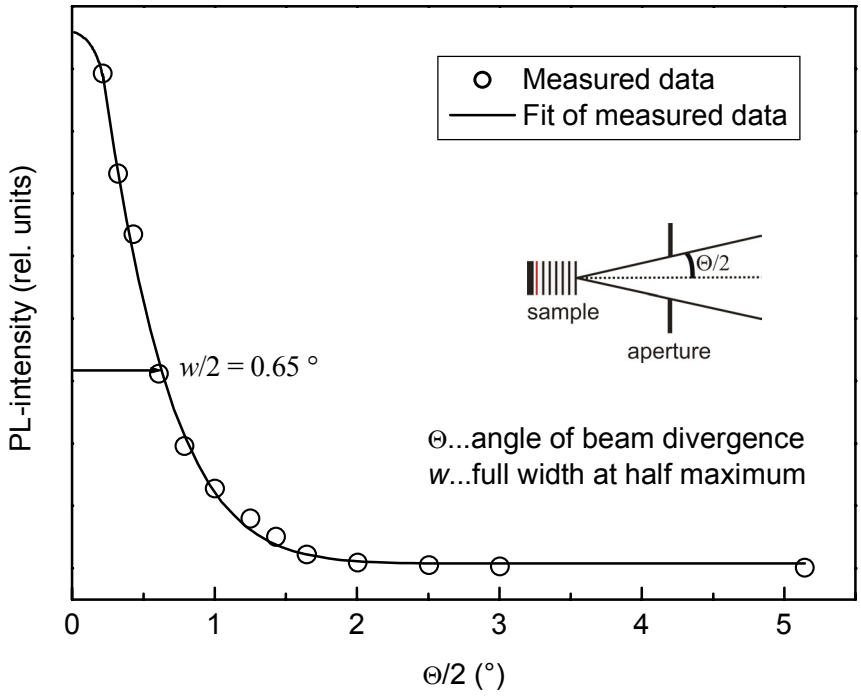

Fig. 2: PL intensity in dependence of half-angle of divergence. Measured data is represented by circles and the fit of measured data by a solid curve. This Gauss distribution results in a total beam divergence of 1.3°.

Conclusion

In conclusion, we have demonstrated microcavity light emitting devices containing either CdSe NCs for operation in the visible at wavelengths around the damping minimum in plastic optical fibers or HgTe NCs with a strong emission in the telecommunication wavelength range. The CdSe based devices show emission from several resonances around 650 nm, with a small mode spacing, solely caused by the large cavity length of 22 microns. This allows one to extract a large fraction of the nanocrystal luminescence from the cavity. In contrast, the optical distance between the mirrors of the HgTe based devices is reduced to obtain a single resonance at the Bragg mirror stop band center. By varying the length of the microcavity, the resonator mode can be well tuned within the Bragg mirror stop band. Since the width of the NC PL is almost as large as the width of the stop band, also the microcavity emission can be tuned between 1.4 and 1.75 microns. This easily enables the adaptation of our devices to applications demanding a certain emission wavelength. Furthermore, the microcavity emission is strongly forward directed and a beam divergence of only 1.3° is demonstrated. Due to the simple and cost effective fabrication of the microcavity devices combined with their favorable optical emission properties with excellent stability also above room temperature, such devices might be attractive alternatives to currently available commercial laser diodes operating in this spectral range. For this electrical excitation is envisaged in the near future.

Acknowledgements

This work was funded by the Austrian Science Fund FWF (Project Y179 and SFB-IRON) and the GMe, Vienna, and in part by the DFG SPP “Photonic Crystals”.

References

[1] J. Roither, M. V. Kovalenko, S. Pichler, T. Schwarzl and W. Heiss, “Nanocrystal based microcavity light emitting devices operating in the telecommunication wavelength range” submitted to Appl. Phys. Lett.

[2] J. Roither, D. V. Talapin, N. Gaponik, A. Eychmuller and W. Heiss, “Highly directional emission from colloidally synthesized nanocrystals in vertical cavities with small mode spacing” Appl. Phys. Lett. 84, 2004, 2223 – 2225

[3] J. Roither, D. V. Talapin, N. Gaponik, A. Eychmuller and W. Heiss, “Colloidally synthesized semiconductor nanocrystals in resonant cavity light emitting devices” Electronics Lett. 38, 2002, 1373 – 1374

High-Mobility n-Channel Organic Field Effect Transistors based on Epitaxially Grown C_{60} Films

Th. B. Singh, N. Marjanović, G. J. Matt, S. Günes and N. S. Sariciftci

Linz Institute for Organic Solar Cells (LIOS), Physical Chemistry, Johannes Kepler University Linz, Austria

A. Montaigne Ramil, A. Andreev, and H. Sitter

Institute of Semiconductor and Solid State Physics, Johannes Kepler University Linz, Austria

R. Schwödiauer and S. Bauer

Soft Matter Physics, Johannes Kepler University Linz, Austria

Introduction

Organic thin-film electronics has developed to a promising technology in the last two decades with demonstrated prototypes of organic thin film transistors, organic integrated circuits for radio frequency identification tags (RFID-tags) [1], [2] and active matrix displays [3]. Organic field effect transistors (OFETs) have also been fabricated in arrays to drive electrophoretic display pixels [4]. The performance of the individual transistor limits the switching speed in an integrated circuit, which can be roughly estimated by the ratio of mobility and channel length of the transistor [3]. To obtain higher switching speed, the search for higher mobility materials is therefore important along with the effort to downscale the transistor geometry.

In this paper, we present results on OFETs fabricated using hot wall epitaxy (HWE) grown C_{60} films on top of an organic insulator. HWE, working close to thermodynamical equilibrium, is well known as appropriate technique to grow highly ordered organic thin films, including C_{60} films. The relatively smooth surface of the organic insulating film interfaced with a highly ordered HWE grown C_{60} film resulted in mobilities of 0.4 – 1 cm^2/Vs and an on/off ratio $>10^4$. The obtained mobility is found to be nearly gate voltage independent with a normalized sub-threshold slope of 8 $V \cdot nF/decade \cdot cm^2$. Furthermore, the field effect mobility has been found to be thermally activated with an activation energy of ~100 meV within the temperature range of 90 – 300 K.

Experimental

A scheme of the device geometry is shown in Fig. 1 (a). The device fabrication starts with the etching of the indium tin oxide (ITO) on the glass substrate. After patterning the ITO and cleaning in an ultrasonic bath, a BCB layer is spin coated at 1500 rpm resulting in a 2 µm thick film. BCB was used as received from Dow Chemicals and curing was done according to the standard procedure. BCB is an excellent dielectric material with a rather low dielectric constant ε_{BCB}= 2.6 and a small, nearly temperature independent thermal expansion coefficient [5]. A 300 nm thick C_{60} film was grown by HWE on top of the dielectric at a substrate temperature of 130 °C. The top source and drain electrodes (LiF/Al 0.6 / 60 nm) were evaporated under vacuum ($2x10^{-6}$ mbar) through a

shadow mask. LiF / Al is expected to form ohmic contacts on fullerenes [6]. The channel length L of the device is 35 µm and channel width W = 1.4 mm, which results in a W/L ratio of ≈40. From the measurement of the BCB film thickness, d = 2 µm and the dielectric constant of BCB, ε_{BCB} = 2.6, a dielectric capacitance C_{BCB} = 1.2 nF/cm^2 was calculated. In our devices we have a d/L ratio ≈0.05 acceptable not to screen the gate field by the source drain contacts. Device transportation from the HWE chamber to the glove box and further electrical characterization (using Keithley 236 and Keithley 2400 instruments) were carried out under argon environment. The surface morphology and thickness of the dielectric was determined with a Digital Instrument 3100 atomic force microscope (AFM) and a Dektak surface profilometer respectively. Device characterization at various temperatures was performed in a He flow cryostat (Cryo Industries) using a Lakeshore 331 as temperature controller.

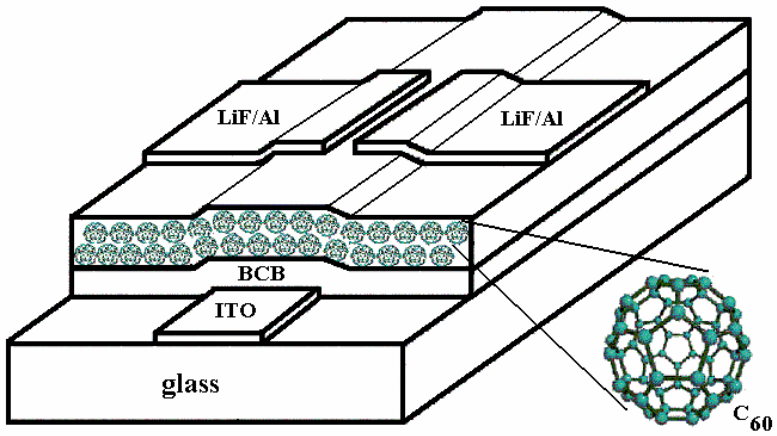

(a)

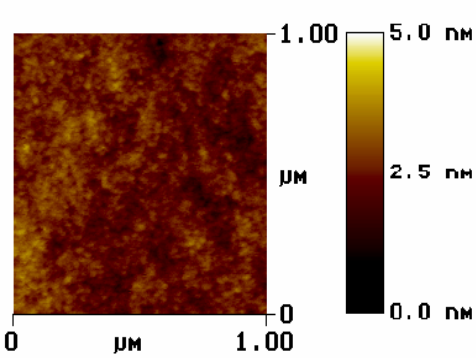

(b)

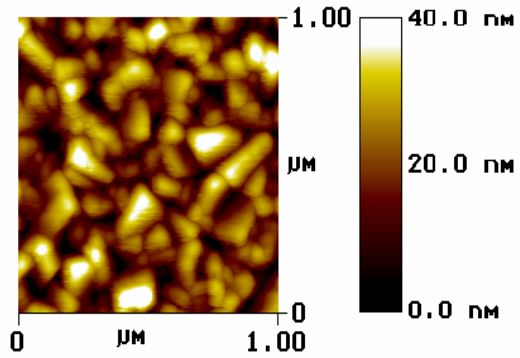

(c)

Fig. 1: (a) Scheme of the staggered n-channel OFET device structure; (b) AFM image of the BCB dielectric surface; (c) AFM image of the C_{60} surface in the channel region of the fabricated OFET.

Results

As shown in Fig. 1 (b), the dielectric layer showed a very smooth surface with a roughness <5 nm. This enables us to grow the next layer (C_{60}) with a very good control of the film morphology (Fig. 1 (c)). A recent study shows that the first couple of monolayers next to the dielectric dominate the charge transport in an organic semiconductor layer.

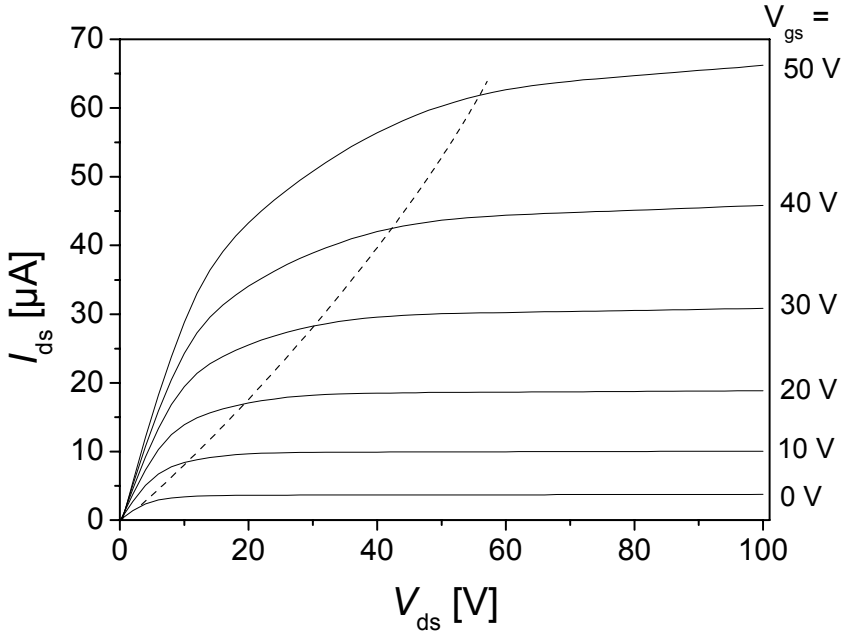

Fig. 2: $I_{ds}(V_{ds})$ curve of the OFET in the accumulation mode. The dotted line is a guide for the eye for saturated I_{ds}. The data shown here are taken in ascending V_{gs} mode with integration time of 1s

Figure 2 shows the transistor characteristics of a device with a well saturated curve occurring pinch off at drain source voltage $V_{ds} \geq V_{gs}$ (gate Voltage). From the slope at V_{ds}= 0 V of the curve V_{gs} = 0 V, we evaluated a conductivity of 5 x 10^{-6} Scm^{-1}. For the same device (see Fig. 3) we measured the transfer characteristics. The data presented in Fig. 3 hold for V_{ds} = 60 V. One can see that the transistor turns on at an onset voltage of V_t = -35 V without significant hysteresis and drain-source current I_{ds} increases quadratically. The device shows an on/off ratio >10^4 which is calculated as a ratio of I_{ds} at V_{gs} = 60 V and I_{ds} at V_{gs} = V_t. We have observed consistently the effect of having large drain-source current even when V_{gs} = 0 V. This effect is minimized when the dielectric layer is preheated at high temperature prior to the deposition of the active layer. This results in the shift of V_t. This effect is proposed to the presence of unintentional dopants at the interface of the untreated dielectric. Interfacial effects seem to play a major role in these devices. From $V_t = -(qn_0d_s/C_{BCB}) + V_{fb}$, where V_{fb} = 0.1 V is the flat band potential (which accounts for the work function difference between the semiconductor and the gate electrode without considering fixed charges at the dielectric and at the interface), d_s is the thickness of the semiconductor, q is the elementary charge and C_{BCB} is the capacitance of the gate dielectric, we were able to estimate the density of free carriers at equilibrium n_o. This yields a relatively high electron density of ~10^{17} cm^{-3}.

As shown in Fig. 3, from the fit to the data using equation (1) [7]:

$$I_{ds} = \frac{\mu W C_{BCB}}{2L}\left(V_{gs} - V_t\right)^2 \qquad (1)$$

we extract a field effect mobility of 0.63 $cm^2V^{-1}s^{-1}$ in the saturation regime for V_{ds} = 60 V (note the fitting line used for the mobility extraction fits the data over a wide range of V_{gs}). However, while we calculated field effect mobility, contact resistance of LiF/Al and C_{60} is not taken into account assuming contact resistance is fairly low. Our studies of the dependence of field effect mobility on metal work functions on soluble methanofullerene based OFETs have shown a highest µ of 0.2 $cm^2V^{-1}s^{-1}$ with LiF/Al as drain-

source electrode. Use of higher work function metal electrodes viz. Cr, Au etc. in these OFETs leads to slightly reduced mobilities. Similarly we have also observed the slight decrease in field effect mobility in C_{60} OFETs with higher work function electrode (not shown here). To our best understanding of OFETs, the device performance and mobility strongly depend on the choice of the dielectric layer mainly due to a different surface energy of the dielectric layer. The sharp turn on of I_{ds} is a measure of the quality of the dielectric/semiconductor interface which is defined by the normalized subthreshold slope, $S = C_{BCB} \mathrm{d}V_{gs}/\mathrm{d}(\log I_{ds})$ [7]. As usually observed in organic FETs, subthreshold slope of 8 V·nF/decade·cm^2 obtained by us is very high which can be reduced by reducing the thickness of the dielectric layer. We presume, the most important factor in achieving this high mobility OFET is the combination of a smooth organic dielectric surface and a highly ordered C_{60} film grown by HWE.

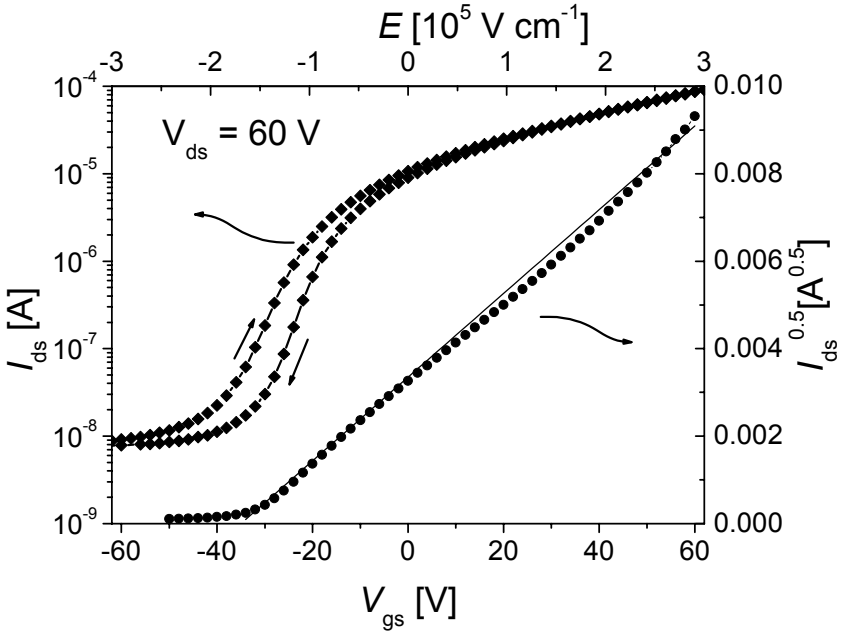

Fig. 3: Semilogarithmic plot of Ids vs. Vgs (left scale) and plot of Ids0.5 vs Vgs (right scale) for the same C60 OFET as in Fig. 2. The full line shows a fit to the data (return curve) using equation (1) from which a field-effect mobility μ = 0.63 cm2/Vs is obtained. Each measurement was carried out with an integration time of 1 s.

Conclusion

In conclusion, we have demonstrated an n-channel OFET with an electron mobility of 0.4 – 1 cm^{2}V^{-1}s^{-1} along with an on/off ratio >10^4 using a solution based organic dielectric BCB film in combination with HWE grown C_{60} films. The obtained mobility is nearly gate voltage independent. Very few studies have been done so far on growing highly ordered organic thin films on top of organic dielectrics partly due to low glass transition temperature and unwanted hysteresis. Use of BCB among other organic dielectrics is based on the fact that its low hysteresis and high glass transition temperature which is an additional advantage for optimizing the film growth condition at high substrate temperatures.

Acknowledgements

Special thanks are to Michael Auinger and Philipp Stadler for technical help. This work was performed within the Christian Doppler Society's dedicated laboratory on Plastic Solar Cells. Furthermore, we acknowledge financial support from the Austrian Foundation for the Advancement of Scientific Research (FWF P15155, P15627 and P15629).

References

[1] Two most recent review articles, (a) W. Clemens, W. Fix, J. Ficker, A. Knobloch and A. Ullmann, J. Mat. Res. 19, 1963 (2004); (b) G. Horowitz, J. Mat. Res. 19, 1946 (2004) and reference there in.

[2] B. Crone, A. Dodabalapur, Y. -Y. Lin, R. W. Filas, Z. Bao, A. Laduca, R. Sarpeshkar, H. E. Katz and W. Li, Nature 403, 521 (2000).

[3] H. E. A. Huitema, G. H. Gelinck, J. B. P. H. van der Putten, K. E. Kuijk, C. M. Hart, E. Cantatore, P. T. Herwig, A. J. J. M. van Breemen and D. M. de Leeuw, Nature 414, 599 (2001).

[4] L. -L. Chua, P. K. H. Ho, H. Sirringhaus and R. H. Friend, Appl. Phys. Lett. 84, 3400 (2004).

[5] R. Schwödiauer, G. S. Neugschwandtner, S. Bauer-Gogonea, S. Bauer and W. Wirges, Appl. Phys. Lett. 75, 3998 (1999).

[6] (a) V. D. Mihailetchi, J. K. J. van Duren, P. W. M. Blom, J. C. Hummelen, R. A. J. Janssen, J. M. Kroon, M. T. Rispens, W. J. H. Verhees and M. M. Wienk, Adv. Func. Mater. 13, 43 (2003)

[7] G. Horowitz, R. Hajlaoui and F. Kouki, Eur. Phys. J. AP 1, 361 (1998).

Continuous Wave Mid-Infrared IV–VI Vertical Cavity Surface Emitting Lasers

G. Springholz, T. Schwarzl, M. Böberl, W. Heiss,

Institut für Halbleiter und Festkörperphysik, Universität Linz, Altenbergerstraße 69, 4040 Linz, Austria

J. Fürst, H. Pascher

Experimentalphysik I, Universität Bayreuth, D-95447 Bayreuth, Germany

Continuous wave emission of mid-infrared IV-VI vertical-cavity surface-emitting laser structures with PbSe as active medium is demonstrated for the 6 to 8 µm wavelength region. The lasers are based on ultra-high finesse microcavity structures formed by high reflectivity EuSe/PbEuSe Bragg mirrors. Optically pumped cw laser emission is observed up to temperatures of 120 K. We achieved internal threshold pump intensities of down to 25 W/cm^2, which is two orders of magnitude smaller than reported so far. The line width of the laser emission is only 18 µeV (0.9 nm) with a strong narrowing as compared to the line width of the cavity resonance. Continuous wave output powers are up to 4.8 mW.

Introduction

Narrow bandwidth coherent mid-infrared emitters are extremely useful for ultrahigh-sensitive chemical gas analysis and atmospheric pollution monitoring [1] because most strong absorption lines of molecular gases are found in the mid-infrared spectral region. Due to their nearly symmetric conduction and valence bands and their very small non-raditative Auger recombination rates [2], the IV-VI semiconductors or lead salt compounds are very well suited for such applications. Therefore, edge emitting IV-VI semiconductor laser diodes have long been used for MIR gas spectroscopy and detection with operation temperatures up to 223 K in continuous wave (cw) [3] and above room temperature in pulsed mode [4]. As compared to edge emitting lasers, vertical cavity surface emitting lasers (VCSELs) offer several advantages such as very small beam divergences, single mode operation, and the possibility of monolithic integration and potentially lower threshold pump powers. For IV-VI lasers, another important advantage of VCSELs is that they can be grown on readily available BaF2 substrates, which have a much higher thermal conductivity and mechanical hardness than the usual high-cost IV-VI substrates. Since their first demonstration [5], [6], the performance of optically pumped IV-VI semiconductor vertical-cavity surface-emitting lasers (VCSELs) has been continuously improved [7], and pulsed laser emission has been obtained up to 65°C [8]. In contrast, cw operation of mid-infrared VCSELs at higher temperatures has not been achieved so far, and the longest wavelength for cw-operating mid-infrared VCSELs reported has been 2.9 µm for a type-II antimonide active region [9]. In the present work, we report the fabrication and operation characteristics of cw PbSe VCSEL samples for long-wavelength emission between 6.7 and 8 µm.

Structure and Design

As our previous photoluminescence studies have shown that PbSe exhibits superior luminescence efficiency as compared to PbTe [10], Se-based compounds were used

for all VCSEL layers. The microcavity structures were designed by matrix transfer calculations [5] – [8]. Due to the strong temperature dependence of the band gap, IV-VI VCSELs have to be tailored for a certain operation temperature [7], [8]. As PbSe emits at 6.5 µm or longer only at cryogenic temperature, the lasers were designed for an operation temperature of around 90 and 4 K. Thus, the VCSEL structure is formed by two high-reflectivity Bragg mirrors consisting of five λ/4 EuSe/$Pb_{0.94}Eu_{0.06}Se$ layer pairs. Due to the high refractive index contrast of 50% between these mirror materials, only five layer pairs are required to obtain a reflectivity well above 99%.

The 2 λ thick cavity region between the mirrors consists of a 2.2 µm $Pb_{0.94}Eu_{0.06}Se$ buffer and a 1.1 µm PbSe active region. The cavity design ensures that neither the PbSe laser emission nor the 5.3 µm pump laser is absorbed in the mirror layers, and that the pump wavelength does not coincide with the mirror stop band. The complete laser structure was grown by molecular beam epitaxy onto (111) BaF_2 substrates at a substrate temperature of 250 °C. Two cw-VCSELs were fabricated for different operation temperatures and emission wavelengths. The first one was designed for operation at liquid He temperature, and thus, the cavity resonance wavelength was set to the 7.9 µm PbSe band gap emission at 4 K. The second VCSEL was designed for 85 K operation with a corresponding PbSe emission at about 6.7 µm. A cross sectional electron microscopy image of this VCSEL is shown in the insert of Fig. 1 (b).

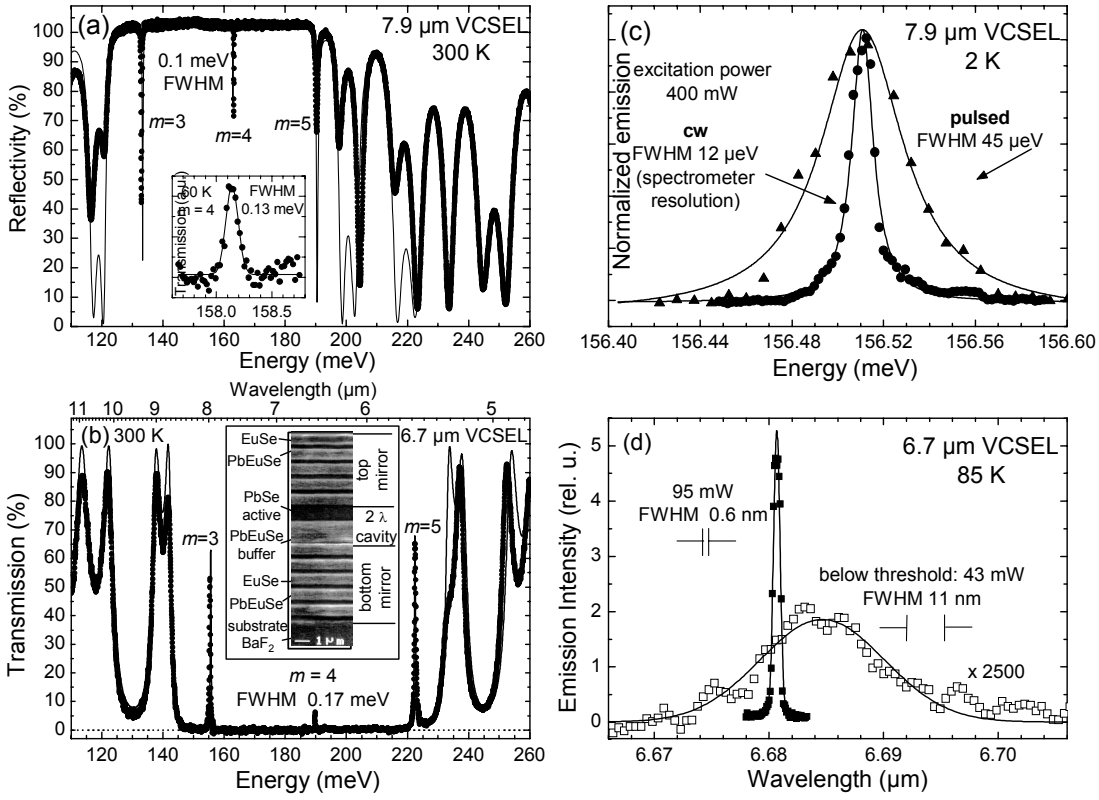

Fig. 1: (a) Reflectivity of the 7.9 µm cw-VCSEL, and (b) transmission of the 6.7 µm cw-VCSEL, both measured at 300 K. The solid lines correspond to the theoretical spectra calculated using the transfer matrix method. The insert in (a) shows the transmission around the central cavity mode at 60 K on an enlarged scale, and the insert in (b) the cross-sectional scanning electron microscopy image of the VCSEL structure. Right hand side: (c) Emission spectra of the 7.9 µm VCSEL at 2 K in cw (dots) and pulsed mode (triangles), both at 400 mW pump power. (d) Emission of the 6.7 µm VCSEL at 85 K at a pump power of 95 mW (■) above threshold and 43 mW (□) below threshold.

Optical Properties

Figure 1 (a) shows the reflectivity spectrum of the 7.9 μm VCSEL measured at 300 K. At this temperature, the spectrum exhibits three narrow cavity resonances of m = 3rd, 4th, and 5th order at 133, 163, and 190 meV (9.33, 7.61, and 6.53 μm), respectively. The measured line width of the 3rd resonance mode is 0.25 meV, whereas that of the central 4th order mode is only 0.10 meV, demonstrating a high cavity finesse of about 400, taking into account the order of the mode. The calculated reflectivity spectrum, shown by the solid line in Fig. 1 (a), is in very good agreement with the experimental data. Owing to the decrease of the energy band gap of PbSe from 279 meV at 300 K to 146 meV at 2 K, at low temperature the higher energy cavity resonances are damped by the interband PbSe absorption. Thus, at 60 K (see insert of Fig. 1 (a)), the 4th order cavity resonance is broadened from 0.10 meV at room temperature to 0.13 meV. At even lower temperatures, the 4th order resonance completely disappears because this wavelength is completely absorbed by the PbSe active region. Comparing the 300 K and 60 K spectra one can see that the spectral position of the resonances shifts to lower energies at a rate of 22 μeV/K to 158 meV or 7.8 μm at 60 L due to the increasing refractive index of the cavity material. For the room temperature transmission spectrum of the 6.7 μm VCSEL (Fig. 1 (b)), again, three cavity resonance peaks are observed, but now at energies of 155, 190 and 223 meV or λ = 8.0, 6.53, and 5.23 μm, respectively. The line width of the central 4th order cavity mode is only 0.17 meV or 7 nm, indicating a cavity finesse of about 300. As the temperature is lowered, again the resonance positions are red-shifted due to the increasing refractive index and below 100 K the central cavity mode becomes damped due to the PbSe absorption.

Laser Emission

Both VCSELs were optically pumped with a cw-CO laser emitting at a 5.28 μm wavelength (235 meV). The pump beam was focused onto the sample surface to a spot size of about 200 μm and the emitted light was detected with an HgCdTe detector through a grating spectrometer using the lock-in technique. The total emitted power was measured with a calibrated detector using an InSb long pass filter. Figure 1 (c) shows the emitted laser line for cw as well as pulsed excitation with 400 mW pump power in both cases. At 2 K, the stimulated emission of the 4th order resonance of the 7.9 μm VCSEL is found at 156.51 meV, *i.e.,* λ = 7.92 μm. This represents the longest emission wavelength of all VCSELs reported to date. For cw operation, an extremely narrow line width of only 12 μeV (0.6 nm) is observed, as found from the Lorentzian line fits shown as solid lines in Fig. 1 (c). This line width is 10 times smaller than the 130 μeV width found for the unpumped cavity resonance in the 60 K transmission measurements of Fig. 1 (a); and it is also much narrower than that observed for pulsed mode emission that is shown by the solid triangles in Fig. 1 (c). At 400 mW peak power excitation, the FWHM of the pulsed laser emission is 45 μeV (2.3 nm), but increases up to 100 μeV when the pump power is increased. This is still below the width of the unpumped cavity and is attributed to dynamical broadening effects. For cw-excitation, the measured line width is exactly the resolution of the spectrometer setup. Thus, the true cw line width must be actually much smaller than 0.6 nm.

The emission spectra of the 6.7 μm VCSEL at 85 K are shown in Fig. 1 (d). At a low pump power of 43 mW, a weak emission at 6.685 μm with an 11 nm FWHM is found (open squares in Fig. 1 (d)), which corresponds to the expected wavelength and line width of the 4th order cavity resonance at 85 K. Therefore, this signal is attributed to spontaneous emission, filtered out by the cavity mode. At a doubled excitation power of 95 mW (filled squares in Fig. 1 (d)), the emitted intensity increases drastically by a factor of 5000 and it is a factor of 20 narrower. The line width as determined by a Gaussian line fit (solid line) is only 0.6 nm or 16 μeV, again limited only by the spectrometer

resolution (denoted by –||– in the figure). Thus, above threshold we observe a very strong spectral narrowing not only with respect to the width of the passive cavity mode, but also compared to the spontaneous emission signal.

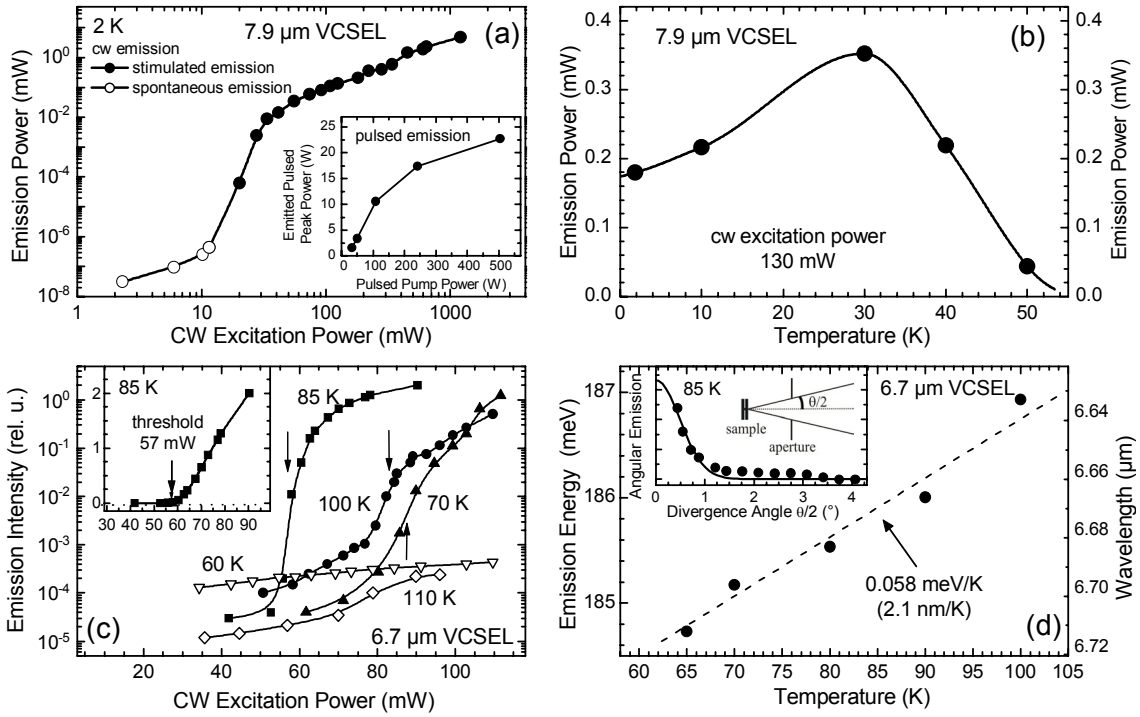

Fig. 2: (a) Cw output power of the 7.9 µm VCSEL plotted as a function of pump power at 2 K: (o) spontaneous emission, (●) laser emission. The 25 mW laser threshold is determined from the inflection point. Inset: pulsed laser output versus excitation power. (b) Cw output power of the same VCSEL at 130 mW pump power plotted versus operation temperature. (c) Cw output intensity of the 6.7 µm VCSEL plotted versus pump power at temperatures between 60 and 110 K: full symbols: stimulated emission, open symbols: spontaneous emission. Insert output intensity versus pump power at 85 K on a linear scale, with the thresholds indicated by arrows. (d) Tuning characteristics of the 6.7 µm VCSEL: emission energy and emission wavelength plotted versus operation temperature. This yields a linear tuning coefficient of +0.058 meV/K or -2.1 nm/K. The insert shows the measured angular emission characteristics of the laser (dots). The solid line represents the Gaussian line fit to the data points.

Figure 2 (a) shows the cw power emitted by the 7.9 µm VCSEL as a function of excitation power. For weak excitation, only spontaneous emission (open circles) is observed. Above threshold, the emitted power rapidly increases (full circles). As can be seen by the inflection point of the S-shaped curve of the double logarithmic plot in Fig. 2 (a), the external laser threshold is 25 mW. Since the pump laser was focused to a diameter of 200 µm, this corresponds to an internal threshold of 25 W/cm^2, where the 63 % reflectivity of the laser structure at the pump energy is taken into account. At an excitation power of 1.2 W, the cw power emitted through one Bragg mirror is 4.8 mW. This is the highest observed from any cw VCSEL in the mid-infrared. For higher excitation powers, pulsed mode excitation was used in order to prevent thermal damaging of the sample. The inset of Fig. 2 (a) shows the emitted pulse peak power as a function of pump power. For 500 W pump pulses, a peak power of 23 W is emitted from one side of the

VCSEL. Due to the symmetric cavity design, the total emitted power is twice the power measured from one side. Therefore, the conversion efficiencies for cw and pulsed operation at maximum output powers are 0.8 % and 9 %, respectively. The maximum pulsed mode efficiency is 20 %, at 100 W pump power. Below 100 W, the slope efficiency determined by linear fits is 24 % whereas for CW operation a value of 1% was found.

The temperature dependence of the 7.9 µm VCSEL emission is shown in Fig. 2 (b) for a constant 130 mW excitation power. Up to 30 K, the spontaneous emission of the PbSe active material shifts closer to the 4^{th} order cavity mode. Thus, the emitted intensity increases. At 30 K, the maximum of the spontaneous emission coincides with the cavity resonance, manifested in best laser performance. Above 30 K, the emitted intensity is reduced because the maximum of the spontaneous emission shifts above the cavity mode. At 57 K, the laser emission is quenched due to complete detuning of resonance and spontaneous emission.

The threshold behavior of the 6.7 µm VCSEL sample is shown in Fig. 2 (c) for different temperatures. Again, the data is plotted on a logarithmic scale to reveal also the sub-threshold signals. For clarity, the measurement for 85 K is also plotted in the inset on a linear scale. The threshold pump power was evaluated for operation temperatures of 70 (triangles), 85 (squares) and 100 K (circles) to be 87, 57 and 83 mW, respectively, as indicated by the arrows at the inflection points of the logarithmic plots. Thus, the minimum threshold is at the design temperature, where the maximum of the spontaneous emission and the cavity mode position coincide. The minimum pump threshold of 57 mW at 85 K corresponds to an internal threshold power density of 67 W/cm^2. In the logarithmic plots one can not only see the sub-threshold signals, but also the emission at 60 and 110 K (open symbols in Fig. 2 (c)), at which only weak and much broader spontaneous emission is observed. Thus, this VCSEL operates only at temperatures between 65 and 100 K because at higher as well as lower temperatures, the PbSe emission is above or below the cavity mode. The maximum observed total cw output power at 85 K is 1.2 mW at a pump power of 230 mW, which corresponds to a conversion efficiency of 0.5 %. We have also fabricated a third VCSEL with a design wavelength of 6.5 µm. This laser shows essentially the same performance as the 6.7 µm laser, but due to the shorter wavelength it lases up to a temperature of 120 K.

For applications of the lasers for molecular spectroscopy, the tuning ability and beam divergence are of crucial importance. These are characterized in detail in Fig. 2 (d) for the 6.7 µm VCSEL. The total tuning range by temperature variation was found to be 70 nm, with a linear tuning coefficient of +0.058 meV/K or –2.1 nm/K. This large tuning range is particularly advantageous for spectroscopy and it is substantially larger as compared to that of III-V quantum cascade lasers operating in the same wavelength range with a typical tuning coefficient of 0.01 meV/K [11]. In addition, we have recently shown that the emission wavelength can also be tuned quite elegantly by applying external magnetic fields [12]. In this case, we have found that the laser emission splits into two circularly polarized lines with opposite polarization. Therefore, the lasing action involves only spin polarized electronic states, *i.e.*, these VCSELs can be viewed as a novel kind of spin laser. We have also determined the angular emission characteristic of the cw VCSELs. As demonstrated in the inset of Fig. 2 (d) for an emission angle of only 1° off the surface normal (see sketch in the inset), the emission intensity (filled squares) essentially drops to zero, and the Gaussian line fit to the emission profile (solid line) yields a half width at half maximum of only 0.5°. This narrow forward directed emission is a clear advantage of the VCSELs as compared to edge emitters. Up to now, the cw-operation temperatures were limited by the pump laser wavelength as well as the temperature dependence of the PbSe photoluminescence emission. It is therefore anticipated that already minor changes in the cavity structure and active region design as well as the use of other pump sources will soon lead to higher cw-laser operation temperatures.

Conclusion

In conclusion, lead salt vertical-cavity surface-emitting lasers offer attractive properties as coherent infrared laser sources. They feature single mode operation, emit circularly shaped parallel beams with extremely small beam divergence, and exhibit very sharp emission lines widths below 12 μeV. Based on the use of high finesse infrared microcavity structures, cw-operation up to 120 K was demonstrated, which is expected to be significantly increased in the near future. In comparison with quantum cascade lasers, the lead salt VCSELs show a substantially larger wavelength tunability, which is of crucial importance for spectroscopy applications.

Acknowledgements

This work was funded by the Fonds zur Förderung der wissenschaftlichen Forschung.

References

[1] M. Tacke, in: Long Wavelength Infrared Emitters Based on Quantum Wells and Superlattices, edited by M. Helm (Gordon and Breach Science, Amsterdam, 2000), pp. 347–396

[2] P. C. Findlay, C. R. Pidgeon, R. Kotitschke, A. Hollingworth, B. N. Murdin, C. J. Langerak, A. van der Meer, C. M. Ciesla, J. Oswald, A. Homer, G. Springholz, and G. Bauer, “Auger recombination dynamics of lead salts under picosecond free-electronlaser excitation” Phys. Rev. B 58, 1998, 12908 – 12914

[3] Z. Feit, M. McDonald, R. Woods, V. Archembault, P.Mak, “Single-mode molecular beam epitaxy grown PbEuSeTe/PbTe buried-heterostructure diode lasers for CO_2 high-resolution spectroscopy” Appl. Phys. Lett. 68, 1996, 738 – 740

[4] U. P. Schiessl and J. Rohr, “60°C lead salt laser emission near 5 μm wavelength” Infrared Phys. Technol. 40, 1999, 325 -330.

[5] T. Schwarzl, W.Heiss, G.Springholz, M.Aigle, H.Pascher, “6 μm vertical cavity surface emitting laser based on IV-VI compounds” Electron.Lett. 36, 2000, 322 – 324

[6] W. W. Bewley, C. L. Felix, I. Vurgaftman, J. R. Meyer, G. Xu, and Z. Shi, “Lead salt vertical-cavity surface-emitting lasers operating at λ = 4.5 − 4.6 μm with optical pumping” Electron. Lett. 36, 2000, 539–540

[7] J. Fürst, H. Pascher, T. Schwarzl, M. Böberl, W. Heiss, G. Springholz, G. Bauer. “MIR IV-VI vertical cavity surface-emitting lasers with zero-, two-, and three-dimensional systems in the active region”, Appl. Phys. Lett. 81, 2002, 208 – 210

[8] W. Heiss, T. Schwarzl, G. Springholz, K. Biermann, K. Reimann. “Above-room-temperature mid-infrared lasing from vertical-cavity surface-emitting PbTe quantum-well lasers”, Appl. Phys. Lett. 78, 2001, 862 – 864

[10] M. Böberl, W. Heiss, T. Schwarzl, K. Wiesauer, G. Springholz, “Mid-infrared continuous-wave photoluminescence of lead salt structures up to temperatures of 190°C” Appl. Phys. Lett. 82, 2003, 4065-4067

[11] T. Allen, S. Blaser, M. Beck, D. Hofstetter, J. Faist, and E. Gini, “Continuous-wave distributed-feedback quantum-cascade lasers on a Peltier cooler” Appl. Phys. Lett. 83 (2003) 1929-1931.

[12] J. Fürst, H. Pascher, T. Schwarzl, G. Springholz, M. Böberl, G. Bauer, W. Heiss, “Magnetic field tunable circularly polarized emission from midinfrared IV-VI vertical emitting lasers” Appl. Phys. Lett. 86, 2005, 021100-2

X-Ray Diffraction from a SiGe Island Quasicrystal

J. Stangl, J. Novak, E. Wintersberger, V. Holy, G. Bauer

Institute for Semiconductor and Solid State Physics, University of Linz, A-4040 Linz

Introduction

Nanometer-sized semiconductor islands and quantum dots have opened up the route to novel optoelectronic and electronic applications. The growth of islands by self-assembly in the Stranski-Krastanow growth mode is a well-established method. In general, self-assembled islands are inhomogeneous in size. An improvement of the size homogeneity can be achieved by growing islands in regular two dimensional (2D) arrays [1] – [5]. Such a 2D island lattice can be extended into a three dimensional (3D) island crystal by stacking island layers separated by spacer layers using appropriate growth conditions [6], [7]. Shape and size of the islands as well as their chemical composition undergo substantial changes during capping mainly due to interdiffusion with the spacer material. Direct images of the morphology of buried islands can be obtained by cross-section transmission electron microscopy (TEM) and scanning tunneling microscopy (STM) (see Ref. [8] and references therein). Alternatively, structural properties of buried islands can be studied by x-ray diffraction (XRD), which yields information on a much larger ensemble of the islands and is particularly sensitive to lattice strains.

We used coplanar high-angle XRD to investigate the size and the chemical composition of Ge/Si islands in a 3D island crystal. The evaluation of the experimental data was based on calculations of diffusely scattered intensity for a model island. For the calculations of the elastic strain fields caused by lattice mismatch between Si and Ge, we refined an analytical solution of continuum elasticity equations, which was used in Refs. [9] – [11] for the calculation of strain fields in two dimensions, for SiGe wires and laterally modulated $InAs_nAlAs_m$ short period superlattices.

Experimental

The investigated sample was grown by solid-source molecular beam epitaxy on Si(001), which was prepatterned with a square grid of pits using electron beam lithography and reactive ion etching. The pit grid is oriented along ⟨110⟩ directions and has a period of 400 nm. The size of the patterned area is 0.5 x 0.5 mm^2. After growth of a 150 nm thick Si buffer layer, further deposition of 6 ML of Ge at 700 °C resulted in 2D ordered islands, with one island per pit. After depositing 30 nm of Si as a spacer layer 12 double-layers of Ge islands and Si spacer layers of about 25 nm were deposited at 650 °C. The topmost island layer was left uncapped for atomic force microscopy (AFM) investigations. The islands grew in the same 2D grid in each island layer due to their preferential nucleation in strain energy minima above the underlying islands in the pits.

A nearly perfect 3D island crystal was produced in this way. Details on growth and atomic force microscopy (AFM) images of the topmost island layer are shown in Ref. [7]. The aspect ratio of the uncapped island sidewalls height/width = 0.2 corresponds to {105} sidewall orientation, which is characteristic for pyramidal islands.

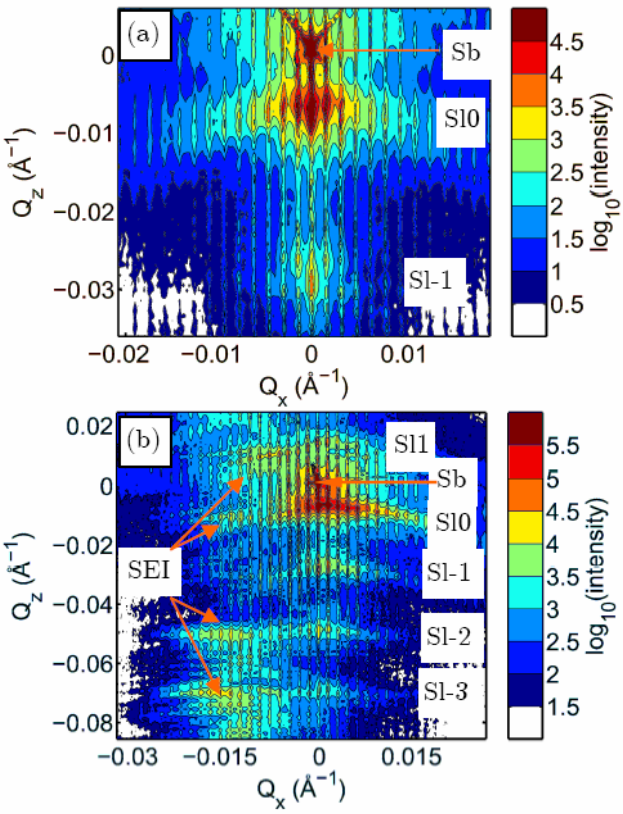

Fig. 1: Measured reciprocal space maps around the (224) (a) and (004) (b) reciprocal lattice points. Vertical satellites, originating from the periodicity of the island layers along the growth direction, are denoted Sl-3 to Sl1. Substrate peaks are denoted by Sb, and SEI denotes stripes of enhanced intensity (see text).

The measurements were carried out at beamline ID10B at the European Synchrotron Radiation Facility (ESRF), Grenoble, at a wavelength of 1.547 Å. High-resolution XRD was measured in coplanar geometry using a Si (111) analyzer in front of a point detector in order to resolve the lateral satellites. Diffusely scattered intensity around the symmetrical (004) and asymmetrical (224) substrate lattice points was measured, the resulting reciprocal space maps (RSMs) are shown in Fig. 1. The Si substrate peaks are denoted by Sb, horizontal stripes of enhanced intensity, denoted Sl-3 to Sl1 in Fig. 1, are vertical satellites due to the periodically repeated motif of island layers / spacer layers. Their distance corresponds to a vertical period of $L_\perp$ = 30.0 ± 0.5 nm.

For the simulations of scattered intensity we used kinematical approximation, as we fitted the intensity distribution beside the crystal truncation rods, where dynamic scattering effects are not important. The expressions used involve the displacement field in the sample, which we calculated by means of an analytic solution of the elasticity equations. We assume that the islands in each island layer form a perfect 2D lattice and that the islands are perfectly stacked above each other. Additionally, the size, shape, and chemical composition of all islands in the 3D island crystal are assumed to be identical. We neglected the uncapped island layer on top of the sample, but rather assume a flat sample surface. In coplanar diffraction geometry, the existence of the uncapped island layer has no significant influence on the scattered intensity.

Due to the lateral periodicity of the island pattern, we performed a Fourier transformation in the expressions of the scattered intensity as well as in the displacement fields and the elastic constants, allowing for an analytic solution of the equilibrium equations of elasticity. Details can be found in Ref. [12].

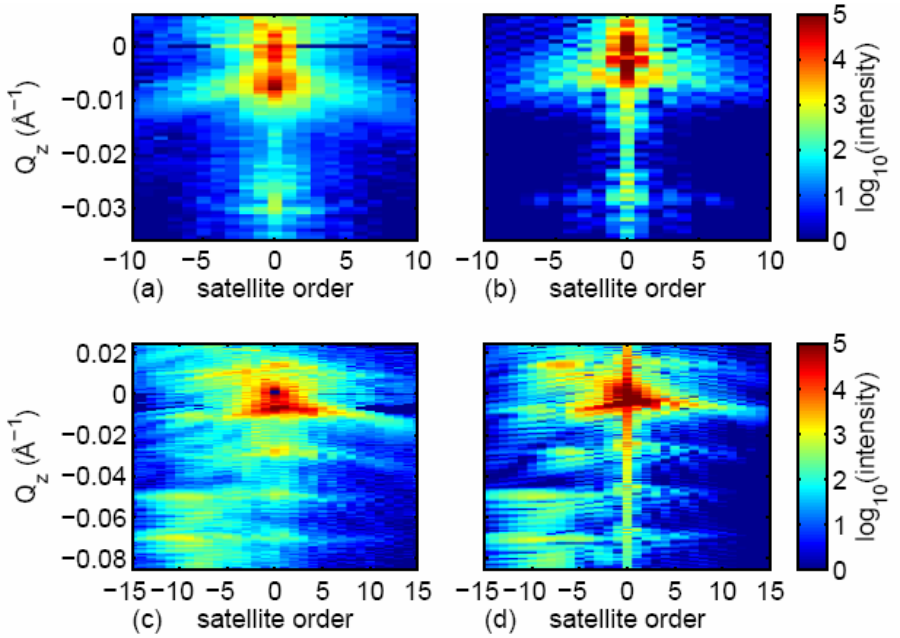

Fig. 2: 2D map of the lateral satellite intensities extracted from RSMs measured around the (004) (a) and (224) (c) reciprocal lattice points. Simulations of diffusely scattered intensity for the (004) (b) and (224) (d) diffractions.

Results

In order to evaluate x-ray data we first fitted the measured intensity profiles along the Q_x axis by series of Lorentzians. Their amplitudes are plotted in Figs. 2 (a), (c) as a function of the satellite order along the [110] direction and Q_z for (004) and (224) diffractions, respectively. The Q_x position of a given lateral satellite order is constant along Q_z, implying vertical replication of the lateral island positions in subsequent layers. The FWHM of the satellites as a function of satellite order is constant and comparable to the instrumental resolution, indicating the excellent long-range order of island positions.

For the simulations of the diffuse intensity and the strain fields all islands were assumed to have the same shape of a truncated cone, characterized by its bottom radius R_{bot}, top radius R_{top}, and height h_i. The Ge content x_i was assumed to be constant within islands. Additionally, a wetting layer (WL) of a constant thickness h_w and a constant Ge content x_w throughout the lateral unit cell was used. A rotational symmetry of the island shape was chosen in accordance with Ref. [13], where the preferential alloying of the island corners due to the surface diffusion of the Si atoms was observed, corresponding to an effective rounding of the islands during capping.

During fitting we made the following observations. (i) The lower the Ge content in the islands, the more intense are the lateral satellites close to the substrate peak. Furthermore, stripes of enhanced intensity within the vertical satellites move closer to the truncation rod. This can be explained by the decrease of the island lattice strain for lower Ge content. (ii) The higher the islands, the further away from the truncation rod the stripes of enhanced intensity are within the vertical satellites. This effect is connected with the larger degree of lattice relaxation in the island layers closer to the top surface. (iii) The vertical shift of the 0^{th} order vertical satellite with respect to the substrate Bragg peak increases with the total amount of Ge in the WL. (iv) Finally, the tilt of the vertical satellites with respect to the Q_x axis increases with the island base radius.

The best simulation (see Figs. 2 (b), (d)) was obtained for island bottom and top radii of R_{bot} = 85 ± 10 nm and R_{top} = 10 ± 10 nm, island height of h_i = 19 ± 4 nm, and a Ge content of x_i = 40 ± 10%. The WL height was h_w = 0.8 nm and its Ge content x_w = 10% (only the product $h_w x_w$ can be determined from the fitting). We obtain an aspect ratio of $\eta = h_i / (R_{bot} - R_{top})$ = 0.25 ± 0.06, close to η = 0.2 of {105} facets typical for Ge pyramids, and different from η = 0.47 of {113} facets typical for Ge domes.

From the simulations also the lateral (ε_{xx}) and vertical (ε_{zz}) strains within the island stack follow (zero strain corresponds to the non-deformed Si lattice). The strain field is almost periodic in the vertical direction only in the region from 4th to 7th island layers; above and below the surface relaxation and influence of the Si substrate destroy the periodicity. The maximum lateral strain of ε_{xx} = 0.9% is observed in compressed SiGe in the top edges of the islands, corresponding to a degree of relaxation of 55% $Si_{0.6}Ge_{0.4}$. The lateral strain minimum of ε_{xx} = –0.5% is observed in compressed Si around the bottom edges of the islands. The vertical strain ε_{zz} increases in the lateral direction from the center of the islands towards their sidewalls. The maximum of ε_{zz} = 3.4% is observed in expanded SiGe in the bottom edge of the islands, and the minimum of ε_{zz} = –2% is observed in compressed Si just above the center of the top island facets.

Conclusion

An analysis of coplanar high-angle x-ray diffraction data was performed and structural information on buried Ge islands was obtained, which form a 3D island crystal. Combining an analytical solution of equilibrium equations of linear elasticity and kinematical scattering theory we successfully simulated the experimental x-ray diffraction data. Comparing the measured reciprocal space maps of the diffracted intensity with simulations, we found that the islands have {105} facets after Si capping, i.e., they have pyramidal shape. The Ge content in the islands is as low as 40 ± 10%. From the fits, also the strain state in and around the buried islands was determined.

References

[1] O.G. Schmidt *et al.*, Appl. Phys. Lett. **77**, 4139 (2000).

[2] G. Jin, J.L. Liu, K.L. Wang, Appl. Phys. Lett. **76**, 3591 (2000).

[3] M. Borgström, V. Zela, W. Seifert, Nanotechnology **14**, 264 (2003).

[4] Bin Yang, Feng Liu, M.G. Lagally, Phys. Rev. Lett. **92**, 25502 (2004).

[5] Zh. Zhong, G. Bauer, Appl. Phys. Lett. **84**, 1922 (2004).

[6] G. Springholz, V. Holý, M. Pinczolits, G. Bauer, Science **282**, 734 (1998).

[7] Zh. Zhong *et al.*, Physica E **21**, 588 (2004).

[8] J. Stangl, V. Holý, G. Bauer, Rev. Mod. Phys. **76**, 725 (2004).

[9] T. Roch *et al.*, Phys. Rev. B **65**, 245324 (2002).

[10] J.H. Li *et al.*, Phys. Rev. B **66**, 115312 (2002).

[11] O. Caha *et al.*, J. Appl. Phys. **96**, 4833 (2004).

[12] J. Novak *et al.*, to be published.

[13] U. Denker, M. Stoffel, O.G. Schmidt, Phys. Rev. Lett. **90**, 196102 (2003).

Sensor Systems

Sensor Systems

M.J. Vellekoop

Institute of Sensor and Actuator Systems, Vienna University of Technology, A-1040 Vienna

In 2004 several new devices have been designed and realized within the ZMNS for the different projects. In the cooperation with the TU Delft (the Netherlands), on-chip particle detectors where made and characterized. These detectors are based on optical (strip photodiodes) and electrical (impedance) measurements. Further, a particle selector and a particle separator, both based on dielectrophoresis have been developed, the last one within the frame of a diploma thesis. The work was presented at the international microTAS conference in Lund, Sweden. In the EU project Microprotein, new layers have been tried out for wetting and electrowetting purposes for manipulation of liquids at the surface of (silicon) chips. Our cooperation with the competence center AC2T have led to novel devices for viscosity sensing which, amongst other things, allow new insight in dispersed fluids. In the frame of an FFF project with the firma Graf, thermal conductivity sensors in silicon have been designed to monitor the ageing of oil.

Cooperations have started with a newly established research center of the Austrian Academy of Sciences (Integrated sensor systems), with ARCS Research, and with Robert Bosch USA. In the frame of the Austrian Nanoinitiative, the MNA Network has been established with partners from the University of Leoben, University of Linz, ARCS Research, IMS (Vienna), IMA, and the University of Agriculture (BOKU) in Vienna.

The research has led to close to 40 publications in scientific journals and international conference proceedings and 1 patent was submitted.

Project Information

Project Manager

Univ.Prof. Michiel J. Vellekoop

Institute of Sensor and Actuator Systems,
Gusshausstrasse 27-29, A-1040 Vienna, Austria

Project Group

Last Name	First Name	Status	Remarks
Agoston	Attila	dissertation	
Beigelbeck	Roman	student	
Hairer	Gabriel	dissertation	
Jachimowicz	Artur	senior researcher	
Jakoby	Bernhard	associate professor	
Keplinger	Franz	postdoc	
Kohl	Franz	postdoc	
Kostner	Stefan	student	
Kuntner	Jochen	dissertation	
Kvasnica	Samuel	postdoc	
Lindenbauer	Thomas	student	
Nieuwenhuis	Jeroen Hans	dissertation	
Pirker	Ewald	technician	
Rocha Wiese Meneses	Daniel Paolo	assistant professor	
Rogler	Gerhard	technician	
Schalko	Johannes	postdoc	
Stangl	Günther	technician	
Svasek	Edeltraud	technician	
Svasek	Peter	technician	
Vellekoop	Michiel J.	full professor	
Zoppel	Sandra	dissertation	

Books and Contributions to Books

1. A. Agoston, C. Ötsch, B. Jakoby:
   "*Evaluation of Sensors for On-line Oil Condition Monitoring*";
   in: "Current Trends in Tribology", K. Vercammen et al. (ed.); Institute for

Terotechnology - National Research Institute, Poland, 2004, ISBN: 83-70204-418-X, L.13 - L.16.

2. D. Rocha Wiese Meneses, P. M. Sarro, M. Vellekoop (ed.):
"*CD-Rom Proceedings of the Third IEEE International Conference on Sensors*";
IEEE Sensors, 2004, ISBN: 0-7803-8693-0; 850 pages.

Publications in Reviewed Journals

1. M. Ando, H. Steffes, R. Chabicovsky, M. Haruta, G. Stangl:
"*Optical and Electrical H_2- and NO_2-Sensing Properties of Au/$In_xO_yN_z$ Films*";
IEEE Sensors Journal, **04** (2004), 2; 232 - 236.

2. R. Beigelbeck, B. Jakoby:
"*A two-dimensional analysis of spurious compressional wave excitation by thickness-shear-mode resonators*";
Journal of Applied Physics, **95** (2004), 9; 4989 - 4995.

3. S. Eder-Kapl, H. Löschner, M. Zeininger, W. Fallmann, O. Kirch, G. Patsis, V. Constantoudis, E. Gogolides:
"*Line edge roughness investigation on hcemically amplified resist materials with masked helium ion beam lithography*";
Microelectronic Engineering, **73-74** (2004), 252 - 258.

4. R. Grössinger, F. Keplinger, H. Hauser:
"*The Design and Construction of a Thin Foil High Field Magnet*";
Physica B, **346-347** (2004), 604 - 608.

5. V. Iordanov, J. Bastemeijer, R. Ishihara, P. M. Sarro, A. Bossche, M. Vellekoop:
"*Filter-protected Photodiodes for High-Throughput Enzymatic Analysis*";
IEEE Sensors Journal, **4** (2004), 5; 584 - 588.

6. B. Jakoby, A. Ecker, M. Vellekoop:
"*Monitorin macro- and microemulsions using physical chemosensors*";
Sensors and Actuators A, **115** (2004), 209 - 214.

7. B. Jakoby, M. Vellekoop:
"*Physical sensors for water-in-oil emulsions*";
Sensors and Actuators A, **110** (2004), 28 - 32.

8. F. Keplinger, S. Kvasnica, A. Jachimowicz, F. Kohl, J. Steurer, H. Hauser:
"*Lorentz force based magnetic field sensor with optical readout*";
Sensors and Actuators A, **110** (2004), 112 - 118.

9. F. Kohl, F. Keplinger, A. Jachimowicz, J. Schalko:
"*A Model of Metal ?Im resistance bolometers based on the electro-thermal feedback effect*";
Sensors and Actuators A, **115** (2004), 308 - 317.

10. J. Nieuwenhuis, F. Kohl, J. Bastemeijer, P. M. Sarro, M. Vellekoop:
"*Intetrated Coulter counter based on 2-dimensional liquid aperture control*";
Sensors and Actuators B, **102** (2004), 44 - 50.

11. J. Nieuwenhuis, M. Vellekoop:
"*Simulation study of dielectrophoretic particle sorters*";
Sensors and Actuators B, **103** (2004), 331 - 338.

12. P. Svasek, E. Svasek, B. Lendl, M. Vellekoop:
"*Fabrication of miniaturized fluidic devices using SU-8 based lithography and low temperature wafer bonding*";
Sensors and Actuators A, 115 (2004), 591 - 599.

Presentations

1. A. Agoston, F. Keplinger, B. Jakoby:
"*A Novel MEMS-Based Viscosity Sensor*";
Presentation: 18th European Conference on Solid-State Transducers (EUROSENSORS XVIII), Rome, Italy; 09-12-2004 - 09-15-2004; in: "*Technical Digest of Eurosensors XVIII*", (2004), ISBN: 88-7621-282-5; 161 - 163.

2. A. Agoston, C. Ötsch, B. Jakoby:
"*Application of microacoustic viscosity sensors for online oil condition monitoring*";
Poster: VDI Fachtagung, Ludwigsburg, D; 03-15-2004 - 03-16-2004; in: "*Sensoren und Messsysteme VDI-Berichte 1829*", (2004), ISBN: 3-18-091829-2; 833 - 836.

3. A. Agoston, C. Ötsch, F. Novotny-Farkas, H. Eisenschmid, B. Jakoby:
"*Sensors for a Lubrication-Monitoring-System*";
Presentation: 14th International Colloquium Tribology, Esslingen, Germany; 01-13-2004 - 01-15-2004; in: "*Tribology and Lubrication Engineering*", W.J. Bartz (ed.); 3 (2004), ISBN: 3-924813-54-X; 1883 - 1889.

4. A. Agoston, C. Ötsch, J. Zhuravleva, B. Jakoby:
"*An IR-Absorption Sensor System for the Determination of Engine Oil Deterioration*";
Presentation: 3rd IEEE Conference on Sensors (IEEE Sensors 2004), Vienna, Austria; 10-24-2004 - 10-27-2004; in: "*CD-ROM Proceedings Sensor 2004*", D. Rocha Wiese Meneses, P. Sarro, M. Vellekoop (ed.); (2004), ISBN: 0-7803-8692-2; 463 - 466.

5. R. Beigelbeck, B. Jakoby:
"*Analytical 3D-Analysis of Compressional Wave Excitation by Thickness-Shear-Mode Resonators*";
Presentation: 3rd IEEE Conference on Sensors (IEEE Sensors 2004), Vienna, Austria; 10-24-2004 - 10-27-2004; in: "*CD-ROM Proceedings Sensor 2004*", D. Rocha Wiese Meneses, P. Sarro, M. Vellekoop (ed.); (2004), ISBN: 0-7803-8692-2; 91 - 94.

6. P. Bertrand, M. Scherer, T. Hilberath, B. Jakoby:
"*Oil condition monitoring sensor for diesel engines*";
Presentation: International Congress The Diesel Engine: Today and Tomorrow, Lyon, France; 05-12-2004 - 05-13-2004; in: "*CD-Rom Proceedings*", (2004), 11 pages.

7. B. Iliev, V. Iordanov, J. Bastemeijer, A. Bossche, P. Sarro, I. T. Young, G.W.K. Van Dedem, M. Vellekoop:
"*Integrated nanoliter sensors reactor chamber for PCR analysis - from the idea to a complete system*";
Presentation: International Conference Sense of Contact, 2004, Wageningen, Netherlands; 03-23-2004; in: "*Proceedings Sense of Contact, 2004*", (2004), ISBN: 954-438-386-7; 6 pages.

8. V. Iordanov, B. Iliev, J. Bastemeijer, A. Bossche, P. M. Sarro, I. T. Young, H. Dietrich, R. van den Doel, G.W.K. Van Dedem, A. Kroon, M. Vellekoop:
"*Integrated sensors for nanoliter bioluminescence and fluorescence bio-chemical analysis*";
Presentation: International Conference Sense of Contact, 2004, Wageningen, Netherlands; 03-23-2004; in: "*Proceedings Sense of Contact, 2004*", (2004), ISBN: 954-438-386-7; 6 pages.

9. V. Iordanov, B. Iliev, J. Bastemeijer, A. Bossche, P. M. Sarro, I. T. Young, G.W.K. Van Dedem, M. Vellekoop:

"*Integrated nanoliter sensors reactor chamber for DNA multiplication - thermal characterization*";
Presentation: International Conference Sense of Contact, 2004, Wageningen, Netherlands; 03-23-2004; in: "*Proceedings Sense of Contact, 2004*", (2004), ISBN: 954-438-386-7; 6 pages.

10. V. Iordanov, B. Iliev, A. Bossche, J. Bastemeijer, P. M. Sarro, I. T. Young, G.W.K. Van Dedem, M. Vellekoop:
"*Integrated Sensor Arrays for Bioluminescence and Fluorescence Bio-Chemical Analysis*";
Presentation: 3rd IEEE Conference on Sensors (IEEE Sensors 2004), Vienna, Austria; 10-24-2004 - 10-27-2004; in: "*CD-ROM Proceedings Sensor 2004*", D. Rocha Wiese Meneses, P. M. Sarro, M. Vellekoop (ed.); (2004), ISBN: 0-7803-8692-2; 810 - 813.

11. V. Iordanov, B. Iliev, V. Joseph, A. Bossche, J. Bastemeijer, P. M. Sarro, I. T. Young, G.W.K. Van Dedem, M. Vellekoop:
"*Sensorized nanoliter reactor chamber for DNA multiplication*";
Presentation: 3rd IEEE Conference on Sensors (IEEE Sensors 2004), Vienna, Austria; 10-24-2004 - 10-27-2004; in: "*CD-ROM Proceedings Sensor 2004*", D. Rocha Wiese Meneses, P. M. Sarro, M. Vellekoop (ed.); (2004), ISBN: 0-7803-8692-2; 229 - 232.

12. B. Jakoby, N. Dörr:
"*Monitoring Phase Transitions in Microemulsions Using Impedance and Viscosity Sensors*";
Presentation: 3rd IEEE Conference on Sensors (IEEE Sensors 2004), Vienna, Austria; 10-24-2004 - 10-27-2004; in: "*CD-ROM Proceedings Sensor 2004*", D. Rocha Wiese Meneses, P. Sarro, M. Vellekoop (ed.); (2004), ISBN: 0-7803-8692-2; 627 - 630.

13. B. Jakoby, F.P. Klinger, P. Svasek:
"*A Novel Viscosity Sensor with Integrated Heater and Temperature Sensor*";
Presentation: 18th European Conference on Solid-State Transducers (EUROSENSORS XVIII), Rome, Italy; 09-12-2004 - 09-15-2004; in: "*Technical Digest of Eurosensors XVIII*", (2004), ISBN: 88-7621-282-5; 600 - 603.

14. B. Jakoby, M. Vellekoop, A. Ecker:
"*Monitoring W/O-Emulsions by Means of Sensors*";
Presentation: 14th International Colloquium Tribology, Esslingen, Germany; 01-13-2004 - 01-15-2004; in: "*Tribology and Lubrication Engineering*", W.J. Bartz (ed.); 3 (2004), ISBN: 3-924813-54-X; 1877 - 1880.

15. N. Kaun, S. Kulka, J. Baena, U. Schade, M. Vellekoop, E. De Lorenzi, B. Lendl:
"*Synchrotron Radiation for On-Chip Mid-IR Detection at the Diffraction Limit*";
Presentation: 8th International Conference on Miniaturized Systems in Chemistry and Life Sciences, Malmö, Sweden; 09-26-2004 - 09-30-2004; in: "*Proceedings 2004*", (2004), 530 - 532.

16. F. Keplinger, R. Beigelbeck, F. Kohl:
"*Simultaneous Measurement of Two Magnetic Field Components Using a U-Shaped Cantilever Device*";
Presentation: 3rd IEEE Conference on Sensors (IEEE Sensors 2004), Vienna, Austria; 10-24-2004 - 10-27-2004; in: "*CD-ROM Proceedings Sensor 2004*", D. Rocha Wiese Meneses, P. Sarro, M. Vellekoop (ed.); (2004), ISBN: 0-7803-8692-2; 1450 - 1453.

17. F. Kohl, R. Beigelbeck, F. Keplinger, A. Jachimowicz, J. Steurer:
"*A Precise 1/f Noise Spectroscopy Setup for Sensor Characterization*";

Presentation: 3rd IEEE Conference on Sensors (IEEE Sensors 2004), Vienna, Austria; 10-24-2004 - 10-27-2004; in: "*CD-ROM Proceedings Sensor 2004*", D. Rocha Wiese Meneses, P. Sarro, M. Vellekoop (ed.); (2004), ISBN: 0-7803-8692-2; 1143 - 1146.

18. S. Kostner, J. Nieuwenhuis, E. Svasek, P. Svasek, A. Jachimowicz, M. Vellekoop: "*Continuous Particle Separator Based on Periodical DEP Elements*"; Presentation: 8th International Conference on Miniaturized Systems in Chemistry and Life Sciences, Malmö, Sweden; 09-26-2004 - 09-30-2004; in: "*Proceedings of µTAS 2004*", (2004), ISBN: 0-85404-643-7; 9 - 11.

19. J. Kuntner, R. Chabicovsky, B. Jakoby: "*Oil Condition Monitoring Using a Thermal Conductivity Sensor*"; Presentation: 18th European Conference on Solid-State Transducers (EUROSENSORS XVIII), Rome, Italy; 09-12-2004 - 09-15-2004; in: "*Technical Digest of Eurosensors XVIII*", K. Riedling (ed.); (2004), ISBN: 88-7621-282-5; 983 - 986.

20. J. Kuntner, B. Jakoby: "*Two-Dimensional FEM Analysis of Pressure Wave Generation Mechanisms in TSM Liquid Sensors*"; Presentation: 3rd IEEE Conference on Sensors (IEEE Sensors 2004), Vienna, Austria; 10-24-2004 - 10-27-2004; in: "*CD-ROM Proceedings Sensor 2004*", D. Rocha Wiese Meneses, P. Sarro, M. Vellekoop (ed.); (2004), ISBN: 0-7803-8692-2; 83 - 86.

21. J. Nieuwenhuis, A. Jachimowicz, P. Svasek, M. Vellekoop: "*High-Speed Integrated Particle Sorters based on Dielectrophoresis*"; Presentation: 3rd IEEE Conference on Sensors (IEEE Sensors 2004), Vienna, Austria; 10-24-2004 - 10-27-2004; in: "*CD-ROM Proceedings Sensor 2004*", D. Rocha Wiese Meneses, P. Sarro, M. Vellekoop (ed.); (2004), ISBN: 0-7803-8692-2; 64 - 67.

22. J. Nieuwenhuis, P. Svasek, P. M. Sarro, M. Vellekoop: "*Particle Discrimination with an Improved Projection Cytometer*"; Presentation: 8th International Conference on Miniaturized Systems in Chemistry and Life Sciences, Malmö, Sweden; 09-26-2004 - 09-30-2004; in: "*Proceedings of µTAS 2004*", (2004), ISBN: 0-85404-643-7; 419 - 421.

23. J. Nieuwenhuis, P. Svasek, P. M. Sarro, M. Vellekoop: "*Particle Size Discrimination with a Liquid Aperture Coulter Counter*"; Presentation: 18th European Conference on Solid-State Transducers (EUROSENSORS XVIII), Rome, Italy; 09-12-2004 - 09-15-2004; in: "*Technical Digest of Eurosensors XVIII*", (2004), ISBN: 88-7621-282-5; 317 - 320.

24. D. Rocha Wiese Meneses, V. Ferrari, B. Jakoby: "*Improved Electronic Readout Circuit for Resonant Acoustic Sensors*"; Presentation: 3rd IEEE Conference on Sensors (IEEE Sensors 2004), Vienna, Austria; 10-24-2004 - 10-27-2004; in: "*CD-ROM Proceedings Sensor 2004*", D. Rocha Wiese Meneses, P. Sarro, M. Vellekoop (ed.); (2004), ISBN: 0-7803-8692-2; 32 - 35.

25. M. Roy, S. Kvasnica, C. Eisenmenger-Stittner, G. Vorlaufer, A. Pauschitz: "*PVD-18: An Analysis of Nanotribological Study of Ti-Containing Hard Carbon Film*"; Presentation: International Convention on Surface Engineering, INCOSURF 2004, Bangalore, India; 08-25-2004 - 08-27-2004; in: "*Proceedings INCOSURF 2004*", (2004), 441 - 450.

26. M. Scherer, M. Arndt, P. Bertrand, B. Jakoby:
"*Fluid Condition Monitoring Sensors for Diesel Engine Control*";
Presentation: 3rd IEEE Conference on Sensors (IEEE Sensors 2004), Vienna, Austria; 10-24-2004 - 10-27-2004; in: "*CD-ROM Proceedings Sensor 2004*", D. Rocha Wiese Meneses, P. Sarro, M. Vellekoop (ed.); (2004), ISBN: 0-7803-8692-2; 459 - 462.

27. B. Valentin, M. Mündlein, R. Chabicovsky, J. Nicolics:
"*Evaluation of a Novel Transepidermal Water Loss Sensor*";
Presentation: 3rd IEEE Conference on Sensors (IEEE Sensors 2004), Vienna, Austria; 10-24-2004 - 10-27-2004; in: "*CD-ROM Proceedings Sensor 2004*", D. Rocha Wiese Meneses, P. Sarro, M. Vellekoop (ed.); (2004), ISBN: 0-7803-8692-2; 115 - 118.

Seminar Talks

1. B. Jakoby:
"*Angewandte Forschung am Institut für Sensor- und Aktuatorsysteme*";
Presentation: FH Vorarlberg Symposium Mikrosystemtechnik für die Industrie, Dornbirn, Austria (invited); 04-28-2004.

2. B. Jakoby:
"*Lab on a Chip und Mikrosensorik*";
Presentation: Mikro- und Nanostrukturen: Anwendungen und Perspektiven, Wirtschaftskammer, Wien (invited); 11-23-2004.

3. B. Jakoby:
"*Zustandsüberwachung von Fluiden mit physikalischen Sensoren*";
Presentation: Gastvortrag Johannes Kepler Universität Linz, Linz, Austria (invited); 06-28-2004.

4. M. Vellekoop:
"*Physical chemosensors*";
Presentation: Smart Sensor Systems Course 2004 (SSS) at TU Delft, Delft, Netherlands; 05-11-2004.

5. M. Vellekoop:
"*Sensing in microfluidic devices*";
Presentation: Gastvortrag TU Warschau, Warschau, Polen (invited); 04-26-2004.

Patents

1. H. Hauser, M. Vellekoop:
"*Verfahren zur zweidimensionalen Manipulation kleiner Volumina von Flüssigkeiten und Festkörpern und Aktuator zur Ausführung des Verfahrens*";
Patent: Austria, No. AT 412.039; submitted: 02-21-2002, granted: 01-15-2004.

Doctor's Theses

1. S. Kvasnica:
"*Modeling, Diagnostics and Application of the Unbalanced Magnetron Discharge for the Deposition of Novel Ti-C:H Interface Layers*";
Reviewer: W. Fallmann, H. Biederman; Institut für Sensor- und Aktuatorsysteme, 2004.

Cooperations

1. AC2T, Wiener Neustadt, F. Franek
2. AMS Unterpremstätten, M. Brandl, F. Schrank
3. ARC Seibersdorf, H. Kroath, C. Nöhammer
4. IMS, E. Fantner, H. Löschner
5. EVG, Schärding, Lind, J. Weixlberger
6. Jenbacher, Jenbach, S. Chvatal
7. OMV, Wien, F. Novotny-Farkas
8. R. Bosch, Reutlingen, Germany, O. Schatz
9. R. Bosch, Stuttgart, Germany, H. Eisenschmidt
10. Ford Motor Company, Dearborn, USA, J.H. Visser
11. Elmar Graf GmbH, Dornbirn, E. Graf
12. Unilever Research, Vlaardingen, The Netherlands, R. Kohlus
13. DSM Research, Geleen, The Netherlands, R. Janssen, P. Vonk
14. Applikon, the Netherlands, A. Oudshoorn
15. National Center for Scientific Research, Demokritos, Athens, Greece, D. Ithakissios
16. National Hellenic Research Foundation, Athens, Greece, I. Siotis
17. TU Wien, B. Lendl, E. Benes
18. Universität für Bodenkultur Wien, U.Sleytr, D. Pum, B. Schuster
19. Fachochschule Wiener Neustadt, Noll
20. Universität Krems, D. Falkenhagen
21. LBI for Biomedical MicroTechnology, Vienna
22. ÖAW Forschungstelle Integrated Sensor Systems, T. Sauter, F. Kohl
23. TU Delft, The Netherlands, A. Bossche, C. Dekker, P.J. French, I.T. Young
24. ETH Zürich (CH), H. Baltes
25. University of Freiburg, IMTEK, Germany, G. Urban, J. Korvink, O. Paul.
26. University of Technology Berlin, Germany, E. Obermeier
27. University Leuven, Belgium, C. Kirschhock

Analytical 3D Hydrodynamical Analysis of Spurious Compressional Wave Excitation by Microacoustic TSM Liquid Sensors

R. Beigelbeck [1] and B. Jakoby [2]

[1] Research Unit for Integrated Sensor Systems
Austrian Academy of Sciences, A-2700 Wr. Neustadt

[2] Institute of Sensor and Actuator Systems
Vienna University of Technology, A-1040 Vienna

Piezoelectric thickness-shear-mode (TSM) resonators are well-established as viscosity and chemical liquid sensors. When immersed in the sample liquid, the resonator excites a strongly damped shear-polarized wave as well as spurious compressional waves in the liquid. The latter are scarcely damped, which can lead to disturbing interferences if they are reflected by obstacles close to the sensor. In order to analyze the spurious compressional wave excitation due to the non-uniform shear displacement across the resonator/liquid-interface, we developed a three-dimensional mathematical model utilizing solutions of the linearized Navier-Stokes equations in the spatial Fourier-domain, which govern the acoustic field in the liquid. We discuss the resulting solutions and illustrate these results by considering practical examples.

Basic Sensor Concept

A typical TSM-resonator for viscosity sensing applications is made of a thin AT-cut quartz disk, which is plated with metal electrodes on both sides of the disk (see Fig. 1). When applying an electric alternating voltage to the electrodes, the resonator starts to vibrate in thickness-shear-mode. The adjacent liquid is entrained by the shear movement of the immersed TSM-resonator, which leads to a change of the resonance frequency and the damping compared to the vibrating resonator in air. By detecting this shift, the viscosity-density product of the liquid can be determined [1], [2].

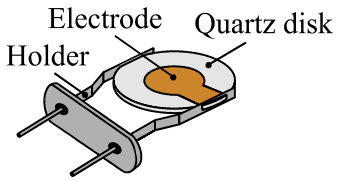

Fig. 1: Typical design of a TSM-resonator for viscosity sensing applications

In the ideal case, a pure and uniform shear displacement across the resonator surface leads to excitation of an evanescent shear wave in the adjacent viscous liquid. However, in the real case, spurious compressional waves are also excited because of

- small out-of-plane displacements due to mode conversion (at clamping points, electrode edges, ...),
- the uncompensated angular momentum of the dominant shear vibration of the quartz disk [3].

Method and Theory

This contribution deals with a generalization of a recently developed two-dimensional model [1]. We decouple the piezoelectric disk and the fluid region (see Fig. 2 (a)) by considering only the liquid and replace the resonator by impressing a non-uniform Gaussian-shaped shear displacement at the interface as it has been observed in practical measurements [1], [2]. Then, the linearized Navier-Stokes equation in the liquid

$$\nabla^2 \underline{\mathbf{u}} + \alpha \nabla(\nabla \cdot \underline{\mathbf{u}}) + \beta \underline{\mathbf{u}} = \mathbf{0}\,,$$

where α and β are fluid parameters [4] and $\underline{\mathbf{u}}(x,y,z)$ is the displacement vector in the liquid, is solved by using a spectral method. The displacement components $\underline{u}_i(x,y,z)$ in the liquid ($i \in \{x,y,z\}$) are represented in terms of compact Fourier double-integrals

$$\underline{u}_i(x,y,z) = \frac{1}{(2\pi)^2} \int_{-\infty}^{\infty} \int_{-\infty}^{\infty} \underline{U}_i(k_x,k_y;z) \exp[-\mathrm{j}(k_x x + k_y y)]\, \mathrm{d}k_x\, \mathrm{d}k_y\,.$$

Here, k_x and k_y are the lateral wave numbers and $\underline{U}_i(k_x,k_y;z)$ is the general solution ($i \in \{x,y,z\}$) in the spectral domain, which reads

$$\underline{U}_x\left(k_x,k_y;z\right) = \underline{U}_{x0}\left[\frac{\left(k_y^2 - \xi_1\xi_5\right)\exp\left(\xi_1 z\right)}{k_x^2 + k_y^2 - \xi_1\xi_5} + \frac{k_x^2 \exp\left(\xi_5 z\right)}{k_x^2 + k_y^2 - \xi_1\xi_5}\right],$$

$$\underline{U}_y\left(k_x,k_y;z\right) = -\underline{U}_{x0}\frac{k_x k_y\left[\exp\left(\xi_1 z\right) - \exp\left(\xi_5 z\right)\right]}{k_x^2 + k_y^2 - \xi_1\xi_5},$$

$$\underline{U}_z\left(k_x,k_y;z\right) = -\underline{U}_{x0}\frac{\mathrm{j}k_x\xi_5\left[\exp\left(\xi_1 z\right) - \exp\left(\xi_5 z\right)\right]}{k_x^2 + k_y^2 - \xi_1\xi_5}.$$

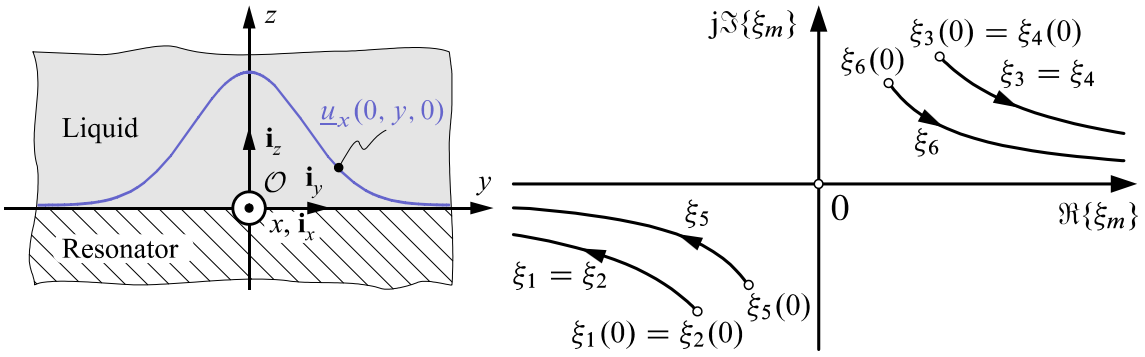

(a) (b)

Fig. 2: (a) Half space model to analyze the wave excitation mechanism of a vibrating TSM-resonator immersed into a liquid. The area $z > 0$ is filled with a linear viscous and adiabatic compressible liquid. The resonator is replaced by an appropriate boundary condition at $z = 0$. (b) Schematic locus of the eigenvalues ξ_m as function of $k = (k_x^2 + k_y^2)^{1/2}$. Note that the real parts of ξ_1, ξ_2, and ξ_5 are negative for any arbitrary value of k, while the real parts of ξ_3, ξ_4, and ξ_6 are always positive. For common liquids is $|\Re\{\xi_1\}| \ll |\Re\{\xi_5\}|$ resulting in a much lower damping for compressional waves.

$\underline{U}_{x0}$ is the 2D-Fourier transform of the boundary condition at $z = 0$. $\xi_1 = (k_x^2 + k_y^2 - \beta)^{1/2}$ and $\xi_5 = (k_x^2 + k_y^2 - \beta/(1+\alpha))^{1/2}$ are the eigenvalues associated to the problem (see Fig. 2 (b)). The real parts of ξ_1 and ξ_5 are related to spatial damping in z-direction, while the imaginary parts correspond to a wave number in z-direction. For small k-values, ξ_5 corresponds to a dominantly longitudinal mode, whereas ξ_1 is related to a dominantly shear polarized mode.

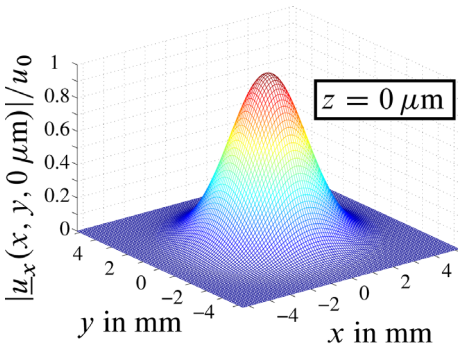

(a)

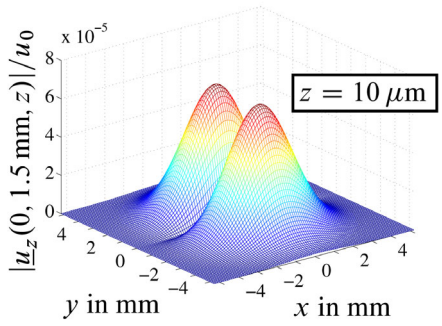

(b)

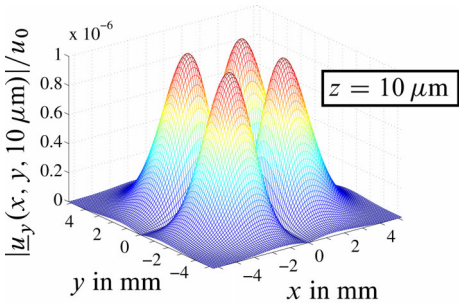

(c)

Fig. 3: (a) Normalized shear displacement $|\underline{u}_x(x, y, 0)/u_0|$ at the resonator surface $z = 0$ as prescribed by the boundary condition. (b) Normal displacement $|\underline{u}_z(x, y, 10\ \mu\text{m})/u_0|$ at $z = 10\ \mu\text{m}$ above the resonator surface. Two major centers of scarcely damped compressional waves are built up above the resonator. (c) Secondary shear component $|\underline{u}_y(x, y, 10\ \mu\text{m})/u_0|$ at $z = 10\ \mu\text{m}$ above the resonator surface. This component shows four major centers and is a by-product of the compressional wave beams.

Results

We consider a frequency of 6 MHz and water as sample liquid. As a result, a dominantly shear polarized wave $\underline{u}_x$ is excited (see Fig. 3 (a)), which is highly damped in z-direction (see Fig. 4 (a)). Simultaneously, two major beams (see Fig. 3 (b)) of scarcely damped compressional waves (see Fig. 4 (b)), represented by normal displacements $\underline{u}_z$, are built up with increasing z. Due to their finite lateral extension, these pressure waves cause secondary shear components in x- and y-directions with amplitudes being typically two orders of magnitude smaller than the associated normal (see Fig. 3 (c)) components $\underline{u}_z$. At this height above the surface, the related secondary amplitudes in

x-direction are still overshadowed by the primary Gaussian shear displacements. Their damping behavior is similar to one of the compressional waves (see Fig. 4 (c)).

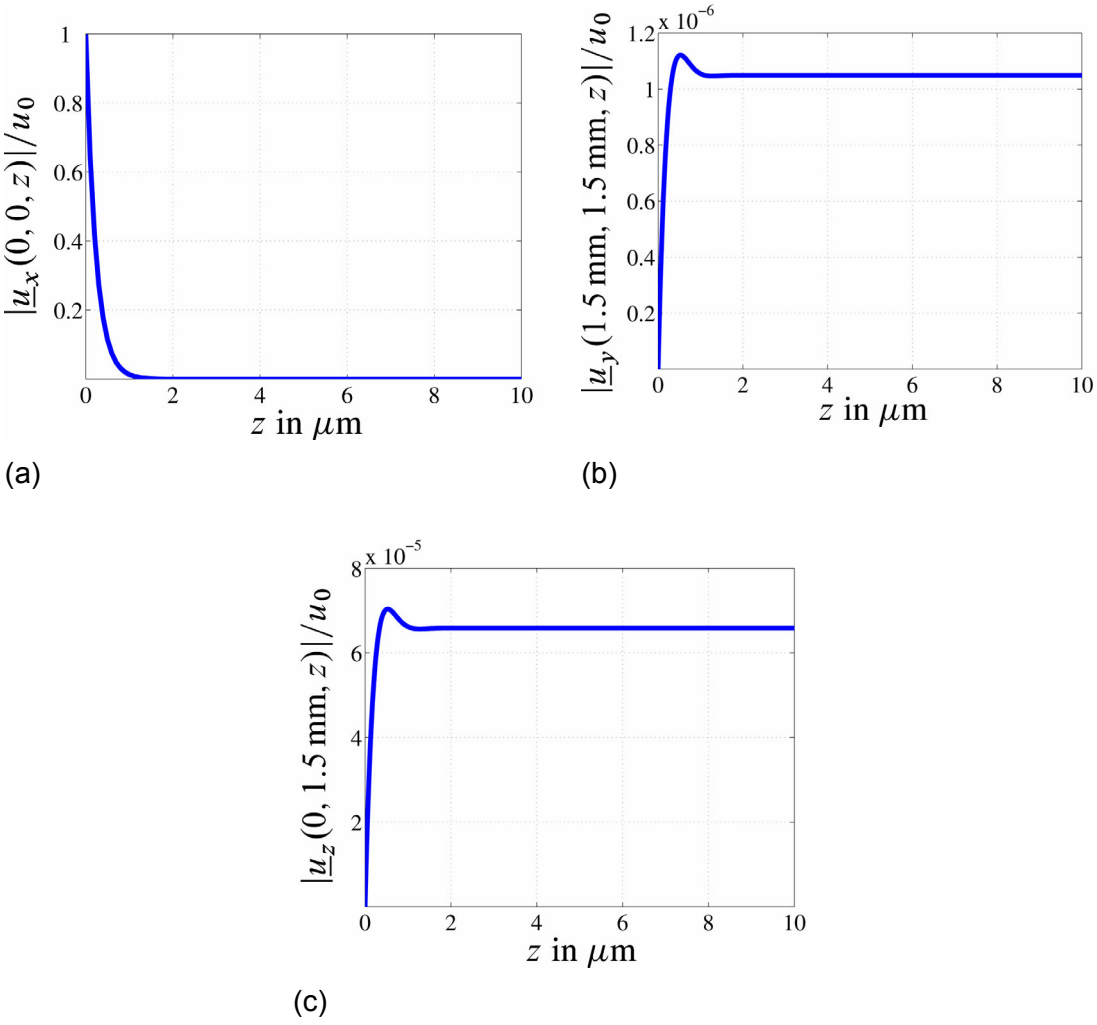

Fig. 4: Comparison of the major peaks of the displacement components with increasing distance z from the resonator surface.

References

[1] B. A. Martin and H. E. Hager: “Velocity profile on quartz crystals oscillating in liquids”, Journal of Applied Physics, 65: 2627, 1989.

[2] B. A. Martin and H. E. Hager: “Flow profile above a quartz crystal vibrating in liquid”, Journal of Applied Physics, 65: 2630, 1989.

[3] E. Benes et al.: “Sensors based on Piezoelectric Resonators”, Sensors and Actuators A, 48:1, 1995.

[4] R. Beigelbeck and B. Jakoby: “A Two-Dimensional Analysis of Spurious Compressional Wave Excitation by Thickness-Shear-Mode Resonators”, Journal of Applied Physics, 95(9):4989, 2004.

Simultaneous Measurement of Two Magnetic Field Components Using a Single U-Shaped MEM Cantilever Device

F. Keplinger [1], R. Beigelbeck [2], F. Kohl [2], and P. Loschmidt [2]

[1]Institute of Sensor and Actuator Systems
Vienna University of Technology, A-1040 Vienna

[2]Research Unit for Integrated Sensor Systems
Austrian Academy of Sciences, A-2700 Wr. Neustadt

A miniaturized sensor capable of measuring simultaneously two orthogonal components of the magnetic flux density is presented. These magnetic field components excite two different resonant modes of a single micromachined U-shaped cantilever. The cantilever vibrations are accomplished by the Lorentz force acting on an alternating electrical current, which flows through a thin film lead attached to the top surface of the silicon cantilever. This lead operates also as a deflecting mirror in an optical readout system which is used to detect the oscillations of the cantilever. By means of two lock-in amplifiers, the output of the readout is converted into two signals related to orthogonal components of the magnetic flux density. The feasibility of the system is proved by measuring contour plots of the magnetic flux distribution of a sample magnet.

Introduction

Micromachined cantilevers enable measurement of a variety of physical parameters such as magnetization or viscosity. These devices offer a high quality factor and achieve a high sensitivity when they are excited at or near a resonant frequency. To measure magnetic fields with cantilever structures, the Lorentz force is utilized on a current carrying lead. Cantilevers vibrating in the fundamental mode are typically used to measure the magnetic flux density in the direction parallel to the arms of the cantilever. The presented approach uses high order oscillation modes to measure the flux density components parallel to the base of the cantilever.

Sensor Principle and Theory

The Lorentz force is used to bend a micromachined cantilever (Fig. 1). Small deflections compared to the length of the cantilever are directly proportional to the applied force. To reach a high sensitivity, the cantilever is excited by a sinusoidal alternating current at the resonant frequency.

The investigated U-shaped cantilever can oscillate in various flexural vibration modes (Fig. 2), whereas the first four modes are of most practical importance. With respect to our design, these modes can be divided into two symmetrical (S1 and S2, where the cantilever arms are moving in parallel) and two antisymmetrical ones (A1 and A2, where the arms move in opposite directions).

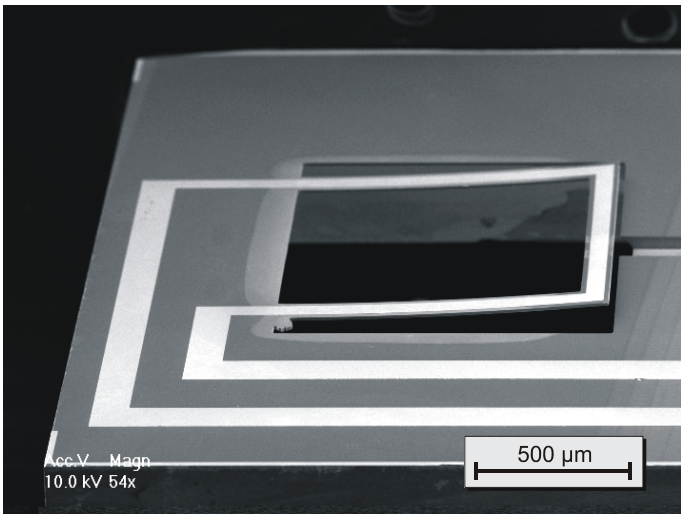

Fig. 1: Micromachined silicon cantilever with a thickness of 12 µm. The bright area represents the gold surface of the lead.

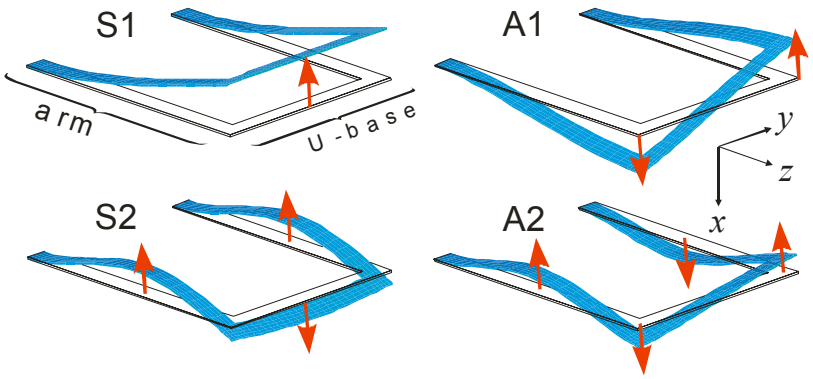

Fig. 2: Visualization of the first two symmetric (S1 and S2) and the first two anti-symmetric (A1 and A2) flexural vibration modes obtained by a finite element analysis.

The oscillating cantilever structure can be described by the classical Euler-Bernoulli beam dynamics theory leading to a set of three (one for each cantilever arm and one for the cantilever base) coupled linear 4th-order partial differential equations which read as

$$\frac{\partial}{\partial \zeta_i^{\,2}}\left(EI_i(z)\frac{\partial^2 \psi_i}{\partial \zeta_i^{\,2}}\right)-\left(f_i-\overline{m}_i(z)\frac{\partial^2 \psi_i}{\partial t^2}\right)=0$$

where $i=1,2$ indicates the arms and $i=3$ the base. Regarding this, EI_i denotes the stiffness, ζ_i the coordinate along the cantilever ($\zeta_{1,2}=z$ and $\zeta_3=y$), f_i the external forces, $\overline{m}_i$ the mass per unit length, t the time, and $\psi_i(\zeta_i,t)$ the deflection along the cantilever.

Experimental

Cantilever Excitation

Each mode can be excited by suitable Lorentz force distributions on different parts of the lead. The fundamental mode S1 is excited by a homogeneous magnetic field in z-direction. The field is parallel to the arms of the cantilever and therefore the forces are generated only at the base of the "U". The first antisymmetric mode A1 is excited by a homogeneous magnetic field in y-direction, where the Lorentz forces develop only along the arms of the cantilever. Due to the different orientation of the electrical current, the arms are bent in opposite directions.

Optical Readout

The vibrations of the cantilever are contact-free sensed using an optical readout. The IR-beam of a commercial available reflective sensor is returned partially by the surface of the gold lead on top of the cantilever and received by the photo transistor of the reflective sensor as shown in the experimental setup of Fig. 3.

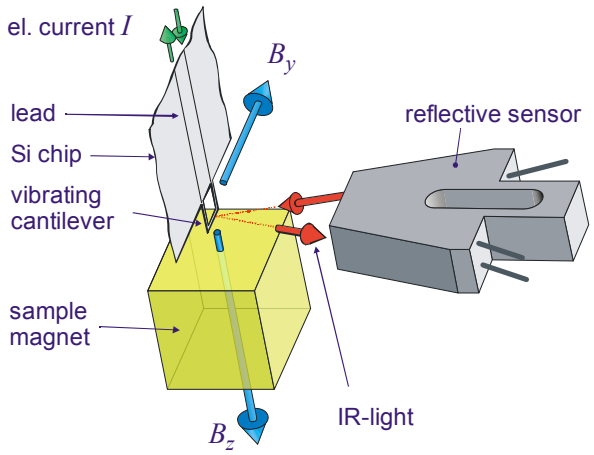

Fig. 3: Experimental setup: The oscillations of the cantilever caused by the Lorentz force modulate the intensity of an infrared beam emitted and detected by a reflective sensor.

Signal Generation for Dual Field Component Measurement

To excite the first symmetric (S1) and the first antisymmetrical mode (A1) simultaneously, the appropriate flux densities have to be present and the composite AC current should match to the resonant frequencies of the flexural vibration modes (Fig. 4). The amplified output signal of the reflective sensor is analyzed by two lock-in amplifiers. Their output signals are proportional to the magnetic flux densities to be measured. The phase information is used to determine the direction of the magnetic field.

Results

A typical measurement example is depicted in Fig. 5, where a permanent magnet of a voice coil actuator which moves the multiple read/write heads of a hard disk is scanned to create a contour plot of the magnetic flux distribution. The distance between magnet surface and cantilever tip is 2 mm.

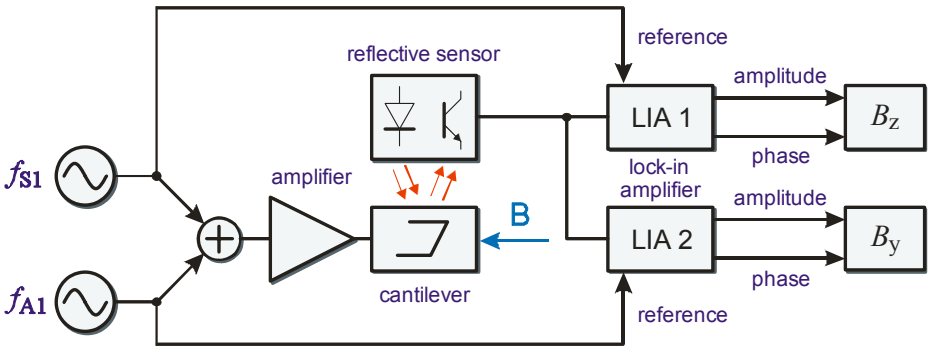

Fig. 4: To excite the symmetric (S1) and the antisymmetric (A1) oscillation modes of the cantilever simultaneously, two AC currents with frequencies according to the resonant frequencies (f_{S1} and f_{A1}) of these modes are added up and amplified. The magnetic flux densities (B_z and B_y) determine the amplitude of the cantilever oscillations and modulate the light reflected by the cantilever surface. The amplified output of the reflective sensor is analyzed by two lock-in amplifiers synchronized to the excitation frequencies. With amplitude and phase information, strength and direction of the magnetic flux density in z- and y-direction can be calculated.

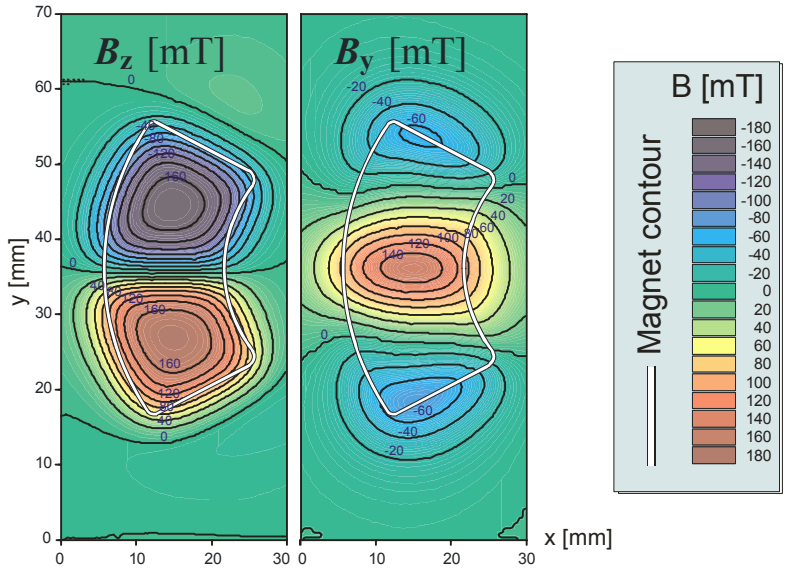

Fig. 5: Contour plots of the magnetic flux density in z- and y-direction of a kidney shaped permanent magnet of a voice coil actuator of a hard disk drive.

Conclusion

Utilization of two vibration modes of a U-shaped cantilever allows simultaneous measurement of two orthogonal flux density components with a single optical read out. The presented design is not feasible for measuring magnetic flux components in x-direction because modes sensitive to this direction have resonant frequencies far beyond 100 kHz and too low amplitudes. To measure all three components, a redesign of the vibrating structure has to be performed.

Oil Condition Monitoring Using a Thermal Conductivity Sensor

J. Kuntner, R. Chabicovsky, and B. Jakoby

Industrial Sensor Systems, Institute of Sensor and Actuator Systems
Vienna University of Technology, Austria

In recent years, the monitoring of oil-based liquids has gained increasing importance in various branches of the industry. In this contribution we discuss the application of a miniaturized thermal conductivity sensor for the monitoring of water contamination and deterioration processes in mineral oil. The sensor, which utilizes the hot film principle, features a molybdenum resistive structure simultaneously serving as heater and sensing element. The experimental results show that both, water contamination and deterioration processes in mineral oil lead to an increased thermal conductivity, indicating the potential of thermal conductivity sensors in the field of oil condition monitoring. Finally we analyzed the sensor's performance numerically in order to further evaluate its applicability and possible design modifications.

Introduction

In recent years, the monitoring of oil-based liquids has gained increasing importance in various branches of the industry. A prominent example is the condition monitoring of lubrication and insulating oils. In both cases the water contamination of oil often cannot be avoided which seriously influences its performance if certain levels are exceeded. In the case of lubrication oil, excessive water content leads to insufficient lubrication and subsequently to abrasive wear and corrosion. In case of insulation oils, increased water content results in a considerable reduction of the breakdown voltage. Thus, the detection of water content in the oil is of major importance.

Comparing the thermal transport properties of mineral oil and water, it turns out that the latter features a five times higher thermal conductivity. This indicates that thermal conductivity is a potential parameter for the detection of water content in mineral oils. In this contribution we investigate the thermal transport properties of W/O emulsions and artificially aged oils using a resistive hot film microsensor.

	ϑ	ρ	c_p	λ
	°C	$\frac{kg}{m^3}$	$\frac{J}{kgK}$	$\frac{W}{mK}$
Water	20.0	998	4183	0.598
Engine Oil	60.0	868	2010	0.140
Insulation Oil	60.0	842	2090	0.120

Table 1: Thermal properties of selected liquids [1].

Theory

During the last four decades many different techniques for measuring the thermal conductivity of liquids, solids, and gases have been developed. For the characterization of the thermal transport properties of fluids, in particular the transient hot-wire method is widely-used (see, e.g., [2]). This technique is based on a thin metal wire, mostly made of platinum, simultaneously serving as both, heater and sensing element. By applying a transient electrical current, the wire and the surrounding medium under investigation start heating up. Recording the corresponding temperature response of the wire enables the determination of the thermal conductivity and diffusivity of the surrounding fluid. Instead of a wire, other heater geometries have also been utilized. In case of the classical transient hot-strip technique a thin metal sheet is used (see e.g., [3]). In micro technology, this sheet is replaced by a thin film structure deposited on a substrate. In order to minimize the influence of this substrate on the sensor's performance various geometries like thin membranes, cantilevers, or micro-bridges can be utilized. However, regarding the applicability in harsh industrial environments, a trade-off has to be found between sensitivity and mechanical robustness. In this contribution we consider a hot film microsensor, which is operated using an adapted transient method.

Considering the small dimensions of the sensor compared to the used sample volumes (15 ml) of the investigated liquids, the corresponding temperature field in some distance from the sensor can be approximated by solving the heat diffusion equation for a thermal point source switched on at $t = 0$:

$$\vartheta(r,t) = \frac{\Phi}{4\pi\lambda r}\,\mathrm{erfc}\left(\frac{r}{\sqrt{4at}}\right) \tag{1}$$

Here Φ denotes the heating power, λ the thermal conductivity, a the thermal diffusivity, and r the radial distance from the point source [1]. Note that for small r, this approximation becomes inaccurate and even yields a non-physical singularity for $r = 0$. The diffusivity is related to the heat capacity c_p by

$$a = \frac{\lambda}{\rho \cdot c_p}, \tag{2}$$

where ρ denotes the mass density. For $t \to \infty$ the complementary error function erfc in Eq. (1) approaches unity such that in the steady state, the temperature distribution depends on the thermal conductivity and the heating power only:

$$\vartheta(r)\Big|_{t\to\infty} = \frac{\Phi}{4\pi\lambda r} \tag{3}$$

Sensor Design and Fabrication

Figure 1 shows the basic layout of the thin film microsensor. The device consists of a glass substrate (5 mm x 2.6 mm x 0.4 mm) with a resistive loop made of molybdenum as resistive sensing and heating element. Molybdenum is known for its linear resistance characteristics, which is valid over a wide temperature range. The shape of the resistive loop is especially designed to allow digital laser trimming. To avoid any chemical interaction between the resistor and the fluid, the molybdenum is covered with a silicon nitride protective layer. The bonding pad area is additionally coated with a nickel chromium adhesive layer and a gold layer. All films have been deposited by RF-sputtering in a Perkin Elmer 4400 diode system. The system allows the deposition of

the nickel chromium and gold films without a vacuum interruption, which ensures the production of solderable contacts.

The film patterning has been carried out by lift off photolithography techniques. The connecting wires are bonded to the contact pads by soldering. The temperature coefficient of the resistive loop was measured to be 0.956×10^{-3}/°C and its resistance was 112.55 Ω at 22.1°C.

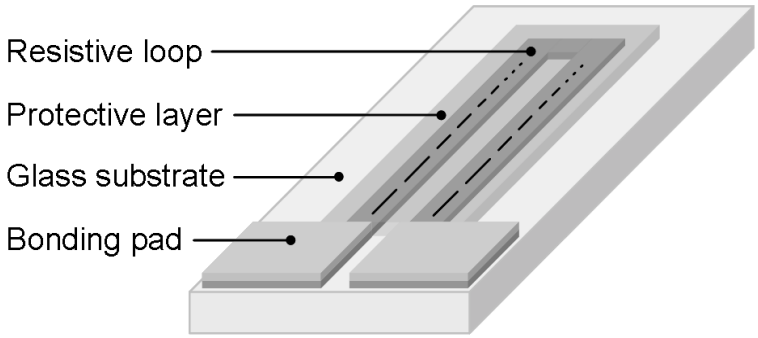

Fig. 1: Design of the hot film sensor.

Measurement Setup

The sensor was inserted into a beaker containing the sample liquid and was electrically connected to a measurement bridge as shown in Fig. 2. The differential bridge output voltage is amplified by an instrumentation amplifier (gain = 25) and recorded by means of a digital oscilloscope. By switching on the power supply (12 V), the heater current is turned on and the temporal evolution of the resistance (and thus the sensor temperature) can be monitored by recording the bridge output voltage. As long as the temperature at the walls of the beaker does not increase significantly, the assumption of an infinitely extended medium, which is also underlying Eq. (1), is approximately valid. In this case the sensor response is basically determined by the thermal material parameters of the surrounding liquid.

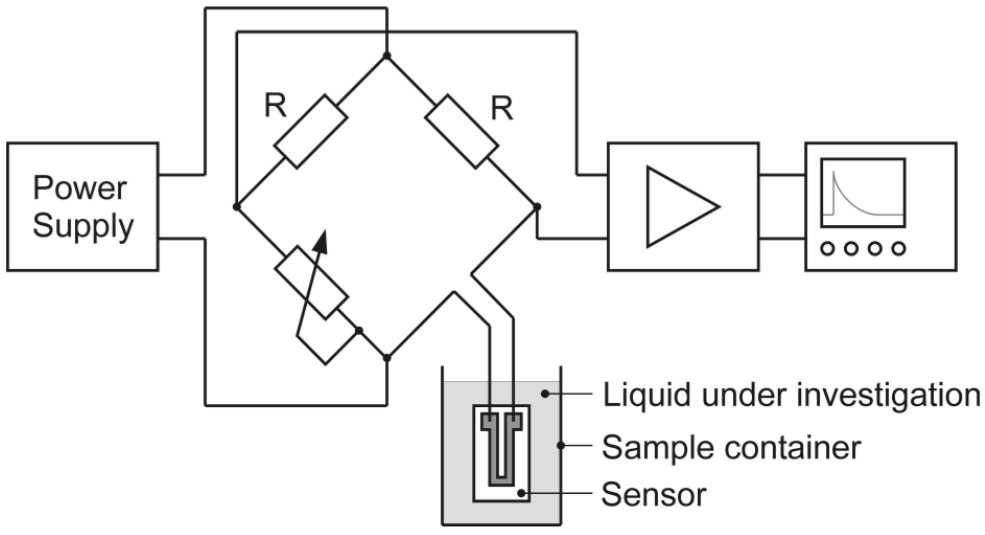

Fig. 2: Measurement Setup (R=470 Ω).

Results and Discussion

First we investigated water contamination in engine oils, where we deliberately contaminated a standard engine oil (SAE 15W40) with DI water, which leads to the formation of an emulsion. Figure 3 shows the resulting temperature rise $\Delta\vartheta$ above ambient (room) temperature versus the time t after switching on, for emulsions featuring a water content of 7%, 15% and 18% by volume compared to the pure oil sample. After the initial transient, the excess temperature becomes essentially determined by the thermal conductivity (see also Eq. (1)). It can thus be seen, that for increasing water contents the thermal conductivity of the emulsions increases, which leads to lower excess temperatures. Compared to pure oil, the excess temperature at t = *20* seconds is reduced by 4.7%, 10.5%, and 13.6%, for the W/O emulsions containing 7%, 15%, and 18% of water by volume, respectively.

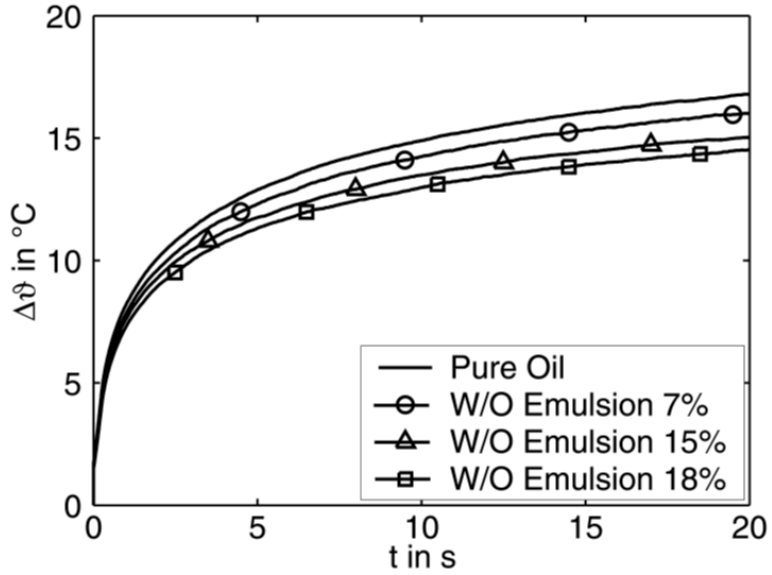

Fig. 3: Temperature rise $\Delta\vartheta$ vs. time t for W/O emulsions of 7%, 15%, 18% b.v. and the corresponding pure oil (SAE 15W40).

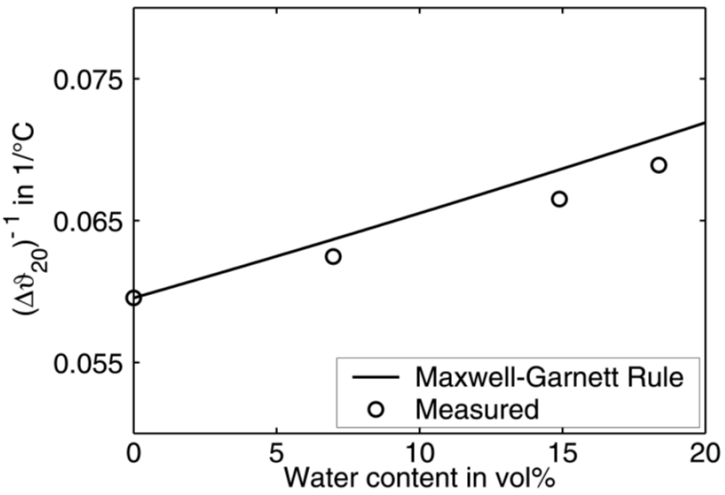

Fig. 4: Inverse of $\Delta\vartheta$ @ t=*20* seconds (which is approximately proportional to λ) vs. water content in % b.v.

Figure 4 shows the inverse of the excess temperature, $1/\Delta\vartheta$, at $t = 20$ seconds versus the water content. At this time the disturbing influence of the boundary is still negligible and the excess temperature has virtually reached its steady state. Thus we can assume that $1/\Delta\vartheta$ will be approximately proportional to the thermal conductivity λ (see also Equ. (1) for $t \to \infty$).

In further experiments we investigated the effect of oxidative deterioration. Figure 5 shows the resulting temperature rise $\Delta\vartheta$ above ambient (room) temperature versus the time t after switching on, for engine oil (SAE 15W40) which was artificially aged at 160°C for 7 days according to a standardized method. It can be observed that the deteriorated oil features an increased thermal conductivity which could be related to water formation due to thermal oxidation processes in the engine oil. We observed a total increase of about 3.4% for the above mentioned ageing conditions.

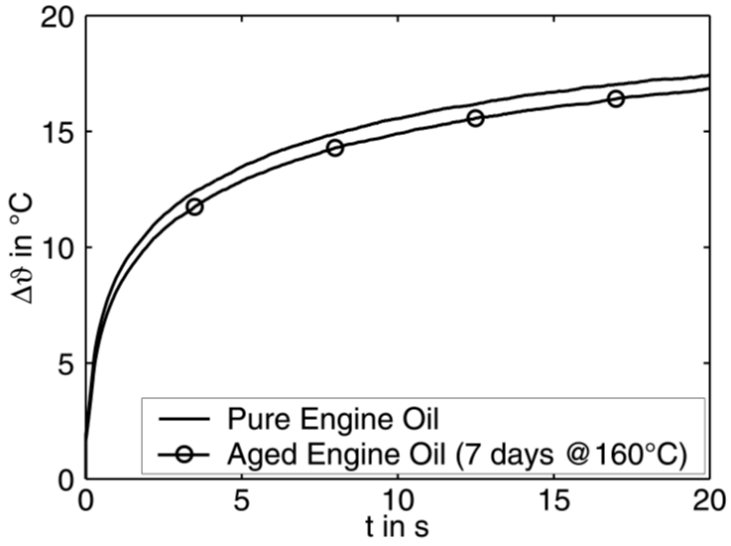

Fig. 5: Temperature rise $\Delta\vartheta$ vs. time t for pure engine oil (SAE 15W40) and artificially aged engine oil (7 days @ 160°C).

According to theoretical considerations, for the steady state the excess temperature of the sensor becomes essentially determined by the thermal conductivity of the surrounding fluid. This mechanism allows to clearly detect water deterioration in mineral oil, but underlies the restriction of a maximum measuring time that must not be exceeded to avoid the disturbing influence of the liquid boundary. To overcome this problem a transient measurement lasting several hundred milliseconds could be utilized, which would correspond to the concept of the above-mentioned hot-wire and hot-strip methods. However, as can be seen, e.g., from the measurement shown in Fig. 3, within this time frame a deviation between different samples can hardly be observed. By considering the sensor design, we find that the initial transient to a certain extent will be determined by the specific heat of the sensor substrate and the liquid. Glass features a specific heat comparable to that of mineral oil and moreover shows a very high thermal conductivity (typically 10 times higher than that of oil). Hence it can be assumed that due to the relatively thick glass substrate, the sensitivity in the initial transient regime is decreased accordingly. However, at the same time the thickness of the sensor increases its physical robustness.

To further investigate on these assumptions, a Finite Element (FE) simulation has been conducted. Figure 6 (a) depicts the simulated temperature rise $\Delta\vartheta$ within the initial transient of 500 milliseconds for an emulsion featuring a water content of 20% by volume

compared to the pure oil sample. In order to evaluate the impact of the substrate thickness on the initial temperature slope, we calculated the initial transient for the same sample liquids but for a sensor structure with a reduced thickness of 5 microns instead of 400 microns. Figure 6 (b) shows the resulting excess temperature and the initial temperature slope. As expected reducing the thermal mass of the sensor results in a steeper slope and in an increased sensitivity with respect to water contamination of the oil. Compared to the pure oil sample, the initial transient slope, $d\Delta\vartheta/dt$, for the emulsion was -13.0% and -24.5% smaller for the thick and the thin glass substrate, respectively. This indicates the increase in sensitivity for the transient measurement method that can be obtained by reducing the influence of the glass substrate by making it thinner. Thus the sensitivity generally increases if a thinner glass substrate is used. In practical applications, the mechanical robustness of the sensor has to be considered as well, which accordingly requires a trade-off in choosing the thickness.

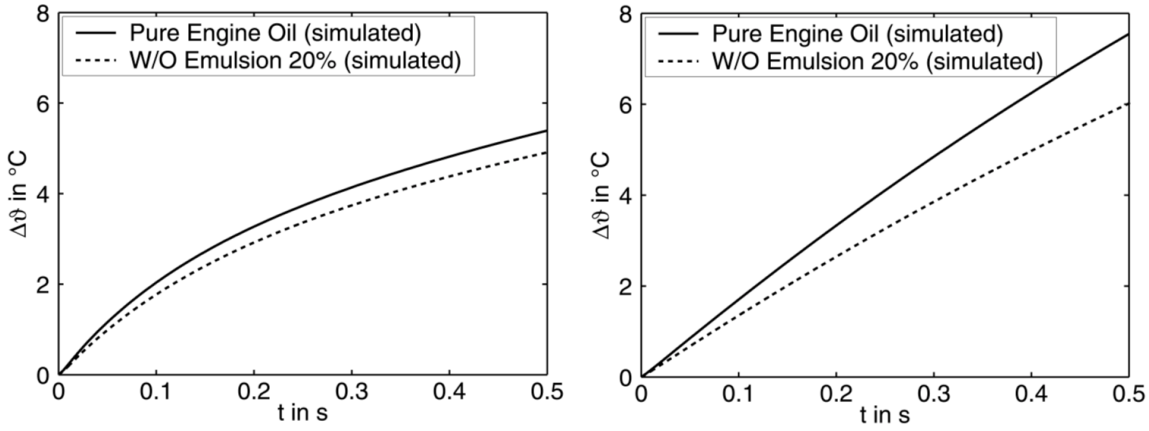

(a) (b)

Fig. 6: (a) Simulated temperature rise $\Delta\vartheta$ vs. time t of the initial transient for W/O emulsions of 20% b.v. and the pure oil. (b) Simulated temperature rise $\Delta\vartheta$ vs. time t for a glass substrate with a reduced thickness of 5 µm.

Conclusion

In this contribution we discussed the applicability of thermal conductivity sensing for liquid condition monitoring. As sample applications we considered the water contamination and the deterioration of mineral oils. For this purpose we performed experiments with a hot film sensor using a resistive thin-film molybdenum structure on a glass substrate. It could be shown that not only water-in-oil emulsions but also aged oils feature increased thermal conductivities compared to the base oils, which indicates that monitoring the thermal conductivity by means of miniaturized sensors could be utilized in oil condition monitoring systems. By means of numerical simulations it was furthermore found that the sensitivity of the sensing approach in the transient regime could be significantly increased by utilizing a thinner substrate, which, however, would reduce the mechanical robustness of the sensor.

Acknowledgements

This work was financially supported by the Austrian “Forschungsförderungsfonds für die gewerbliche Wirtschaft”, Project 806801.

References

[1] U. Grigull, and H. Sandner, “Wärmeleitung”, 2nd edition, Springer, 1990.

[2] J.J. Healy, J.J. de Groot, and J. Kestin, “The theory of the transient hot-wire method for measuring thermal conductivity”, Physica C, Vol. 82, 1976, pp. 392 - 408.

[3] S.E. Gustafsson, E. Karawacki, and M.N. Khan, “Transient hot-strip method for simultaneously measuring thermal conductivity and thermal diffusivity”, J. Phys. D: Appl. Phys., Vol. 12, 1979, pp. 1411 - 1421.

Microsensor for the Measurement of the Transepidermal Water Loss of Human Skin

M. Mündlein [1], R. Chabicovsky [1], J. Nicolics [1], B. Valentin [1], P. Svasek [2], E. Svasek [2], T. Komeda [3], H. Funakubo [3], T. Nagashima [3], M. Itoh [3]

[1]Institute of Sensor and Actuator Systems, Vienna University of Technology, A-1040 Wien

[2]Ludwig Boltzmann Institute of Biomedical Microtechnique, A-1040 Wien

[3]Shibaura Institute of Technology, Faculty of Systems Engineering, Saitama-City, 330-8570 Japan

We have developed a novel microsensor to measure the emission of water from human skin. Measurement of the transepidermal water loss (TEWL) is used for studying the water barrier function of the skin. The microsensor consists of a ceramic substrate carrying a thin film interdigital electrode system covered with a highly hygroscopic salt film. The change of capacitance of the electrode system per unit of time is a measure for the TEWL value. We demonstrate the different measuring results with normal skin and atopic skin.

Introduction

The protective function of the human skin shields the body not only from external influences (e.g. germs) but also prevents it from drying up. The stratum corneum (outer part of the skin) is flexible as long as it contains more than 10% water, but it becomes hard and brittle when dehydrated. Dermatologists universally recognize the unaffected skin of patients with atopic dermatitis by the fact that it tends to be dry and slightly scaly [1]. Different techniques have been developed to measure the skin properties that are influenced by the water content. Among the most widely used techniques are those involving the measurement of the skin impedance [2] – [5]. In this case the sensor chip must be brought into direct contact with the skin and therefore, a completely flat front surface of the sensor chip is necessary [6], [7]. One disadvantage of this type of sensor is the pollution of the chip caused by the skin.

A further possibility to investigate the skin health is the measurement of the transepidermal water loss (TEWL) expressed in grams per square meter and per hour [8] – [10]. This is an important parameter for evaluating the efficiency of the water barrier function. The more perfect the skin protective coat is, the higher the water content and the lower the TEWL. Disorders such as atopic dermatitis arise when the barrier function does not work properly. TEWL measurements allow the discovery of disturbances in the skin protective function in an early stage. By this way the onset of dermatological therapies can be accomplished in good time.

Different methods for TEWL measurement from local skin sites have been described: closed chamber methods and open chamber methods [9]. In this work we use a new type of sensor in a closed chamber arrangement. This arrangement offers the advantage of reduced influence of the environment resulting in more stable and reproducible measurements.

Measuring Principle and Sensor Technology

When the sensor device touches the skin a small hermetically closed measuring chamber is formed. A miniaturized humidity sensor is located on the top of this chamber in a distance of about 1.4 mm away from the skin surface (Fig. 1). The water vapor emitted from the skin fills the measuring chamber and causes an increasing relative humidity inside the chamber. A part of this humidity condenses on the comparable cold humidity sensor surface causing there a growing film of water. The growing rate of this film can be expressed by the change of the sensor impedance within a defined time interval.

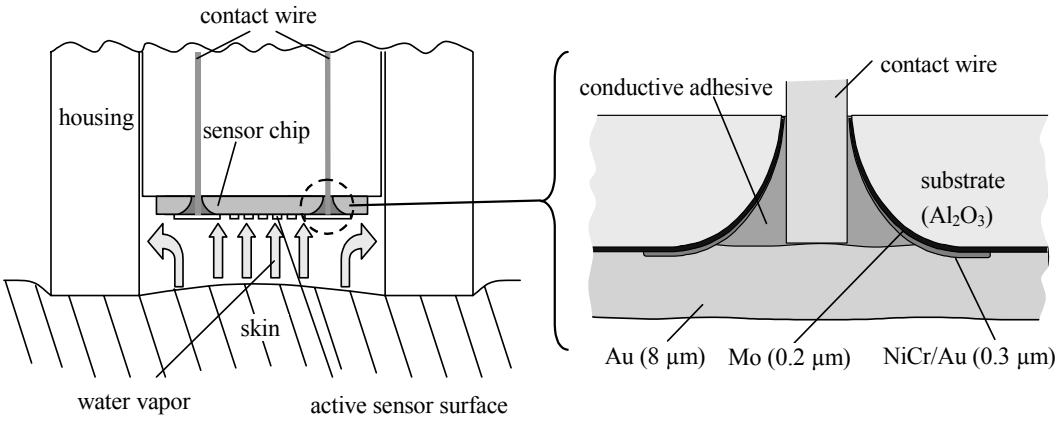

Fig. 1: Schematic cross sectional view of the TEWL-sensor with closed measuring chamber (increasing concentration of water vapor in the chamber after touching the skin). The funnel-shaped holes are produced by a special laser drilling process. The thick gold layer is deposited by electroplating.

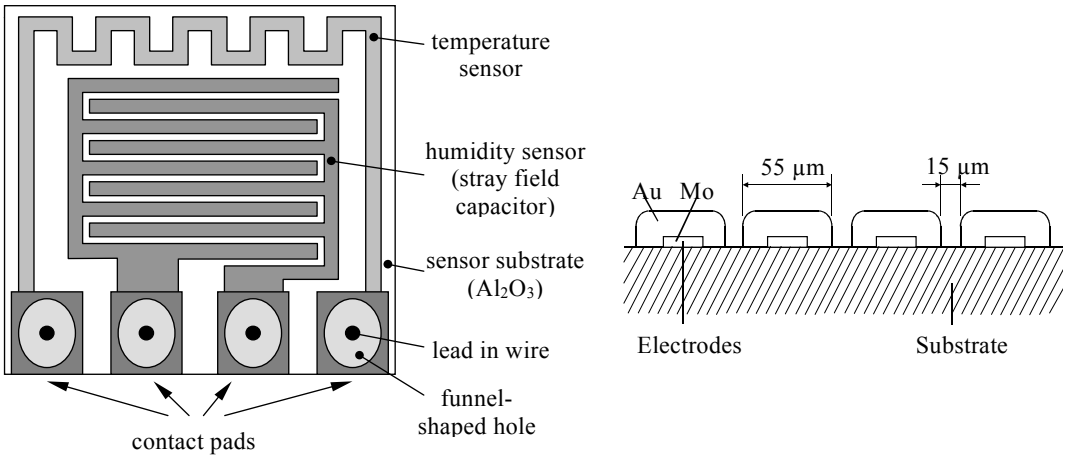

(a) (b)

Fig. 2: (a) Schematic structure of the thin film microsensor. The chip dimensions are 5 mm x 5 mm x 0.6 mm. (b) Schematic cross sectional view of the electrode system.

The novel microsensor used in this work consists of a small ceramic substrate (5 mm x 5 mm x 0.6 mm) carrying a metallic interdigital electrode system (Fig. 2). We have used a double-layer system of molybdenum and gold for the sensor electrodes. The molyb-

denum film has been deposited by rf-sputtering; the rather thick gold film (8 µm) has been produced by electroplating. The width of the electrodes is about 55 µm; the gap between them is approximately 15 µm. The active moisture sensing area is 1.75 mm x 3.15 mm. The contacts of the electrodes are made of a sputtered layer system of molybdenum, nickelchrome and gold. The lead-in wires are guided through funnel-shaped holes to the rear substrate surface (Fig. 1). These holes were laser-drilled into the ceramic substrate using a CO_2-laser. The lead-in wires are bonded to the contacts by using an isotropically conductive adhesive. The result is a completely flat front surface of the sensor [6], [7]. This fact is important for the application as a TEWL-sensor. The sensitivity is significantly improved by covering the active area of the sensor chip with a hygroscopic inorganic salt film. All technological work has been carried out in the Institute of Sensor and Actuator Systems of the Vienna University of Technology.

Measurements and Results

The measurements have been carried out in the Shibaura Institute of Technology in Japan. We have used an LCR-meter HP 4285A connected to a computer. The measuring frequency was 500 kHz and the measuring voltage was 100 mV. We have used an equivalent circuit R parallel C and the capacitance C was chosen as the output quantity (Fig. 3). However, for further measurements carried out at the Vienna University of Technology we have used the conductance as the output quantity [10].

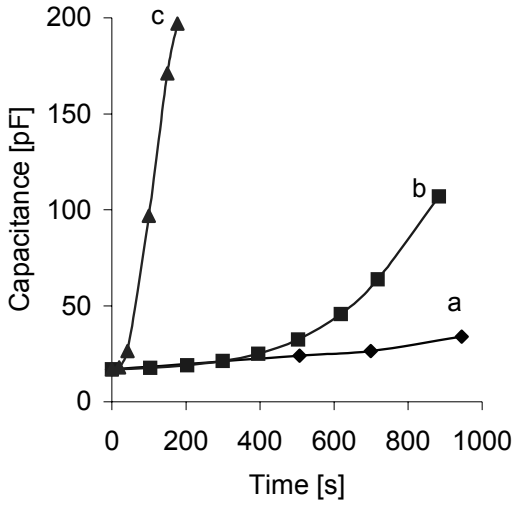

Fig. 3: Capacitance as a function of time. Curve a: normal skin of an elderly male person. Curve b: normal skin of a young male person. Curve c: atopic skin of a young male person. Measurements have been carried out at 500 kHz and 100 mV on the right forearm in a room with stable conditions (relative humidity 30%, temperature 23 °C).

Conclusion

The transepidermal water loss is an important factor for characterizing the health condition of human skin. TEWL measurements allow the discovery of dysfunctions of the skin even before they are visible. A measuring device with a novel moisture sensor in a closed chamber configuration has been introduced. The slope of the capacitance vs. time characteristic of the sensor can be used as a measure for the TEWL-value of the investigated skin.

Acknowledgements

We are very grateful to Prof. Dr. Fritz Paschke, Vienna University of Technology, for financial support. Furthermore, we want to thank Prof. Dr. Ryszard Jachowicz, Warsaw University of Technology, for valuable discussions on the topic of this paper. We also acknowledge the friendly assistance of Prof. Dr. Jolanta Schmidt from the University Clinic of Dermatology, Medical University Vienna.

References

[1] M. Watanabe, H. Tagami, I. Horii, M. Takahashi, A.M. Kligmann: “Functional analyses of the superficial stratum corneum in atopic xerosis”, Arch. Dermatol. 127, 1991, pp. 1689-1692.

[2] M. Mündlein, J. Nicolics, R. Chabicovsky, N. Sekiguchi, T. Komeda, H. Funakubo, G. Stangl: “Innovative packaging concept of a miniaturized skin moisture sensor and first measuring results”, Proc. 2nd European Medical and Biological Engineering Conference-EMBEC 2002, Vienna, Austria, December 4-8, 2002, pp. 968-969.

[3] N. Sekiguchi, T. Komeda, H. Funakubo, R. Chabicovsky, J. Nicolics, G. Stangl: “Microsensor for the measurement of water content in the human skin”, Proc. 14th European Conference on Solid-State Transducers (EUROSENSORS XIV), August 27-30, 2000, Copenhagen, Denmark, pp. 407-410.

[4] M. Mündlein, A. Brunner, J. Nicolics, R. Chabicovsky, N. Sekiguchi, T. Suzuki: “Prototype of a skin humidity sensor and initial experiments”, Proc. 25th International Spring Seminar on Electronics Technology (ISSE 2002), Prague, Czech Republic, May 11-14, 2002, pp. 95-99.

[5] N. Sekiguchi, T. Komeda, H. Funakubo, R. Chabicovsky, J. Nicolics, G. Stangl: “Microsensor for the measurement of water content in the human skin”, Sensors and Actuators B 78 (2001), pp. 326-330.

[6] M. Mündlein, A. Brunner, R. Chabicovsky, G. Stangl, J. Nicolics: “A new interconnection technology for the attachment of sensors”, Proc. 24th International Spring Seminar on Electronics Technology (ISSE 2001), Calimanesti-Caciulata, Romania, May 5-9, 2001, pp. 277-281.

[7] G. Hanreich, J. Nicolics, M. Mündlein, H. Hauser, R. Chabicovsky: “A new bonding technique for human skin humidity sensors”, Sensors and Actuators A 92 (2001), pp. 364-369.

[8] J. Serup, G. Jemec: “Handbook of non-invasive methods and the skin”, Chapter 9.1, J. Pinnagoda, R.A. Tupker, “Measurement of the Transepidermal Water Loss”, CRC Press Inc., 1995, pp. 173-178.

[9] M. Mündlein, J. Nicolics, R. Chabicovsky, P. Svasek, E. Svasek, T. Komeda, H. Funakubo, T. Nagashima, M. Itoh: “Packaging of a thin film sensor for transepidermal water loss measurements”, Proc. 26th International Spring Seminar on Electronics Technology, May 8-11, 2003, Stara Lesna, Slovak Republic, pp. 328-333.

[10] B. Valentin, M. Mündlein, R. Chabicovsky, J. Nicolics: “Evaluation of a novel transepidermal water loss sensor”, CD-ROM Proceedings of the IEEE Sensors 2004 Conference, Vienna, Austria, October 24-27, 2004, pp. 115-118.

Particle Discrimination with an Improved Projection Cytometer

J.H. Nieuwenhuis [1], P. Svasek [2], P.M. Sarro [3], M.J. Vellekoop [1]

[1] Institute of Sensor and Actuator Systems, Center for Micro and Nanostructures, Vienna University of Technology, Austria

[2] Ludwig Boltzmann Institute of Biomedical Microtechnology, Vienna, Austria

[3] Laboratory of ECTM – DIMES, Delft University of Technology, Delft, The Netherlands

An integrated cytometer is presented based on optical projection. A sheath flow focuses the particles closely over an integrated optical sensor capable of counting, sizing and measuring the shape of particles. Measurements demonstrate good repeatability and the ability to discriminate between particles based on their optical properties.

Cytometers are instruments for particle analysis based on the optical properties of the particle. In literature different integrated sheath-flow chambers have been presented (some early ones can be found in [1], [2]), but the optical sensors are often located off-chip. In this paper an integrated projection cytometer is presented that has a built-in optical sensor.

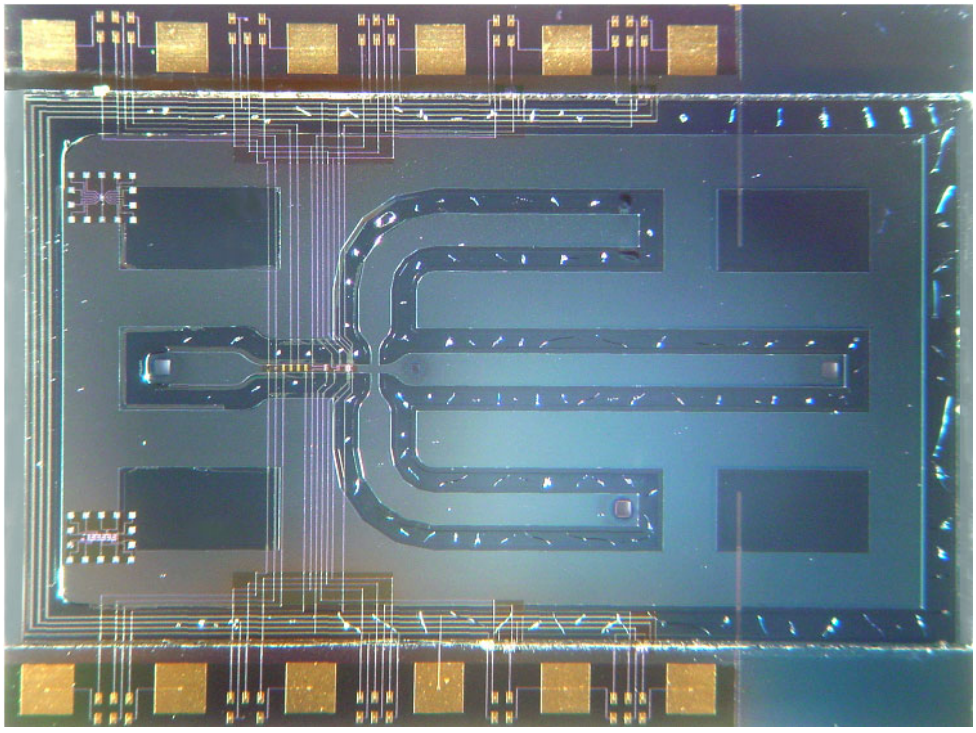

Fig. 1: The cytometer chip (1.5 x 2 cm^2)

The device (Fig. 1) consists of a transparent flow-channel that has an elongated photo-diode (1 x 50 μm^2) integrated in the bottom of this channel, aligned perpendicular to the direction of flow. By means of a non-coaxial sheath flow the sample liquid containing the particles is focused over the optical sensor. The chip is illuminated from the top and when a particle now passes over the sensor its optical properties are registered. The small projection distance realized by the sheath-flow minimizes the optical distortion of the particle projection, without the need for any additional optical components.

The shape of the sensor signal, caused by a passing particle, depends on the optical properties of the particle (Fig. 2). Since the sensor only consists of a single photodiode the optical properties of the particle are integrated along a line perpendicular to the direction of flow.

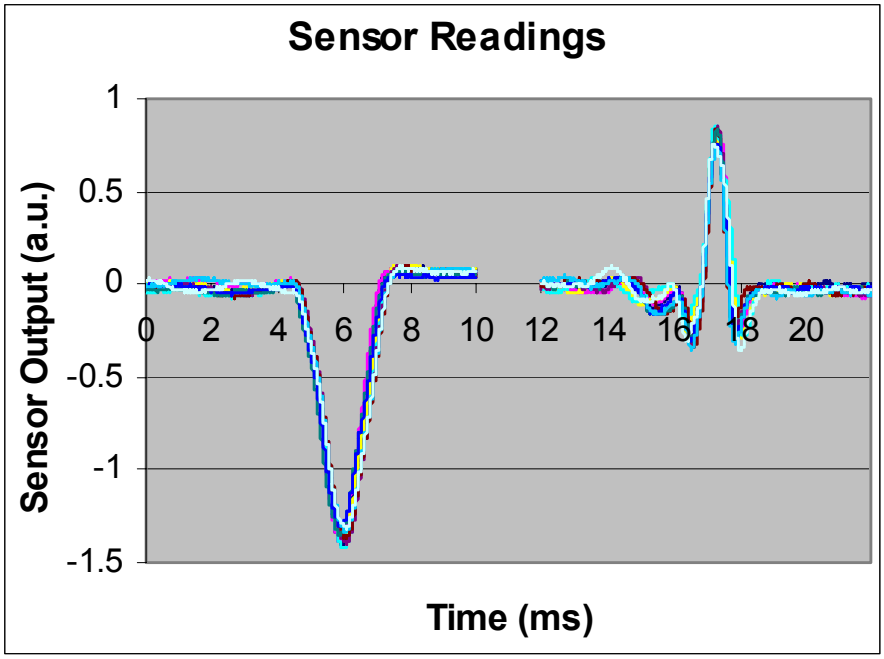

Fig. 2: Ten measurements printed on top of each other for 10 µm radius silver coated particles (left) and 12 µm radius plain particles (right) demonstrate the repeat-ability

References

[1] R. Miyake, H. Ohki, I. Yamazaki, R. Yabe, A Development of Micro Sheath Flow Chamber, proc. of MEMS '91, 1991, pp. 265-270.

[2] D. Sobek, A.M. Young, M.L. Gray, S.D. Senturia, "A microfabricated flow chamber for optical measurement in fluids", proc. MEMS '93, 1993, pp. 219-224.

Sensor Interface Electronics

Daniel Rocha

Industrial Sensor Systems, Institute of Sensor and Actuator Systems
Vienna University of Technology, Austria

The importance of tailored electronic readout circuits in biosensing applications has in the past often been neglected. In this contribution we demonstrate the relevance of the issue considering a practical example of closely coupled co-design of micro- and nanosystems: a high-quality recording platform for single ion channel measurements on functionalized artificial lipid membranes.

Introduction

Ion-channels on cell membranes play crucial roles in physiology and pathophysiology and are important drug targets [1]. Microelectrode-based electrophysiological techniques which access the interior of a cell and can directly measure the minute currents through these channels have been employed in the past for the study of ion-channels.

The most successful of these techniques and the current golden standard is the patch-clamp technique [2]. Although traditionally performed manually and thus yielding very low throughputs in the order of 10 data points/technician/day, during the last decade several automated high-throughput screening (HTS) lab-on-a-chip systems have been proposed which have throughput rates going up to 20.000 data points/day [3]. The quality of the data produced by these systems is however not yet high enough to resolve single ion-channel currents in a repeatable manner.

Recording the sub-picoampere currents flowing through single ion channels in cell membranes with sub-millisecond resolution has up to date been difficult and often impossible due to both the limitations of the readout electronics and the difficulty of establishing a repeatable clean interface between the cell and the biosensor so as to form a so-called gigaseal. Yet, such recordings would yield valuable information in the study of the highly dynamic processes occurring upon e.g. channel gating or the membrane relaxation after potential steps and phase transitions and thus open way to significant advances in ion channel research.

In this paper we describe a low-noise amplifier design which is part of a planar patch-clamp chip being developed at our institute in cooperation with the Centre of Nanobiotechnology (CNB, University of Natural Resources and Applied Sciences, Vienna, Austria) for the recording of single ion channel currents on arrays of functionalized supported artificial lipid bilayer membrane (BLM) patches The topic of this contribution is the design of an amplifier for optimal noise performance to be employed in single ion channel current measurements.

Envisioned System

Together with the CNB [4] we are developing a low-noise single ion-channel recording platform in which an array of functionalized artificial lipid membrane patches with implanted ion channels will be patterned on a solid support (see Fig. 1) including provision for a clean interface to the electronic measurement setup.

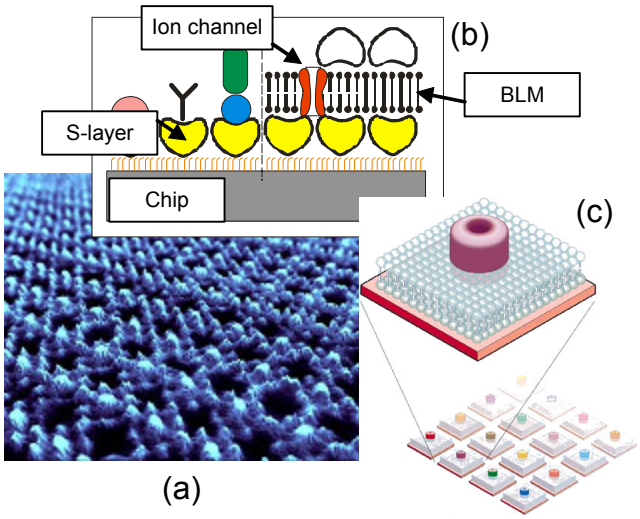

Fig. 1: Functionalized supported lipid bilayer membranes (BLM) [4]. (a) AFM of BLM support layer based on S-layer proteins. (CNB/BoKu), (b) and (c) schematic representations of respectively a supported BLM and an array of BLMs with implanted ion channels.

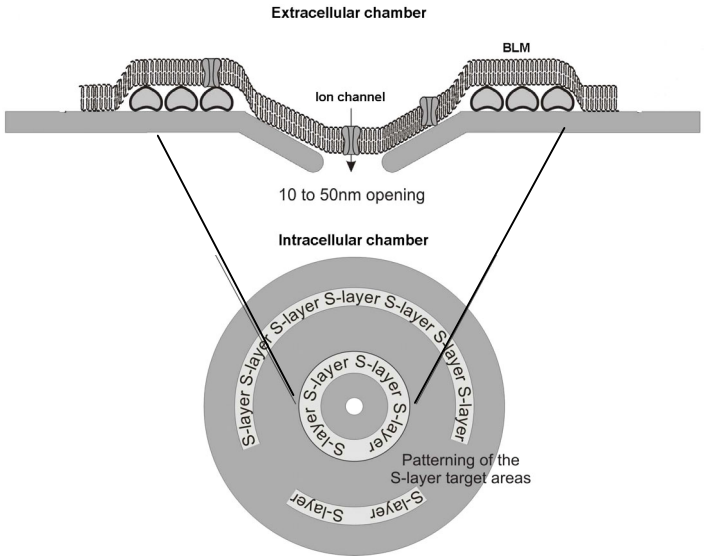

Fig. 2: Biomimetic cell-chip interface for improved adhesion of the cell membrane to the substrate so as to reach seal resistances in the order of 100 GΩ and above. Side view (top figure). Top view (bottom figure).

When looking at the minimization of noise, one of the most important features for high quality single ion channel recordings is a good seal between the intra and extracellular measurement chambers. Any current path having a conductance comparable to a single ion channel's conductance (1 – 150 pS) would generate an excessive amount of noise and lead to it being impossible to discern the minute signal current flowing through the ion channel from the noise generated by the leakage conductance.

On the one hand, we intend to improve the seal impedance by one order of magnitude when compared to traditional on-chip patch-clamp measurement setups so as to reach

seal resistances in the order of 100 GΩ and above. For that purpose we will employ a biomimetic interface based on S-layer proteins (see Fig. 2). By providing conditions which closely match the cell's natural environment, we expect the adhesion to the substrate to be vastly improved thus yielding better quality seals.

On the other hand, low-noise electronics need to be delivered, which will amplify the low-power signals to more robust levels that may easily be transported off-chip for further processing. The design of such an amplifier is the subject of the following section.

Optimal Low-Noise Amplifier Design

In the quest towards studying singular ion channels artificially implanted into engineered BLM patches having widths and lengths in the range of a few hundred nanometers, the need arises for optimal interfacing between the biosensor and the readout electronics.

In order to reach input-referred noise levels well below 100 fA in a band from 0 to 20 kHz, one must necessarily match the amplifier's input stage to the source impedance. An electrical lumped-element model corresponding to a membrane patch including the seal impedance and the access resistance is given in Fig. 3. This impedance is seen to be mainly capacitive in the frequency range of interest.

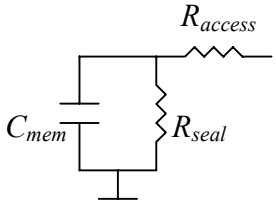

Fig. 3: Lumped element model of a membrane patch. C_{mem} has a typical density of 1 µF / cm^2 , for the 1 µm^2 patches we are targeting C_{mem} ≈ 10 fF. A good seal will have resistances of R_{seal} > 100 GΩ and R_{access} will typically be a few MΩ. For the frequencies of interest, the one dominant component is C_{mem}.

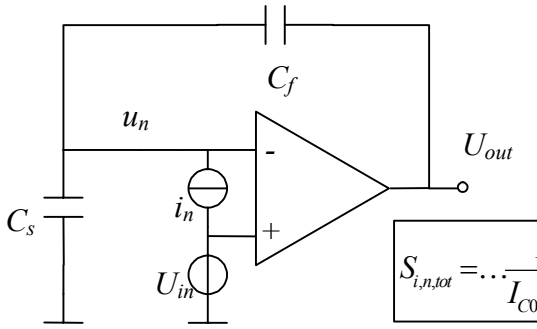

Eq. 1

$$S_{i,n,tot} = \ldots \frac{L^2}{I_{C0} C_{g,tot}} \omega^2 \left(C_f + C_s + C_{g,tot} \right)^2 \left(1 + \frac{f_k}{f} \right)$$

Fig. 4: Feedback configuration including noise sources u_n and i_n. Equation 1 shows the dependence of the total input-referred noise current power spectral density with C_s, C_f, the total gate capacitance $C_{g,tot}$, the gate length of the input transistor L and the inversion coefficient I_{C0}. One can see that L should be chosen to be minimal, the transistor should biased deep in strong inversion and $C_{g,tot}$ should be equal to C_f + C_s

One possible feedback configuration for the amplifier would be the transimpedance amplifier shown in Fig. 4. Notice that capacitive feedback has been used in order to eliminate noise contributions stemming from the passive elements. The main source of noise thus comes from the amplifier itself and is originated mainly by the drain noise current. It can be modeled by the two equivalent sources i_n and u_n at the amplifier's input port (see Fig. 4), where it can be shown that i_n is proportional to $C_{g,tot} = C_{gs} + C_{gd}$ and u_n is inversely proportional to $C_{g,tot}$. Both noise sources have a component stemming from the drain current's thermal noise and another due to its 1/f noise. The thermal noise component is minimized for a minimal gate length L, $C_{g,tot} = C_f + C_s$ and when the input stage is biased deep in strong inversion (I_{C0} >> 1, see Equation 1 in Fig. 4 and Fig. 6).

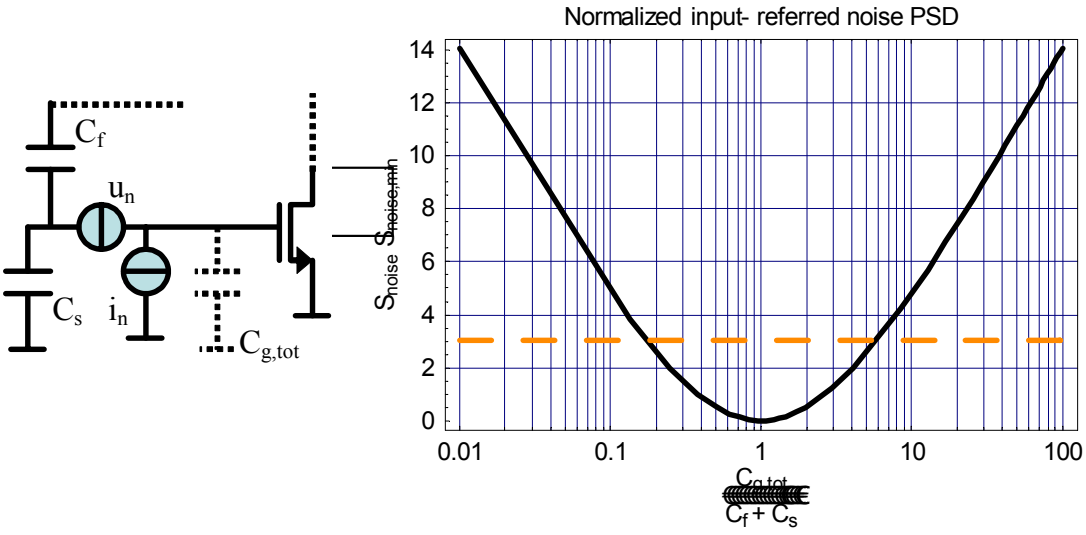

Fig. 5: Normalized input-referred noise power spectral density (PSD) as a function of the ratio of the input stage's capacitance ($C_{g,tot}$) and the sum of the feedback and source capacitances (C_f+C_s).

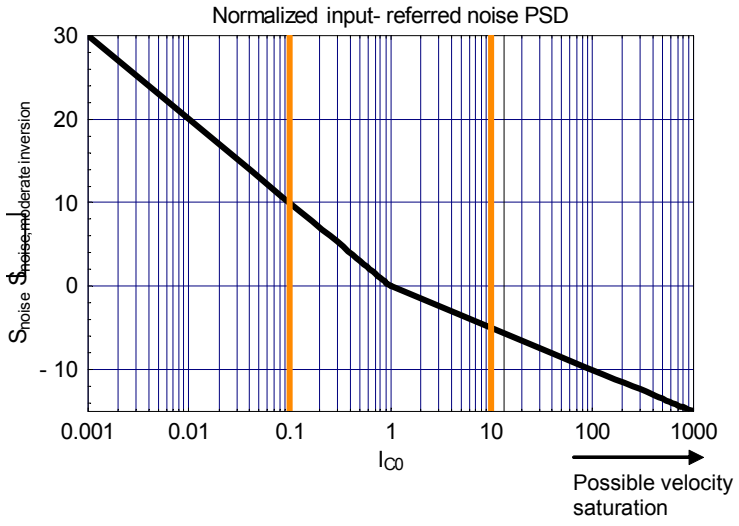

Fig. 6: Normalized input-referred power spectral density (PSD) as a function of the inversion coefficient (where I_{C0} = 1 corresponds to the center of moderate inversion)

For the very small source capacitances corresponding to nanosized BLM patches, the optimal input stage transistor sizes will thus become very small, consequently yielding an increase in 1/f noise. In order to reduce the 1/f noise component, the autozeroed architecture depicted in Fig. 7 has been employed [5]. It uses an auxiliary amplifier for reducing the 1/f noise component of the main amplifier and has the advantage that both input terminals of the main amplifier are permanently usable, as needed for the feedback configuration depicted in Fig. 4. On phase Φ_2, the auxiliary amplifier autozeroes itself in order to become a very low-offset amplifier which is subsequently used for measuring the main amplifier's offset and 1/f noise, canceling it via a low-frequency feedback path.

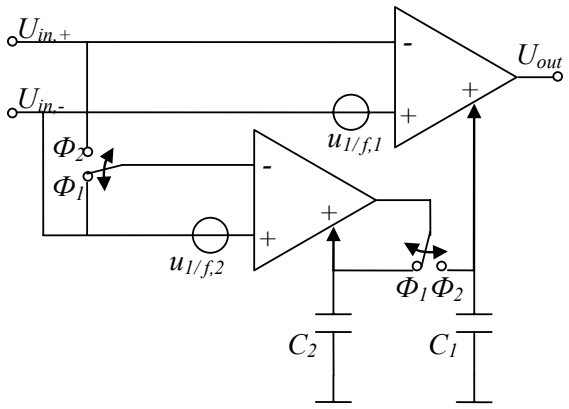

Fig. 7: Autozeroed amplifier. Both the main and the auxiliary amplifiers have an additional control input for offset cancellation. $U_{out}=A\ (U_{in+} - U_{in-}) + A_{Az}\ U_{1/f}$. On phase Φ_1 the auxiliary amp autozeroes itself, thus becoming a very low offset sense amplifier for the main amp's offset voltage which is detected on phase Φ_2. The control voltages are held on capacitors C_1 and C_2 respectively during phases Φ_1 and Φ_2 respectively.

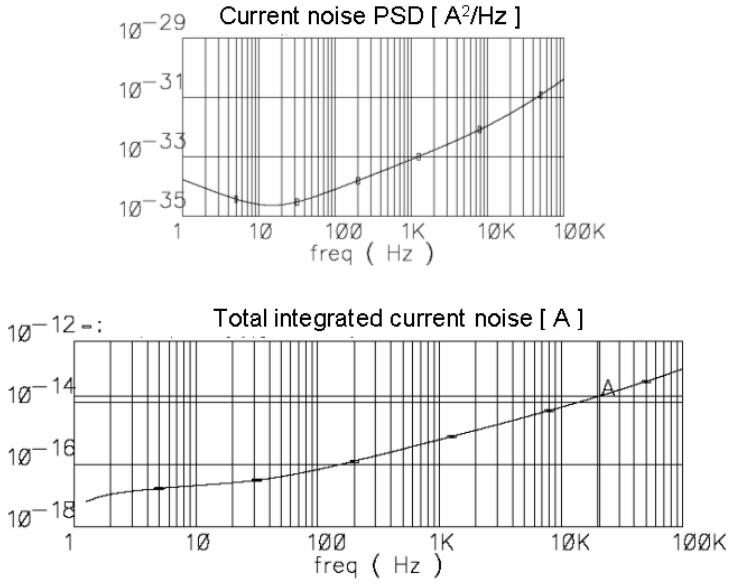

Fig. 8: Simulated noise power spectral density (top) total input-referred noise current. Results obtained with periodic noise analysis using Spectre RF simulator. At 20 kHz a total inband noise of 16.4 fA was obtained.

Simulation results show that it is possible to reach noise levels of about 17 fA for 1 µm x 1 µm patches using a standard 0.8 µm CMOS process from austriaMicrosystems (see Fig. 8).

Conclusion

The design of a low-noise amplifier for optimal noise performance to be employed in a state-of-the-art recording platform for the measurement of sub-picoampere currents flowing through single ion channels implanted on artificial lipid bilayer membrane (BLM) patches has been presented. The resulting amplifier features a simulated total inband noise of 16.4 fA in a band spanning from 0 to 20 kHz, which represents about one order of magnitude improvement in noise performance when compared to current state-of-the-art patch-clamp amplifiers.

Acknowledgements

The author would like the thank Professors Dr. U. Sleytr, Dr. D. Pum and Dr. B. Schuster of the Centre of NanoBiotechnology (CNB, University of Natural Resources and Applied Sciences, Vienna, Austria) for the close cooperation during the past year.

References

[1] Hille, B., *Ion Channels of Excitable Membranes*. 3rd ed. 2001: Sinauer Associates.

[2] Sakmann, B. and E. Neher, *Single-Channel Recording*. 2nd ed. 1995: Kluwer Academic Publishers.

[3] Comley, J., *Patchers vs. Screeners.* Drug Discovery World, 2003: pp. 47-57.

[4] Pum, D.; Schuster, B.; Sara, M.; Sleytr, U.B., *Functionalisation of surfaces with S-layers*, IEE Proceedings - Nanobiotechnology, vol. 151 (3), pp. 83-86, Jun. 2004.

[5] Coln, M.C.W., *Chopper stabilization of MOS operational amplifiers using feed-forward techniques*, IEEE J. Solid-State Circ., vol. 16, pp. 745-748, Dec. 1981.

SU-8-Based Fluidic Devices

P. Svasek [1], E. Svasek [1], B. Lendl [3], M. Vellekoop [2]

[1] Ludwig Boltzmann Institute of Biomedical Microtechnology, Gusshausstrasse 27-29, A-1040 Vienna, Austria

[2] Institute of Sensor and Actuator Systems, Vienna University of Technology, Austria

[3] Institute of Chemical Technology and Analytics, Vienna University of Technology, Austria

Introduction

During the last years SU-8 has become a widely used material for MEMS and miniaturized fluidic devices. It can be deposited by spin- or spray coating in a wide range of layer thicknesses. Because of the low UV absorption of the resist a standard UV mask aligner can be used for exposure, even for thick layers. Processing of SU-8 includes the following steps:

1. Deposition of the resist by spray- or spin coating
2. Drying at 95 °C on a hotplate
3. Exposure
4. Post exposure bake (PEB): Crosslinking of exposed resist
5. Development: unexposed resist is dissolved
6. Hardbake: The remaining structures are completely crosslinked. The resist gets its final mechanical strength and chemical stability.

Flow cell for Infrared Detection in Capillary Electrophoresis Systems

To use FTIR-spectroscopy as a powerful detection method in capillary electrophoresis an infrared transparent flow cell had to be designed because the fused silica capillaries normally used in CE are not transparent to IR. An appropriate material for infrared transparent devices is CaF_2. It shows very good optical properties, i.e. high transmittance in the mid-IR range (wavenumber 4000...700).

Fabrication of the CE cell

The cell consists of two plates of CaF_2, each 1 mm thick (see Fig. 1). On one of these plates there is a Titanium layer which acts as an optical aperture. This is necessary because with the given optical setup the IR-beam cannot be focused inside the flow channel only. The 200 nm thick titanium layer is deposited by evaporation and patterned by conventional lift-off technique. This metal structure must be completely isolated from the flow channel, otherwise gas bubbles would be produced by electrolysis.

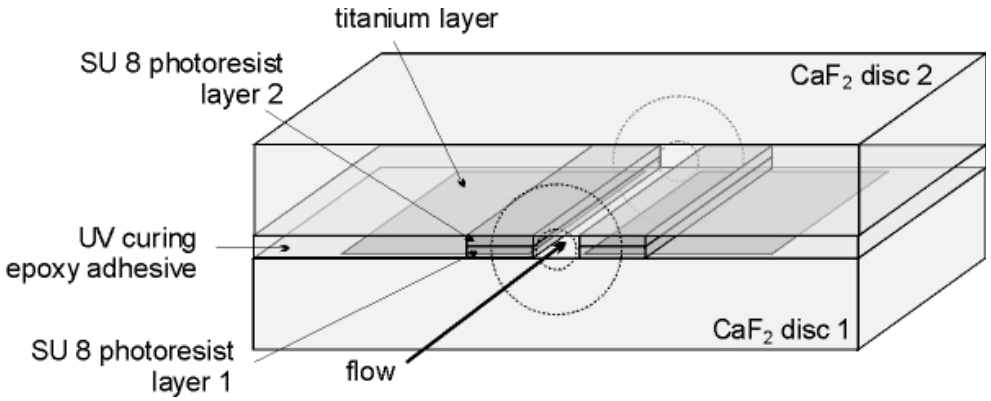

Fig. 1 Schematic drawing of the CE-cell

The channel is formed by two lines of SU-8 on each CaF_2 plate, each of them 100 µm wide. The distance between these two lines and thus the width of the channel is 150 µm. The height of the SU-8 lines is 7.5 µm, half of the desired height of the cell. The CaF_2 wafers (diameter 30 mm, thickness 1 mm) are spin-coated with SU-8 and softbaked. After UV-exposure using a SUSS MJB3 mask aligner and an appropriate photomask the resist is post-exposure-baked (90 °C for 10 min.) and developed. The unexposed and therefore not crosslinked areas are dissolved during the development process. The developer used is PGMEA (propylene glycol monomethyl ether acetate).

Two wafers (one with and one without metal structure) are superimposed, aligned and pressed against each other during the hardbake process. Consequently a bond is established between corresponding SU-8 structures because the hardbake temperature of 200 °C induces the complete crosslinking of the SU-8. This hardbake is necessary to achieve the full mechanical strength and chemical resistance of the SU-8.

Finally the area outside the SU-8 lines is filled with UV-curing epoxy adhesive (Delo Katiobond 4653) and the waferstack is diced with a dicing saw. We get 40 devices from one waferstack with a diameter of 30 mm. The final dimension of the cell is 2 x 5 x 2 mm^3. The capillaries (I.D. 50 µm, O.D 360 µm) are coupled to the cell by means of a metal support and an elastic gasket that is applied to the tip of each capillary [1].

The two surfaces of each cell where the capillaries are coupled (inlet and outlet of the flow channel) are polished with 3 µm lapping film to achieve a tight connection between the capillaries and the cell. Results obtained with the help of this setup are discussed elsewhere [1], [4].

Micromixer for FTIR-Spectroscopy

This mixing device is used for the investigation of chemical reactions by FTIR-spectroscopy combined with in-situ mixing of two reactants. The IR-beam directly passes the mixing chamber. The optical pathlength (the height of the mixing chamber) is 10 µm (see Fig. 2). The optical pathlength should not exceed 20 µm because of the strong absorption of water and organic solvents in the mid-IR region, which otherwise would result in a bad signal-noise-ratio.

The mixing device is Y-shaped. Two sheets of liquid are superimposed inside the mixing chamber and mixed by diffusion. Because of the cross-section of the mixing chamber (1 mm wide, 10 µm high) the mixing time is approx. 50 ms. The mixer is used in the “stopped-flow-mode”, i.e. the two liquids are injected by means of a double syringe pump. The two streams are separated by the separation membrane until they meet

inside the mixing chamber. This membrane is a 2 µm thick silver membrane. During the injection there is hardly any premixing. Then the flow is stopped, the reactants are mixed by vertical diffusion and the chemical reaction takes place. This reaction is investigated by time resolved FTIR-spectroscopy [2], [3]. The micromixer is fabricated by means of a 2-layer lithography, which combines SU-8 and metal, together with a polymer-based wafer bonding technique.

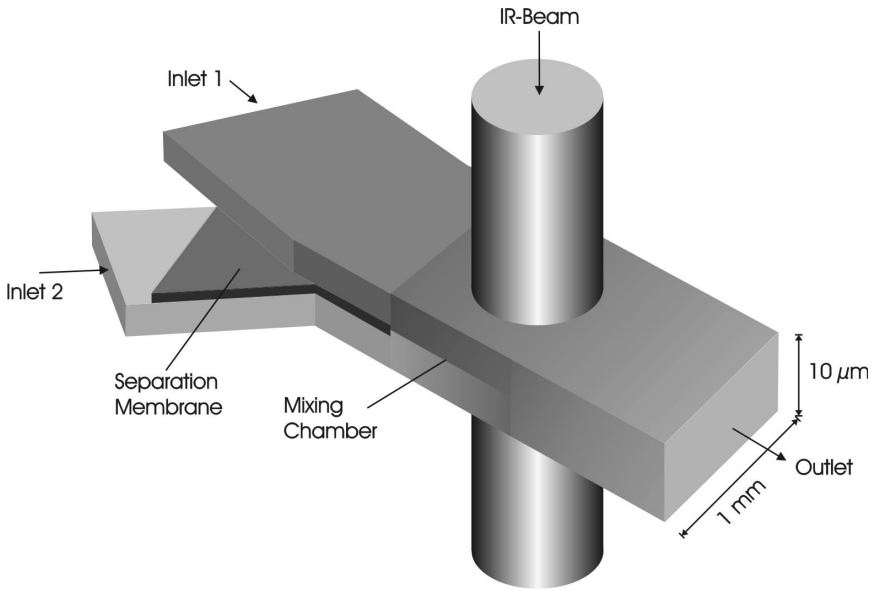

Fig. 2: Principle of the Micromixer (drawing not to scale)

Preparation of the Micromixer

As mentioned above, Calcium Fluoride is used as substrate material. The wafers which are used have a diameter of 100 mm, a thickness of 1 mm and are double side polished. A 4 µm thick layer of SU-8 is deposited by spin-coating onto both wafers. To achieve this layer thickness, the SU-8-50, which has a rather high viscosity, has to be diluted 4:1 (vol.) with GBL (gamma-butyro-lactone). Spin coating is done at 5000 rpm. After spin-coating the wafers are softbaked at 90 °C for 30 min. Exposure of wafer #1 is done by means of a SUSS MA 150 mask aligner. Wafer #1 is the bottom wafer. It carries the structures for inlet 2 and the separation membrane (see Fig. 2). Exposure is followed by a post-exposure bake at 90 °C for 10 min. The baking processes are performed using a hotplate.

To form the separation membrane a 2 µm thick metal layer is deposited by evaporation on top of the exposed (but undeveloped) SU-8 layer. We choose Ag as a material for this layer for two reasons: Evaporated Ag layers show no internal stress and therefore they do not bend when released. Additionally, it is possible to deposit Ag by thermal evaporation with relatively low power at a temperature well below 1000 °C. Consequently no UV light is generated, which would otherwise expose the wafer during the evaporation process, because the SU-8 layer is still sensitive to light. Evaporation is done in a Balzers BAK 550 evaporation system.

The Ag layer is then covered by positive photoresist AZ 1512 HS. The photoresist is processed as usual and the Ag layer is wet etched to form the structure of the separation membrane. As an etchant a 45% (WT) solution of Fe(NO3)3 in water is used. This solution does not attack the SU-8. The photomask for the Ag layer is compensated for the underetch of the Ag structure.

Finally the AZ positive resist is removed by undiluted developer AZ 400k and the SU-8 structure is developed with PGMEA. To dissolve unexposed SU-8 underneath the metal structure takes quite some time (approx. 2 hours for channels of 1 mm length). Wafer #1 now carries the structures of inlet 2 and the separation membrane (see Fig. 3). The narrow SU-8-lines inside the flow channel are necessary to guide the flow and to keep the Ag membrane in place.

On wafer #2 (the top wafer) the structure of inlet 2 is fabricated as usual from a 4 µm thick layer of SU-8. Subsequently the holes for 2 inlets and 1 outlet per mixer are drilled by means of a high speed spindle and diamond tools. So far the SU-8 structures on both wafers are not hardbaked and therefore the polymer is still able to establish a bond to other materials during hardbake.

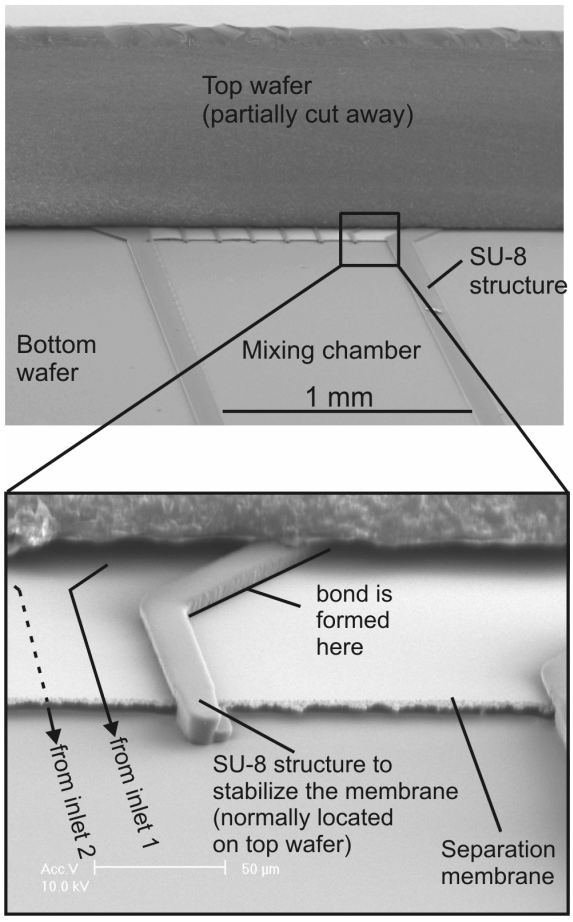

Fig. 3: SEM micrograph of the mixing device with the top wafer partially cut away

To complete the production process of the micromixer both wafers need to be bonded together in order to form a closed fluidic structure. The simple bonding process which was described in this paper for bonding of the CE cell wafers can be applied for the micromixer as well, but shows a poor yield in this case.

SU-8 Wafer Bonding

Both wafers are superimposed to form a sandwich configuration, and aligned. Hardbaking is done in an EVG 501 wafer bonder. The wafers are pressed against each other with a contact force of 2000 N and heated to 180 °C for 1 hour. Because of this high

temperature the SU-8 is hardbaked and a bond is established between the SU-8 structure on the top wafer and the SU-8-Ag-structure on the bottom wafer (see Fig. 3).

A drawback of this bonding method is the fact that the layer thickness uniformity of spin-coated SU-8 layers is limited. For a layer thickness of approx. 4 µm we were able to achieve thickness differences as low as 0,05 µm. Due to these differences the corresponding structures are not completely in close contact. Therefore some voids remain after bonding.

To overcome this problem it is possible to increase the contact force. SU-8-structures which are not hardbaked are plastic and can be deformed. Consequently some gaps or voids can be closed if a higher contact force is applied. The required force depends on the contact area as well as on the aspect ratio of the structures to be bonded. For this reason this method is feasible for the CE-cell (higher structures, smaller wafers), but not for the micromixer (lower structures, larger wafers). If the structures are deformed too much, the desired shape and height of the fluidic structures can not be maintained and will vary throughout the wafer area.

Another way to avoid insufficient bonding is to add some soft “adhesive” which fills the gaps caused by non-uniform layer thickness. Again the material of choice is SU-8, but this time without UV exposure. Unexposed SU-8 is thermoplastic, and it even fills gaps because of capillary forces. SU-8 is crosslinked when heated to 150...200 °C – it behaves like thermally cured epoxy adhesive.

If SU-8 is used for building fluid structures and – in unexposed form – for waferbonding, the unexposed SU-8 has to be patterned. This method is described in Fig. 4:

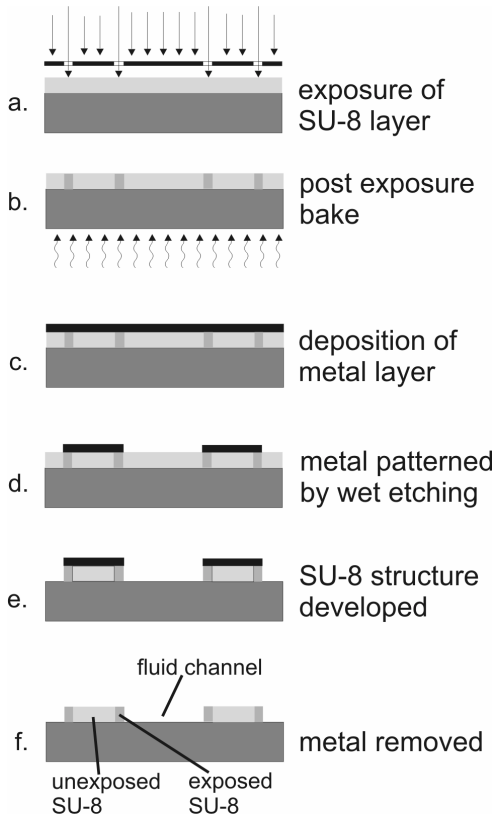

Fig. 4: Preparation of the top wafer for bonding. The drawing shows the cross-section of a channel and its sidewalls

After exposure and PEB (see Fig 4 (a) and (b)) a metal layer is deposited on top of the SU-8 layer by evaporation. This metal layer (1 µm Ag) is patterned by wet etching (see Fig. 4 (c) and (d)). Now the areas where unexposed SU-8 is necessary for bonding are surrounded by narrow lines of exposed (hard) SU-8 and covered by metal. After development of SU-8 and removal of the metal layer (see Fig. 4 (e) and (f)) the wafer is ready for bonding.

With this bonding method it is not necessary to apply a high contact force, because remaining gaps are closed by the unexposed (soft) SU-8. Therefore the structures are not deformed and their correct height and shape is maintained during the bonding process.

Alignment of the wafers for bonding is done in an EVG AL6 mask aligner. Then the waferstack is clamped to the bond tool and inserted into an EVG 501 wafer bonder.

Bond parameters are as follows:

1. Contact force of 1000 N is applied. Temperature of top and bottom heaters is ramped up to 180 °C with a ramp of 3 °C/min.
2. Temperature of 180 °C is maintained for 1 h
3. Temperature is ramped down to room temperature with a ramp of 2 °C/min.
4. Contact force is removed

Conclusion

With the method described in this paper it is possible to manufacture miniaturized fluidic devices in a batch process. The combination of SU-8 and metal layers allows building up structures which contain fluid channels in more than one plane.

Wafer bonding with SU-8 is a method for the batch fabrication of closed fluidic devices. If infrared transparent wafers are used these devices can be used for IR spectroscopy.

If hard and soft (i.e. exposed and unexposed) SU-8 is used in combination, this wafer bonding method is a means to overcome the problem of non-uniform layer thickness of the SU-8 layers. Additionally, this method allows the bonding of wafers which contain e.g. conducting lines or other structures that cause a topographic surface.

References

[1] M. Kölhed, P. Hinsmann, P. Svasek, J. Frank, B. Karlberg, B. Lendl: On-Line Fourier Transform Infrared Detection in Capillary Electrophoresis; Anal. Chem., 74 (2002), 3843 - 3848.

[2] P. Hinsmann, J. Frank, P. Svasek, M. Harasek, B. Lendl: Design, Simulation and Application of a new Micromixing Device for Time Resolved Infrared Spectroscopy of Chemical Reactions in Solution; Lab on a Chip, 1 (2001), 16 - 21.

[3] B. Lendl, P. Hinsmann, P. Svasek, J. Frank: Device for Label-Free Bio-Ligand Interaction Studies based on Time resolved Fourier Transform Infrared Spectrometry; Proceedings of the µTAS 2002 Symposium; (2002), ISBN: 1-420-1009-5; 221 - 223.

[4] B. Lendl, M. Kölhed, P. Hinsmann, M. Haberkorn, P. Svasek, B. Karlberg: Online Mid-IR (Quantum Cascade Laser and FTIR Spectrometric) Detection in Capillary Based Separation Systems; Proceedings of the µTAS 2002 Symposium; (2002), ISBN: 1-4020-1009-5; 599 - 601.

3-901578-14-5